Max-Planck-Institut für Physik
(Werner-Heisenberg-Institut)

First Observations of the GRB Prompt and Early Afterglow Emission Phase at $\sim 100\,\mathrm{GeV}$ Energy Regime with the 17 m Ø MAGIC Imaging Atmospheric Cherenkov Telescope

Dissertation an der Mathematisch-Naturwissenschaftlichen Fakultät
der Universität Rostock
vorgelegt von

Markus Garczarczyk

Summary

Gamma ray bursts (GRBs) are one of the most enigmatic cosmic objects, releasing enormous amount of energy in our cosmos within a very short time. My thesis deals with the search for very high energy (VHE) gamma-ray (shortcut γ-ray) emission from GRBs with the MAGIC telescope. In particular, I describe the efforts carried out to observe the burst while it is still active.

GRBs are sudden flashes of γ-rays, which occur randomly in the sky and outshine all other sources during their activity. The duration of GRBs vary from milliseconds to few minutes. Often the time structures are complex with very high variability. Based on their durations, GRBs are broadly classified into two groups: Short and long, with $\sim 2\,\mathrm{s}$ as a dividing line between them. Long GRBs show in most cases afterglow emission observable in the longer wavebands, lasting much longer than the initial bursts, e.g. for hours to months. Multi-wavelength observations of the prompt and afterglow emissions have provided advancement in our knowledge of the energetic events in recent years. Despite extensive studies in the past few decades, the mechanism of GRBs and the processes of their progenitors still remain unexplained.

More experimental data, covering a large energy range, is needed to allow better modelling of the ongoing processes. The goal of the MAGIC project is to contribute to the understanding of the GRBs. The MAGIC telescope is the world largest imaging atmospheric air Cherenkov telescope (IACT) for ground based γ astronomy. Numerous technical innovations were developed in order to allow repositioning speeds to any arbitrary sky coordinates of less than $20\,\mathrm{s}$. Because of the cosmological distances of the GRBs, γ-rays above $50 - 300\,\mathrm{GeV}$ are mostly absorbed by interaction with low energy photons of the extragalactic background light (EBL), e.g. they will not reach detectors on Earth. In the past, in some cases, photons of up to $18\,\mathrm{GeV}$ were detected from GRBs by satellite experiments (EGRET). The spectra did not show any energy cut-off up to the detector limits of approx. $20\,\mathrm{GeV}$. The small detection area of satellite borne experiments limits the sensitivity at higher energies and new attempts need to be performed to explore the emission region beyond this energy limit. The ground based experiments have less constraints on the detector size. However, they have to suppress the by many orders of magnitude larger background of charged cosmic rays. Which is much more difficult than in space borne detectors.

Several attempts were performed in the past by ground based experiments to observe GRBs in the VHE regime, all of them without significant detection. The water Cherenkov detectors have large fields of view and allow to search for coincidence triggers with the satellites. However, their sensitivity is very poor and the resulting upper limits lie orders of magnitude above any theoretical model assumptions. The IACTs on the other hand, need to be positioned to the GRB coordinates on the sky. The previous IACT generation had either too small detection area, resulting in high energy threshold, or too heavy construction, limiting the slewing velocity.

The thesis reports about the observations of nine GRBs with the MAGIC telescope in the VHE regime. The follow-up observations were triggered by the GRB coordinates network (GCN). The first GRB observation by MAGIC was performed on April 21st, 2005 (GRB050421). In the following year eight further GRBs were observed by MAGIC. In two cases follow-up observations started while the GRB prompt emission was still ongoing (GRB050713a and GRB050904). These are the first ever prompt emission observations of VHE γ's from an GRB event with an IACT and show the capability of the MAGIC telescope. No evidence of VHE γ-ray emission from these observations was found and upper limits at energies $\sim 100\,\mathrm{GeV}$ are given. The sensitivity of MAGIC allows setting the upper limits to at least three orders of magnitude lower than in the past.

My thesis expands also beyond the analysis of the GRB data. The technical part describes the study and improvements of the optical quality of the MAGIC telescope. Even though, at first both parts seem to be widely separated from each other, without the active mirror control (AMC) one would not be able to build a large telescope, which makes quick follow-up observations of the short lasting phenomena possible. The AMC allows to bypass the physical and mechanical limitation in the design of large past telescopes and opens new possibilities for the next generation experiments.

The two key parameters, which allow fast slewing of the MAGIC telescope, are the light-weight carbon fiber-epoxy tube structure and the use of light-weight diamond milled aluminium mirrors. The compromise between stability and light-weight lead to small, but for the telescope crucial mirror dish deformations. The $236\,\mathrm{m}^2$ mirror surface is therefore segmented into smaller pieces and each of them can be adjusted to correct the occurring deformations. The corrections are automatically performed with the AMC system, another "first" in IACTs. In order to keep the optical quality of the telescope constant, re-focussing of the mirror segments each time the telescope changes its orientation, is required. Starting with the commissioning phase of the novel system, new methods to improve the focussing procedures were studied. The use of look-up tables was implemented especially for the GRB follow-up observations. The promising quality and speed of this method lead also to its implementation during standard observations. For the monitoring of the optical performance of the telescope a new, high sensitive CCD camera was installed. The new subsystem allows to measure the point spread function (PSF) with high precision. In addition, the camera provides for the first time a precise measurement of the overall mirror reflectivity of an IACT. This measurement is very important for the reduction of systematic errors. Finally, the outlook and further improvements of the AMC system for the future experiments are discussed.

Zusammenfassung

Gammastrahlungsblitze (GRB, aus dem Englischen Gamma Ray Bursts) sind die derzeit rätselhaftesten kosmischen Phänomene, bei denen gewaltige Mengen an Energie in kürzester Zeit in den Kosmos ausgestrahlt werden. Meine Arbeit beschäftigt sich mit der Suche nach der hochenergetischen γ-Strahlen Emission von GRBs mit dem MAGIC Teleskop. Speziell beschreibe ich die Bemühungen, die durchgeführt wurden, um GRBs während ihrer aktiven Phase zu beobachten.

GRBs sind Blitze von γ-Strahlung, die an einer unvorhersagbaren Position am Himmel erscheinen und während ihrer Aktivität alle anderen Quellen überstrahlen. Die Dauer der GRBs variiert von Millisekunden bis zu einigen wenigen Minuten. Die Struktur ist oft komplex und von hoher Variabilität. GRBs können anhand ihrer Dauer grob in zwei Gruppen eingeteilt werden, je nachdem, ob sie kürzer oder länger als 2 s andauern. Lange GRBs weisen in den meisten Fällen ein Nachleuchten auf. Das Nachleuchten ist bei längeren Wellenlängen beobachtbar und dauert viel länger als der eigentliche γ Blitz. Es kann zwischen einigen Stunden bis zu einigen Monaten andauern. Gleichzeitige Beobachtungen von γ Blitzen und der zugehörigen Nachleuchtphasen bei mehreren Wellenlängen haben in den vergangenen Jahren zu einem besseren Verständnis dieser energiereichen Prozesse beigetragen. Trotz umfangreicher Studien in den vergangenen Jahrzehnten können der Mechanismus von GRBs und die Prozesse in deren Quelle immer noch nicht vollständig erklärt werden.

Um die Prozesse besser modellieren zu können, ist es notwendig, Beobachtungsdaten über einen großen Energiebereich zu sammeln. Das Ziel des MAGIC Projektes ist es unter anderem zum Verständnis der GRB beizutragen. Das MAGIC Teleskop ist das weltgrößte abbildende atmosphärische Cherenkov-Teleskop (IACT, aus dem Englischen Imaging Atmospheric Cherenkov Telescope) für bodengebundene γ-Astronomie. Zahlreiche technische Neuerungen wurden entwickelt, um das Teleskop innerhalb von 20 s auf eine beliebige Himmelskoordinate ausrichten zu können. Gammastrahlen mit Energien größer als $50 - 300$ GeV werden wegen der kosmologischen Entfernungen der GRBs zum größten Teil durch die Photonen der Kosmischen Hintergrundstrahlung absorbiert, d.h. sie erreichen niemals die Detektoren auf der Erde. Bei einigen GRBs hat der EGRET Detektor Photonen bis zu 18 GeV beobachtet. Das gemessene Spektrum reicht bis zu der Energiegrenze des Detektors von 20 GeV. Die kleinen Detektorflächen der Satellitenexperimente begrenzen die Sensitivität bei höheren Energien. Neue Methoden müssen verwendet werden, um die Emission über diesem Energielimit zu untersuchen. Bodengebundene Experimente haben eine größere Detektorfläche. Anderseits müssen sie den im Vergleich zu Satellitenexperimenten um einige Größenordungen höheren Untergrund der geladenen Kosmischen Strahlung unterdrücken.

Es wurden bereits einige Versuche unternommen, mit bodengebundenen Experimenten die hochenergetische Komponente der GRBs zu beobachten, jedoch ohne signifikanten Nachweis. Wasser-Cherenkov Detektoren haben ein großes Gesichtfeld und damit ist die Wahrscheinlichkeit groß, dass sich ein GRB zufällig im Gesichtfeld ereignet, das gleichzeitig von einem

Satelliten beobachtet wurde. Die Sensitivität von Wasser-Cherenkov Detektoren ist jedoch sehr gering und die resultierenden oberen Grenzen um einige Größenordnungen über den theoretischen Vorhersagen. Anderseits müssen IACTs auf die GRB Himmelskoordinaten ausgerichtet werden. Bei der älteren Generation von IACTs limitierte eine sehr schwere Konstruktion die maximale Verfahrgeschwindigkeit, sodass der GRB schon lange nicht mehr aktiv war, wenn das Teleskop vollständig ausgerichtet war. Zusätzlich waren aufgrund der zu geringen Detektorfläche die Energieschwellen zu hoch.

Diese Arbeit berichtet über die Beobachtungen von neun GRBs im sehr hohen Energiebereich (VHE, aus dem Englischen Very High Energy) mit dem MAGIC Teleskop. Die Beobachtungen wurden aufgrund eines Alarms aus dem GRB Koordinaten Netzwerk (GCN, aus dem Englischen GRB Coordinates Network) eingeleitet. Die erste GRB Beobachtung mit MAGIC erfolgte am 21. April 2005 (GRB050421). Im folgenden Jahr wurden acht weitere GRBs mit MAGIC beobachtet. Die Beobachtung startete in zwei Fällen während der aktiven Emissionsphase des GRB (GRB050713a und GRB050904). Dies sind die ersten Beobachtungen von GRBs im VHE γ-Strahlen Bereich während der aktiven Emissionsphase. Sie demonstrieren die Fähigkeiten des MAGIC Teleskops. Emission von VHE γ-Strahlung konnte in keinem der neun Fälle nachgewiesen werden und obere Grenzen bei $\sim 100\,\mathrm{GeV}$ wurden ermittelt. Die hohe Sensitivität von MAGIC erlaubt eine um drei Größenordnungen bessere Bestimmung von oberen Grenzen als zuvor.

Meine Doktorarbeit geht über die Analyse von GRB Daten hinaus. Der technische Teil beschreibt Studien und Verbesserungen der optischen Qualität des MAGIC Teleskops. Auf den ersten Blick scheinen beide Teile wenig miteinander zutun zu haben. Ohne die aktive Spiegelkontrolle (AMC, aus dem Englischen Active Mirror Control) wäre man allerdings nicht in der Lage große Teleskope zu bauen, die schnelle Nachbeobachtungen der kurzen Phänomene ermöglichen. Die AMC ermöglicht die physikalischen und mechanischen Grenzen bei der Konstruktion von großen Teleskopen zu umgehen und zeigt neue Möglichkeiten für die nächste Generation von IACTs auf.

Die zwei Schlüsselparameter, die eine schnelle Ausrichtung des MAGIC Teleskops ermöglichen, sind die Leichtbaukonstruktion des Spiegelträgers und das geringe Gewicht der Aluminiumspiegel. Der Kompromiss zwischen Stabilität und geringem Gewicht führte zu kleinen, jedoch für ein Teleskop kritischen, Spiegelträgerverformungen. Der $236\,\mathrm{m}^2$ Reflektor ist deshalb in kleinere Spiegelsegmente unterteilt. Jedes dieser Elemente kann verfahren werden und damit die Verformungen kompensieren. Die Korrekturen werden durch das AMC System automatisch durchgeführt. Um die optische Qualität des Reflektors zu gewährleisten, sind Neufokussierungen der Spiegelsegmente nach einer Änderung der Teleskopposition notwendig. Während der Inbetriebnahme des neuartigen Systems wurden neue Methoden zur Verbesserung der Fokussierung entwickelt. Der Einsatz von Nachschlagtabellen (LUT, aus dem Englishen Look-Up Table) wurde speziell für die Beobachtung von GRBs eingeführt. Die gute Qualität und schnelle Fokussierung mit dieser Methode wurde bald auch für die regulären Beobachtungen als Standard eingeführt. Ein neues System, bestehend aus einer sensitiven CCD Kamera, wurde für die Messung der optischen Eigenschaften des Teleskops gebaut. Dieses Subsystem ermöglicht die Messung der Fokussierung mit hoher Präzision. Zusätzlich gibt es die Möglichkeit der Messung der relativen Reflektivität des gesamten Reflektors. Diese Messung ist speziell für die Reduzierung der systematischen Fehler bei der Energiebestimmung der γ-Strahlen wichtig. Schließlich schlägt diese Arbeit weitere Verbesserungen der AMC für zukünftige Experimente vor.

Contents

List of Figures

List of Tables

List of acronyms and abbreviations

ADC	Analog-Digital-Converter
AGN	Active Galactic Nucleus
AMC	Active Mirror Control
AMControler	Active Mirror control Controller
a.s.l.	above sea level
a.u.	arbitrary unit
Az	Azimuth
BAT	Burst Alert Telescope (SWIFT)
BATSE	Burst And Transient Source Experiment
BeppoSAX	Satellite per Astronomia X "Beppo" in honor of Giuseppe Occhialini
CANGAROO	Collaboration of Australia and Nippon (Japan) for a GAmma Ray Observatory in the Outback
CCD	Charge Coupled Device
CGRO	Compton Gamma Ray Observatory
CL	Confidence Level
CMB	Cosmic Microwave Background
CORSIKA	COsmic Ray SImulation for KAscade
CU	Crab Unit
DAQ	Data AcQuisition
Dec	Declination
DT	Discriminator Threshold
EBL	Extragalactic Background Light
EGRET	Energetic Gamma Ray Experiment Telescope
ESA	European Space Agency
FADC	Flash Analog-Digital-Converter
FEM	Finite Element Method
FITS	Flexible Image Transport System
FOV	Field Of View
FWHM	Full Width Half Maximum
GCN	Gamma ray burst Coordinates Network
GLAST	Gamma ray Large Area Space Telescope
GRB	Gamma Ray Burst
GSPOT	Gamma Sources POinting Trigger
HE	High Energy
HEGRA	High Energy Gamma Ray Astronomy
H.E.S.S.	High Energy Stereoscopic System
HETE	High Energy Transient Explorer
HPD	Hybrid Photo Detector
IACT	Imaging Atmospheric Cherenkov Telescope
IBAS	Integral Burst Alert System
IBIS	Imager on Board the INTEGRAL Satellite
IC	Inverse Compton
INFN	Instituto Nazionale di Fisica Nucleare
INTEGRAL	INTErnational Gamma-Ray Astrophysics Laboratory
IR	Infra-Red

ISM	InterStellar Medium
LIDAR	LIght Detection And Ranging
LONS	Light Of the Night Sky
LUT	Look-Up Table
MAGIC	Major Atmospheric Gamma ray Imaging Cherenkov
MARS	MAGIC Analysis and Reconstruction Software
MC	Monte Carlo (simulation)
Mkn	Markarian
NOT	Nordic Optical Telescope
ph	photon
ph.e.	photo-electron
PMT	Photo-Multiplier Tube
PSF	Point Spread Function
QE	Quantum Efficiency
RA	Right Ascension
RF	Random Forest
RICH	Ring Imaging CHerenkov
RMS	Root Mean Square
SBIG	Santa Barbara Instrument Group
SED	Spectral Energy Density
SiPM	Silicon Photo Multiplier
SMDriver	Stepping Motor Driver
SN	SuperNova
SSC	Synchrotron Self Compton
STACEE	Solar Tower Atmospheric Cherenkov Effect Experiment
TCP/IP	Transmission Control Protocol over Internet Protocol
TDRS	Tracking and Data Relay Satellite
UL	Upper Limit
UT	Universal Time
UVOT	Ultra Violet Optical Telescope (SWIFT)
VCSEL	Vertical-Cavity Surface-Emitting Laser
VERITAS	Very Energetic Radiation Imaging Telescope Array System
VHE	Very High Energy
VHF	Very High Frequency
XRT	X-Ray Telescope (SWIFT)
Zd	Zenith distance

Chapter 1

Universe in gamma rays

Besides thermal and nuclear processes, high energy (HE) processes also occur in our Universe. Information about the so-called relativistic Universe (astronomers use the word non-thermal Universe) can be obtained by the observation of γ-rays. Although being only a tiny fraction of the HE cosmic rays, γ's offer important advantages as cosmic messengers:

- They fly on straight lines from the point of origin.
- They are mass-less and any time variability measured on Earth can be directly related to source activity changes.
- As HE particles they must originate from parent processes of at least the same or higher energy (except blue shifted processes).

The energy band of γ-ray astronomy extends from $\sim 100\,\mathrm{keV}$ to $100\,\mathrm{TeV}$, e.g. over more than nine orders of magnitude. The field can be separated into two domains: *Satellite experiments* and *ground based experiments*. Satellite borne detectors cover the range between $\sim 100\,\mathrm{keV}$ to $20\,\mathrm{GeV}$. However, energies above $20\,\mathrm{GeV}$ cannot be measured with the current space detectors because of their limitation in small detection areas. Gamma rays cannot penetrate the Earth's atmosphere without being absorbed and scattered. The VHE domain ranges from $\sim 10\,\mathrm{GeV}$ to about $100\,\mathrm{TeV}$. This range is accessible to ground based IACTs. This chapter describes processes, which can generate HE particles and objects in the Universe where acceleration takes place. A special focus on GRBs is given in § 1.2 because their observation and analysis is part of this thesis.

1.1 Physics of cosmic rays

The existence of cosmic rays (HE particles coming from outer space) was first noticed during a series of balloon flights by Victor Hess in 1912. Their composition is dominated mostly by protons and helium nuclei. Only about 2% of the particles are electrons and positrons and less then 0.1% are photons in the form of γ-rays. The fraction of neutrinos is unknown.

Figure 1.1 shows the energy spectrum of cosmic ray nuclei at the top of the atmosphere. In the region where the energy spectrum is unaffected by the solar wind, the differential fluxes can be described by a segmented power-law formula in the form of:

$$\frac{dN}{dE} \propto E^{-\alpha} \qquad \alpha = \begin{cases} 2.7 & E < 10^{16}\ \mathrm{eV} \\ 3.0 & 10^{16} < E < 10^{19}\ \mathrm{eV} \end{cases} \tag{1.1}$$

For the highest energies above 10^{19} eV, the index appears to be larger and the distribution flatter. The two breaks in the spectrum at around $10^{15} - 10^{16}$ eV (the "knee") and $10^{18} - 10^{19}$ eV (the "ankle") may indicate the energy limits of different cosmic ray accelerators. While the origin of the low energy part (up to 10 GeV) can be traced back to the Sun, the HE part up to the knee is believed to originate from *galactic accelerators* and those above the knee from *extra-galactic accelerators*. The measured cosmic ray spectrum is affected by the interaction with the interstellar medium (ISM) indicating that the averaged source spectrum is harder ($\alpha \approx 2.1$).

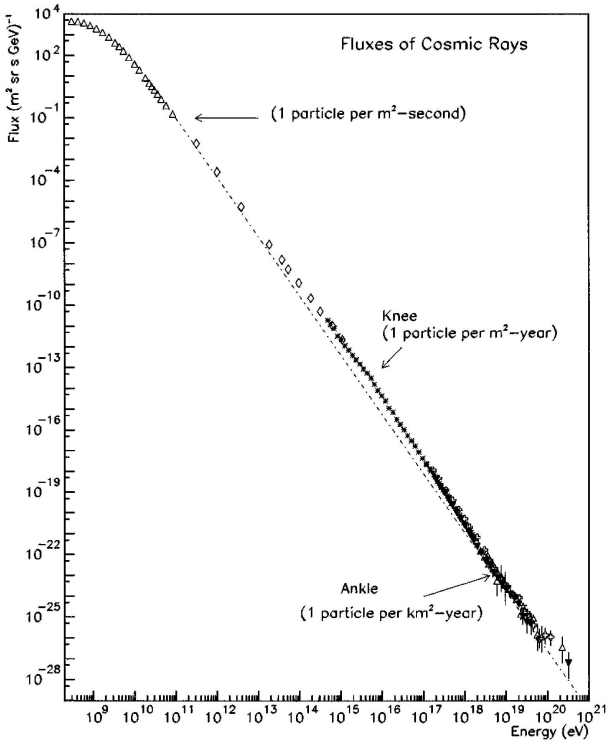

Figure 1.1: Compilation of measurements of the differential energy spectrum of cosmic rays. Figure from [1].

1.1.1 Gamma ray production processes

Electromagnetic radiation may be *thermal* or *non-thermal*. Thermal radiation emerges from a population of electromagnetically interacting particles in thermal equilibrium, with their mean energy characterised by the particles temperature. The radiation spectrum follows a *blackbody* spectral distribution. For higher temperatures the distribution shifts its median towards higher energies. For thermal γ-rays of 1 MeV the corresponding temperature is about $2 \cdot 10^9$ K.

Nonthermal processes are more typical sources of γ-rays. In general, all elementary particles, which couple to electromagnetic processes, may be sources of γ-rays. Cosmic particle spectra of non-thermal processes are normally described by power-laws of the type $dN/dE \propto E^{-\alpha}$ with $\alpha \simeq 1 - 3$. The main physical processes responsible for the production of γ-rays are briefly explained in the following. Detailed descriptions can be found in [2, 3].

Synchrotron radiation: Ultra-relativistic charged particles accelerated in magnetic fields emit synchrotron radiation. The radiated energy originates from the velocity component perpendicular to the magnetic field $v \otimes B$. The resulting synchrotron photon spectrum peaks at energies:

$$E_\gamma = 1.5 \cdot 10^{-5}\,\mathrm{GeV} \cdot \left(\frac{E_\mathrm{e}}{1\,\mathrm{TeV}}\right)^2 \cdot \left(\frac{B}{1\,\mathrm{G}}\right) \tag{1.2}$$

where E_e is the electron energy and B the magnetic field strength perpendicular to the electron trajectory. Energetic electrons ($\sim 1\,\mathrm{GeV}$) moving in the interstellar magnetic field (few µG) therefore radiate synchrotron photons observable in the radio regime. Higher photon energies are generated in objects with strong magnetic fields, e.g. as present in jets.

Bremsstrahlung: Charged particles passing very close to an atomic nucleus or ion are accelerated or decelerated through their electric fields. The trajectory of the moving particle is substantially changed and radiation along the velocity vector is emitted. Bremsstrahlung is the most important radiation mechanism for γ-ray energies below 100 MeV. It is responsible for the diffuse galactic γ radiation of up to 100 MeV, caused by electrons interacting with the ISM.

Inverse Compton scattering: Low energy photons can gain energy in collisions with energetic charged particles. In the collision, part of the particle energy E_e is transferred to the photon. After the collision the average γ-ray energy results in:

$$E_\gamma \simeq 6.5 \cdot 10^{3}\,\mathrm{GeV} \cdot \left(\frac{E_\mathrm{e}}{1\,\mathrm{TeV}}\right)^2 \cdot \left(\frac{E_\mathrm{ph}}{1\,\mathrm{eV}}\right) \tag{1.3}$$

where E_ph is the original photon energy. As for an observer on Earth the original photon energy gets multiplied with the square of the Lorentz factor ($\Gamma \gg 1$) of the electron, photons can be up-scattered to VHE in these collisions.

Decay and annihilation: The pion is an elementary particle involved in the strong nuclear interaction. Pions are created in collisions of energetic protons with ambient gas nuclei or dense radiation fields. Neutral pions (π^0) decay with $> 99\%$ probability into two γ-rays, with an energy of $\sim 70\,\mathrm{MeV}$ in the rest frame, i.e. half the rest mass of the pion. Annihilation of particle-antiparticle pairs can also produce γ-rays. The lightest particle-antiparticle pair ($e^- e^+$) produce two photons with an energy of 511 keV in the rest frame of the annihilation process. In jet environments the energies of the decay products can be Doppler-shifted to higher values.

Boosting of the rest frame towards the Earth of the here mentioned processes can often be responsible for VHE γ-rays. In extreme cases, such as anticipated in GRBs (see § 1.2), the cosmic outflow of the charged parent particles can have Γ factors in the order of 1000.

1.1.2 Gamma ray interaction and absorption processes

Photons and neutrinos are not affected by magnetic fields and point therefore to their origin. They are best suited to study the astrophysical processes in the Universe. However, when travelling cosmological distances, VHE photons can interact with the EBL. The interaction processes vary with the energy of the γ-ray and are as follows:

- **Photoelectric absorption:** Photons can get absorbed by atoms by knocking out an electron. This is the dominant process at energies below about 100 keV.
- **Compton scattering:** Electrons are hit by the HE photons, and gain a fraction of the photon's kinetic energy in the collision. This is the dominant process in the 0.1 MeV to a few MeV regime.
- **Pair creation:** In the presence of electric or magnetic fields, the γ-ray energy can be converted into a particle-antiparticle pair. Because of momentum conservation, these two particles move in opposite directions. The same process can occur in dense photon fields through collisions of energetic photons ($\gamma_{\mathrm{HE}} + \gamma_{\mathrm{EBL}} \rightarrow e^- + e^+$). The threshold for this process depends on the photon energies and the scattering angle θ:

$$E_{\mathrm{HE}} \cdot E_{\mathrm{EBL}} \cdot (1 - \cos\theta) \geqslant 2\left(m_{\mathrm{e}}c^2\right)^2 \tag{1.4}$$

  where m_{e} is the electron mass and c the speed of light. The cross section for this process therefore peaks slightly above the threshold.

1.1.3 Gamma ray horizon

The Universe is full of quanta of low energy radiation. Major components stem from starlight and from the cosmic diffuse 2.7 K microwave background, a remnant of the Big Bang. Due to the pair creation process energetic VHE γ-rays get gradually absorbed as they travel large distances. The higher the energy of the γ-ray, the lower the energy of the background photon can be. For γ-rays of tens of TeV, even far-infrared photons contribute to the absorption. Therefore, the degree of absorption tends to increase with the γ-ray energy. The flux $\Phi(E, z)$ seen from Earth from a hypothetical γ-ray source at redshift z, can be parameterised with the following formula:

$$\Phi(E, z) = \Phi(E, 0) \cdot \exp\left[-\tau(E, z)\right] \tag{1.5}$$

The optical depth $\tau(E, z)$ is defined as the path length, at which the photon flux is attenuated by a factor 1/e. It needs some assumptions on the cosmological parameters like the Hubble constant H_0, the characteristic density n_0 and the spectral EBL density $dn(\epsilon)/d\epsilon$ to calculate $\tau(E, z)$ [4, 5]. The condition $\tau(E, z) = 1$ defines the so-called *gamma ray horizon*, which is shown in figure 1.2 [6]. For a source at a given redshift z, γ-ray spectra should show a cutoff or should at least steepen around the energy displayed in the figure. The degree of the absorption, and hence the precise energy of the cutoff, depends on the intensity and spectrum of light in intergalactic space and hence allows measuring this intensity from spectral distortions. The intensity of starlight is of significant cosmological interest, because it represents the light emission of galaxies summed over the entire history of galaxy formation since the Big Bang [7].

Direct measurements even near Earth are very difficult, because of overwhelming amounts of foreground light originating in the solar system or in our own galaxy [8]. A heavily debated peak in the light spectrum at wavelengths around $1-2$ µm [9], e.g. might be an indication of emission from the very first stars in the Universe, but could also be a remaining foreground contamination.

An alternative approach is the study of absorption features imprinted on the γ-ray spectra of distant extragalactic objects, by interactions of those γ-rays with the EBL photons. Experiments sensitive in the $10-100$ GeV energy band can help to measure the EBL and to constrain cosmological parameters [10].

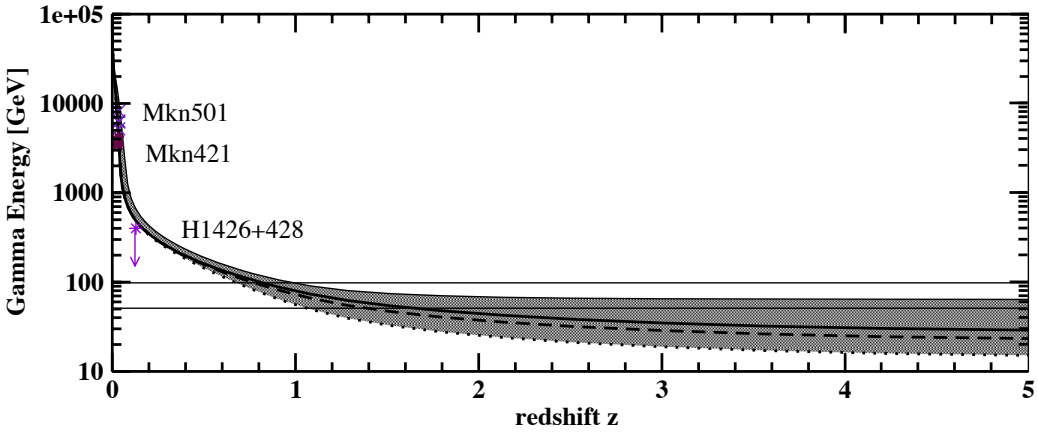

Figure 1.2: Gamma ray horizon. The shadowed area indicates the parameter space due to different cosmological and EBL models. Also plotted are published cut-off energies of the two VHE sources Mkn 501 and Mkn 421, and an upper limit of H146+428 coming from not detecting the cut-off energy. Figure from [6].

GRBs are classified as the most distant objects measured at high energies (for the redshift distribution see figure 6.34). Absorption processes of VHE γ-rays limit very strongly the detectability of these sources by IACTs. With an energy threshold of 50 GeV, the MAGIC telescope (see § 2.3) is able to detect VHE γ-rays up to $z \approx 1$ for zenith observations. However, it has to be taken into account that the energy threshold E_{thr} of an IACT scales with the observation zenith angle Θ following an empirical formula:

$$E_{\mathrm{thr}}(\Theta) = E_{\mathrm{thr}}(\Theta = 0) \cdot (\cos\Theta)^{-2.7} \tag{1.6}$$

increasing E_{thr} at higher zenith angles Θ and therefore strongly limiting the maximal detectable distance of the source, respectively reducing useful measurements to small zenith angles and in turn to a smaller number of candidates. It should be noted that the current uncertainties on the EBL are large. In the recent years the measurements indicate quite some reduction and it might be possible that at 50 GeV the Universe is much more transparent than estimated $10-15$ years ago.

1.1.4 Cosmic gamma ray sources

A variety of sources exist in the Universe, which can generate VHE photons. Here I will summarise the objects, which are targets for the MAGIC telescope. Detailed descriptions can be found in [3].

Supernova Remnants

Supernova (SN) remnants are leftovers from explosions of massive stars at the end of their life. When the mass of the star exceeds about eight solar masses, nuclear fusion in the star core continues up to the formation of iron. Because of the maximal binding energy of ^{56}Fe, the nuclear fusion stops there and the gravitational force causes an implosion of the star's core. In the collapse of the core the external shells, composed of lighter elements, are ejected into the ISM, forming a nebula. The core itself becomes a compact object, a neutron star or a black hole, depending on the mass. The first object observed by an IACT was the supernova remnant called *Crab Nebula*, located in our Galaxy (see figure 1.3). It is the strongest steady TeV γ-ray source in the sky and is therefore used as a calibration source by all IACTs in the northern hemisphere.

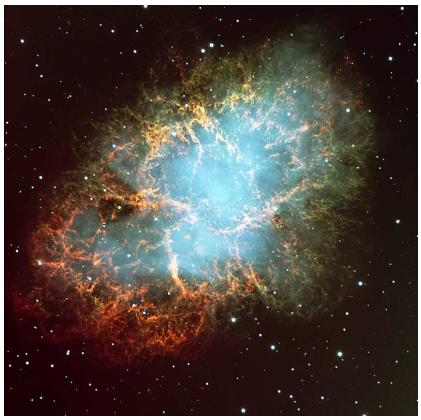

Figure 1.3: Optical image of the Crab Nebula.

Pulsars

Pulsars are fast rotating objects, discovered due to their apparently periodic photon emission. It is generally believed that pulsars are created in SN explosions, leaving behind fast spinning neutron stars. Young pulsars exhibit pulsed emission periods of typically milliseconds, while older pulsars have slowed down to periods of up to a few seconds. The pulsed emission is beamed along the magnetic field axis, which usually itself is misaligned to the rotational axis. The emitting cone rotates therefore, passing the line of sight to the Earth in regular time intervals. Figure 1.4 shows an artist view of a pulsar with a companion star.

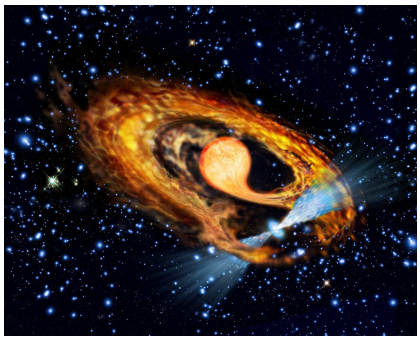

Figure 1.4: Artist view of a pulsar and its bloated red companion star.

Pulsars produce the strongest known magnetic fields in the Universe, reaching up to 10^{12} G. The neutron star itself has a mass of $1.4-3\,M_{\odot}$ with diameters of ~ 20 km. About 1500 pulsars have been detected so far, 35 out of them emit in X-rays and 9 also in γ-rays. No pulsed emission at energies > 10 GeV has been detected yet. Of special interest is the regime below and close to 100 GeV, where the favourite models differ significantly in the predicted spectra. The *polar cap model* [11, 12] predicts synchrotron radiation from accelerated particles in the polar caps, which in turn interacts with the strong magnetic field and creates $e^{\pm}$ pairs. This model does not predict emission beyond 50 GeV while the *outer gap model* predicts spectra up to 100 GeV [13, 14]. In the outer gap model VHE γ-rays are produced by inverse Compton (IC) scattering of electrons with infrared (IR) and optical photons outside the gap.

Active Galactic Nuclei

Active Galactic Nuclei (AGN) are small galaxy cores of strong photon emission embedded in an otherwise typical galaxy. The emission from the core may be highly variable and very bright, compared to the rest of the galaxy. Models of AGN concentrate on the concept of having a supermassive black hole in the center of the galaxy. The dense central galaxy provides material, which accretes onto the black hole, releasing a large amount of gravitational energy. A part of the energy in this hot plasma is emitted as X-rays and γ-rays. All these objects emit jets of matter that can extend to very large distances. Depending on the observation angle with respect to the jet axis, a rich phenomenology of AGNs can be observed, leading to many classes and sub-classes. For γ-ray astronomy the most important ones are those where the jet points directly towards the Earth, called *BL Lacs* or *blazars*. The observed emission is dominated then by phenomena occurring in the jet region, which cause variable emission on timescales from minutes to days. The current two best studied VHE γ-ray emitting AGNs are the blazars Mkn 501 and Mkn 421. Figure 1.5 shows an artist view of a AGN as described above.

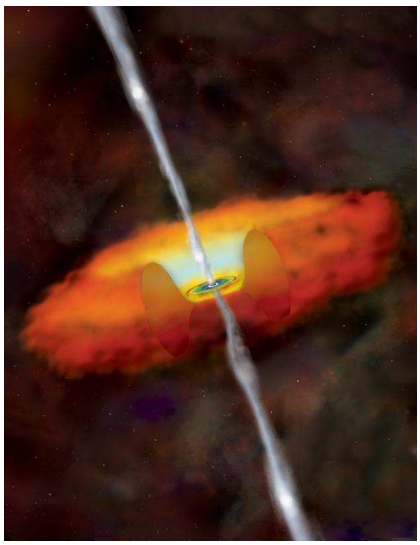

Figure 1.5: Artist view of a AGN.

Microquasars

Microquasars are X-ray binary stars with a compact object (either a neutron star or a stellar-mass black hole) accreting matter from a companion star, as shown in figure 1.6. Radio and X-ray observations have led to the presumption that microquasars behave as scaled down AGNs. Microquasars show resolved radio emission that is thought to arise from a relativistic outflow akin to AGN jets, in which particles can be accelerated to high energies. The timescales near the black hole are in the first order proportional to the mass of the black hole. Therefore, ordinary quasars take centuries to go through variations a microquasar experiences in one day. This makes microquasars quite well suited for the study of relativistic jets. The recent detections of LS 5039 by H.E.S.S. [15] and LSI +61 303 by the MAGIC experiment [16] have shown that particles are also accelerated up to the VHE domain in these systems.

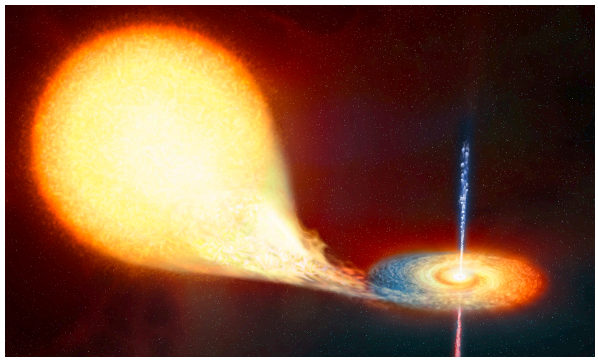

Figure 1.6: Artist view of a microquasar.

Only a small part of the known γ-ray sources in the Universe have been resolved so far. From the 271 steady sources detected by the EGRET experiment in the MeV to 10 GeV domain [17] more than 150 are still unidentified (see figure 2.11). It is a challenge for new experiments to identify the sources, to determine more precisely the sky coordinates and to resolve the emission characteristics in order to give input to theories.

1.2 Gamma ray bursts

GRBs are violent outbursts of HE cosmic rays somewhere in the Universe. During their short emission periods, GRBs become the brightest single objects in the Universe. Despite over 30 years of intensive research, the nature of the GRBs and their energy generation mechanisms remain largely unknown. The origin of the GRBs is among the most essential and still unsolved problems in present-day astrophysics.

1.2.1 Prompt emission phase: Phenomenology and facts

GRBs were first detected in late 1960s by the military Vela satellites monitoring compliance of the nuclear test ban treaty. The discovery became public only several years later [18].

A new era in GRB research opened in 1991 with the launch of the CGRO, whose groundbreaking results were summarised in [19]. The most significant results came from the all-sky survey by BATSE on board of the CGRO. The detector recorded, at a rate of one event per day, over 2700 bursts in total. The sensitivity of the BATSE instrument in the $50 - 300\,\mathrm{keV}$ band was $0.5\,\mathrm{ph\,cm^{-2}\,s^{-1}}$, corresponding to energy flux sensitivities $\lesssim 10^{-7}\,\mathrm{erg\,cm^{-2}\,s^{-1}}$. Some of the results are as followed:

Celestial distribution: One of the main results from BATSE observations is illustrated in figure 1.7. It shows that GRBs are isotropically distributed in the sky, suggesting a cosmological distribution.

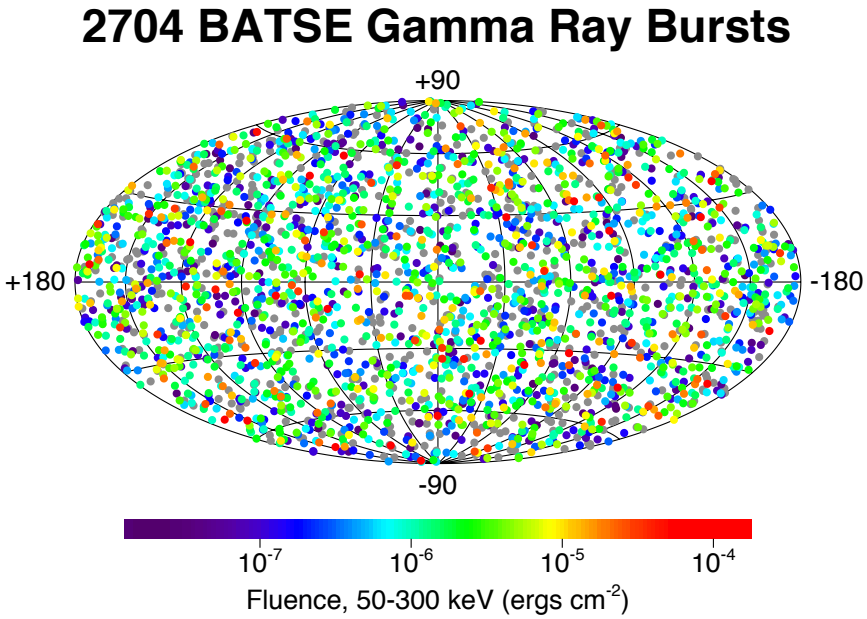

Figure 1.7: The celestial distribution of 2704 GRBs, as seen by BATSE over a nine year period.

Durations: GRBs are short outbreaks of γ-rays of up to at most 1000 s. The γ-ray light curves show a time dependence ranging from a smooth, fast rise and quasi exponential decay, through curves with several peaks, to variable curves with many peaks, and substructure down to milliseconds in some bursts, as shown in figure 1.8.

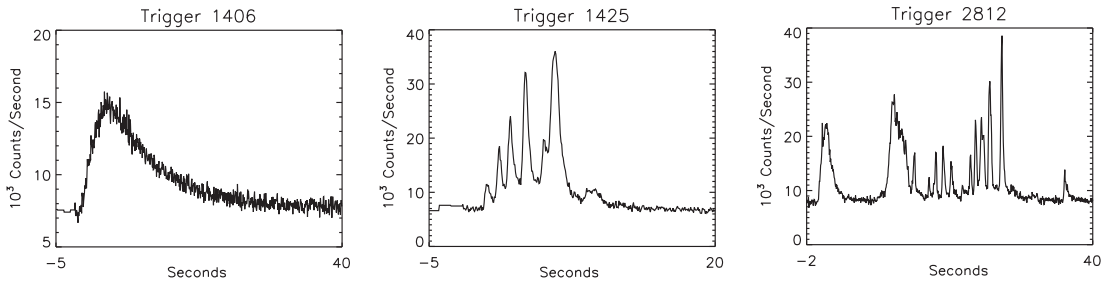

Figure 1.8: Some typical GRB light curves observed by BATSE.

The shortest time variability in the observer frame was found to be $\delta t \sim 10^{-2}\,\mathrm{s}$. A naive estimate of the size of the emitting region for the source at rest implies that its radius must be $R \leqslant c \cdot \delta t$, i.e. as small as $R \sim 3 \cdot 10^3\,\mathrm{km}$. A enormous number of photons in such a small volume should produce $e^- e^+$ pairs in $\gamma\gamma$ interactions, when considering the observed energy release of $\langle E_{\mathrm{iso}} \rangle \approx 10^{53}\,\mathrm{erg}$. The emitting region becomes optically thick, i.e. the mean free path l_γ of a photon before a creation of an $e^- e^+$ pair becomes less than R, so that the optical depth $\tau_{\gamma\gamma} \equiv R/l_\gamma > 1$. The photon energy would degrade and the spectrum becomes thermalised. In conclusion, a thermal spectrum would be expected. This conflicts with the observed non-thermal spectra leading to the so called *compactness problem*. The conflict can be solved if one supposes that the emitting region moves towards the observer with an extreme relativistic speed with Lorentz factor $\Gamma \gg 1$. The actual size of the emitting region becomes than $\sim \Gamma^2 \cdot c \cdot \delta t$, and the optical depth correspondingly smaller. However, Lorentz factors of $\Gamma \sim 10^2 - 10^3$ are required to reduce the optical depth below unity.

The duration of a GRB is usually defined in terms of the time scale over which 90% of the γ-rays were detected: The T_{90} parameter. The durations at MeV energies range from $10^{-2}\,\mathrm{s}$ to about $10^3\,\mathrm{s}$, with a well defined bimodal distribution of bursts being longer or shorter that $T_{90} \sim 2\,\mathrm{s}$. In figure 1.9 the distribution of T_{90} for the 2041 BATSE GRBs is shown [20]. In addition, 168 SWIFT bursts detected until September 2006 are included[1]. The long bursts are linked to the explosive collapse of the cores of young, massive stars in sub-luminous, star-forming galaxies. The short busts on the other hand, are explained by the enormous energy released when two compact objects – remnants of exploded stars in the form of highly dense neutron stars or black holes – merge. It should be noted that there is an anticorrelation between spectral hardness and duration, the short ones being harder [21].

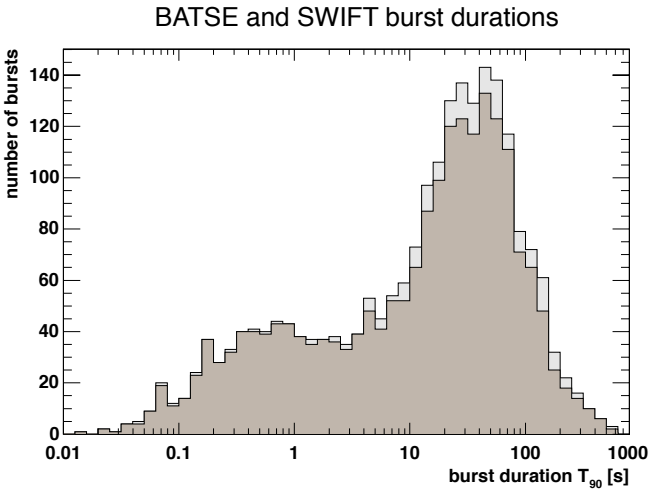

Figure 1.9: Bimodal burst duration distribution of the 2041 BATSE bursts (dark brown). The brighter distribution includes the latest 168 SWIFT GRBs.

[1] `http://swift.gsfc.nasa.gov/docs/swift/archive/grb_table/`

Spectra: The prompt emission spectra of GRBs are very hard with a peak energy E_{peak} of few hundred keV. The spectra can be best fitted with the *Band function* [22]. It consists of two smoothly connected power-laws in the form of:

$$F(E) = \begin{cases} A \cdot \left(\frac{E}{100\,\mathrm{keV}}\right)^{\alpha} \cdot \exp\left(\frac{-E(2+\alpha)}{E_{\mathrm{peak}}}\right) & \text{for} \quad E < E_{\mathrm{break}} \\ A \cdot \left(\frac{(\alpha-\beta)E_{\mathrm{peak}}}{(2+\alpha)\cdot 100\,\mathrm{keV}}\right)^{\alpha-\beta} \cdot \exp\left((\beta-\alpha)\cdot\left(\frac{E}{100\,\mathrm{keV}}\right)^{\beta}\right) & \text{for} \quad E > E_{\mathrm{break}} \end{cases} \tag{1.7}$$

with:

$$E_{\mathrm{break}} \equiv \frac{(\alpha-\beta)\cdot E_{\mathrm{peak}}}{2+\alpha} \tag{1.8}$$

where $F(E)$ is the flux, A is the normalisation factor (in units of $\mathrm{ph\,keV^{-1}\,cm^{-2}\,s^{-1}}$) and α and β are the low and HE spectral indices. Their distribution is shown in figure 1.10. Most of the BATSE bursts did not show any break in the energy spectrum up to the detector energy limits ($\sim 300\,\mathrm{keV}$). For the majority the fits resulted in a spectral index of $\beta = -2.25$. Some bursts were detected up to very large γ-ray energies, supporting the idea that the spectra might extend up to the VHE range. Equation 1.8 gives the break energy E_{break} of the Band model, at which the spectrum changes from the low-energy to the high-energy power-law. Whereas E_{peak} in equation 1.7, is the energy, at which the νF_{ν} spectrum peaks. The distributions of both energies, from a sub-sample of BATSE bursts, are also shown in the figures below. An overview of observations and theories for VHE γ-ray emission is given in § 1.2.6.

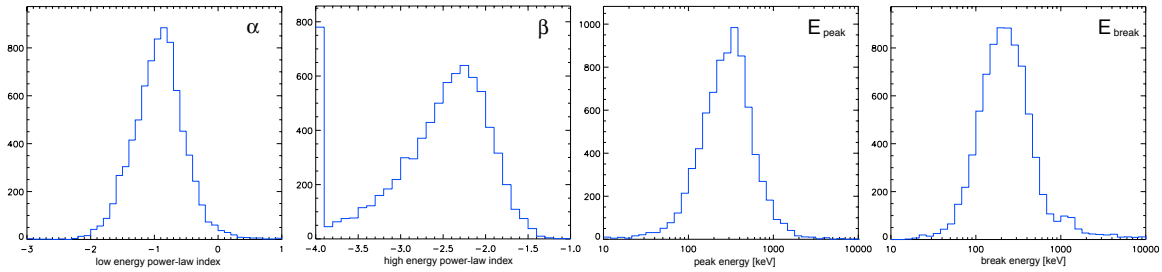

Figure 1.10: Distribution of the four parameters in the Band function [23]. In total 8459 time-resolved GRB spectra of 350 bright GRBs observed by BATSE have been taken into account. From the left: a) Low energy spectral index α, b) High energy spectral index β (bursts, which could not be fitted beyond E_{break} are included in the first bin), c) Peak energy E_{peak} and d) Break energy E_{break}.

1.2.2 GRB afterglow phase

The breakthrough to GRB afterglow observations came with the launch of the BeppoSAX satellite [24] in 1996. The satellite was equipped with a coded mask wide field camera, sensitive at energies of $2 - 25\,\mathrm{keV}$. In case of a trigger, the spacecraft was able to slew to the GRB sky coordinates and start the observation with the narrow field instruments, sensitive in the $0.1 - 10\,\mathrm{keV}$ energy band. In almost all cases a fading X-ray afterglow was detected. The precise determination of the burst coordinates with the narrow field instruments and the prompt dissemination through the GCN (see § 2.4.1) allowed ground based experiments to also observe the target in due time.

The current generation of GRB satellites use the same technique as BeppoSAX. The SWIFT satellite [25], currently the most sensitive detector, triggers on GRBs with the coded mask wide field (1.4 sr field of view (FOV)) burst alert telescope (BAT) [26]. The sensitivity of BAT is a complicated function of burst duration and spectral shape. In practice BAT detects bursts in the energy range $15 - 150\,\mathrm{keV}$ at fluences as low as $\sim 10^{-8}\,\mathrm{erg\,cm^{-2}}$. The satellite has also the capability for rapidly slewing to pointing its X-ray telescope (XRT) [27] and ultra-violet optical telescope (UVOT) [28] onto the burst location. With respect to BAT, the XRT can detect a source of a much lower flux level in the observed $0.3 - 10\,\mathrm{keV}$ band. The UVOT is designed to capture the photons at wavelengths between $170 - 600\,\mathrm{nm}$. It has the sensitivity of a 4 m Ø ground-based telescope, able to detect a 24 magnitude B-star in 1000 s.

The canonical afterglow light curve

BeppoSAX could be re-pointed to the GRB coordinates within $6 - 8\,\mathrm{h}$ after the initial trigger, and detect the X-ray afterglow at an initial level of $\sim 10^{-13}\,\mathrm{erg\,cm^{-2}\,s^{-1}}$. The SWIFT spacecraft needs only $\sim 70\,\mathrm{s}$ for the slew and offers the opportunity to lower the gap between the prompt emission and the late afterglow. Our current understanding of the GRB evolution is shown in figure 1.11. It includes five components beside the prompt emission itself:

1. Initial steep decay with a typical slope of $\alpha \approx -3$ or steeper.
2. Shallower-than-normal decay component with a typical slope of $\alpha \approx -0.5$.
3. Normal decay component with a typical slope of $\alpha \approx -1.2$.
4. Possible post-jet-break steep decay component with a slope of $\alpha \approx -2$.
5. One or more erratic X-ray flares.

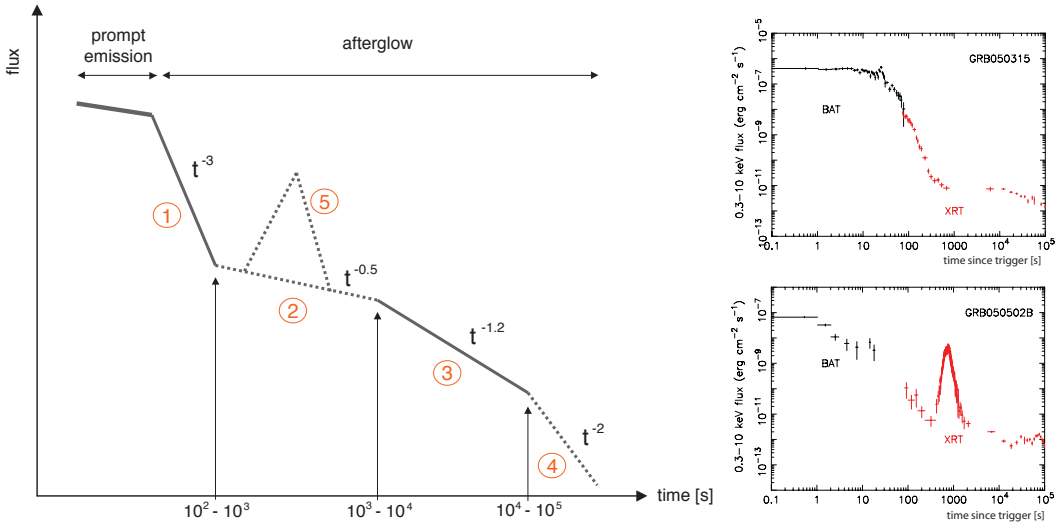

Figure 1.11: Temporal evolution of a typical GRB light curve. *Left:* Four power-law light curve segments together with a flaring component are identified in the afterglow phase. Other three components are only observed in a fraction of bursts; They are marked as dashed lines. The typical temporal indices are indicated in the figure. *Right:* Light curve examples from SWIFT BAT and XRT data.

Not every segment shows up in every burst, but all the light curves could in principle be understood within such a general framework. Measuring the light curves will bring eventually valuable information to understand the prompt emission to afterglow transition, the GRB emission sites, the central engine activity, the forward-reverse shock physics and the GRB immediate environment. For a full discussion see [29].

The most interesting component are the bright **X-ray flares** detected in nearly half of the SWIFT GRBs [30, 31, 32]. These flares typically occur hundreds of seconds to hours after the trigger, but in some cases they occur several days later. The amplitude of the X-ray flare can range from a factor of $\lesssim 500$ (see GRB050502b in figure 1.11) to, in most cases, a factor of $3-10$, compared with the background afterglow component. These flares carry an enormous amount of energy and have been associated with ongoing activity of the burst inner engine or late internal shocks.

Optical and radio afterglows

GRBs are multiwavelength emitters. The study of optical counterparts turned out to be very important in the study of the GRB phenomenon, e.g. establishing the nature of the afterglow emission (synchrotron emission) and assessing their extragalactic origin [33]. GRB optical counterparts can be initially extremely bright. However, the delayed emission, even though it is long lived with respect to the prompt event, still fades quite rapidly, and the host galaxies of GRBs are in general very faint, because of their cosmological distance. Only about 50% of the GRB afterglows could be detected in optical wavelengths. The rest half are optically "dark", though nearly all of these have X-ray and/or radio afterglows.

At epochs between few hours and days after the GRB the optical afterglow decays following approximately a temporal power-law $t^{-\alpha}$ with an index α ranging from $0.7-2$. The behaviour is a consequence of the relativistic forward shock, which develops into the ISM and accelerates the particles (see § 1.2.4). In addition, prompt emission at optical and IR wavelengths, simultaneous with a GRB, or delayed by a few seconds, was recently observed [34, 35, 36]. This emission is distinct from the afterglow, because it is probably produced by a reverse shock propagating through the explosion ejecta. The prompt optical emission contemporaneous with the GRB carries important information on the central engine and explosion mechanism.

Spectra of bright optical afterglows allowed, in a number of cases, the detection of absorption lines and thus measurements of the redshift were done. The redshift ranges from $z = 0.0331$ (GRB060218 [37]) up to $z = 6.39$ (GRB050904 [38] and § 6.2.6) with a mean value of $\langle z \rangle = 2.2$. This makes GRBs one of the most distant class of objects observed until now.

1.2.3 GRB progenitor scenarios

It is now generally accepted that long GRBs result from the death of a rapidly rotating massive star [39, 40]. The star core collapses to form a black hole surrounded by an accretion disc or torus. The accreting material liberates gravitational energy either in the form of neutrinos or via magneto-hydrodynamic processes. During the collapse the star core escapes the star and material from the center of the star is beamed into relativistic jets. The jets are oriented along the rotation axis of the stellar core. The jets contain a relatively modest amount of baryonic material moving at high Lorentz factors Γ.

Up to now all our knowledge about the emission from GRBs came from the study of long bursts. Short burst were too rapid fading to be localised by observatories. This has changed in the SWIFT era. The data for the first short bursts detected by SWIFT [41, 42, 43] strongly support the idea that the γ-ray emission arises from a jet powered by a merger of two compact

objects, most likely two neutron stars or a neutron star and a black hole. The new data have shown that the X-ray emission from some short bursts can be detected long after T_{90}, allowing a direct comparison of the early X-ray emission between short and long GRBs.

For both types of GRBs, it is thought that the jet flow is inhomogeneous, leading to internal shocks caused by variable Lorentz factors [44, 45]. The shocks produce variable γ-ray emission when viewing jets within the opening angle.

Supernova - GRB connection

An increasing number of recent observations support the association of at least some long GRBs with core collapse SN events. GRB980425 was the first burst with evidence for a physical association with a SN (SN 1998bw [46]). Most recently further GRB/SN associations, based on the spectroscopic detection of a SN spectrum in the GRB afterglow, added robust evidence for the association of the two phenomena. Examples are: GRB021211/SN2002lt [47], GRB030329/SN2003dh [48, 49], GRB031203/SN2003lw [50], GRB050525a/SN2005nc [51], and more recently GRB060218/SN2006aj [37]. More details can be found in [52] and references therein.

1.2.4 GRB models

The currently best studied theories of GRBs and their afterglows are the **fireball** and the **cannonball** models. Despite their similarly sounding names, these two models are completely different in their basic hypotheses, in their descriptions of the data and their predictions. Here I will review the basic ideas of the two leading models.

The fireball model

The fireball model was first introduced in 1986 [53, 54]. The model has been modified and changed in many details. The most popular ones [55, 56] assume that GRBs are emitted from highly relativistic conical fireballs produced in hypernovae - a hypothesised rare class of superenergetic type Ic SNe, generated by direct collapse of massive stars to black holes. Figure 1.12 illustrates the fireball model.

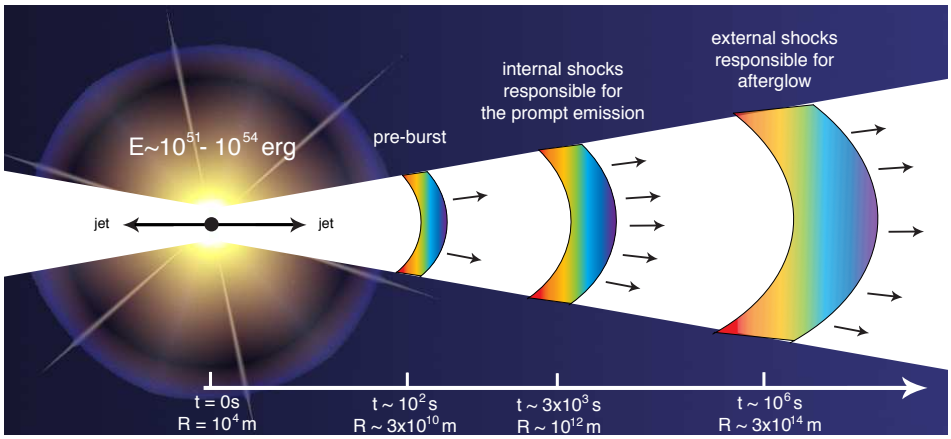

Figure 1.12: The fireball model and its internal/external shock scenario. The colour coding indicates shells moving at different velocities within the jet.

The GRB pulses are assumed to be produced by synchrotron emission from collisions between highly relativistic conical shells ejected in the hypernovae explosion. The GRB afterglow is assumed to be synchrotron radiation, emitted when the merged shells collide with each other or with the ISM. They drive a forward blast wave into the ISM and a reverse shock into the merged shells.

The cannonball model

The cannonball model [57, 58, 59, 60] describes the GRBs and their afterglows as bipolar jets of plasma balls ("cannonballs"), which are ejected in ordinary core collapse SN explosions along the rotation axis of the precursor. An accretion disk or torus is produced around the newly formed compact object. It originates from stellar material left behind by the SN explosion. As observed in microquasars [61], each time when part of the accretion disc falls abruptly onto the compact object, a pair of cannonballs made of ordinary atomic matter are emitted with high bulk Γ factors.

The cannonballs move in opposite directions, along the rotational axis, where matter has already fallen back onto the compact object due to lack of rotational support. The γ-rays of a single pulse in a GRB are produced as a cannonball coasts through the SN glory. The electrons enclosed in the cannonball Compton up-scatter photons to higher energies. Each pulse of a GRB corresponds to one cannonball. The timing sequence of emission of the successive individual pulses in a GRB reflects the chaotic accretion processes. Its properties are not predictable, but those of a single pulse are. An schematic view of the cannonball model is shown in figure 1.13.

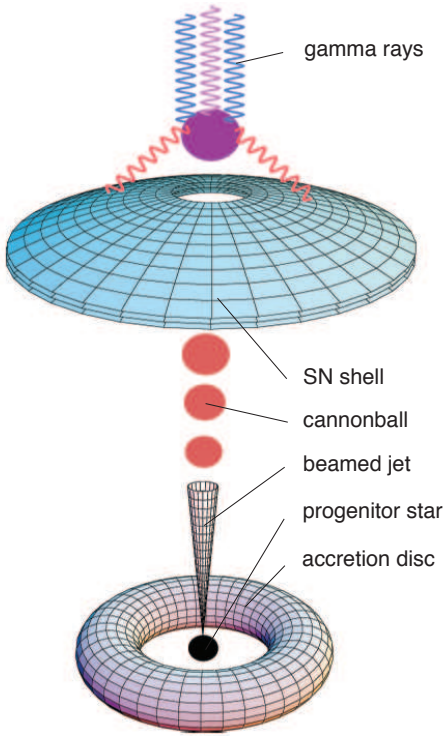

Figure 1.13: The cannonball model of GRBs and their afterglows. Figure adopted from [57].

An interesting aspect of both models is that due to the high beaming factor ($\Gamma \sim 1000$) only about one out of $\sim 10^5$ GRBs are seen. Namely, only in the case the highly collimated beam points towards the Earth. Thus the observation of $1-2$ GRBs/day is consistent with the rate of SN explosions in the Universe. Due to the high Γ factor the light curve is very much compressed and the energy in the observer frame boosted to high energies.

1.2.5 GRBs as standard candles

Since it was realised that GRBs occur at large redshifts, it became of great interest to understand whether they could be used as standard candles, i.e. distance indicators. At a first glance, GRBs are all but standard candles. The isotropic equivalent energy, i.e. their energy output in photons, assuming they radiate isotropically in every direction with the same properties, is:

$$E_{\rm iso} = F_{\rm bol} \cdot \frac{4\pi \cdot D_L(z)^2}{1+z} \tag{1.9}$$

where $F_{\rm bol}$ is the burst bolometric fluence, z its redshift and D_L its luminosity distance. This quantity is easy to determine, provided that the burst has been detected and its redshift measured. A basic knowledge of its spectrum is necessary in order to perform a bolometric correction. Compilation of $E_{\rm iso}$ for 30 bursts showed that this quantity is on average $E_{\rm iso} \approx 10^{53}$ erg and spans at least three orders of magnitude but does not correlate well with the redshift of the bursts [62]. The isotropic equivalent energy is therefore not a good standard candle. For comparison, type Ia SNe have an root mean square (RMS) scatter of 0.075 decade.

The recent discovery of the **Ghirlanda correlation** [63] opened new possibilities. This relation uses the fact that GRBs are collimated sources with a typical angle $\Theta_{\rm jet}$ of few degrees. The estimate of the jet opening angle is made with the measure of the achromatic jet break[2] time $t_{\rm break}$, i.e. the time (typically between 0.5 and 6 days) when the afterglow light curves steepen. The measurement of $\Theta_{\rm jet}$ allows to correct $E_{\rm iso}$ and derive the collimation corrected energy:

$$E_\gamma = E_{\rm iso}\,(1 - \cos\Theta_{\rm jet}) \tag{1.10}$$

The Ghirlanda correlation consist in a strong coherency between the peak energy $E_{\rm peak}$ from the νF_ν energy spectrum and E_γ [64]. For the recent sample of 19 GRBs the best fit relation is:

$$\left(\frac{E_{\rm peak}}{100\,{\rm keV}}\right) = (2.82 \pm 0.02)\left(\frac{E_\gamma}{3.72\cdot 10^{50}\,{\rm erg}}\right)^{0.69\pm0.04} \tag{1.11}$$

A very tight correlation between E_γ and $E_{\rm peak}$ is obtained, as shown on the left side in figure 1.14. The scatter of the points around the correlation yields a $1-\sigma$ dispersion of 0.15 decade, approximately twice as large as the scatter of type Ia SNe.

Placing a GRB on the *Ghirlanda plot* requires a measurement of many different parameters. The measure of the peak energy of photons in the prompt GRB emission requires broadband coverage, from X-rays to soft γ-rays. Most of the SWIFT bursts do not have an adequately large band, unless observed simultaneously with HETE-2 or Konus Wind. On the other hand, the measure of the beaming corrected energy requires a knowledge of the opening angle of the GRB. This can be obtained only with continuous sampling of the afterglow light curve to unambiguously identify an achromatic break that can be associated with the geometry of the fireball or cannonball. Finally, a good measure of the opening angle of the jet requires the knowledge of the density profile of the medium surrounding the GRB.

The Ghirlanda correlation makes GRBs standard candles in the sense that, similarly to the stretching-luminosity correlation of SN Ia [66], it allows to derive the GRB true energy. The correlation can be used to test the cosmological parameters and study the nature of the dark matter. The right plot in figure 1.14 shows the constraints on the mass density of the Universe Ω_M and the energy density associated with the so-called cosmological constant Ω_Λ parameters obtained with the sample of 19 GRBs. Although the contours obtained with small sample are tight, due to the low number compared to SN Ia and cosmic microwave background (CMB) measurements, GRBs are detected out to very high redshifts and can give therefore better constraints in combination with other cosmological probes.

[2] A achromatic jet break is a steepening in the flux decay rate of the afterglow emission that occurs when the edges of the jet become visible as it decelerates. It causes an simultaneous brake at all wavelengths and is mainly observed in the optical afterglows.

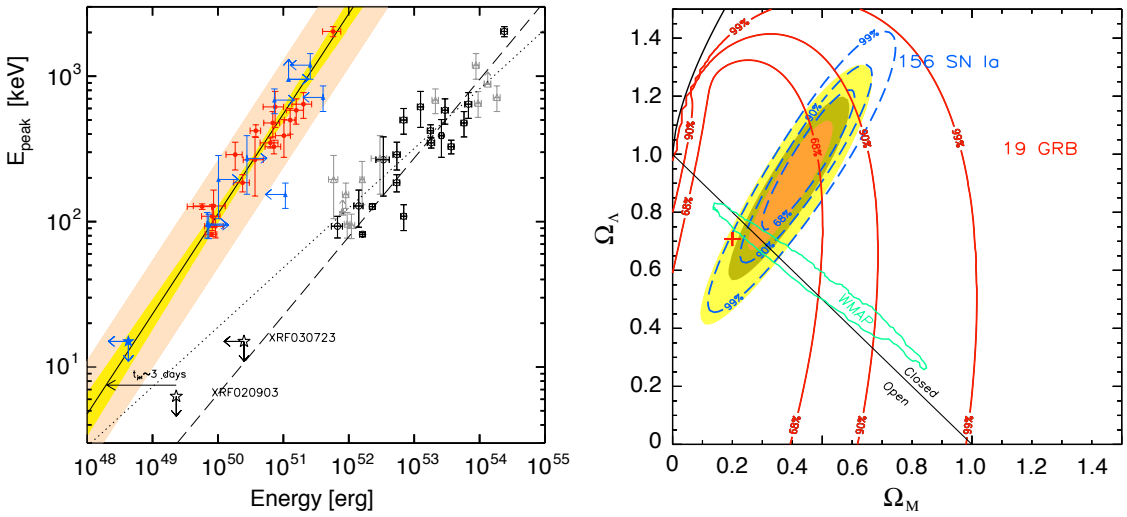

Figure 1.14: Results from the Ghirlanda correlation: *Left:* Rest frame peak energy $E_{\rm peak}$ versus isotropic (black/grey, open symbols) and collimation corrected (colour, filled symbols) energy. The data points are the 19 GRBs with measured z, $E_{\rm peak}$ and $t_{\rm break}$, for which the collimation corrected energy could be computed. *Right:* Constraints of the cosmological parameters Ω_M and Ω_Λ obtained with the same burst sample. The contours obtained with the 156 SN Ia and with the WMAP data are shown in addition. Figure from [65].

1.2.6 VHE gamma rays from GRBs

Several attempts were made in the past to observe GRBs in the GeV and TeV energy range, each indicating some excess over background but without stringent evidence. So far, only seven GRBs were observed above $E > 30\,\mathrm{MeV}$ by the EGRET detector, and in three of them photons with energies $E > 1\,\mathrm{GeV}$ were detected [67, 68, 69, 70]. The observed spectra are consistent with a power-law behaviour with no HE cutoff up to the maximum energy observable by the instrument. Taking into account the small FOV of the EGRET detector ($\sim 0.6\,\mathrm{sr}$) and its limited sensitivity, the small number of VHE detections does not contradict the idea that all GRBs could have a VHE component.

The burst GRB940217 [67] is most cited when discussing VHE components in GRBs. The EGRET detector recorded three photons with energies $E > 2\,\mathrm{GeV}$ from this event, particularly one $E \approx 18\,\mathrm{GeV}$ photon, delayed $\sim 1.5\,\mathrm{h}$ after the burst onset (see figure 1.15).

Several models have been proposed to explain the delayed GeV emission from this event: Electron IC emission scenario in the forward shock [71, 72], hadron-process scenario [73, 74], and scenario invoking electromagnetic cascade processes of TeV γ-rays in the IR/microwave background [75, 76, 77, 78]. Supported by the recent discovery of delayed X-ray flares during the afterglow phase, new models came up suggesting VHE emission due to IC processes of the flare photons. Depending on the origin of the IC emission, the GeV-TeV flares may overlap with the X-ray flares, or may not correlate but become instead smoother and longer [79]. The emission mechanism in this case can be restricted with a simple correlation analysis.

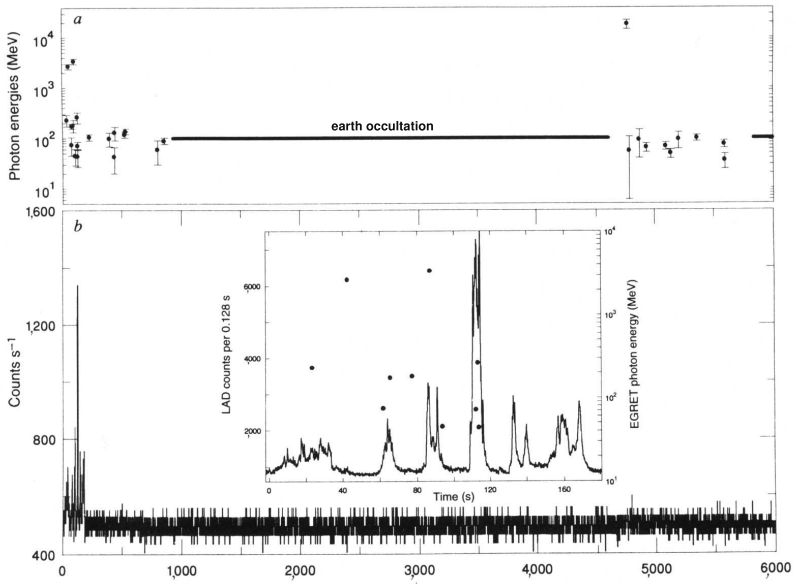

Figure 1.15: Light curves of the GRB940217. *Top:* Events recorded by the EGRET spark chamber, recording the time, energy and arrival direction of individual photons. The horizontal line indicates periods where no data are available due to Earth occultation. *Bottom:* Count rates of ULYSSES satellite in the $25 - 150\,\mathrm{MeV}$ energy range. The burst is evident at the beginning of the light curve. *Inlet:* Expanded plot of the BATSE light curve with the arrival times and energies of the EGRET photons. Figure from [67].

Many other groups reported coincidence or follow-up observations of GRBs beyond the keV/MeV range: The TIBET air shower array [80], the WHIPPLE IACT [81, 82], the HEGRA AIROBICC Cherenkov array [83], the Milagrito experiment [84], the GRAND array [85], the Milagro detector [86, 87] and the STACEE Solar Array [88]. However, none of these observations provided a highly significant excess.

Observations of GRBs in the VHE regime have the potential to constrain theoretical models of both the prompt and the afterglow emission phase. Photons at energies in this energy range produce e^-e^+ pairs in the GRB fireball. Spectral observations at VHE energies can provide therefore useful constrains on the bulk Lorentz factor, resulting from the required optical depth [89, 90]. In addition, HE photons suffer interactions with the EBL photons before reaching the observer. The e^-e^+ pairs produced in this interaction can IC scatter again on the most numerous EBL photons, giving rise to the delayed secondary spectrum, which ranges typically up to hundreds of GeV [76, 91].

Chapter 2

Imaging atmospheric Cherenkov telescopes

In the previous chapter I summarised the current findings and the many concepts of the physical processes, which are responsible for the acceleration of cosmic rays, as well as their interactions with hadrons or photons, while travelling through the Universe. Here I will characterise the methods used to explore the cosmic ray spectrum in the VHE domain. Generally, the rule holds that the higher the γ-ray energies are, the lower are the γ-ray fluxes (see figure 1.1). Therefore large detector areas are necessary to observe the spectrum in the VHE domain. Gamma rays of all energies are fully absorbed by the Earth atmosphere, the HE ones by creating extended showers of electrons, positrons and photons. The formation of particle cascades is outlined in § 2.1. Ultrarelativistic shower particles with $\beta > \beta_c$ ($\beta_c = 0.9997$ at sea level) create Cherenkov light, which can be detected by appropriate detectors, for example by the IACT. Due to the very low refractive index (changing with altitude, as described in § 2.2) the Cherenkov light is basically collimated in the shower direction. While showers below a few TeV stop high up in the atmosphere (e.g. direct detection of particles by ground based detectors is impossible), the Cherenkov light can easily be measured by ground based telescopes, albeit only during clear dark nights. The Cherenkov light carries quite some information on the main shower parameters (total energy, shower extension etc.), which can be used to discriminate between γ-induced and hadron-induced showers. The MAGIC telescope is such a detector and § 2.3 addresses its features. The secondary particles from the cascades of γ-rays with energies above 10 TeV can reach the ground and can be detected directly. The extremely low fluxes limit the sensitivity of IACTs at these energies. Large air-shower arrays with scintillator detectors or water tanks could instead be used for their detection. For instance, the Pierre Auger observatory[1] covers more than 3000 km^2 detection area and allows to measure fluxes lower than one particle per km^2 per century. Finally, in § 2.4 I describe the cooperation between the space based experiments and ground based facilities, with the common goal to solve the long lasting mystery of GRBs.

[1] `http://www.auger.org`

2.1 Shower development in Earth atmosphere

An air shower is a cascade of particles triggered by the interaction of a single HE primary cosmic ray nucleus or photon with atoms in the Earth atmosphere. Depending on the impinging primary particle one makes the distinction between *electromagnetic* and *hadronic* air showers. The interpretation of these events is, however, difficult. There is little information on the energy and type of the primary cosmic ray - these have to be derived from the shower properties. Since even the point of the first interaction in the atmosphere is not known, the observer has to derive first the degree of the shower development.

The interpretation of air shower results is done on the basis of Monte Carlo (MC) simulations of the shower development. Figure 2.1 shows shower examples for proton and photon cascades, as simulated with CORSIKA [92]. While hadronic showers show large transversal extension with irregular distribution on the ground, electromagnetic showers are elongated, narrow, "cigar" shaped formations. The observed air shower features are compared to shower models that describe the derivation of the primary particle energy and type. Conclusions cannot be made for individual cascades because of the fluctuations in shower development. Therefore one needs a reasonably large statistical sample. In the following, I will describe briefly the electromagnetic and hadronic air showers.

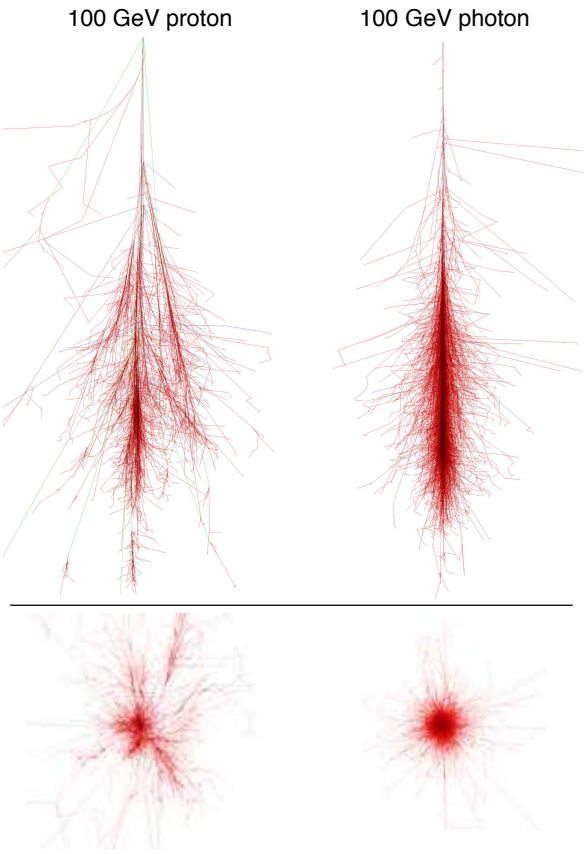

Figure 2.1: Electromagnetic and hadronic shower profile simulation with CORSIKA. *Left:* Shower development caused by a 100 GeV proton. *Right:* Shower induced by a 100 GeV photon. *Top:* Longitudinal shower development. *Bottom:* Projection of the transversal image of the shower on the ground. Figure from [93].

Electromagnetic showers

The development of an electromagnetic shower in the atmosphere starts with the production of an e^-e^+ pair. In the presence of the Coulomb field of the atmospheric nucleus, new γ-rays are generated via bremsstrahlung. The energy loss due to bremsstrahlung is proportional to the energy of the electron E_e and the radiation length X_0^e:

$$-\frac{dE_e}{dX} = \frac{E_e}{X_0^e} \qquad \text{with} \qquad X_0^e = 37\,\mathrm{g\,cm^{-2}} \qquad \text{(in air)} \tag{2.1}$$

Analogously, the pair creation process can be characterised by a mean free path $X_0^\gamma = 9/7 \cdot X_0^e$.

The secondary particles created in both processes are again electrons, positrons and photons, as illustrated in figure 2.2. Multiple scattering and the Earth magnetic field deflects them away from the primary γ-ray direction, the so-called *shower axis*, and the particles form a disc of a few metre thickness that moves downwards with a speed higher than the speed of light in the medium (air). The energy of the secondary particles decreases as the shower development proceeds. The cascade dies out when the particle energy reaches the critical energy for the bremsstrahlung $E_c = 81\,\mathrm{MeV}$. Below E_c ionisation becomes the dominant energy loss process of electrons.

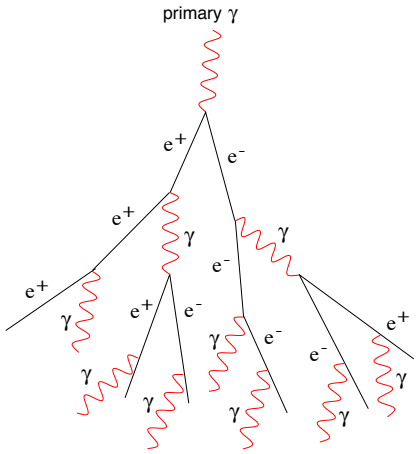

Figure 2.2: Electromagnetic air shower cascade.

The **longitudinal development** of the shower can be described by the evolution of the number of electrons N_e versus the depth of the atmosphere. An analytical approach was derived in [94] and is called the "approximation B":

$$N_e(t, E_0) \simeq \frac{0.31}{\sqrt{\ln(E_0/E_c)}} \cdot \exp\left[t \cdot (1 - 1.5 \ln s)\right] \tag{2.2}$$

where E_0 is the energy of the primary photon. This solution is a function of the shower age parameter s that describes the stage of the shower development:

$$s = \frac{3t}{t + 2\ln(E_0/E_c)} \tag{2.3}$$

This in turn is related to the atmospheric depth X in radiation lengths t:

$$t = \frac{X}{X_0} \approx \frac{X_{\mathrm{air}}}{X_0 \cdot \cos(\Theta_{\mathrm{shower}})} \cdot \exp\left(-\frac{H}{H_0}\right) \tag{2.4}$$

The atmospheric depth determines the thickness of the atmosphere along the shower axis. The incidence angle of the shower Θ_{shower}, as well as atmospheric parameters like the column height of the air $X_{\mathrm{air}} = 1013\,\mathrm{g\,cm^{-2}}$ and the scale height of the pressure $H_0 = mg/RT \approx 7.1\,\mathrm{km}$ and the height a.s.l. enter into the equation.

The meaning of s is given by the derivative $dN_e(t, E_0)/dt$: For $0 < s < 1$, $dN_e(t, E_0)/dt > 0$ and N_e increases; At $s = 1$, $dN_e(t, E_0)/dt = 0$ and N_e reaches maximum and finally, when $s > 1$, $dN_e(t, E_0)/dt < 0$ and the shower starts to die out. Figure 2.3 shows the depth-dependence of the number of electrons (shower profiles) for showers initiated by γ-rays of energies above 30 GeV. Gamma ray induced air showers with energies below $\sim 30\,\mathrm{TeV}$ have their shower maximum well above the MAGIC telescope. Showers below $\sim 100\,\mathrm{GeV}$ die out before reaching the ground, while more energetic showers enter deeper into the atmosphere.

The position of the shower maximum, the so-called $X_{\max}$, can be obtained from equation 2.3, by inserting $s = 1$:

$$t_{\max} = \ln \frac{E_0}{E_c} , \qquad X_{\max} = X_0 \cdot \ln \frac{E_0}{E_c} \tag{2.5}$$

The resulting maxima for energies between 30 GeV and 1 TeV range from 12 km to 8 km. This is the reason why the MAGIC telescope reflector is focussed to 10 km [95] (see also § 3.5). It gives the best image for both the head and the tail of the shower.

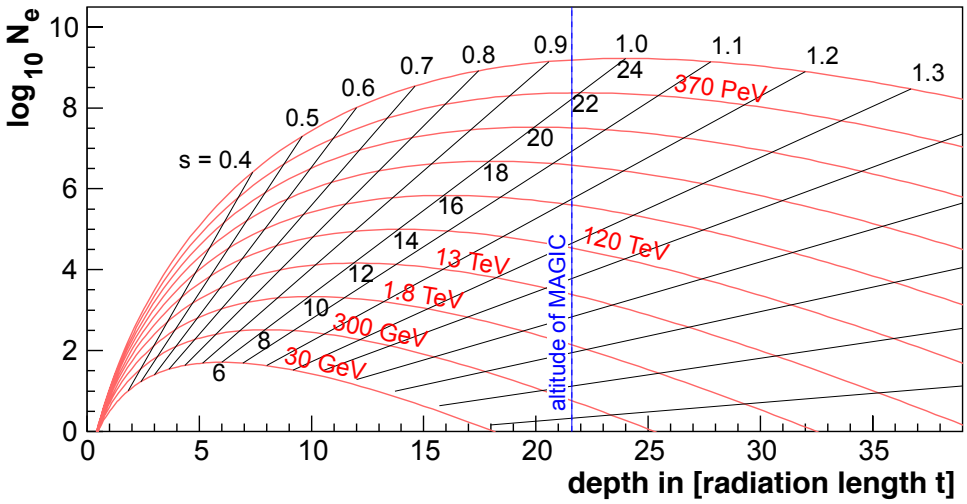

Figure 2.3: Longitudinal development of an electromagnetic shower. Several red lines are used for different primary energies E_0. The values $\ln(E_0/E_c)$ are shown right under the corresponding line.

The **transversal development** of the shower can be modelled by the Nishimura-Kamata-Greisen (NKG) formula [96, 97], that gives the density of shower electrons as:

$$\rho(r, t, E_0) = K \cdot \frac{N_e(t, E_0)}{R_M^2} \cdot \left(\frac{r}{R_M}\right)^{s-2} \cdot \left(1 + \frac{r}{R_M}\right)^{s-4.5} \tag{2.6}$$

where $\rho(r, t, E_0)$ is the $e^{\pm}$ density as a function of the distance r to the shower axis, the radiation length t and primary particle energy E_0. K is a normalisation constant. The Molière radius R_M is defined by the length in the air with a thickness of atmosphere as follows:

$$R_M = 21.2\,\text{MeV} \cdot \frac{X_0}{E_c} \approx 9.3\,\text{g cm}^{-2} \qquad \text{(in air)} \tag{2.7}$$

Hadronic showers

Hadronic showers are cascades initiated by a hadronic interaction of a nucleon or a heavier nucleus. In the first interaction a large fraction of the nucleon energy (about 1/2) is transferred to secondary mesons, both charged and neutral. Apart from second-order collective effects the same happens in nucleus-nucleus interactions where more than one nucleon from the primary nucleus can participate in the interaction.

The principal schematics of hadronic showers is shown in figure 2.4. About 90% of all secondary particles produced in a hadronic shower are pions. About 2/3 of the secondary pions are $\pi^{\pm}$ and 1/3 are π^0. Secondary neutral pions decay immediately (lifetime $\tau = 8.4 \cdot 10^{-17}$ s) into two γ-rays, unless their energy is extremely high. The daughter γ-rays start electromagnetic cascades practically at the interaction point. Therefore in each hadronic interaction about 1/3 of the energy is transferred to the electromagnetic component.

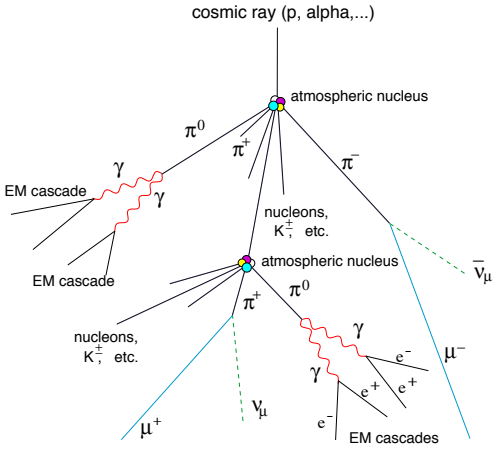

Figure 2.4: Hadronic air shower cascade.

Charged pions have much longer lifetime ($\tau = 2.6 \cdot 10^{-8}$ s) – they can either decay or re-interact. This interaction/decay competition of all charged mesons determines the details of the development of hadronic showers. HE charged pions, with their large decay length, because of time dilatation, almost exclusively interact. Low energy pions decay into a muon and a muon neutrino: $\pi^{\pm} \rightarrow \mu^{\pm} + \nu_{\mu}(\overline{\nu}_{\mu})$. The decay channel $\pi^{\pm} \rightarrow e^{\pm} + \nu_e(\overline{\nu}_e)$ is strongly suppressed due to helicity conservation. The muons themselves interact almost exclusively by ionisation and usually reach the ground before decaying (lifetime $\tau = 2.2 \cdot 10^{-6}$ s).

The development of the hadronic skeleton of the shower can be observed by its muon component. There is of course a truly hadronic component consisting of nucleons and mesons, but the number of hadrons is significantly smaller than the muons, electrons and photons and can hence be neglected in the general discussion. Single muons with a large transversal momentum can travel far from the shower core. A part of them form ring images (see figure 4.21), which can be recognised and rejected with the IACT technique.

The hadronic showers initiated by heavier nuclei can be described by the *superposition approximation* [98]. It represents the shower initiated by a nucleus of mass A and total energy E_0 as a superposition of A showers initiated by nucleons of energy E_0/A. The average depth of maximum for the hadronic showers then becomes:

$$X^A_{\max} = X_0 \cdot \ln\left[\frac{2 \cdot (1 - K_{el}) \cdot E_0}{(\langle m \rangle/3) \cdot E_c \cdot A}\right] + \lambda_N(E_0) \tag{2.8}$$

where λ_N is the depth of the first interaction, K_{el} is elasticity in the interaction and $\langle m \rangle$ the number of secondary pions generated, 1/3 of which are neutral. The number of electrons (size) at the shower maximum is:

$$N_e^{\max} = \frac{1}{2}\frac{\langle m \rangle}{3}\frac{E_0 \cdot (1 - K_{el})}{E_c} \tag{2.9}$$

With reasonable choice of values for $K_{el} = 0.5$, $\langle m \rangle = 12$ and $\lambda_N = 80\,\mathrm{g\ cm^{-2}}$, the depth of maximum of a 10^5 GeV proton initiated shower is estimated at about $550\,\mathrm{g\ cm^{-2}}$ and the size at maximum is about $6 \cdot 10^4$ electrons. The number of muons can be estimated with the formula:

$$N^A_{\mu} = A\left[\frac{E_0/A}{\epsilon_{\pi}}\right]^{\beta} = A^{1-\beta} \cdot N^p_{\mu} \qquad \text{with} \qquad \beta = \frac{\ln(2/3\langle m \rangle)}{\ln\langle m \rangle} = 0.85 \tag{2.10}$$

where ϵ_π in an effective energy and β the fraction of charged pions in the multiplicity, i.e. showers initiated by heavy nuclei generate more muons than proton showers.

All the equations are energy dependent and only account for the first-generation pions. These estimates cannot be very exact, but still contain the main features of the shower development – the size at maximum is proportional to the primary energy and $(X^A_{\max} - \lambda_N)$ is proportional to its logarithm.

For protons the characteristic interaction length is larger than the corresponding electromagnetic interaction length. Thus hadronic showers penetrate deeper into the atmosphere than electromagnetic ones of the same energy. Moreover, hadronic showers show larger fluctuations from shower to shower, compared with the electromagnetic case.

A detailed study of the hadronic shower development implies the application of models of nuclear interaction to a huge number of particles. MC simulations are the best tools for the study of hadronic showers behaviour. The nucleus cross-sections for HE interactions in the atmosphere are extrapolated from accelerator experiment results at lower energies, though containing some uncertainties.

2.2 Imaging atmospheric Cherenkov telescope technique

The charged particles of the electromagnetic air showers are mostly relativistic. These particles produce Cherenkov light in the atmosphere. Using this effect allows the detection of primary γ-rays with energies well below the threshold of instruments that detect the shower tail particles [99].

2.2.1 Nature of the Cherenkov radiation

The emission of Cherenkov radiation is connected to the coherent response of a medium to the passage of a relativistic charged particle. The atoms/molecules of the medium close to the passing particle are distorted by its electric field, as shown in figure 2.5. The polarised atoms return to their normal configuration when the particle has moved away. During the distortion the atoms behave like elementary dipoles, and so the regions along the particle track receive a very brief electromagnetic pulse. If the particle moves faster than the speed of light in the medium, the symmetry along the particles trajectory is no longer preserved. The resultant dipole field shows up even at large distances from the track. At a distant point, the wavelets from all parts of the track can be in phase in this scenario, which produces a net polarisation field.

Assuming the particle's velocity to be $v = \beta \cdot c$, then the particle traverses the distance AB in the time Δt and the light the distance $AC = \Delta t \cdot (c/n)$, where n is the refraction index of the medium (see right drawing of figure 2.5). In this case, by Huygens construction, the appropriate wavelets from positions along the particles trajectory are coherent and form a plane wave front BC. This quantitative description results in two main properties: For a certain medium with $n(\lambda)$, there is a threshold velocity for a charged particle with the mass m_0 to emit Cherenkov photons of wavelength λ:

$$v > \frac{c}{n(\lambda)} \qquad \text{equivalent to :} \qquad E > m_0 c^2 \cdot \frac{n(\lambda)}{\sqrt{n^2(\lambda) - 1}} \tag{2.11}$$

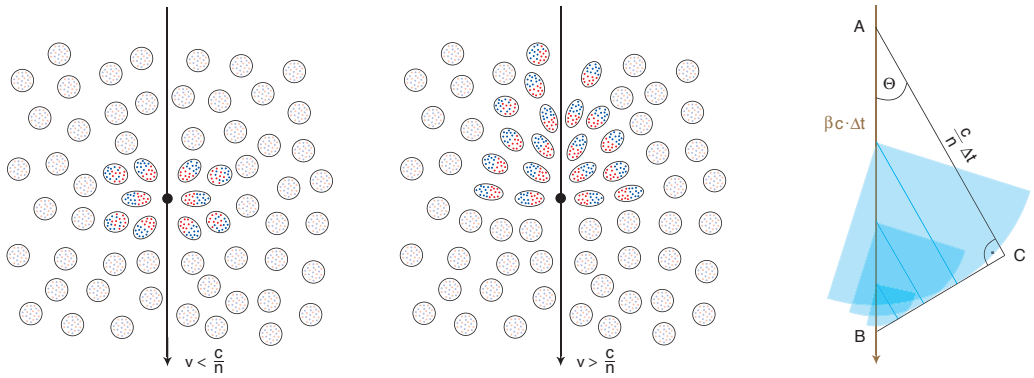

Figure 2.5: Polarisation of a dielectric medium due to a moving charged particle. *Left:* Particle speed higher than speed of light. *Center:* Particle speed bigger than speed of light. *Right:* Coherence shown by Huygens construction. For explanations see text.

The angle of emission (called Cherenkov angle) is given by:

$$\cos\Theta_c = \frac{1}{n(\lambda)\cdot\beta} \qquad \text{with} \qquad \beta = \frac{v}{c} \tag{2.12}$$

where Θ_c is the angle with respect to the direction of the particle velocity. The photons are emitted on a narrow cone around the direction of the particle. The opening angle Θ_c is a function of the density of the air and, thus of the height of emission, as illustrated in figure 2.6. It increases downwards but is always less than about 1.4°. The electromagnetic shower has an opening angle of typically $\Theta_c = 1.2°$ at 2200 m, 0.75° and 0.36° at 10 km and 20 km a.s.l., respectively. Each individual electron produces a Cherenkov cone. The sum of all Cherenkov photons emitted from particles flying along or close to the shower axis, i.e. the particles from the shower core, uniformly illuminate a ring of ~ 120 m radius at altitudes of 2200 m a.s.l. At larger distances from the shower axis the photon density decreases exponentially and forms the shower halo, as shown in figure 2.7. The radius of Cherenkov light pool is only little dependent on the primary particle energy E_0 but more on the altitude and the zenith angle of the observation.

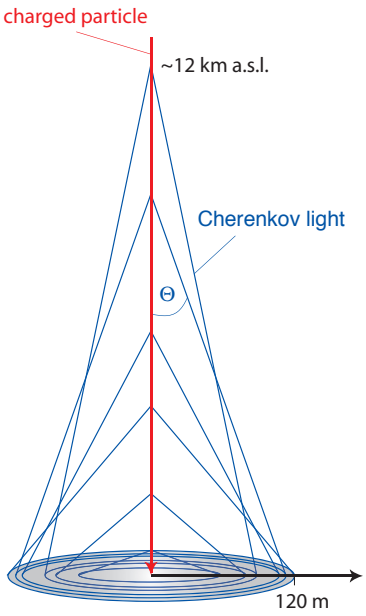

Figure 2.6: Formation of the Cherenkov light pool.

The number of Cherenkov photons N_c produced by a single relativistic particle per unit path length amounts to:

$$\frac{dN_c}{dx} = 2\pi Z^2\alpha \int_{\lambda_1}^{\lambda_2} \left(1 - \frac{1}{n^2(\lambda)\beta^2}\right)\frac{d\lambda}{\lambda^2} \tag{2.13}$$

where Z is the charge of the ionising particle in units of e and $\alpha = 1/(\hbar c) = 1/137$ is the fine structure constant. In an electromagnetic air shower, about 500 Cherenkov photons in the spectral range between 300 nm and 600 nm are created per GeV of incident γ-ray energy.

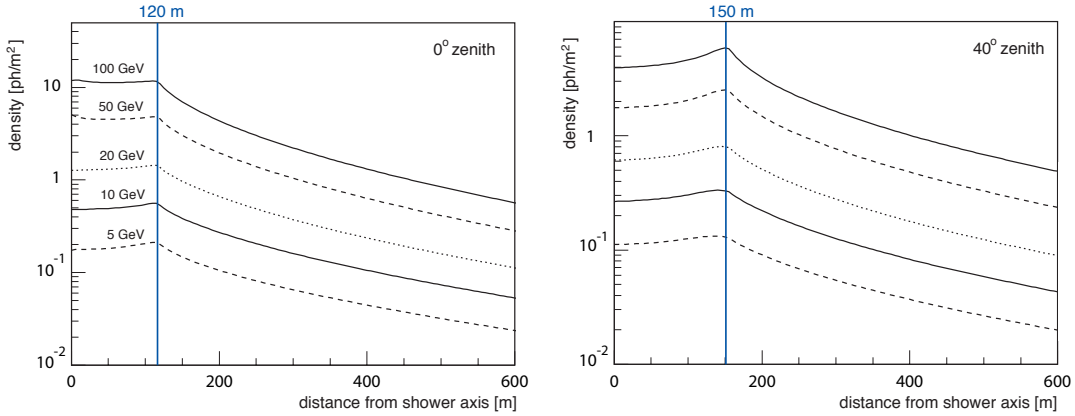

Figure 2.7: Lateral distribution of Cherenkov photons on ground (at 2200 m a.s.l.). The radial distribution is uniform up to ~ 120 m from the shower axis. The position of the hump is dependent on the zenith angle of the observation and not on the primary particle energy E_0.

2.2.2 Attenuation of Cherenkov photons in the atmosphere

Not all Cherenkov photons generated in the air shower reach the detector. The following processes have to be taken into account when simulating the Cherenkov photons propagating down to the ground from the point of generation high up in the atmosphere:

a) The absorption of Cherenkov photons is strongly dependent on the thickness of the atmosphere, or in other terms, on the zenith angle of the observation. For wavelengths $\lambda < 290$ nm the absorption by ozone molecules ($O_3 + \gamma \rightarrow O_2 + O$) dominates, while H_2O and CO_2 molecules interact with photons of wavelengths $\lambda > 800$ nm.

b) Multiple scattering of the low energy $e^{\pm}$ in the shower tail can result in quite large deflections from the shower axis. In turn, Cherenkov photons can also be emitted at large angles to the shower axis. These photons form the "halo" tails shown in above figure 2.7.

c) The Cherenkov photons itself interact with molecules in the air via *Rayleigh scattering*. The cross section varies with the wavelength and is proportional to λ^{-4}. UV light is therefore strongly affected. Rayleigh scattering is the dominant attenuation process in the case of good weather conditions.

d) In the presence of particles larger than the photon wavelength (water droplets, small ice crystals, dust or calima[2]) in the atmosphere, *Mie scattering* occurs. The cross section is proportional to λ^{-a} with $1 \leqslant a \leqslant 1.5$. Above a certain altitude this attenuation is only important in the case of bad atmospheric conditions. While Rayleigh scattering is very predictable, Mie scattering is highly variable (depends on aerosol size, shape and dielectric constant) and a source of systematic uncertainty when determining fluxes.

The final averaged Cherenkov photon spectrum observable at 2200 m a.s.l. from a simulated electromagnetic shower is shown in figure 2.8. The spectrum from showers at high zenith angles is shifted towards longer wavelengths, as shown with the blue and orange curves. The

[2]Calima is fine dust or sand blown over the Atlantic Ocean from the Sahara Desert to the Canary Islands.

Cherenkov photon spectrum peaks in the UV range. Above $\sim 650\,\mathrm{nm}$ the light of the night sky (LONS) has strong emission lines. Therefore one usually measures below this wavelength.

The light losses of the first three attenuation processes described before are well predictable and can be included in the MC simulation of γ-ray showers. On the other hand, weather conditions are variable on short time scales and have obviously strong impact on the observation with Cherenkov telescopes. However, instruments capable of quantifying the atmospheric differential extinction coefficient along the line of sight can be used to monitor the observational conditions. At the MAGIC site a *LIDAR* and a *Pyroscope* are implemented to measure the atmospheric transmission [100].

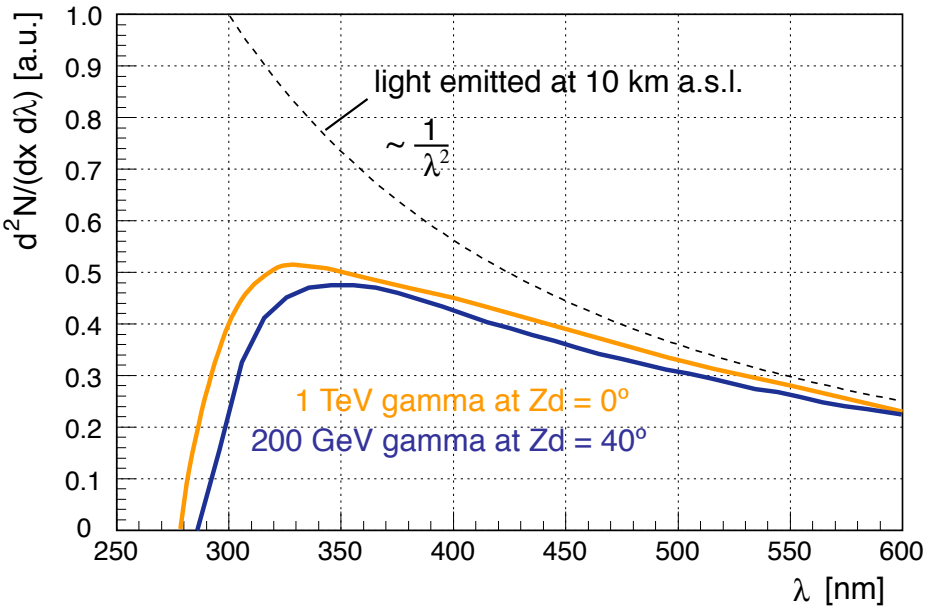

Figure 2.8: Spectrum of the Cherenkov photons from electromagnetic cascades in the atmosphere. The absorption effects are apparent by comparing the total light produced at 10 km height (dotted line) with the measured spectra (solid lines). The two solid, coloured lines represent the spectra for different zenith angle observations and energies, normalized to the same initial spectrum.

2.2.3 Principle of the IACT technique

The main difference of IACTs with respect to optical or radio telescopes is that it does not directly detect the radiation emitted by the astrophysical object under study. It detects the relativistic cosmic rays originating from the source indirectly, by the cascades produced in the Earth atmosphere. The cosmic rays (both hadrons and γ) produce very short Cherenkov light flashes. Their duration and pattern depends on the type of the particle: Cherenkov light from a γ-ray shower has a time spread of typically $\Delta t_\gamma \approx 3\,\mathrm{ns}$ (FWHM) (see figure 4.6), while the light from hadron initiated showers can last up to $\Delta t_\mathrm{h} \approx 10\,\mathrm{ns}$ (example shown in figure 4.7). In addition, the hadronic cascades are isotropic in arrival directions. Enhancements of electromagnetic showers from a hypothetical source position is a proof for γ-ray emission from the source direction.

The diffuse LONS or bright stars in the FOV of the telescope produce a steady flux of photons, with only statistical fluctuations. The same is valid under moon light, where the

scattered light could increase by factor ~ 10. Using fast sampling rates of the Cherenkov light, one can reduce the impact of the background light almost entirely. The light detectors used in the camera of current IACTs are photo-multiplier tubes (PMTs) with very fast response times.

The working principle of an IACT is shown in figure 2.9. If the telescope is placed inside the Cherenkov light pool, a fraction of this light is reflected by the mirror and imaged onto the pixelised camera, situated in the focal plane of the mirror. According to equation 2.12, the Cherenkov angle in the first order depends on the height of the emitting region. Consequently, there exists a good correspondence between the relative position in the camera and the emission region of the Cherenkov light. For showers parallel to the telescope axis, light from the lower part of the shower is mapped further away from the camera center (see figure 2.9).

The images formed in the telescope camera are projections of the shower development and can be used to extract information about the particle type, energy and incident direction. The method used to parameterize the images is called the **Hillas parametrisation** and is described in § 5.4.

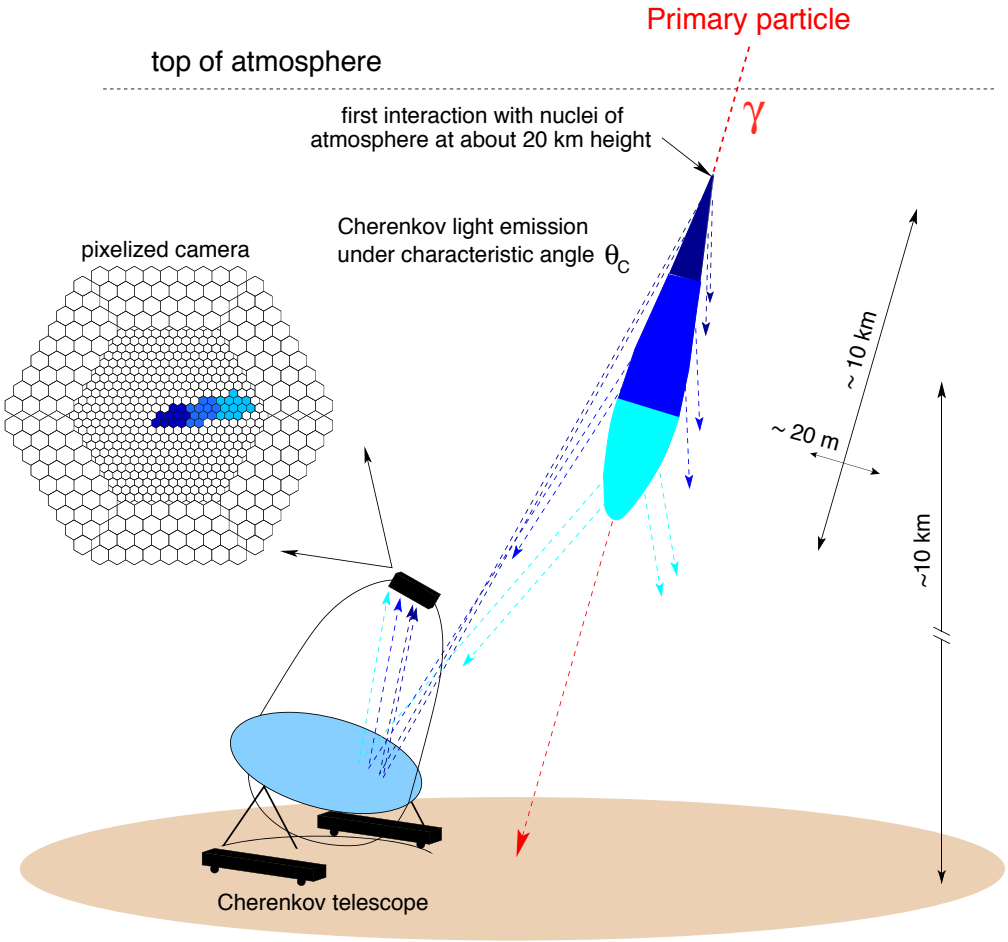

Figure 2.9: Working principle of an IACT.

2.3 The MAGIC telescope

The Major Atmospheric Gamma ray Imaging Cherenkov (MAGIC) telescope is currently the largest and technologically most advanced IACT [95]. It is located at the Observatory del Roque de los Muchachos (28.75° N, 17.89° W, 2200 m a.s.l.), on the Canary Island of La Palma.

Figure 2.10: A photograph of the MAGIC telescope.

The main goal of the experiment is to open and explore the current observation gap between 30 GeV and 300 GeV in the spectrum of the cosmic electromagnetic radiation. The particular goal of MAGIC is to observe the γ-ray sky below 100 GeV. This energy band may be decisive for several important scientific topics: The physics of various galactic and extragalactic γ-ray sources, the study of EBL, GRBs, pulsars, indirect detection of dark matter, test of quantum gravity and the long lasting problem of the origin of cosmic rays.

Gamma ray observations below 20 GeV are carried out by satellite detectors. Due to the power-law decrease of the γ-ray flux towards higher energies, the size limited space borne detectors ($< 1\,\mathrm{m}^2$ detection area) loose rapidly their sensitivity. Conversely, Cherenkov telescopes reach effective detection areas of about $10^5\,\mathrm{m}^2$. However, due to the low photon flux, the previous IACT generation with small mirror areas was not able to observe below 300 GeV. Thanks to its $236\,\mathrm{m}^2$ reflector and numerous technical innovations introduced for the first time in this field, MAGIC now provides high enough sensitivity to reach a detection threshold of only 50 GeV. The small energy gap – in comparison with the more than seven orders of magnitude extended cosmic γ-ray spectrum (see figure 1.1) – is interesting, mainly because only a small fraction of the HE emitting sources detected by satellite experiments have been confirmed by ground based detectors. The left hand side of figure 2.11 shows the skymap with the 271 EGRET sources, and for comparison the right hand side shows the currently known 41 VHE sources.

The limited number of VHE sources is due to very low fluxes in general, spectral cutoffs of many sources (e.g. pulsars) and the increasing cross-section for absorption of the γ-rays with the microwave and IR photons at higher energies. Only γ-rays lower than a certain cutoff energy may arrive from large distances (see figure 1.2).

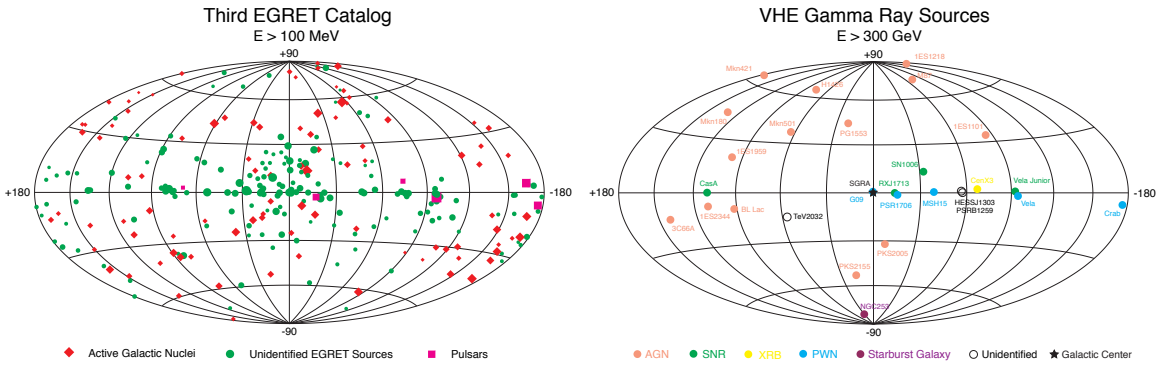

Figure 2.11: Skymap of VHE γ-ray sources. *Left:* 271 point sources detected by EGRET in the energy band 100 MeV $< E <$ 10 GeV. Figure from [17]. *Right:* Discovered VHE γ-ray sources. Currently (fall 2006) 41 sources have been detected (not all sources in the galactic plane are shown).

Since most GRBs occur at redshifts $z > 1$, a low energy threshold is crucial for their observation. In addition to the low threshold and high sensitivity, MAGIC incorporates two other exclusive design features, introduced especially for the detection of GRBs:

- The light-weight construction enables the telescope to point to an arbitrary position on the sky within less than 20 s after the notification of the coordinates from satellite experiments. In the initial phase of operation this has been reduced to 100 s for safety reasons and performance studies of the fast operation.
- Observation in the presence of Moon and twilight significantly increases the duty cycle of the experiment.

Since my thesis is dedicated to GRB studies, I will focus on the telescope key parameters related to their observation. The telescope drive system, which allows the fast slewing of the telescope follows in § 2.3.1. The GRB alert system, responsible for the validation of the GRB alerts from satellites, is described in detail in § 2.4.2. The conditions to build a 17 m Ø light-weight mirror support space frame and the need for high stiffness contradict each other. The modern design concept of large optical telescopes is followed and deformations of the support frame are corrected by the AMC. The AMC system, developed, built and maintained by myself is described in § 3. A more detailed discussion of the physic goals and remaining hardware components can be found in [95, 101, 102].

2.3.1 Telescope drive system

The drive system of the MAGIC telescope [103] has to meet two basic demands: On the one hand, during normal operation, the 64 t telescope has to be repositioned accurately, and has to track a given sky position with high precision. On the other hand, in response to a GRB alert, it has to be powerful enough to reposition the telescope to any arbitrary sky coordinates within seconds.

Tracking celestial objects with the alt-azimuth mount requires movements with variable speed along both axes. In order to allow continuous observation of a given source the movement range in azimuth spans from $\varphi = -90°$ to $\varphi = +418°$, where $\varphi = 0°$ and $\varphi = 90°$ denotes the geographical north and east, respectively. Due to this constraint, repositioning to new coordinates can require more than a 180° turn. The zenith angle movement ranges from

$\Theta = +105°$ to $\Theta = -70°$, where the change in sign implies the backward movement over the zenith. The so called *reverse mode* is not yet used, because hysteresis in the dish deformation makes both the tracking and focussing procedures difficult to handle.

The current repositioning time of on average 40 s in the **fast movement mode** is limited by the following factors [104]:

- The acceleration speed in azimuth is limited by the available power. At acceleration outreaching the available power, the motors cannot provide enough torque and the electronic control system overreacts. Emergency stops issued by the drive controllers are the consequence. This deficiency can be circumvented by installing additional capacitors, which would provide short-term additional power during acceleration. The current best value for the acceleration has been set to $0.11\,\mathrm{m\,s^{-2}}$. Alternatively it would be better to use the so-called torque control instead of speed control.

- The maximum velocity of the telescope is limited by the maximum possible deceleration speed and the path length required for a full stop. Hardware end-switches ensure that in case of emergency the telescope stop is fully controlled by the drive controllers without software interaction. For a given deceleration, the maximum velocity is given by the emergency stop path length. From these constraints, the current maximum velocity of $0.67\,\mathrm{m\,s^{-1}}$ was determined.

Up to July 2005 the standard repositioning speed was also used for the follow-up observations of GRBs. Recently, the performance was improved (see table 6.4) and slewing in azimuth by $\Delta\varphi = 180°$ is achieved within < 50 s. The repositioning time in elevation is not critical in the sense that it will never take more than 20 s. Further improvements of the repositioning time would be achieved when using the reverse mode, by shortening substantially the distances in azimuth and by widening the ranges for deceleration. The requirement of reaching any position in the sky within < 20 s can then be fulfilled.

2.4 Observation of GRBs with ground based experiments

GRBs occur at random times in unpredictable directions. In order to get a significant enough detection rate, dedicated satellite experiments for GRB surveys need to observe large portions of the sky. Large FOV results in poor spatial resolution and crowded field at the detector. Therefore new satellite experiments, like SWIFT for example, are equipped with additional detectors, which allow studying the source with higher precision and in a broader wavelength range. These special detectors have smaller FOVs and need therefore to be aligned to the new sky position. This is done by slewing the satellite and performing follow-up observations with some delay after the GRB onset. Ground based experiments are larger than the satellite detectors and therefore much more sensitive. In order to allow follow-up observations of GRB events by ground based experiments, the GCN was invented. The next two chapters describe the GCN, as well as its connection with the MAGIC telescope. In § 2.4.3 a systematic study of the quantity of GCN alerts in the first observation period of the MAGIC telescope is shown.

2.4.1 GRB coordinates network

The GRB coordinates network was established in 1994 [105]. Its aim was to distribute the GRB sky coordinates from the BATSE detector – on board of the CGRO – to ground based experiments, while the GRB was still ongoing. After the de-orbiting of CGRO, the previously called *BATSE COordinates DIstribution NEtwork* (BACODINE) was renamed by the more general name GCN[3]. Three satellite experiments provided in the past GRB locations to the GCN in real-time: SWIFT [25], HETE-2 [106] and INTEGRAL [107]. Since April this year the HETE-2 satellite is no more fully operational and only SWIFT and INTEGRAL activate the follow-up observations.

The main task of the GCN is to distribute the GRB coordinates to registered clients around the world. In addition, it allows the GRB community to share quickly their observation results over mailing lists (GCN circulars). Figure 2.12 schematically shows the flow of telemetry data from the satellites through the GCN to the clients. The data flow between the satellite and the GCN is different from experiment to experiment:

- The SWIFT spacecraft transmits the GRB information to the closest of the 3 in-orbit TDRS satellites, which then gets transmitted to the White Sands ground station in New Mexico. From there, the messages get passed to the GCN system at Goddard Space Flight Center through an internet socket connection [26].

- The HETE-2 spacecraft send the GRB position information to one of the 14 dedicated ground stations via VHF. These stations were distributed along the equator, and thus always ensured coverage of the satellites orbit. The information was sent from the corresponding station to the MIT mission control center via internet and forwarded directly to the GCN [108].

- The INTEGRAL spacecraft does not generate alerts on board. It sends all data to the ESA Mission Operation Center (MOC) in Darmstadt. From there it gets continuously transmitted over a dedicated line to the INTEGRAL Science Data Centre (ISDC), where the INTEGRAL burst alert system (IBAS) program filters out triggers from possible GRB events. The IBAS alert packages, containing the position of the GRB, are sent to the GCN via internet [109].

The time delay in the distribution of coordinates is the sum of several factors. First of all there is a delay onboard the satellite. This is variable and depends on the instrument and of course on the intensity and the time profile of the GRB event. The average delay to accumulate a $5\,\sigma$ detection is about 5 s, but it can last much longer. Before the alert package is transmitted, conversion to sky coordinates and a comparison with a list of known variable sources is performed. This procedure depends again on the detector and lies in the range of $\sim$ 2 s. The signal propagation delay to the ground station is small ($\sim$ 0.6 s) and the distribution through TCP/IP protocol to the various ground based instruments takes less than 1 s. Based on the GRB follow-up observations by MAGIC (summarised in table 6.4), time delays between the burst onset T_0 up to the receipt of the alert are typically more than 13 s and have to be taken into account.

[3] `http://gcn.gsfc.nasa.gov`

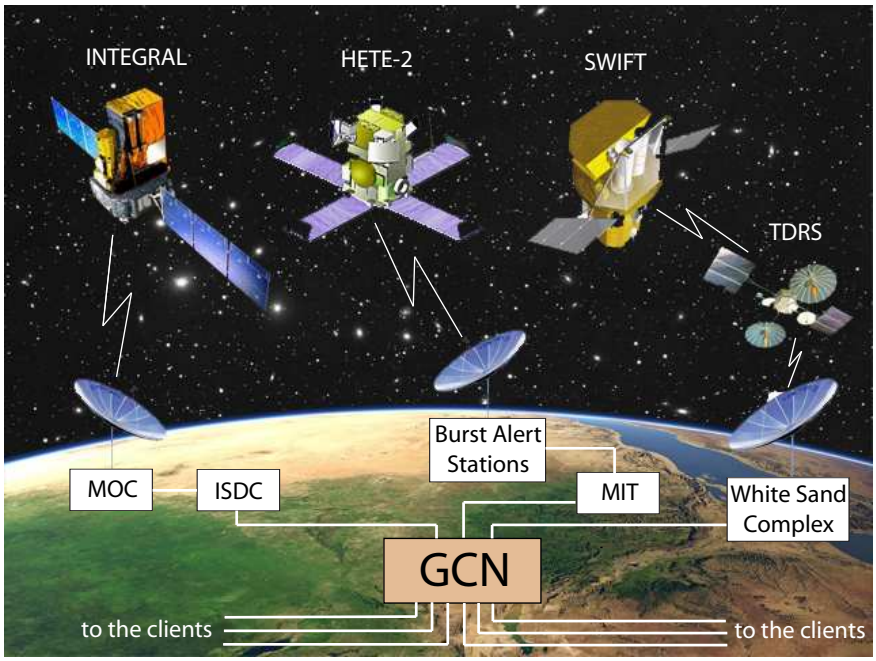

Figure 2.12: GRB alert data telemetry from the three satellites through the GCN to the clients.

2.4.2 GRB alert system of the MAGIC telescope

The GCN provides GRB alerts over different ways (e-mail, pager, phone, fax etc.) to its clients. The shortest delay between validation of signal at ground and acceptance of the alert at the client of $0.1-2.0\,\mathrm{s}$ is warranted with the TCP/IP internet socket connection, connecting a computer at the instrument site directly with the GCN computer over internet. The time delay of the propagation of the coordinates package varies with the distance between the two computers.

Gamma Sources Pointing Trigger

The internet socket connection method is used in the MAGIC project. A *Gamma Sources POinting Trigger* (gspot) demon program [110] performs a full-time survey of the alerts provided by GCN and validates them with the predefined observability criteria. The satellite experiments distribute different kinds of information over GCN. In the first stage, gspot filters out alert packages from selected satellites, which contain all mandatory information. In the second step, the remaining packages are validated based on the following criteria:

- The Sun has to be below the astronomical horizon (zenith $> 108°$).
- The angular distance from the GRB to the Moon has to be $> 30°$.
- The zenith angle for the GRB observation has to be smaller than $60°$. In case of moon shine the maximal zenith angle is reduced to $55°$.

Limits on the maximum zenith angle have been set due to the increasing energy threshold for larger zenith observation (see equation 1.6). Assuming an energy threshold of $E_0 = 50\,\mathrm{GeV}$ at zenith, the threshold for $60°$ is accordingly $E_{60°} = 325\,\mathrm{GeV}$ and for $55°$ $E_{55°} = 225\,\mathrm{GeV}$.

These limits are supported by the fact that most of the GRB events are situated at redshift $z > 1$, for which HE photons above 100 GeV get absorbed by the EBL (see figure 1.2). As the redshift of the source is normally only known a few days later from optical follow-up observations, one is obliged to observe all candidates. Although the later redshift info can classify the observation as useless.

If the before mentioned criteria are fulfilled, the GRB coordinates are sent to the telescope central control system. The telescope operator crew is informed acoustically and needs to accept the new observation. After affirmation, the telescope starts to reposition to the GRB sky coordinates in the *fast movement* mode and takes data. The data flowchart of the gspot program is shown in figure 2.13.

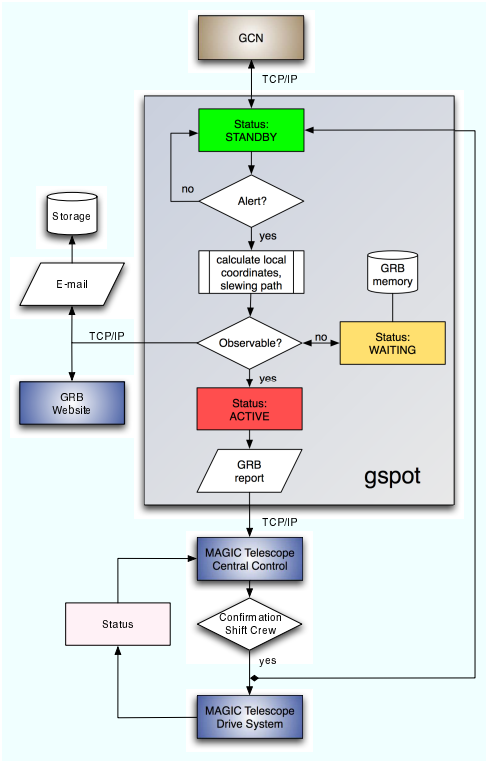

Figure 2.13: Data flowchart of gspot.

Observation time

Data taking is normally scheduled for two hours after the burst onset T_0. However, due to the unilateral decisions of competing groups, the observation time has been reduced to ~ 30 min from the beginning of the data taking. Shortening of the observation time is especially critical, because models described in § 1.2.6 predict possible VHE γ-ray emission also during the GRB afterglow phase. Recent discoveries of strong X-ray flares in the typically fading afterglow phase (see § 1.2.2) support multiwavelength observation lasting up to few hours after the burst onset.

If the observability criteria are not fulfilled in the moment when the alert package is received, but will become observable within two hours after the burst onset, gspot enters into a warning state. This can happen if the source location is for example below the predefined zenith range. The alert gets resent when all criteria become fulfilled.

Observation during moon shine

Increased LONS during moon shine is for most IACTs a reason to suspend data taking. The PMTs get damaged due to large anode currents. Especially the last dynode(s) are damaged due to the intense electron bombardment, while the cathode is unaffected. MAGIC uses PMTs with only six dynodes running typically at a low gain of $\sim 3 \cdot 10^4$, e.g. damage at enhanced background light levels is avoided and observation during moon shine is possible, albeit with a higher threshold. Only the four full moon nights in the month are excluded from observations. Caution is required while repositioning the telescope in the presence of Moon. Since the telescope camera lids are not closed during the repositioning to the GRB sky coordinates, an accidental flash of the Moon would initiate the camera control system to trip the high voltage for safety reasons. The safety procedure prevents subsequent immediate data taking. To avoid crossing the Moon on the direct repositioning path, an intermediate target between the initial telescope position and the GRB position is computed. The telescope slewing goes over the intermediate target, in safe distance from the Moon. For safety reasons one has to accept longer repositioning times.

Further functions of gspot

All alerts received by gspot are sent to an internal mailing list, allowing the monitoring of the GCN activity. Furthermore, information about alerts and status of the program can be viewed anytime at the system web page: `http://www.magic.iac.es/site/grbm/`.

2.4.3 Activity of the GCN alerts

The first observation cycle of the MAGIC telescope started early 2004, short after the commissioning phase. In the first few months extensive tests of gspot were carried out. The fully automatic operation of the alert system started in April 2005.

Until the end of the first observation period (April 2006) in total 405 alerts have been received by gspot. Figure 2.15 and table 2.1 summarise the alerts by the three satellite experiments: SWIFT, HETE-2 and INTEGRAL. A big part of the alerts (45%) did not contain the coordinates or were marked by the detector as not a GRB event. These alerts do not disturb the normal operation program, since the response of the telescope is suppressed. More critical are the alerts, which later turn out to be generated by a known γ-ray source or an artefact of the satellite detector. Almost half of the GRB observations by the MAGIC telescope were responses to such fake alerts. This led to a waste of observation time. 52% of the HETE-2, 36% of the INTEGRAL and 15% of the SWIFT alerts were later recognised as fake events. Summarising the observations, 23 responses to GCN alerts were performed by MAGIC. Out of these attempts only 12 real GRB events were observed. The list of the bursts and results from MAGIC observations are shown in § 6.2.

We have studied the capabilities of the MAGIC telescope to observe GRBs already in the project design phase [111]. Of special interest was the **duty cycle** of the experiment. It represents the percentage of the time in a year the facility is able to take data. Figure 2.14 shows the duty cycle in units of observable solid angle times for each day of the year 2001. For the determination of the duty cycle, in addition to the observability criteria described on the page 33, the following weather parameters have been adopted:

- Relative humidity of the air $< 80\%$.
- Wind speeds $< 10\,\mathrm{m/s}$.

This information was obtained from the NOT weather station database[4], located at the Observatory del Roque de los Muchachos in La Palma. The study showed that in 2001, a duty cycle of $1.157\,\mathrm{sr}\cdot\mathrm{year}$ was archived. This corresponds to 9.2% with respect to the $4\,\pi \times 1\,\mathrm{year}$ full sky coverage. When comparing the number of GCN alerts with the number of MAGIC follow-up attempts in 2005/2006, one gets a duty cycle of 10.3%. It is in good agreement with our foregoing hypothetical study.

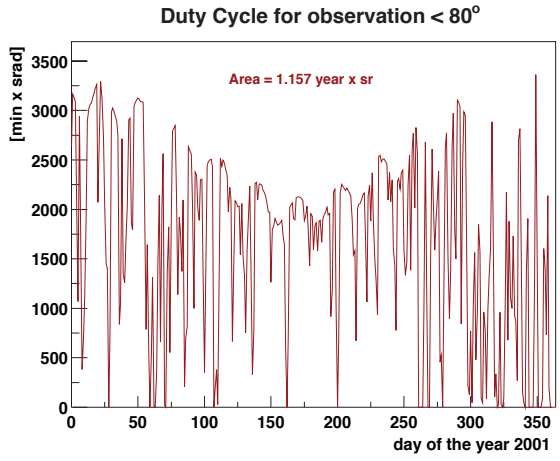

Figure 2.14: Duty cycle for GRB observations on La Palma based on weather conditions in 2001. Adopted from [111].

[4] `http://www.not.iac.es/cgi-bin/weather-archive.pl`

	HETE-2	SWIFT	INTEGRAL	total
all alerts	193	190	22	405
alerts with coordinates	42	159	22	223
fake alerts	21	24	8	53
alerts from real GRB events	21	135	14	170
follow-up observations by MAGIC	7	13	3	23
real GRBs observed by MAGIC	2	9	1	12

Table 2.1: Summary of the GCN alerts received by gspot during the MAGIC's first observation cycle between April 2005 and April 2006.

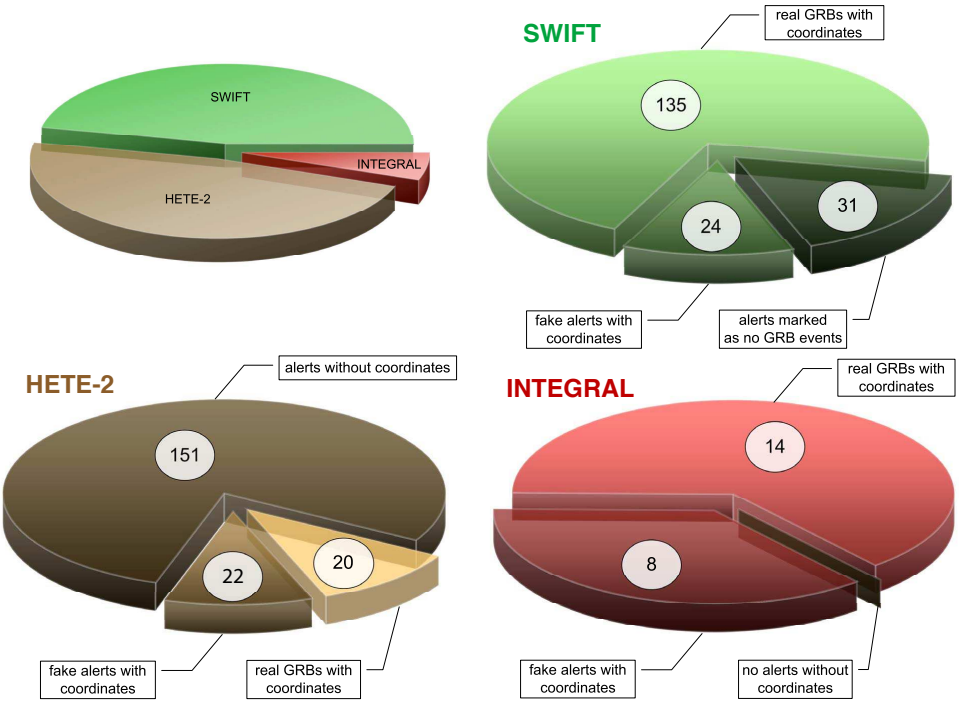

Figure 2.15: Summary of the GCN alerts received by gspot in the first observation cycle of the MAGIC telescope. The pie histograms quantify the alerts by the SWIFT (green), HETE-2 (brown) and INTEGRAL (red) satellites. Detailed information about alerts containing coordinates, number of fake alerts and number of real triggered GRB events by the satellites are given.

Chapter 3

Active mirror control of the MAGIC telescope

Nearly all hardware components of the MAGIC telescope needed improved technologies in order to reach the design goals of the project, e.g. lowering the trigger energy threshold down to 50 GeV or building an instrument, which is able to perform rapid follow-up observations of GRBs. To achieve these goals a stiff, light-weight space frame structure made of carbon fiber-epoxy tubes was built to minimize the telescope's weight. Because of the large diameter, the requirement of low weight and financial constraints it was not possible to construct a completely stiff frame. As a result some residual deformations remain, depending on the pointing direction. Figure 3.1 shows the PSF of the 17 m Ø mirror affected by deformations of the mirror support structure. The influence of gravitationally-induced deformations is large enough to require an active mirror control (AMC). The general concept follows the design of modern, large optical telescopes, in which deformations are not avoided by super-heavy structures but the segmented mirror is dynamically corrected.

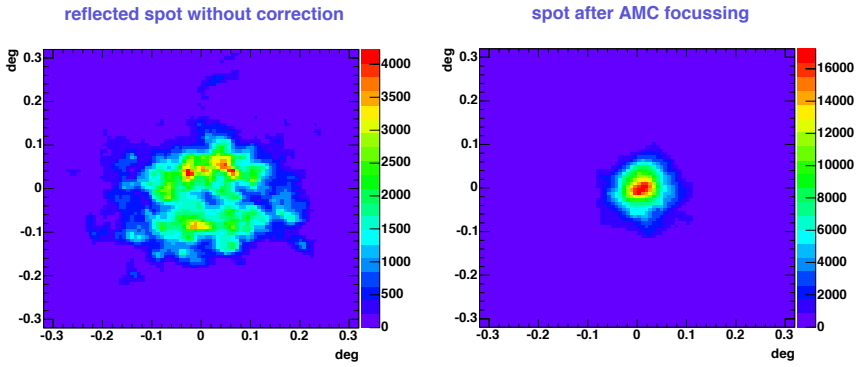

Figure 3.1: Effect of the mirror dish deformations on the PSF of the MAGIC telescope. Images of the reflected spot from a star at the focal plane of the telescope. *Left:* Light distribution after a change of zenith angle by 60°. *Right:* Image after re-focussing of the reflector with the AMC.

The first ideas to correct the MAGIC telescope dish deformations were presented in 1995 [95, 112, 113]. Based on these prototypes, I developed the elements for an AMC during my diploma thesis [114]. After the design and testing phase of the MAGIC AMC prototype, I took over basically the production process of both the mechanic and electronic components. I assembled the complete MAGIC telescope reflector with mirrors and all AMC components

on the telescope structure and am still responsible for its maintenance. The original software was designed by Martin Merck from the University of Wuerzburg. In 2004 the software part was taken over by Adrian Biland from the ETH Zurich. Since the beginning we worked in close cooperation in order to improve the functionality of the whole system. The improvement and maintenance of the AMC took a big part of my time during the last three years. The following chapter reviews the main concepts of the AMC system. It gives detailed information for all components, the topology and lastly ideas for possible improvements.

3.1 Adaptive and active optics systems for large telescopes

Because of the high cost of a telescope in space, there has been significant effort to improve the quality of ground-based telescopes. In the quest for greater light-gathering, telescope arrays and segmented mirrors have been built. The latter is the consequence of the difficulties to produce single large mirrors with diameters $d > 8\,\mathrm{m}$, to make them sufficiently stiff and to control the temperature of the material. The segmented mirror approach requires active control of the segments positions to maintain mirror shape and image quality. The goal of optical correction systems is to reduce the aberrations and the deformations of the mirrors holding structure. The correction systems can be divided into two groups:

- **Adaptive optics:** Optical observations with ground based telescopes are limited by seeing effects. Astronomical seeing refers to the blurring and twinkling of astronomical objects, such as stars, caused by turbulences in the Earth's atmosphere. The adaptive optics is a powerful tool to reduce the distortion of the wavefront entering the telescope. The corrections are generally applied to a relatively small optical element in an optical path of the telescope. They are continuously readjusted on a time scale measured in milliseconds. For a good overview of the principles of adaptive optics see [125].
- **Active optics:** These systems have lower reaction times and are used to correct the deformations of the mirror support structure.

The adaptive and active optics techniques have therefore to be distinguished from each other.

The MAGIC telescope does not need adaptive optics, because the objects under study are VHE γ-ray induced air showers developing at $\sim 10\,\mathrm{km}$ height. The VHE photons are detected indirectly by the Cherenkov light generated in shower cascades in the Earth's atmosphere. The fluctuations in the shower development are considerably higher than the effects of wavefront distortions.

3.2 Motivation for an active optics system for MAGIC

Independent of its size, each telescope has strong requirements on the stiffness of the reflector frame. An increase of the mirror diameter is therefore a challenging task. There are three main perturbations, which affect the optical performance:

1. As the elevation angle of the telescope changes, the **varying gravitational loads** deform the mirror cell. By moving from horizon to zenith the deformation is dominated by a parabolic sagging of the cell.
2. As the **temperature** of the mirror support structure varies with the season, the expansion of the cell causes changes of the overall frame geometry.

3. In addition **wind** forces, especially for telescopes without a dome, have an impact on the frame deformations. Its extent depends on the strength of the wind and its impact direction.

Two solutions are possible to counteract these deformations:

a) Construct a very heavy and stiff reflector frame.

b) Allow for small deformations by constructing a light-weight support structure and correct its mirror profile.

The existing IACTs like H.E.S.S. [116], CANGAROO [117] and WHIPPLE / VERITAS [118], have reflector diameters $d \leqslant 12\,\mathrm{m}$ and larger pixels, e.g. coarser image sampling. Their heavy steel construction guarantees that the PSF remains within the tolerance during operation. One requires usually a PSF smaller than differences in size between γ and hadron images. The heavy construction is already an obstacle for fast repositioning of the telescope. The goal of the MAGIC project was on the one hand a large mirror area, on the other hand a light-weight structure to allow fast slewing for GRB follow-up observations.

The 17 m Ø space frame of the MAGIC telescope is made of carbon fiber-epoxy tubes of low weight and high stiffness. The knots are made from aluminium. The construction nearly has the young's module parameter of steel but at a quarter of the weight, e.g. the carbon fiber space frame weights at least a factor five less than a equally deforming one made from steel tubes. In addition the carbon fiber-epoxy combination has lower thermal extension and higher vibration damping than steel. Within the frame of financial constraints and the maximum weight of six tons, it was not possible to construct a completely stiff frame. Extensive numerical simulations based on the *finite element calculation method* (FEM) were carried out by the company MERO[1]. To evaluate and optimize the stability of the dish, not only the weight of the construction and the mounted mirrors, but also forces caused by wind and ice deposition were taken into account in the simulation. Figure 3.2 shows the result for one particular case: The telescope positioned at 45° zenith angle and a simulated horizontal wind pressure of 150 Pa. The numbers in the figure represent the deviations of the knot positions from the ideal parabolic form, in units of mm.

Table 3.1 summarizes the final results of the simulations: The maximal deviation caused by a tilt of the mirror dish by 45° in the elevation results thereby in maximal sagging of 3.7 mm, while in combination with wind loads it can reach values of up to 6.1 mm. It should be noted that in the simulation the relative deviation between two neighbour knots never exceeds 0.2 mm. Sagging of the mirror frame along the optical axis does not influence the focus. Only relative tilts of the panels deteriorate the PSF. In ideal case the deviation of 0.2 mm would cause a shift of the mirror spot of 6.4 mm at the 17 m distant camera plane. In reality the deformations tend to be bigger, mainly because of larger weights of the telescope camera and of the not-planned counterweights, causing a higher total weight than was taken into account during the simulation.

The distortion of the mirror dish frame results in a blurring of the PSF and needs to be corrected. *Adaptive optics* systems have been used for more than 20 years in optical astronomy. The actuators are based on piezo crystals, because of the small range of operation at precision of $\leqslant 100\,\mathrm{nm}$. The crystals have the property to expand or contract when applying a voltage, e.g. the expansion for $\pm 1000\,\mathrm{V}$ is in the range of ± 100 µm. These elements cannot be used

[1]Since May 2006 the company MERO Structures Inc. has become Novum Structures. Further information can be found at the company web page: `http://www.novumstructures.com/`

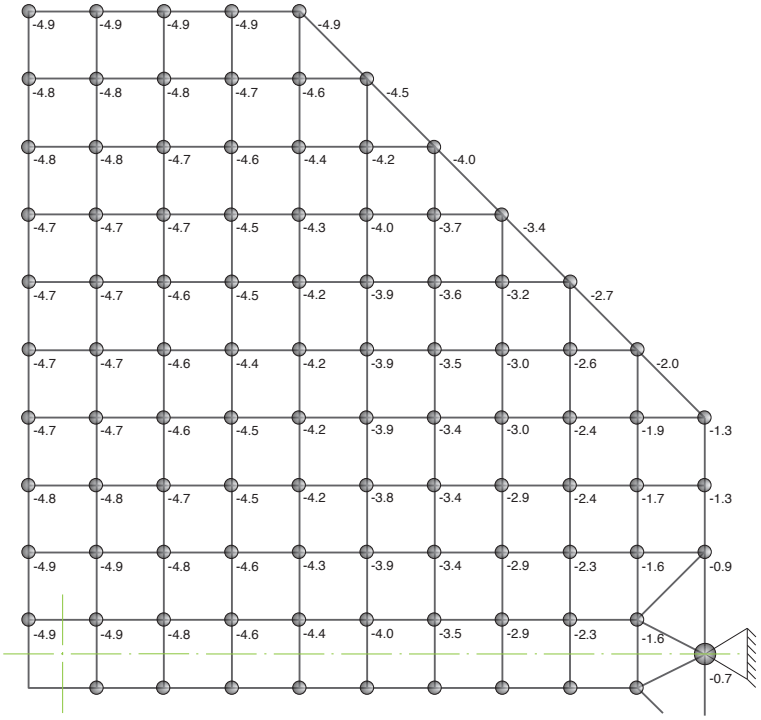

Figure 3.2: Deformation of the MAGIC mirror dish under gravity force and wind load. FEM simulation results for an elevation angle of 45° and 150 Pa wind pressure. The values (in mm) represent the distortions of the knots with respect to the ideal parabolic shape. For illustration, only one quarter of the dish is shown.

	ΔZd	maximum	minimum
Deviation by varying the zenith angle:	$0° - 45°$	3.67 mm	−2.23 mm
	$45° - 90°$	2.23 mm	−3.67 mm
Deviation by impact of 150 Pa wind pressure:	45°	4.26 mm	−4.13 mm
	90°	6.11 mm	−1.44 mm

Table 3.1: Results from the FEM simulation for the mirror dish deformations of the MAGIC telescope.

for MAGIC, because of the too small displacement range, their delicate construction and high cost.

The *active optics* was proposed to be implemented in an IACT for the first time in the design phase of the MAGIC telescope[2]. After some delay, the main idea was also adopted in other experiments. The CANGAROO [119] and H.E.S.S. [120] projects nowadays use actuators to align the mirror segments in a non-recurring way, just after their installation. The H.E.S.S. II telescope, an IACT with a 28 m Ø mirror, is currently in the construction phase. Despite its 540 t construction, the optics will require an active mirror control system [121], similar to that used in MAGIC.

[2]It is interesting to note that a more rigid frame avoiding active control would require a much heavier construction, making the entire costs much higher than for AMC.

I have strongly contributed to the design and developed the AMC system for the MAGIC telescope [114, 122, 123]. The goal was to continuously counteract the mirror dish deformations and to provide a sharp focus at every zenith angle position. In addition, the AMC gives the unique opportunity to focus the reflector at different focal lengths. Since the distance to the air shower maxima depends on the observational zenith angle (depth of Earth atmosphere), this is an interesting feature to be used for better reconstruction of the shower image parameters. The main components of the AMC are illustrated in the technical drawing below. In the next chapters I will describe the individual components in more detail.

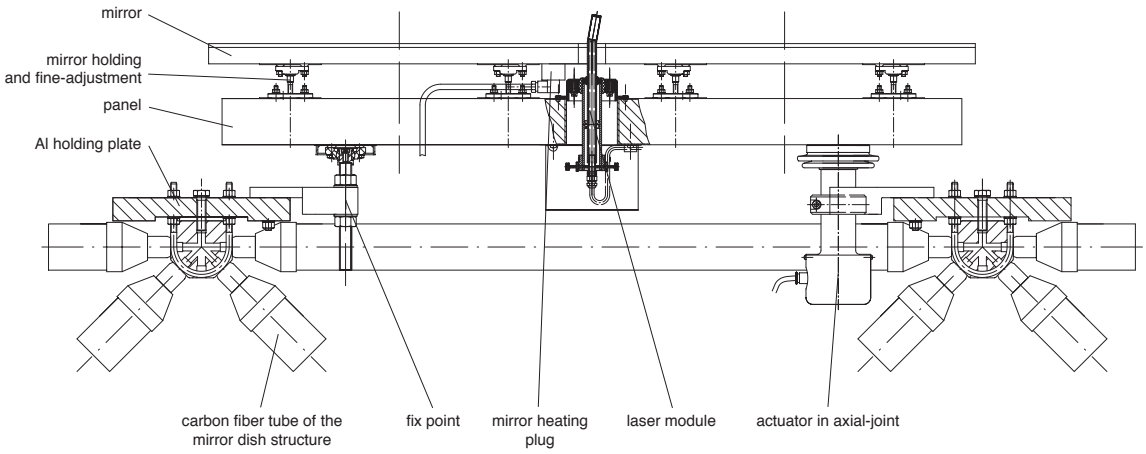

Figure 3.3: Technical drawing of a panel. Components like the laser module, the fixed point and the actuator in axial-joint (not shown is the second actuator in the cardan-joint) are parts of the AMC.

3.3 Working principle of the AMC

The reflector of the MAGIC telescope consists of 956 square shaped mirror facettes. Always four (three at the inclined edges of the mirror frame) facettes are mounted on light-weight sandwich panels. The 247 panels are attached to the carbon fiber support frame at three points, as shown in figures 3.3 and 3.4. Two of the mounting points are equipped with actuators, used to adjust the tilt of the panel. The three support points have different lateral freedom. One actuator has full lateral freedom (achieved with the cardan-joint), while the other actuator can swing in only one axis (axial-joint). The third support point has no lateral freedom (fix point). The support points are attached with the panel using Igus[3] Igubal flange-mount bearings. This arrangement fully constrains the position and orientation of the panel. It allows the panel material to expand and avoids stress on the

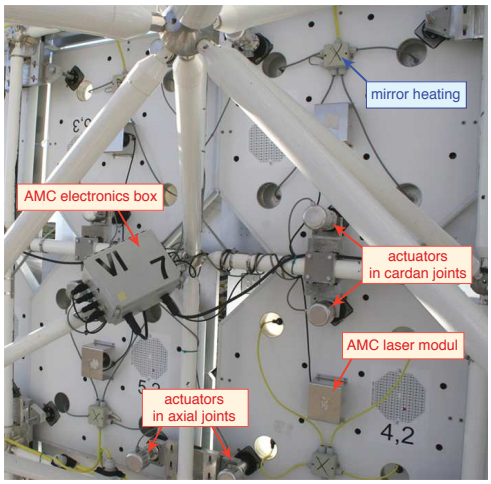

Figure 3.4: Photo of the AMC components (labelled in red) mounted to the panels of the MAGIC telescope.

[3] http://www.igus.com

mirrors when moved. Figure 3.4 shows also the cabling of the mirror heating. The mirror heating is used to keep the mirror surface free of ice or condense water, in the case of bad weather conditions (see § 4.1.3).

3.3.1 Focussing of the panels with the use of lasers

The schematics of the AMC is shown in figure 3.5. In the center of each panel a computer controlled laser module is pre-adjusted, pointing towards the camera lid. A CCD camera, mounted in the central part of the mirror dish, records the position of the laser spot. The PMT camera center, and consequently the reference point for the focussing, is determined with four LEDs mounted at the lids. This approach has a consequence: The gravitational sagging of the PMT camera at increasing elevation angle (which can reach up to $\Delta y \approx 40\,\mathrm{mm}$) results in unintentional shift of the mirror focus, when adjusting the panels with lasers. When correcting the laser position for Δy, the panel tilts its normal with an angle β. Since light rays get reflected on the mirror surface, their resulting angle is 2β and the overall mirror focus becomes shifted by the distance $2 \cdot \Delta y$. However, this effect is corrected within the *bending model* of the telescope drive system [115].

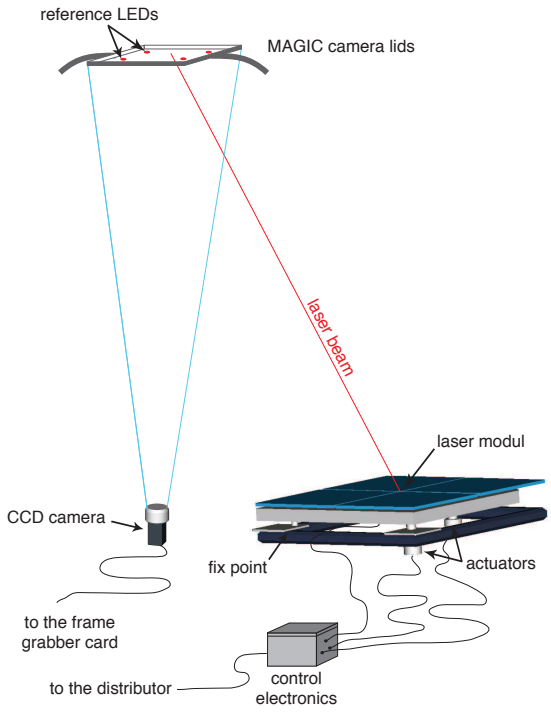

Figure 3.5: Schematic drawing of the AMC working principle.

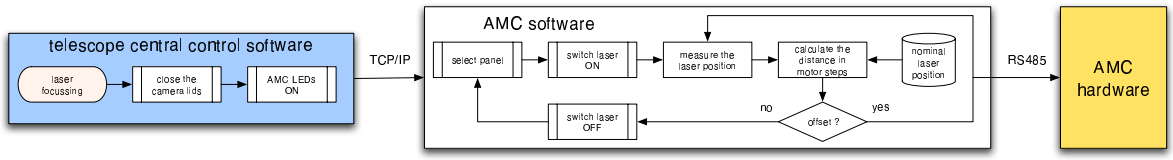

Figure 3.6: Flowchart of the AMC laser focussing procedure.

The basic principle of the AMC focussing procedure using lasers is illustrated in the flowchart above. The sequence is as follows:

1. Select a panel and switch on the laser.

2. Measure the position of the laser spot with respect to the PMT camera center. The camera center is determined by the four LEDs mounted on the lid.

3. Calculate the deviation of the measured laser spot with respect to its nominal position. The nominal laser spot position is saved during the main focussing procedure (see § 3.5).

4. Calculate the required movement for both actuators. The number of motor steps results from the distance of the current laser spot position to the nominal position. The conversion from camera CCD pixel coordinates to motor steps and the movement vectors were obtained with dedicated calibration run for each panel.

5. Send the number of motor steps to the corresponding AMC micro-controller card. The electronics control the actuator movement and give a feedback about its status and motor position to the operating software.

6. Recapitulate steps 2 to 5 until the pre-set tolerance between the nominal position and current laser spot position is reached. The precision of the focussing is pre-set to 0.5 CCD pixels, which correspond to 1.2 mm in the camera plane (for more details see page 52). If the procedure was not successful within three iterations, report an error to the software.

7. Switch to the next panel and repeat the sequence.

The time required for a full laser adjustment of the MAGIC reflector is currently approx. 3 min. In addition one has to close the telescope camera lids and reopen them before continuing observations, which may take additional 30 s. This is much too long for GRB follow-up observations. Therefore, for the fast repositioning mode towards the GRB location, a new focussing method was implemented. It is described in the following chapter.

3.3.2 Focussing of the panels with the use of look-up tables

In § 2.3 I have described the efforts carried out to make the MAGIC telescope able to observe the prompt emission phase of GRBs. Follow-up observations of GRBs by ground based experiments are usually performed at large zenith angles (see table 6.4 for the MAGIC observations up to now), simply because the number of bursts increases linearly with the observable sky area and thus larger zenith angle observations are more likely. On the other hand, because of the lower energy threshold (see equation 1.6), standard observations of IACTs are preferred close to zenith. From our experience, a new refocussing of the MAGIC reflector is advisable for telescope repositioning angle changes of $\Delta Zd > 10^\circ$ (no azimuth angle dependence of the PSF is expected or was observed). This implies that refocussing of the reflector for GRB observations is required in most cases.

Because of financial, space and weight restrictions the actuators were not equipped with shaft-encoders but stepping motors with quasi digital incremented motion. Therefore one has the possibility to record the relative movement of each actuator. The positions are kept in memory of the driver cards as long as the electronics is powered. The AMC software reads the positions of all motors after it is started and keeps them in memory as long as the program is running.

At the beginning of each night all actuators are initialised. During the **initialisation** the stepping motors are moved from the lower to the upper end-switch (see figure 3.11) and the distance (in motor step units) is recorded. The actuator piston is then moved to the central position, calculated from the number of motor steps needed for the movement between the two end-switches. This central position is the *"zero" reference* for each actuator. From this position the actuator has maximal freedom for movement in both directions. Further details, design and error diagnostics of this procedure can be found in § 3.4.

After a laser adjustment the position of both actuators (with respect to the *"zero" reference*) is recorded. The numbers are saved in a text file. The file contains all actuator positions for the corresponding telescope orientation in zenith and azimuth direction. Because of the

format, the file is called **look-up table** (LUT). After repositioning the telescope, one can search for the file with the closest distance to the current telescope orientation and adjust the motors to the nominal positions, obtained from this LUT.

The reference LUTs used by the AMC software need to be generated in a separate procedure: The telescope is looped in elevation in steps of 5° from −60° to +80°. At each position, a laser adjustment is carried out and the corresponding LUT is generated. Figure 3.7 shows an example of the motor movements of one panel in units of motor steps.

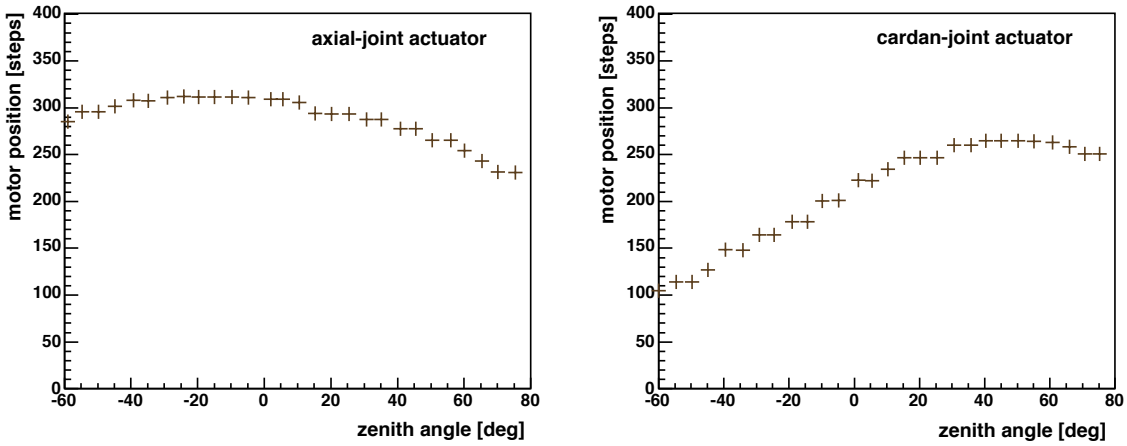

Figure 3.7: Movement of the actuators of the panel (-4,-2), when moving the dish from −60° to +80° in declination and requiring to keep the PSF constant. The ordinate units are motor steps and the abscissa units the zenith angle. Two motor steps at this axis correspond to 10 µm longitudinal movement of the actuator. For the normal operation mode in the zenith range between 0° and 80°, the required corrections of this particular panel are: 78 steps (∼ 0.39 mm) for the axial-joint actuator and 44 steps (∼ 0.22 mm) for the cardan-joint actuator.

Figure 3.7 shows the *desired* zenith range of $-60° \leqslant Zd \leqslant 80°$ for GRB observations. However, when crossing the zenith, the change of the gravitational force direction causes in some cases an unpredictable hysteresis of the actuator positions (in 15% of the panels). The hysteresis results in a ∼ 3 mm jump of the actuator position. The large deviation originates probably from the fixation of the actuators or rotation of the carbon fiber tubes. Currently the problem is avoided by restricting the range of operation in declination to $Zd > 0°$.

A turn over the zenith would allow to substantially reduce the required re-positionning time of the telescope for GRB follow-up observations for part of the events, as well as allow to operate the fast slewing more efficient and faster (because the range for slow-down can be significantly enlarged and, in turn, increase the speed in azimuth between −90° to +50°). The telescope dish including mirrors and camera weighs only about 20 t, i.e. 1/3 of the complete telescope weight. The movement in elevation is therefore significantly faster than in azimuth, as well as the total range being shorter.

The course of the actuator movements versus zenith angle follows a smooth second order polynomial function, as seen in figure 3.7. Each actuator has its individual characteristics, dependent primarily on its position on the telescope dish structure. Figure 3.8 shows the overall dish deformation by the change of the zenith angle from 60° to 10°. The figure results from the extracted actuator movements required for the correction of the PSF.

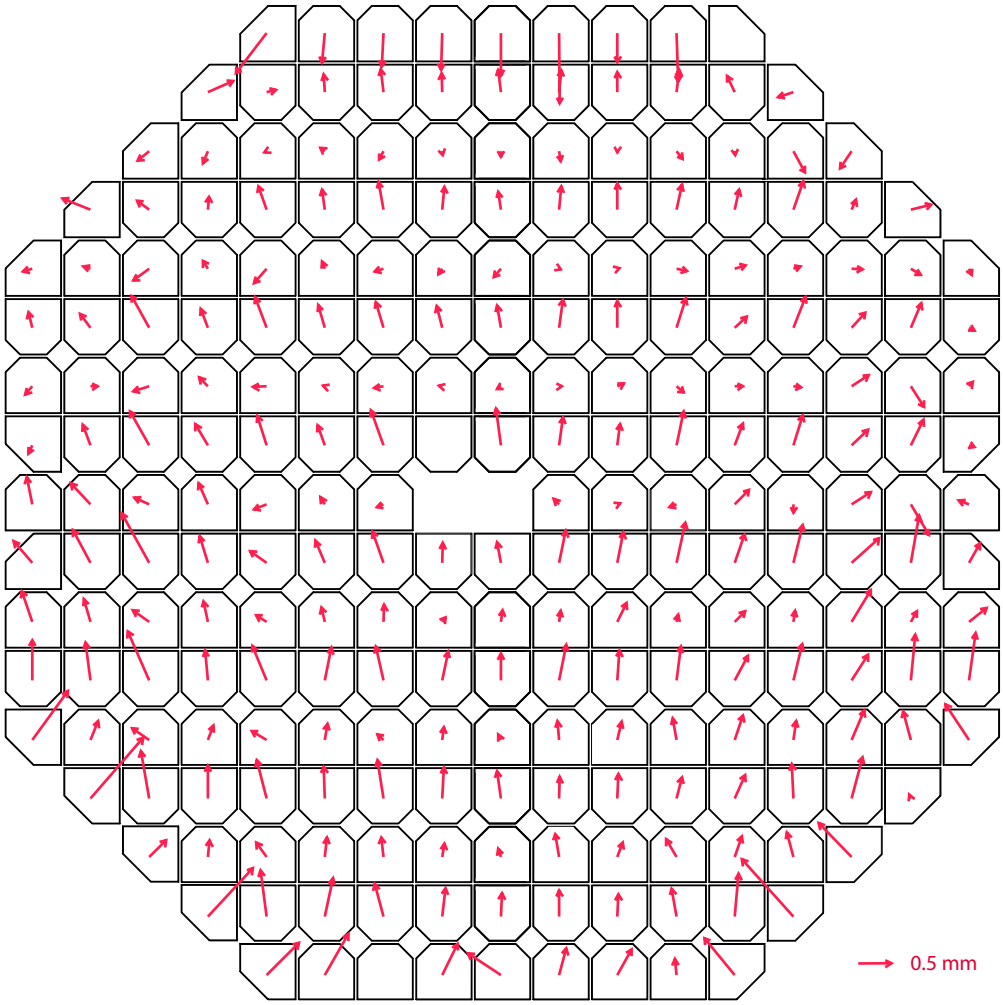

Figure 3.8: Deformation of the mirror dish structure of the MAGIC telescope by changing the elevation angle from 60° to 10°. The vectors indicate the amount and the direction of the tilt of the panels.

In the case of a GRB alert, the telescope central control software sends the source position zenith and azimuth angles immediately to the AMC software. All panels are then adjusted to these coordinates using the closest available LUT. Thanks to the eight independent transmission lines (see § 3.4), on average 10 s are needed to refocus the panels with the LUTs. The early notice from the central control software already allows to start the focussing during the slewing of the telescope. An optimal PSF is guaranteed when the telescope has reached the burst sky coordinates and starts data taking.

The short focussing time and the experience that the MAGIC mirror dish deformations are reproducible, also lead to the use of LUTs during normal observation. However, the determining factor for this decision was the degrading PSF after laser adjustment, which I will discuss in § 3.5.3. The advantage of the LUT focussing is that no lasers are used and the data taking does not need to be interrupted. The re-focussing can be done automatically, while tracking and observing a source. The AMC software checks the current telescope orientation and re-adjusts the panels, if the zenith angle changes by more than 5°.

The disadvantages of this method are the temperature dependent mirror dish structure expansion and some ageing effects. They have a direct impact on the quality of the PSF. Long time PSF measurements, shown in figure 4.20, indicate such an expansion, which depends on seasonal temperature variations. The resulting error of $\Delta\sigma \sim 0.05°$ on the PSF, however, is smaller than the degradation of the laser focussing procedure and, for the moment, has to be accepted. It should be kept in mind that temperature changes over night are very low (typically $2-3°$ C), e.g. below year changes. Also routine updates of the LUTs will correct for ageing effects. On the other hand wind pressure changes cannot be corrected by the current method.

3.4 AMC components and setup

Now, after the introduction of the basic idea and focussing principle of the AMC, I will discuss the individual components, as well as the layout of the system.

The AMC hardware can be divided into mechanical and electronic components. The **actuator**, the **laser module**, the **CCD camera**, as well as the **LEDs** mounted on the camera lids, are part of the mechanical elements. The electronics on the other hand are composed of custom-made **micro-controller** and **motor driver cards**.

The control of the 62 electronic boxes is split into eight independent branches. Figure 3.10 shows the schematics of the cabling of the individual panels within the AMC structure. Because of the telescope dish geometry, this results in a somewhat different number of boxes within individual branches. The splitting reduces the probability of simultaneous breakdown of the whole system. The arrangement allows easy access and localisation of possible errors. The quasi simultaneous operation and control of eight panels at the same time allows to reduce the overall focussing time. However, because of identification problems, only one laser spot can be viewed at a time with the CCD camera. For the LUT focussing the division into parallel operating branches significantly reduces the required focussing time.

Figure 3.9 shows the block-scheme of the electronics of the AMC on the telescope dish. Each box controls four panels with eight actuators and four laser modules. The layout of the box will be described later in this chapter. The boxes are arranged in series along one line, requiring unique addressing of the micro-controller cards. The RS-485 interface in half-duplex mode is used to communicate with the AMC central computer.

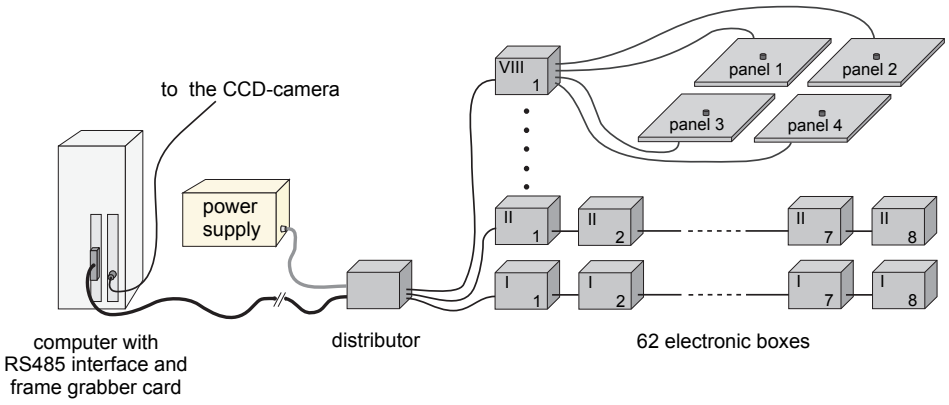

Figure 3.9: Schematic drawing of the cabeling of the AMC electronic boxes.

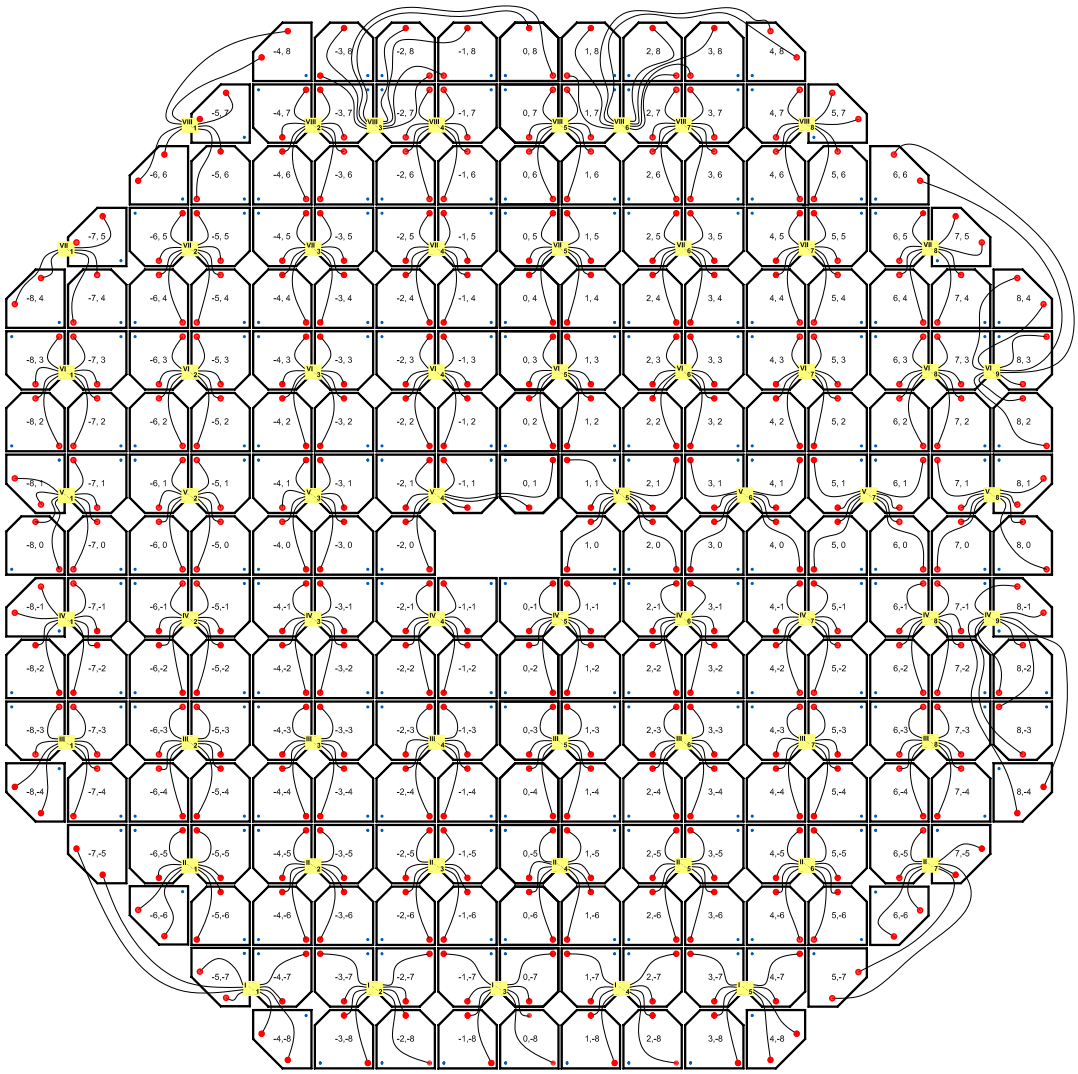

Figure 3.10: Sectioning of the panels and actuators in the AMC structure. Cabling of the actuators (red points) with the corresponding electronic boxes on the MAGIC dish structure is shown.

The actuator

The actuator has two functions: On the one hand it has to fix the panel to the telescope dish structure, and on the other hand it has to tilt the panel in the desired orientation and correct for the dish deformations in this way. The design of the actuator had to fulfil the following criteria [114]:

1. High accuracy and reproducibility of the longitudinal movement.
2. Maximal error of 40 µm in the direction perpendicular to the mirror surface. The error includes the sum of the holding-joint, as well as the actuator unit itself.
3. A longitudinal movement range of ~ 30 mm with a resolution of ~ 10 µm per motor step. The large movement helps during the assembling of the panels on the dish structure (less accurate pre-adjustment during the fixation necessary). In addition it gives the

opportunity to defocus the mirrors in case of an accidental exposure to sun light[4]. This is an emergency solution in the case the telescope cannot be positioned back to the *parking position*[5], where it is safe during daytime. From the FEM simulation of the dish deformations due to gravitational force and wind loads, maximal corrections of $\sim 0.2\,\mathrm{mm}$ were obtained (see table 3.1). This distance represents the nominal operation range of the actuator. Because of the 17 m focal length, a resolution of $\sim 10\,\mu\mathrm{m}$ per motor step is required. In this configuration one motor step corresponds to a transverse focal movement of $\sim 0.34\,\mathrm{mm}$ in the camera plane. With a typical PSF of the MAGIC reflector of $r_{80} = 21.1\,\mathrm{mm}$ (see table 4.4), the least step of the actuator is well above the requirement. In our case the accuracy of the focussing is limited by the CCD resolution and the laser spot dimensions.

4. Maximal holding force of 500 N. In normal operation 130 N act on each holding point of the panel. However, the telescope structure was designed to withstand winds of 165 km/h. The forces acting on each holding point, for the worst case of perpendicular wind direction sum up to 500 N.

5. Operation at temperatures between $-10°$ C and $50°$ C, with a small temperature expansion along the longitudinal movement direction.

6. Withstand abrasion by sand and dust. Selection of proper materials for moving parts.

7. No degradation when exposed to UV light, as well as being water-proof according to the IP 67 (DIN 40050) standard.

8. Maximal costs of 150 €/actuator.

9. Lifetime of > 50000 movement cycles.

The above listed requirements could not be satisfied with the devices available on the market. While the actuators used for the H.E.S.S. telescopes are based on automotive products used to drive car windows [116], a new development was required for the MAGIC telescope.

Figure 3.11 shows the technical drawing of the AMC actuator. The individual components are labelled and the main elements will be described in the following.

Stepping motor: The two phase hybrid stepping motor of the company EC Motion[6] (*ECM 265-E 1.0A*) has a maximal torque of 50 Ncm, when operated with 5 V and 1 A. The holding torque without applied power is 3.5 Ncm. Because of the relative high slope and negligible friction of the ball screw, the motor has to be powered in stand-by mode. In order to avoid slipping minimal current of 125 mA/winding = 250 mA/actuator is necessary. With the $5\,\Omega$ resistance per winding one obtains a power consumption of $\sim 160\,\mathrm{mW}$ per actuator.

[4] Current operation experience shows that this risk is extremely low, if normal operation and emergency instructions are followed.

[5] Due to high costs, IACTs are usually not covered with a dome. In order to prevent damage of the telescope structure or fire by reflected sunlight from the huge mirror area, the telescope remains in a predefined parking position during day time and bad weather conditions. In the case of MAGIC, the parking position is in north direction.

[6] `http://www.ec-motion.com`

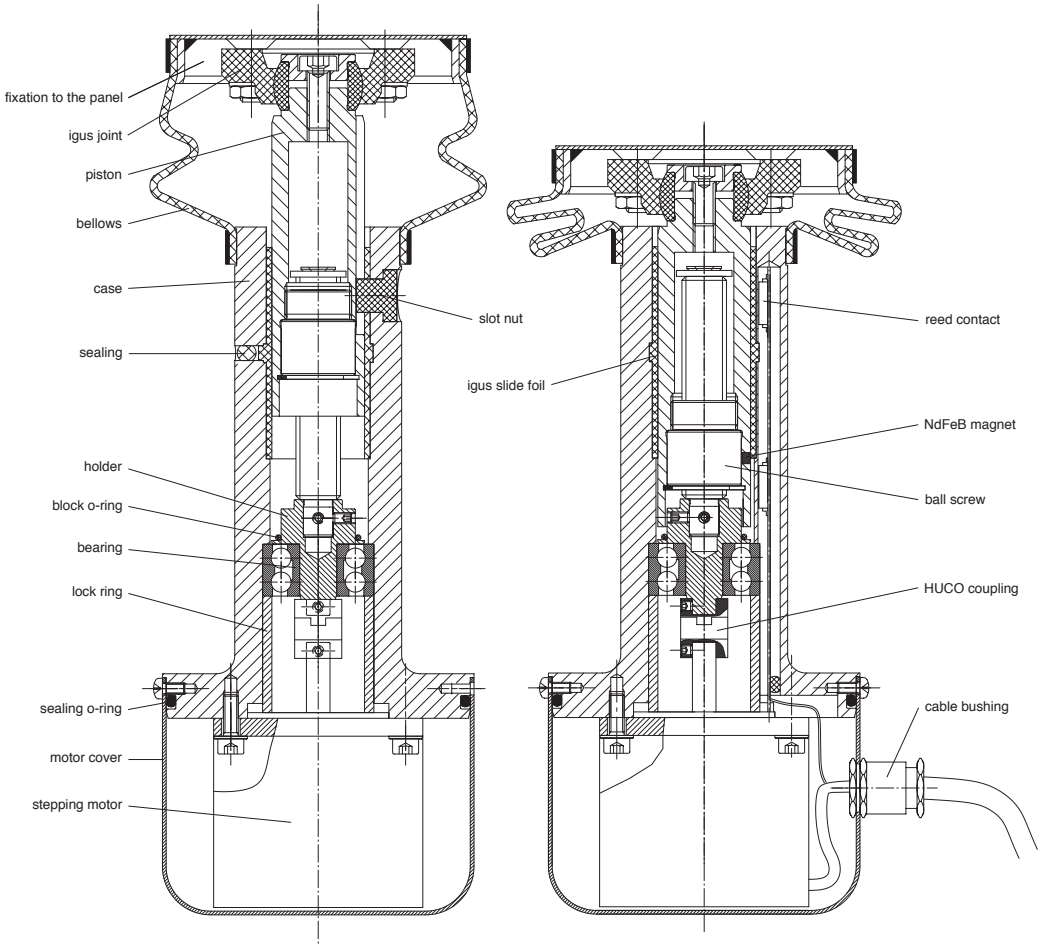

Figure 3.11: Technical drawing of the actuator of the MAGIC AMC system in two positions.

Ball screw: The rotational movement of the motor is transferred to longitudinal movement using the ball screw of the company Eichenberger Gewinde[7] (*type Carry FG*). The pitch of the thread is 2 mm and the maximal range 37 mm. The ball screw has a longitudinal tolerance of $\leqslant 10\,\mu$m and minimal friction.

End-switches: The movement range of the actuator is limited by end-switches. Meder[8] *Reed switches* (*MK-16-C-2*) composed of two magnetic contacts were used. A small NdFeB magnet, inserted in the piston, activates the switch when approaching the lower or upper end of the operation range. When the Reed switch is closed, the electronics stops the motor movement. In the AMC scheme the end-switches are also used to initialize the motor positions, required for the LUT focussing (see § 3.3.2). Tests carried out during my diploma thesis [114] showed that the switching accuracy w.r.t. the number of motor steps (when using the full lengths of the actuator movement) was very high and reproducible to one motor step. Temperature and humidity do not affect the accuracy. Therefore the end-switches are reliable references for the initialisation of the actuator position.

[7] `http://www.gewinde.ch`
[8] `http://www.meder.com`

The laser module

Figure 3.12 shows the technical drawing of the laser module, mounted in the center of the panel. The heart of the device is a semiconductor laser of the company Quarton Inc.[9] (*VLM 650-11 LPA*). The $2 \pm 1\,\mathrm{mW}$ laser emits light at the wavelength of $\lambda = 655 \pm 10\,\mathrm{nm}$. The light is focussed onto the 17 m distant camera lids to a spot of $\sim$ 10 mm Ø. The laser is embedded into a rig allowing rough and fine adjustment of the laser beam orientation. Both adjustment mechanisms were used to align the laser beam towards the common mirror spot. The device is protected by means of an aluminium plate to prevent unintentional displacements and damage by persons working close to it.

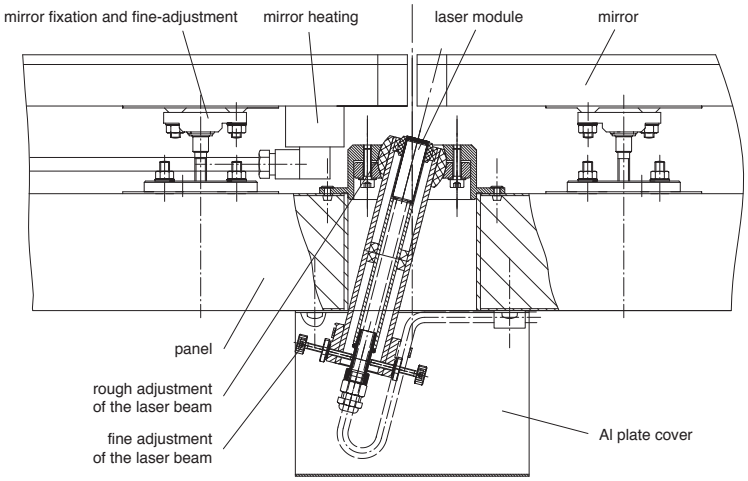

Figure 3.12: Technical drawing of the laser module of the AMC system. The fixation in the panel center, fine and rough adjustment mechanism are shown.

The most distant panels from the telescope dish center (panels at the four inclined edges of the telescope dish, assembled with three mirror units) needed a special laser mount. Because of the large angle from the mirror normal to the focal point, the laser module needed to be placed above the mirror surface. The special design is shown in the drawing in figure 3.3.

Electronics and power supply

The AMC control electronics is a custom-made design, developed by Varuzhan Danielyan from the Yerevan Physics Institute. Although commercial driver electronics for stepping motors are available on the market, they would be too expensive to be adapted for the $\sim$ 500 actuators. Furthermore, additional drivers for the laser modules would be needed. Therefore we decided to use an in-house design of the electronics to control the actuators, laser modules and the communication with the central control PC.

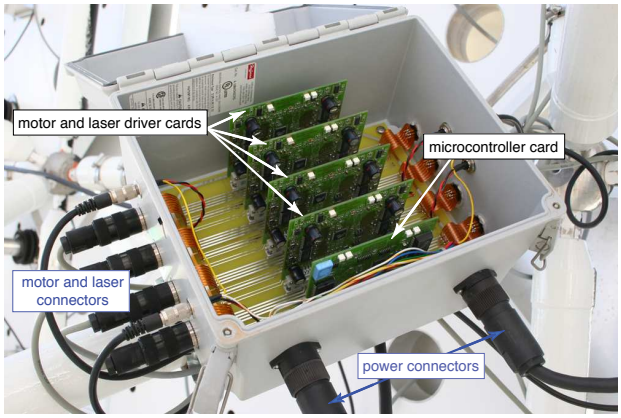

Figure 3.13: Control electronics for the actuators and laser modules of the AMC.

The controller cards are located in boxes, which are mounted on the mirror dish structure behind the panels, as shown in figure 3.13. Each box controls four panels. In this configuration 62 boxes are required for

[9] `http://www.quarton.com`

all 247 panels. Each box houses one controller card, responsible for the communication with the AMC control PC, by means of a dedicated control software and transmission of the commands to the four motor and laser driver cards inside the box. The so-called *AMController* card has a unique ID and can be addressed directly by the software. In addition, the card is equipped with humidity and temperature sensors, which allow to monitor the water tightness of the box.

The control commands are forwarded to the corresponding motor and laser driver cards inside the box. In total 250 of the so-called *SMDriver* cards are used. All of them are identical, addressed by the position, in which they have been inserted on the main board inside the box. The SMDriver card controls the movement of the stepping motors and switches the laser modules. The stepping motor driver allows one to set manually the winding currents and frequency. The movement of the actuator is stopped when one of the end-switches react.

Both cards are equipped with ATMEL[10] *ATmega163* micro-controllers. The chips have two kinds of memory: The SRAM is programmed with the software for the communication and steering of the hardware components, while the EPROM memory on the SMDriver cards is used to remember the position of the stepping motors. The cards can be programmed with the driver software inside the boxes. It makes updates and modifications of the software easy.

For the communication between the computer and electronics, the RS-485 interface in half-duplex mode is used. The interface allows the control of the AMC hardware over more than 150 m twisted pair cables.

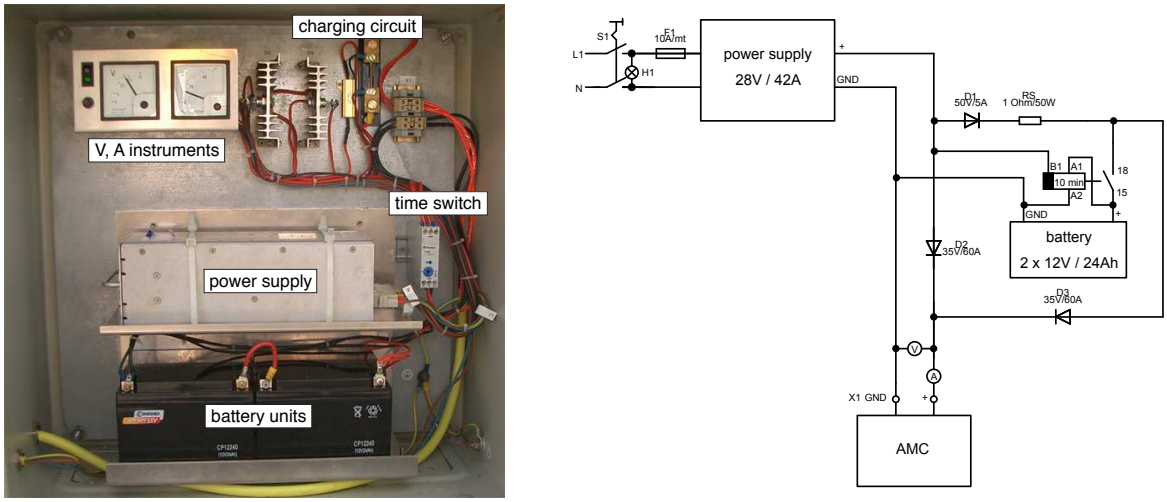

Figure 3.14: AMC power cabinet mounted on the east tower of the MAGIC telescope. *Left:* Image of the inside of the power cabinet. *Right:* Electric circuit of the power cabinet.

The power for the electronics, actuators and lasers is provided by a 28 V, 42 A power supply. The power cabinet is mounted on one of the telescope towers, close to the mirror dish structure. It should be noted that the stepping motors require only 5 V, but they need currents of 1 A for the operation. In order to use thin cables the power supply provides 28 V, which reduces the currents by almost factor six, when converting to the actuator operating voltage. In order to keep the panels in their position, the actuators need to be powered in the stand-by mode. Summing up the currents for the motors, the logic and the voltage conversion efficiency one obtains currents of up to 12 A in the stand-by mode. The power consumption

[10] `http://www.atmel.com`

of the AMC in the stand-by mode is therefore $\sim 340\,\mathrm{W}$.

To prevent de-focussing of the reflector during short power cuts, two batteries are placed in the power cabinet[11]. Figure 3.14 shows the power cabinet and its electrical circuit. The batteries can inject more current for the AMC system if required. Currents of up to 90 A during short time periods are available and the movement of all actuators at the same time is in principle possible.

The AMC CCD camera

The AMC system needs a CCD camera to monitor the laser spot positions on the lids of the MAGIC camera. I have selected the *EHDkamPro02* monochrome CCD camera from the company EHD imaging GmbH[12] for this purpose. The CCD chip has 752×582 pixels. Using a lens system with the focal length of $f = 75\,\mathrm{mm}$, one obtains a resolution of 2.05 mm/pixel at the focal plane of the telescope. The FOV of the camera is $\sim 3.5°$.

The software determines the spot position based on a weighted mean, with weights corresponding to the intensity of the laser spot. The accuracy depends on the wind conditions and the overall shape of the laser spot. For good weather conditions we achieved a spot position reproducibility of 0.2 CCD pixel (0.4 mm). At higher wind speeds the reproducibility is reduced to 0.3 CCD pixel (0.6 mm). The **precision for re-focussing** of the mirrors is therefore better than 1 mm.

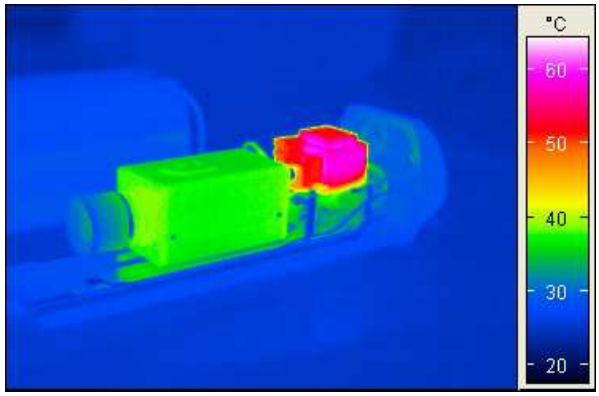

Figure 3.15: IR image of the AMC CCD camera.

The AMC CCD camera is mounted in the central square of the telescope dish structure, viewing directly the MAGIC camera lids and the four LEDs used to determine the position of the camera center. Figure 3.15 shows an image of the AMC camera taken with a IR camera ($8 - 12\,\mu\mathrm{m}$). The image illustrates the temperature of the camera and the power supply.

3.5 Focussing procedures for the MAGIC reflector

The main units of the MAGIC reflector are the panels, adjusted with the AMC. However, the panels themselves are composed of smaller mirror segments. The mirror segments have been pre-adjusted to a common spot, as described in § 4.1.2. To fine-focus the mirrors on the one hand and to focus the panels on the other hand, different methods are required. In the following, I will describe the three methods implemented for the MAGIC telescope:

1. During the normal telescope operation the lasers and LUTs are used to correct the mirror dish deformations. These methods are described in § 3.3. However, before the software controlled focussing can be done, one needs to calibrate the individual panels. The calibration is done based on the next two methods.

[11] The electricity supply system on the island is not very stable and frequent short-term voltage drops occur. The battery acts as a short term uninterruptible power supply, as well as surge protector in case of glitches.

[12] `http://www.ehd.de`

2. The fine focussing of the individual mirror segments to a common spot is done with an artificial light source. In the first year of the MAGIC operation this method was also used to focus the overall reflector. This method is described in § 3.5.1.

3. The complexity of the previous method and the implementation of the SBIG camera (see § 4.2) encourage us to try the use of a bright star to focus of the panels. This method is described in § 3.5.2.

3.5.1 Focussing of the mirrors with the use of an artificial light source

Thanks to the topography of the experiment site at the Observatorio del Roque de los Muchachos, one has the possibility to mount a distant artificial light source (the so-called Roque lamp), which can be pointed towards the telescopes. The method was first implemented for the HEGRA telescopes [126], where the individual mirrors needed to be adjusted by hand. Figure 3.16 shows the Roque lamp mounted on top of the mountain, pointing towards the telescope, as used for the focussing procedure.

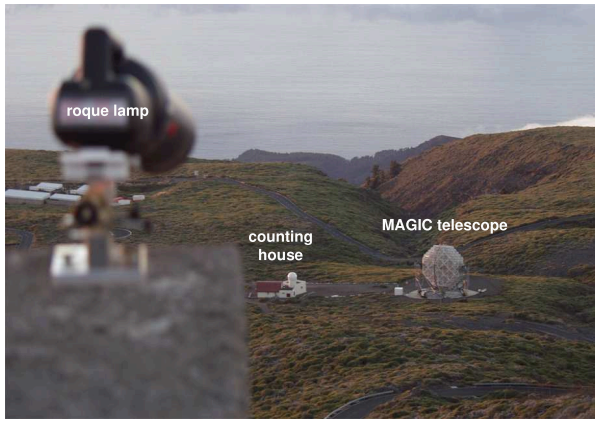

Figure 3.16: Focussing of the MAGIC mirrors with an artificial light source mounted at $\sim 980\,\mathrm{m}$ distance from the telescope.

The custom-made design of the lamp consists of a mount, which allows to fine-adjust the lamp orientation in both axes. The lamp is a common flashlight with a parabolic reflector of $\sim 120\,\mathrm{mm}$ Ø. It gives a collimated beam of light, covering the size of the telescope reflector area at 980 m distance. In order to suppress the amount of scattered light a $\sim 500\,\mathrm{mm}$ long tube is mounted in front of the lamp. Two 6 V, 250 mAh batteries are used to power the lamp. The power can be remotely switched on and off from the counting house.

The main advantage of the artificial light source is its brightness. The reflected spots of the individual mirrors can be seen with a standard CCD camera, or even by eye. The short integration time of the CCD camera drastically shortens the required time for a focussing. In addition, the telescope does not need to track the light source, which allows physicists to work on the dish structure and fine-focus the individual mirror segments on panels. Climbing on the telescope during movement is not allowed for security reasons. However, there are also disadvantages of this method:

- The use of a bright artificial light at an astronomical site is not allowed during dark nights. Even when the light of the Roque lamp is collimated to a narrow beam, it may disturb the optical telescopes. Therefore the Roque lamp can only be used during times of moon shine. The other experiments need to be informed beforehand each time one plans to use the lamp.

- The distance of 980 m is far from optimal in order to focus the reflector to infinity (or to 10 km in the case of MAGIC). The telescope camera needs to be shifted by $\sim 300\,\mathrm{mm}$ along the optical axis, in order to compensate the different object distance of the Roque lamp and the shower center of gravity.

- Different to spherical reflectors, a parabolic reflector requires additional corrections, when focussed with this method. For spherical mirrors the camera shift is alone sufficient to correct for different object distances. The corrections required for parabolic reflectors will be described later in text.

The Roque lamp is mainly used when the four individual mirror segments mounted on the panels need to be fine focussed. Its high luminosity is a benefit when monitoring the spots of the individual $50 \times 50\,\mathrm{cm}^2$ mirror segments at the focal plane of the telescope. The same procedure performed with a star would require significantly longer CCD exposure times. The fine focussing of the mirror segments was once performed after their installation. Since then, the Roque lamp was only used in the case of a mirror element replacement. In the beginning (before the SBIG camera was installed) the Roque lamp was also used to focus the panels to a common spot. To do so, one needs to apply corrections for the focal length, which I will address in the following.

Focussing of a parabolic reflector with a nearby light source

During the focussing procedure the telescope points towards the Roque lamp. The starguider system [104] is used to ensure that the telescope's optical axis is aligned exactly with the lamp. An offset would influence the pointing accuracy of the telescope and would afterwards require corrections to the bending model.

The individual mirror spots are projected onto a screen (white sheet of paper), mounted in front of the plexiglass window of the PMT camera (see figure 4.11). In order not to overlay the individual light spots, the mirrors are slightly tilted away at the beginning. After the exact position of the PMT camera center is determined, the following steps are taken:

- A panel is selected and *initialised*. During the initialisation the actuators are moved from the lower to the upper end-switch. From the number of motor steps between the end-switches the central position of the actuator is calculated. Subsequently the actuator is moved to the determined central position.

- As the next step the reflected light spot of the panel is moved towards the MAGIC camera center. The required tilt of the panel is adjusted with both actuators. This procedure is still done manually, however it is planned to fully automatize it in the near future. For the determination of the position the SBIG camera is used. The accuracy of the focussing by human eye is of the order of $\pm 2.5\,\mathrm{mm}$.

- After the adjustment of the spot, the position of both actuators is saved. Also the position of the corresponding laser spot at the camera lids is recorded. The laser spot position, with respect to the four LEDs on the camera lid, defines the nominal orientation of the panel and its focus.

The procedure is repeated with all 247 panels. The left side of figure 3.17 shows the light spots of 103 panels in the defocused mode. On the right side of figure 3.17 the overall PSF of these panels after focussing is shown. The time required for a full focussing of the MAGIC reflector in the described way is $\sim 7\,\mathrm{h}$. Therefore such an adjustment can be completed during one full moon night.

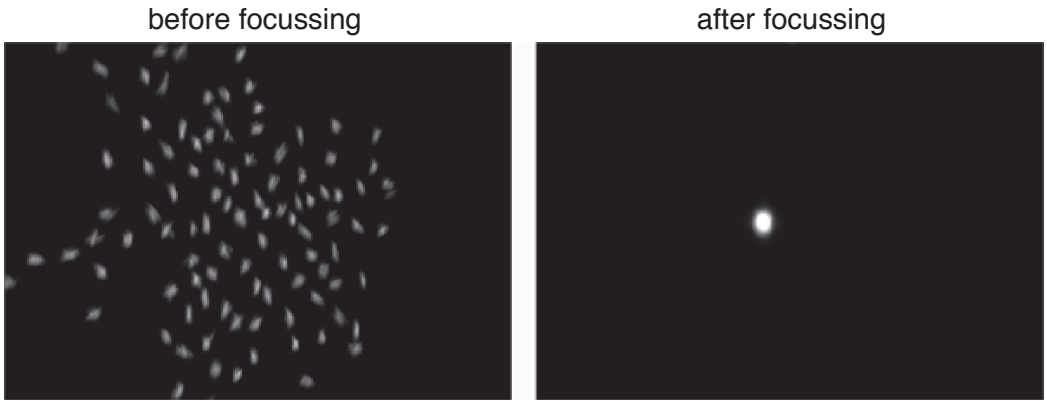

Figure 3.17: Photographs of the mirror spots before and after focussing with the Roque lamp. *Left:* Image of 103 light spots in defocused mode. *Right:* Overall PSF of these panels after focussing. The size of the spot is well below the diameter of an inner PMT pixel.

Correction of the focal length

The not moving artificial light source is usually set at some finite, not too distant location. From the paraxial mirror-image equation, valid for spherical mirrors,

$$\frac{1}{f} = \frac{1}{s} + \frac{1}{s'} \tag{3.1}$$

where f is the focal length, s is the distance of the object and s' is the distance of the projected image, it follows that only rays from infinity are focussed in f. Using $f = 17\,\mathrm{m}$ and $s = 980\,\mathrm{m}$, the distance to the Roque lamp, one obtains the object plane at $s' = 17.300\,\mathrm{m}$. This is 300 mm further away from the reflector than its nominal focal length for infinity focus. To compensate for the large difference in distance, the MAGIC PMT camera needs to be relocated. Its mounting on four rails allows to relocate the camera body along the optical axis, as shown in figure 3.18. The camera position for a 10 km focus can be calculated using equation 3.1; it results in $s' = 17.030\,\mathrm{m}$. The focal length difference between infinity focus and 10 km focus is therefore 30 mm. The relocation of the MAGIC PMT camera along the optical axis allows to focus the reflector to different focal lengths. A ruler and the positions for the different focal lengths are indicated in the figure on the right side.

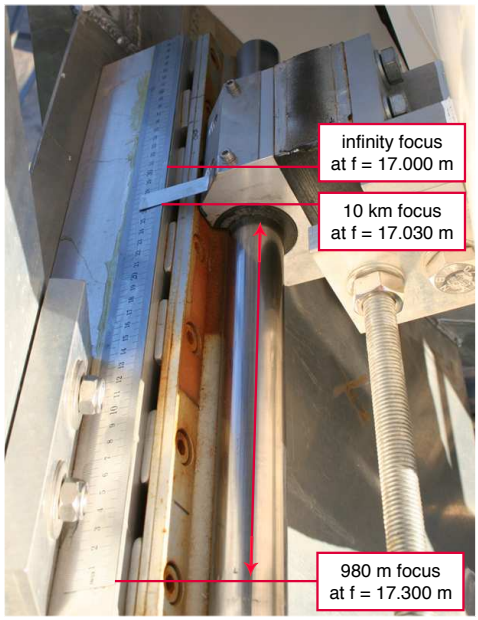

Figure 3.18: Photograph of the relocating mechanism of the MAGIC PMT camera. The positions for the different focal length settings are indicated in the figure.

As mentioned before, during the focussing a white sheet of paper, fixed on the plexiglass in front of the PMTs, is used. The distance between the paper and the Winston cone plane is 27 mm, as shown in figure 4.11. Since the shower images are mapped at the Winston cone plane, this distance has also to be taken into account when determining the final position of the camera body.

The optimal position of the focal plane is very crucial for the quality of the PSF. Because of $\langle f/d \rangle = 1.05$, the PSF changes linearly with the focal plane offset. Figure 3.19 shows the difference on the PSF when focussed at infinity at the left hand side and at 10 km on the right side. The image was taken from the same star with the same exposure time.

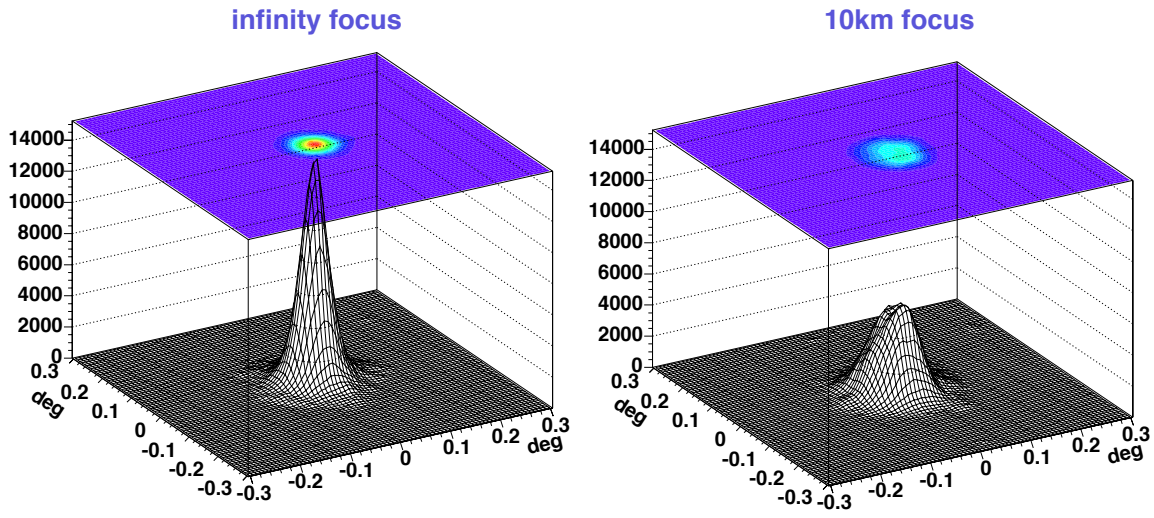

Figure 3.19: PSF of the MAGIC telescope for infinity (left) and 10 km focus. Reflected image of Menkalinan (1.85 mag) taken with the SBIG camera with exposure time of 2 s. Image from September 27$^{\text{th}}$, 2006. The corresponding PSF is: $r_{80} = 17.27$ mm for infinity and $r_{80} = 21.73$ mm for 10 km focus.

Correction required for a parabolic reflector

In contrast to a sphere, a parabola can only focus an image at infinity. This effect results from the fact that the individual mirrors of a parabola have different focal lengths. While a mirror segment in the center of the reflector has a focal length of 17.0 m, a mirror at the edge of the reflector, with a distance of 8 m to the optical axis, has a focal length of 18.4 m. The error on the PSF introduced by this aberration is shown in the middle plot of figure 3.20. For the mirrors in the central area of the reflector the effect is small, at larger distances from the optical axis the effect becomes comparable to the size of an inner PMT pixel.

The wrong position of the focal plane adds linearly to the parabola effect. The resulting degradation of the PSF is shown in the right plot of figure 3.20. While the focal plane can be corrected by shifting the MAGIC camera position, the effect of the parabola, however, can not be corrected by camera movements. Therefore, we developed algorithms to modify the orientation of each individual panel in order to correct the error introduced during the focussing with a nearby light source.

Figure 3.21 illustrates the required corrections to focus a reflector with a nearby light source. In the case of a parabolic, as well as a spherical mirror, a ray from infinity is focussed in f'_{mirror}, the focal point of the mirror. A ray from a finite distance s_{roque}, like the Roque lamp, is focussed to a point s'_{roque} at a larger distance than the focal length f'_{mirror}.

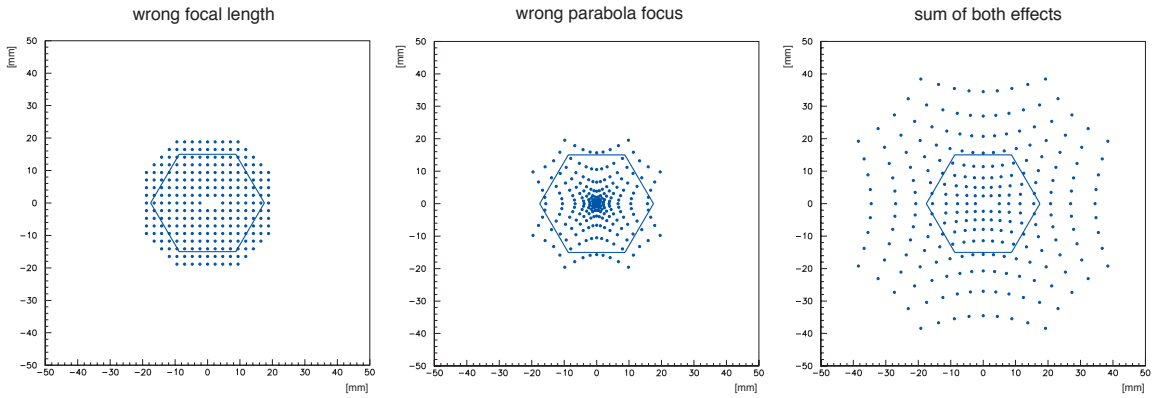

Figure 3.20: Errors on the PSF introduced due to the wrong focussing of a parabola with a nearby light source. The individual points represent the position of the light spot center for each individual panel, calculated from numerical simulations. The size of the central PMT pixel is indicated by the hexagon for comparison. *Left:* Errors introduced due to the 27 mm distance between the plexiglass and the Winston cones. *Center:* Errors introduced due to focussing of a parabolic reflector with a light source not located at infinity. *Right:* Sum of both errors.

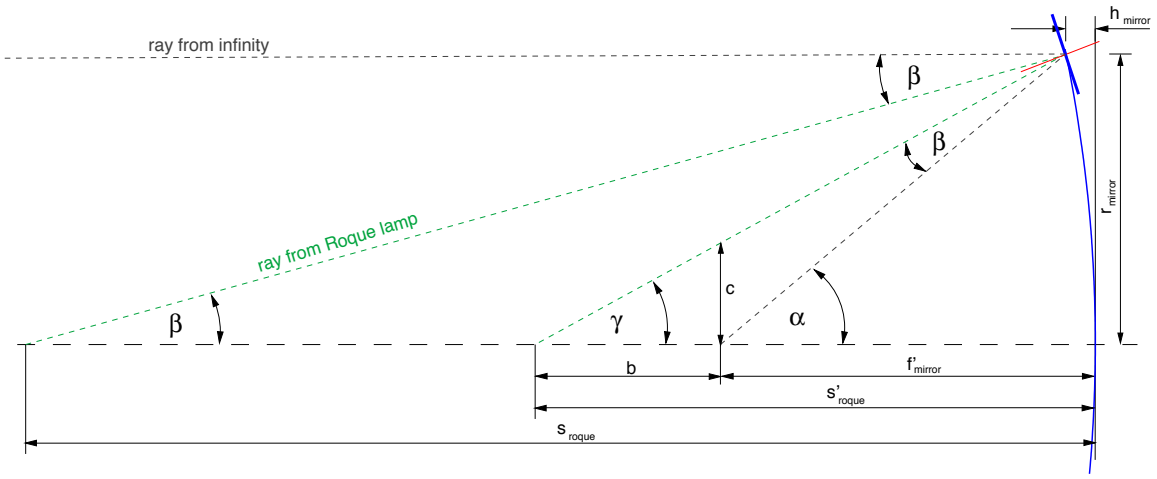

Figure 3.21: Schematics of the focussing procedure with a nearby light source.

Based on this schematics one can calculate the angles α, β and γ by using the following equations:

$$\alpha = \arctan\left(\frac{r_{\mathrm{mirror}}}{f'_{\mathrm{mirror}} - h_{\mathrm{mirror}}}\right) \tag{3.2}$$

$$\beta = \arctan\left(\frac{r_{\mathrm{mirror}}}{s_{\mathrm{roque}} - h_{\mathrm{mirror}}}\right) \tag{3.3}$$

$$\gamma = \alpha - \beta \tag{3.4}$$

The focal length for an individual mirror, when focussed with the Roque lamp, is given as:

$$s'_{\text{roque}} = \frac{r_{\text{mirror}}}{\tan\gamma} + h_{\text{mirror}} \tag{3.5}$$

where h_{mirror} is the height of the mirror at the radial distance r_{mirror} from the optical axis of the telescope. For a parabolic reflector h_{mirror} can be calculated using the equation:

$$h_{\text{mirror}} = \frac{r^2_{\text{mirror}}}{4 \cdot s'_{\text{roque}}} \tag{3.6}$$

From this equation the new focal distance s'_{roque}, for any arbitrary mirror element at the radial distance r_{mirror}, can be calculated. The offset c for each mirror can be obtained from the simple rule of three:

$$\frac{c}{b} = \frac{r_{\text{mirror}}}{s'_{\text{roque}} - h_{\text{mirror}}} \tag{3.7}$$

Using the same correlation one can also calculate the required corrections for focussing to different distances, e.q. for 10 km. The AMC software incorporates this feature. The magnitude of the shift of the focal spot on the focal plane is calculated for each panel. The obtained shift is multiplied by factor two and applied during the laser focussing. The factor two is required, as the movement of the laser on the camera plane always corresponds to a movement of the image spot by twice this distance.

This method can easily be extended and zenith angle dependent focal lengths could be adjusted. Because of the changing depth of the Earth's atmosphere with varying zenith angles, the distances to the maxima of the Cherenkov light showers vary[13]. The optimum focal lengths for different zenith angle observations are currently under study.

With the implementation of the SBIG camera (§ 4.2) focussing with stars has become possible. This method will be described in the following chapter.

3.5.2 Focussing of the MAGIC reflector with stars

The standard AMC CCD camera (see § 3.4), used to monitor the laser spots, is barely sensitive enough to resolve the reflected images of the Roque lamp from individual panels. When selecting a new camera for PSF and reflectivity measurements, our goal was to resolve the individual spots of stars from single mirror elements. The high sensitivity and dynamic range of the SBIG camera allows for this and thus opens new possibilities to focus the MAGIC reflector.

In a first approach we used the star Polaris (2.02 mag). It was selected because its position does not need to be tracked by the telescope[14]. Tracking a star over a large zenith range during the focussing would result in co-instantaneous deformations of the mirror dish structure. In addition the measurement with Polaris can be repeated every night at any time. Polaris is observable for MAGIC at a zenith angle of 61°.

[13] The shower maximum of a $100 - 200$ GeV γ-ray shower is typically at 0.4 air-mass, measured from the top of the atmosphere.

[14] In our epoch Polaris is rotating around the celestial pole at a radius of 0.7°.

To shorten the time of the focussing procedure, a group of panels is projected at the spectralon reflector on the camera lids (see § 4.2). The panels are divided into groups according to the eight independent branches of the AMC cabling. To avoid overlaps, the spots are arranged in a predefined pattern, as shown in figure 3.22. The figure shows the image of 33 reflected spots from single panels, taken with the SBIG camera with a 30 s exposure time. The time required to align the panels into the predefined positions and take a series of images sums up to about 15 min. The images are then analysed offline. The center of gravity for each individual panel is calculated and its position compared with the nominal position. Thanks to the pattern of the individual spots this is in most cases possible. The offsets are converted back into laser coordinates and afterwards corrected.

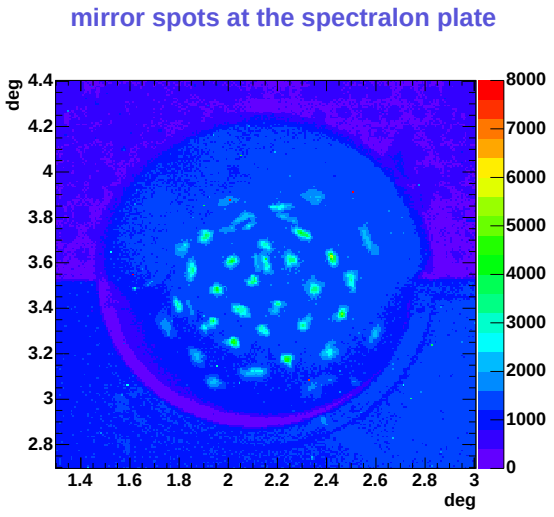

Figure 3.22: Reflected star spots from a group of panels at the Spectralon plate. A 30 s image taken with the SBIG camera from Polaris.

This method is still in the development phase. Many manual steps will be automatised in the near future and allow relatively fast re-focussing.

3.5.3 Problems with the AMC laser modules

The main idea of the AMC system is based on the use of the laser modules. The method is simple and robust, if the following assumptions are fulfilled:

1. The angle between the mirror panel normal and the laser beam should not change, i.e.:
   - The laser module has to be rigidly coupled to the panel.
   - The mounting should not be affected by temperature gradients.
   - The mounting should not be affected by humidity changes.
   - The mirrors on the panel should not defocus.
2. The laser spot shape at the focal plane should not change with time and varying weather conditions.
3. The optics of the CCD camera should not change.

The last point is ensured by using a high quality lens with a fixed focal length. In addition, the relative distances between the LEDs on the camera lids are monitored each time an image is taken. The laser spot size and intensity would need to change significantly in order to influence the weighted mean localisation algorithm used in the AMC. This effect has not been observed yet, neither in the laboratory nor on the telescope. Point 2 can therefore be also excluded.

The sometimes observed longterm degradation of the PSF after the laser adjustment, therefore has to be attributed to point 1: The angle between the laser spot and the focal spot of the mirrors. Several attempts were performed to search for the reason. First we inspected

the fixation of all laser modules on the panels. We found that in 18% of the panels the screws, which fix the laser module, were loose or some of them even missing. Consequently, all screws were replaced and glued in addition. After the subsequent refocussing, however, the trend for the PSF degradation still remained.

We first tested the lasers alone in order to find out if the laser light emitting region on the laser diode shifts its position. No shift was observed. Therefore the observed drift could be attributed to the mounting. Next, we started to test a sub-sample of eight complete laser modules. The modules were fixed to a stiff profile and mounted on a concrete wall, in order to guarantee a stable holding. The laser spots were projected onto a 34 m distant screen and observed with a close-by CCD camera. Different tests were carried out, resulting in the following findings:

Long time stability: The laser spots were observed on a day-by-day basis at room temperature. During the first days a significant drift of the laser spots could be seen. The spots moved away from their nominal starting position by up to 15 mm. The drift affected all spots and could be explained by the relaxation of local distortions in the material, resulting from the fixation. The drift decreased with the time and stopped after two weeks. This effect influenced the degradation of the PSF just after the maintenance of the laser module screws. For the future one has to take the relaxation of the material into account and wait at least two weeks before focussing the panels.

Temperature: During the second test temperature gradients were simulated. The complete laser module support was heated and the laser spot positions recorded. A temperature dependent drift of the spots was observed. The drift was determined to 0.53 mm/°C for the test setup. It corresponds to a laser spot movement of 0.31 mm/°C at the telescope camera plane. The temperature does not change much within one night at the telescope site. However, seasonal temperature gradients of up to 20 °C have to be taken into account. The choice of the material used for the holding of the laser module has to be reconsidered for the next generation of the AMC.

Humidity: We also simulated the impact of humidity, which could only have an affect on the plastic material of the Igus ring. We have not observed a influence of humidity on the laser spot positions.

From the test of the complete laser modules the reason for the drift could not be allocated. In the next step the individual components of the holding structure need to be explored. For the time being the LUT procedure was enhanced and is used as standard focussing method during the observation. Improvements and solutions for the future are listed in the next chapter.

3.5.4 Current status of the AMC system

The AMC performance has been improved significantly in the last years. The still unsolved problem with the laser modules is bypassed by the use of LUTs. This helped significantly to guarantee constant PSF quality during the observations. The implementation of the SBIG camera was the decisive factor for the development of new focussing methods. The star adjustment become a very promising feature. It eliminates the corrections required for the focussing of the parabolic mirror with a nearby light source. In addition, the required time for the focussing reduced significantly by the use of the predefined pattern of the mirror spots.

By automatising the individual tasks in the near future, full focussing of the MAGIC reflector can be performed within several minutes.

3.5.5 Improvements of the AMC in the future and MAGIC-2

The MAGIC-2 telescope is currently under construction. Figure 3.23 shows a recent photograph of the MAGIC site. The MAGIC-2 telescope structure is located in the front of the photograph, the MAGIC-1 telescope is standing behind. The distance between the two telescopes is 85 m. The two telescope concept allows for coverage of a larger detection area. At the same time the effective exploitation of the stereoscopic approach allows a more precise determination of the arrival directions of the γ-rays and suppresses efficiently the background of the hadronic showers. It is planned to complete the construction and start observations with both telescopes by the end of 2007.

Figure 3.23: Photograph of the MAGIC-1 (left) and MAGIC-2 (right) telescopes.

The MAGIC-2 telescope will be essentially an improved clone of the first one. The telescopes frame, the drive system and the individual telescope trigger will be copies of the original design, as well as the system for the optical transmission of the analog signals. The parabolic reflector will be composed of $1 \times 1\,\mathrm{m}^2$ mirrors, different from the panels with four mirror segments as in MAGIC-1. The camera will consist of 1039 PMTs of 0.1° FOV. The camera design incorporates the possibility to exchange individual modules and implement Hybrid Photo Detectors (HPDs), which reach peak quantum efficiency (QE) above 50%, but are less robust than normal PMTs at present, and Silicon photomultipliers (SiPMs), which have potentially the highest QE but are still in an early stage of development.
The AMC system will also be upgraded [124]:

1. The main change and improvement of the AMC-2 is achieved with the use of IR lasers. The laser modules will emit light at 1300 nm, in a region where the PMTs of the MAGIC-2 camera are not sensitive. This will allow to use the lasers during data taking, without interfering the observations. Concurrent re-focussing of the panels will improve the PSF quality, e.g. mirror dish deformations caused by constant wind loads will be corrected.

2. The use of IR lasers also requires the use of an IR camera. The focussing principle introduced for AMC-1 is retained: The laser spot, projected at a surface, is monitored with the camera and the deviation from the nominal laser spot position is corrected. However, one cannot use the camera lids anymore and the projection plane for MAGIC-2 has to be placed outside of the FOV of the PMT camera, e.g. two diffuse Teflon reflectors at both sides of the camera.

3. The control electronics and the stepping motor drivers will be installed inside the actuator housing. Each actuator will have a unique address and can be controlled individually by the AMC software.

4. The cabling scheme, as shown in figure 3.10, is kept. The mirrors are divided again into eight branches in order to prevent a breakdown of the whole system in the case of one serial cable branch. The electronic boxes act only as power distributors and drivers for the laser modules.

5. The mounting of the laser module is improved in order to guarantee better fixation. Also the actuator housing, especially the motor cover is slightly modified.

6. The Reed end-switches are replaced by hall sensors and a directional magnet, providing the possibility to retrieve roughly the actuator position. Software stop will be used.

Chapter 4

Optical performance of the MAGIC telescope

The assembling of single mirrors to panels, mounting of the panels on the telescope dish structure, pre-adjustment and focussing was my responsibility during the first period of my thesis work. Long term measurements of the PSF, refocussing in 1/2 year cycles, as well as the exchange of degraded mirrors continued up to the end of my thesis. The final optical performance of the MAGIC telescope is in first order dependent on the quality of the single mirrors and their pre-adjustment on the panels. In second order the AMC system takes care of the adjustment of the individual panels to one common spot. Its functionality guarantees the quality of the PSF during the observation on a long day-by-day basis. This chapter describes the main characteristics of the MAGIC reflector. It contains the technical description of the new subsystem, equipped with a very sensitive CCD camera, which was built to make the relevant studies. Based on measurements and numerical simulations of the PSF of the telescope, the impact of aberrations and the reflectivity of the mirrors are presented.

4.1 Introduction to the MAGIC reflector

The large reflecting surfaces needed for the imaging of atmospheric showers, the required optical quality and the cost of large milled spherical surfaces are the reasons why IACTs have a reflector composed of a mosaic of smaller elements. By increasing drastically the size of the reflector, the time dispersion of the Cherenkov light flashes becomes large compared to the intrinsic shower light flash duration. Since the time spread of Cherenkov photons depends on the primary particle energy and nature, good time resolution can be used to discriminate shower types and to reduce the LONS. A parabolic (= isochronous) mirror profile allows to minimise the instrumental time resolution, but requires mirrors with different radii of curvature. For a paraboloid the local curvature of the surface R_{lc} as a function or the radial distance r from its center is given by the formula:

$$R_{\mathrm{lc}} = r \cdot \left[1 + \left(r^2/R^2\right)\right]^{3/2} \tag{4.1}$$

where R is the vertex radius of curvature. As an example, for a paraboloid with the focal length $f = R/2 = 17\,\mathrm{m}$ and an reflector diameter d satisfying $\langle f/d \rangle = 1.05$, the radius of curvature at the edge is about 9.5% larger than at the center.

The main reflector characteristics of the MAGIC design are:

- The mirror surface is tessellated. The total mirror area of the reflector is about 236 m^2, the largest mirror ever built for this kind of instrument.
- The mirror segments are aluminum sandwiches with diamond-milled surfaces, with a high reflectivity and optimum optical quality. The aluminum surface is coated with a hard, transparent, $60 - 80$ nm layer of $Si0_2$, protecting it against weather damage and ageing. The sandwich construction ensures stiffness and low weight.
- The optical quality of the mirror elements is such that the PSF of the reflector, i.e. the light spot, is smaller than a camera pixel. The spherical mirror elements have different radii to imitate the overall parabolic surface.
- The heating system integrated in the mirrors prevents dew deposition and icing when needed.
- The reflector surface is approximated by a paraboloid of octagonal shape. The on-axis focal length is 17.0 m, increasing for the edge mirrors to 18.4 m, e.g. with $\langle f/d \rangle = 1.05$.

4.1.1 Single mirror elements

The surface of the MAGIC reflector is segmented into 964 smaller mirror elements with the side lengths of 500 mm × 500 mm [127]. Each mirror element is an aluminium honeycomb core, sandwiched between two outer 1 mm thick aluminium layers. On the one side of the sandwich a 5 mm thick AlMgSi alloy is glued. The front plate is worked and polished with milling machines and provide the final reflecting surface. The surface of the individual mirrors is machined to a spherical shape with the radius of curvature approximated to the parabola. Figure 4.1 shows the distribution of the mirror radii of curvature, as produced for the MAGIC telescope. The original mirror design [95] comes from the Max-Planck-Institut für Physik in Munich, which produced 30% of the mirror surface. The remaining 70% was built at the INFN Laboratories in Legnaro, Padua. The characteristics and differences of the two designs are summarised in the table 4.1 and shown in figure 4.2.

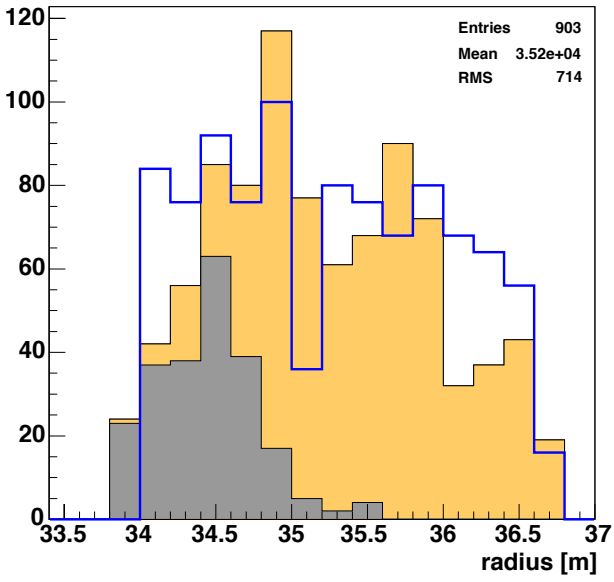

Figure 4.1: Distribution of the mirror radii of curvature used for the MAGIC telescope. The orange colour represents the Padua mirrors, while the grey colour shows the Munich mirrors. Because of their smaller radius, Munich mirrors are mounted in the central part of the telescope dish structure. The blue line shows the required radii for an ideal approximation of a parabola. Figure from [128].

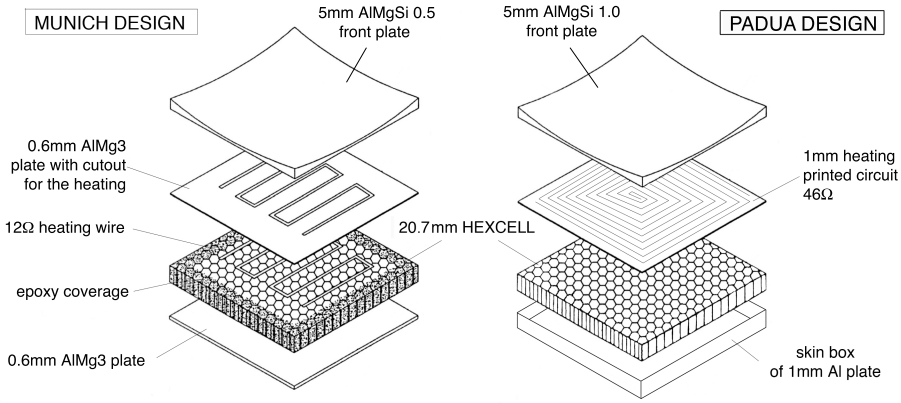

Figure 4.2: Exploded view of the Munich design (left) and Padua design (right) mirror elements.

	Munich design	**Padua design**
outer dimensions	$495 \times 495\,\mathrm{mm}^2$	$500 \times 500\,\mathrm{mm}^2$
front plate	5 mm AlMgSi 0.5 alloy	5 mm AlMgSi 1.0 alloy
outside material	back plate of 1 mm thick AlMg3 plate; sides covered with epoxy foam	the HEXCELL structure is inserted into a 1 mm Al bottom skin, formed as a box
heating	isolated heating wire placed inside a milled channel in the Al plate, resistance of $12\,\Omega$	printed circuit with embedded heating strips placed directly under the frontal plate, resistance of $46\,\Omega$
weight	4.2 kg	4.0 kg

Table 4.1: Main differences between the Munich and Padua mirror designs.

Diamond milling technique

The production of the mirror starts with a rough pre-milling of the aluminium front plate. The machining is done by fixing the mirror onto a rotating plate and using a T-shaped tool, the so-called *fly-cutter*, as shown in figure 4.3. The final shape is a spherical surface of radius $R = r/\sin\vartheta$, where r is the radius of the milling tool and ϑ is the angle between the rotation axis of the milling tool and that of the plate.

The final reflecting surface is obtained by using a diamond tip of $\sim$ 1 m radius of curvature with the same *fly-cutter* technique. The roughness of the surface is well below 10 nm RMS after the diamond milling. A more detailed technical and fabrication description can be found in [127, 128].

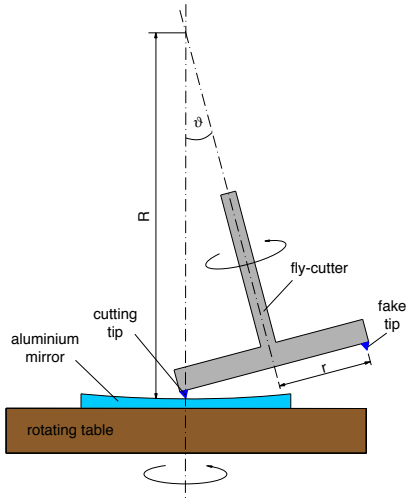

Figure 4.3: Sketch of the *fly-cutter* technique.

4.1.2 Panel units assembled with mirrors

In order to reduce the number of adjustable elements for the AMC, four mirrors are grouped onto one support basis, the so-called panel. At the four inclined edges of the dish, as well as close to the elevation axis panels with three mirrors are used. This results in 223 four mirror panels and 24 three mirror panels, as shown in the figure 4.5. The 60 mm thick and 960 mm × 960 mm large panel has a similar sandwich construction like the mirror elements: It is composed of an aluminium HEXCELL honeycomb core, covered by two 1 mm thick AlMg3 plates to form a stiff and light-weight unit. The panel is truncated at two corners to reduce its weight, which finally results in 11 kg. Tests of the surface deformations by applying weights corresponding to mass of the mirrors and wind load were carried out. The result was a maximal deviation from the plane surface of 0.04 mm, acceptable for the purpose.

Each individual mirror is fixed to the panel at three points. The holding points are composed of a fine thread spindle and a Igus joint. The spindles allow precise alignment of the mirror, while the Igus joints guarantee stress-free fixation. The technical drawing of the setup is shown in figure 3.3.

The mirror production is a long term process. To speed-up the construction of the telescope, the mirror area was assembled in few steps. Once a larger amount of mirrors was ready, they were allocated and grouped (based on their focal lengths) to panels. The individual mirrors on the panel have to be pre-aligned to form a common spot. Figure 4.4 shows the setup used for the pre-alignment of the mirrors. The panel is illuminated with a parallel beam of light. The parallel beam of light is produced with four prototype mirrors by placing a 100 W halogen lamp with 6 mm baffle in their focus. The panel is attached to a "windmill" carrier, which allows to tilt (β) and rotate (α) the panel and simulate its later orientation and position at the telescope dish structure. By adjusting the screws on the three fixation points of the mirror the individual spots at the projection screen can be superimposed to one common focus. Finally, the laser module is mounted on the panel and its beam aligned with the reflected spot. After the installation of the panels at the telescope dish structure, all panels were fine-adjusted.

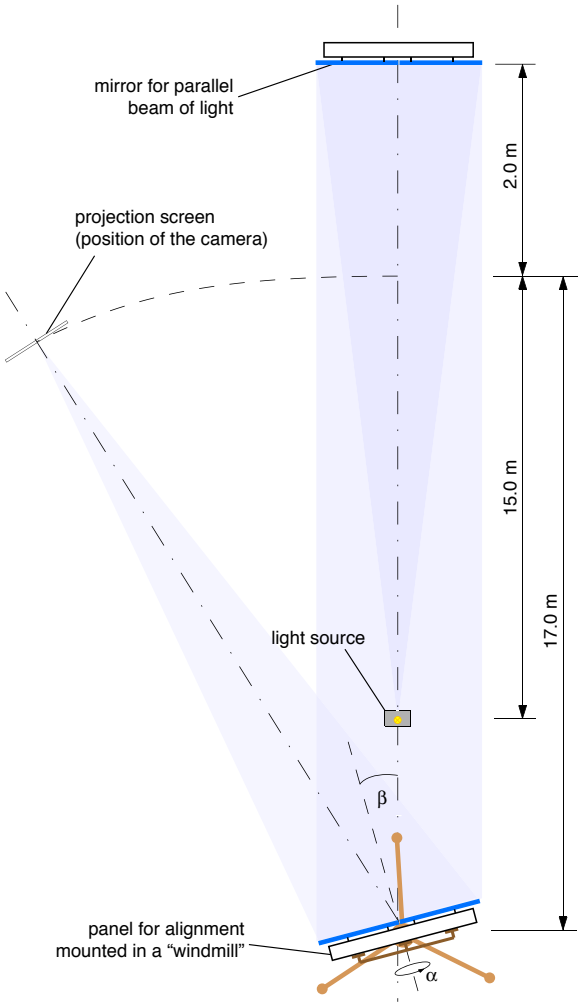

Figure 4.4: Scheme for the mirror pre-adjustment setup.

4.1.3 Performance of the mirror heating system

To prevent dew deposition and icing of the mirror surface a mirror heating system was developed. Inside the mirror sandwich structure a heating band in the case of the Munich design mirror, or a heating printed circuit in the Padua mirror design, were implemented. Because of the different resistance of the two concepts (see table 4.1) the four Munich mirrors on a panel are connected in series, while the Padua mirrors are in parallel connection. It results in a resistance of $\langle R \rangle = 46\,\Omega$ per each panel and gives an equal overall heating power among the individual panels.

The design incorporates two heating modi: The *basic* mode and the *de-icing* mode. In the basic mode all panels are powered simultaneously and 50 V and 1 A are available per each panel. In the de-icing mode groups of up to 15 panels are powered with 100 V and 2 A per panel. Table 4.2 shows the resulting heating power for the four and three mirror panel composition. The ambient temperature during the test was 23.8° C. Similar tests were performed at the telescope site. Due to the lower ambient temperature of $\sim 12°$ C and because of wind, heating of $\Delta T = 3°$ C in the basic mode and $\Delta T = 6°$ C in the de-icing mode were achieved.

mirror type	voltage	current	temperature
4 mirror panel	50 V	1.05 A	30.7° C
	100 V	2.08 A	46.2° C
3 mirror panel	50 V	1.38 A	39.1° C
	100 V	2.74 A	70.0° C

Table 4.2: Temperatures achieved with the MAGIC mirror heating system. The ambient temperature during the test was 23.8° C.

4.1.4 Chess board structure of the panels

The original design of the MAGIC reflector was aimed to reproduce the ideal paraboloid surface. However, trying to maximise the mirror area the required space between the panels turned out to be under-estimated. The resulting space is the sum of the precise installation of the mirrors on the panel and the panel installation on the telescope dish structure. Collisions between neighbouring panels during the actuator movements and gradual misalignment of the individual mirrors caused a degradation of the PSF. The panels were repositioned following the so-called *chess board* structure. They have been given a difference in height of +40 mm for the raised and −20 mm for the lowered panels, with respect to their nominal position. Figure 4.5 illustrates the arrangement of panels.

The 60 mm difference in height corresponds to 120 mm path difference for light rays and results to a time separation of 0.4 ns. If there are smearing effects larger than 0.4 nm (transit time spread in PMTs, sampling rate etc.) then one will not see this effect.

To understand the influence of the chess board structure on the optical quality of the reflector and the photon arrival time distribution, MC simulations were performed. In the first step the effect on the PSF was calculated for infinity and 10 km focus, as well as aberration effects due to photons arriving displaced to the optical axis for both the nominal parabolic shape and for chess board structured reflector. The ray-tracing showed that staggering of the panels does not spoil the optical characteristics of the reflector. Chapter 4.3.1 addresses the influence of aberrations for off-axis pointing in more detail.

The 60 mm difference in height between the two mirror layers of the chess board structure cause a separation of the arrival times of the primary isochronous reflector. Dedicated MC simulations were performed of the arrival times from γ, proton and muon induced Cherenkov light signals for an ideal paraboloid and a chess board structured reflector (description of the electromagnetic and hadronic showers can be found in § 2.1). The Cherenkov light generated from 100.000 proton, 50.000 muon and 38.000 γ particles in the atmosphere was simulated using CORSIKA v6.023. The particle incoming direction was set to 20° zenith and 0° azimuth for better comparison. The Cherenkov photons generated in these simulations hit the two different reflector types and were reflected at the mirror surface towards the common focus. Showers providing > 200 photons can trigger the telescope. The arrival time distribution of showers surviving the $SIZE$ cut at the camera plane was inspected (description of the $SIZE$ parameter can be found in § 5.4).

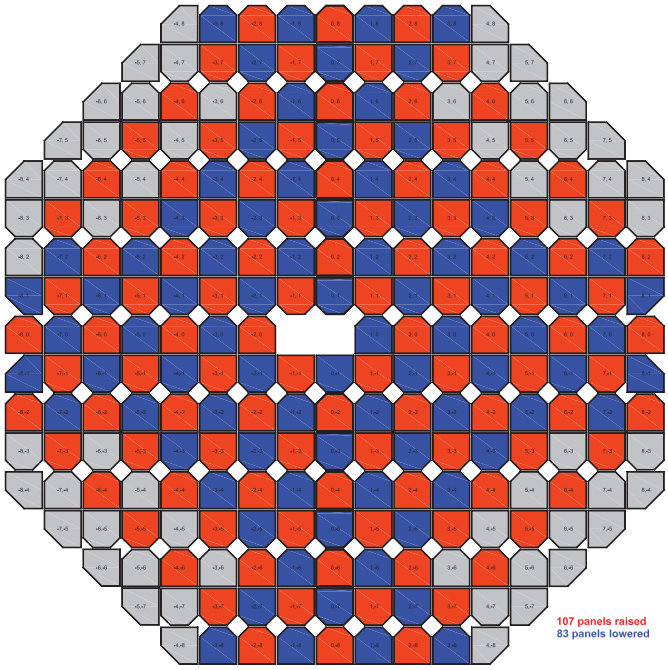

Figure 4.5: Chess board assembling of the panels at MAGIC telescope dish.

Gammas: The simulated γ-rays in the energy range between $10\,\text{GeV} < E_\gamma < 10\,\text{TeV}$ lead to $\sim 327 \cdot 10^3$ Cherenkov photons after the $SIZE$ cut. The arrival time distribution of the photons in the camera plane, after the corresponding reflection, is shown in figure 4.6. Comparing the results of the simulation a 0.175 ns shift of the mean arrival time was found for the chess board structured reflector. However, both distributions have an equal RMS, therefore no degradation of the data quality with the chess board structured reflector is expected.

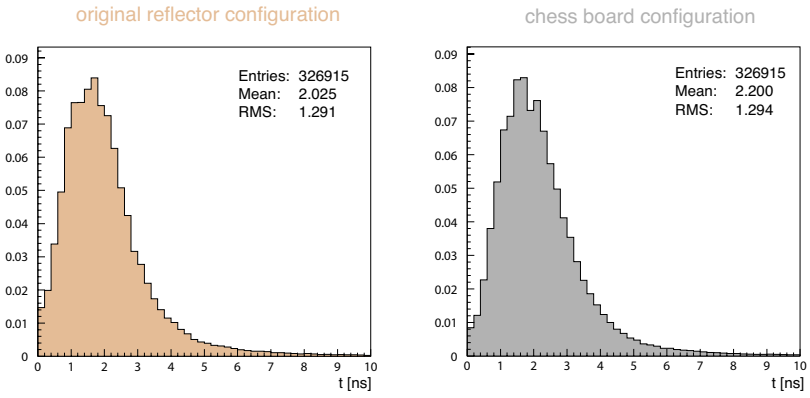

Figure 4.6: Arrival time distribution of γ-ray introduced Cherenkov photons for the ideal parabolic (left) and chess board structured reflector (right).

Protons: The simulated protons in the energy range between 30 GeV $< E_p <$ 30 TeV lead to $\sim 308 \cdot 10^3$ Cherenkov photons, which survived the $SIZE$ cut. Since charged cosmic rays arrive isotropically from all directions and hadronic showers are wider, a view cone of 5° was set. The arrival time distribution is shown in figure 4.7. Due to the chess board structure the arrival times of the small amount of Cherenkov photons from low energy protons spread more and cause the deficit in the first time bin. There is an enhancement in the arrival time of photons at 6 ns and 10 ns for the chess board structure. This is very likely an artefact of the simulation.

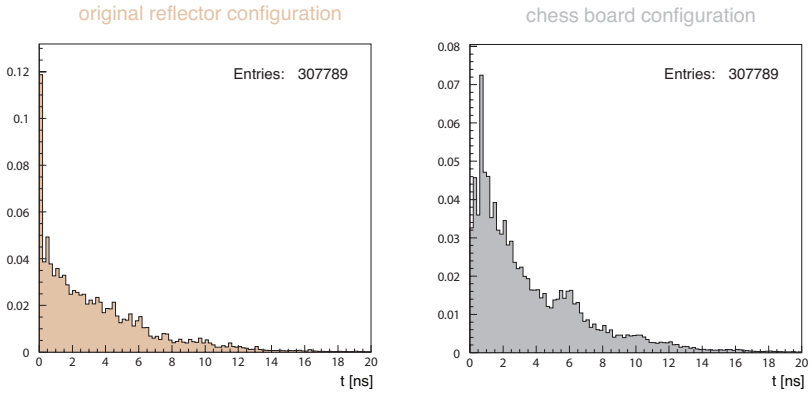

Figure 4.7: Arrival time distribution of proton introduced Cherenkov photons for the ideal parabolic (left) and chess board structured reflector (right).

Muons: The simulation contained muons with the energy range 10 GeV $< E_\mu <$ 1 TeV. The first interaction in the atmosphere was set to $\sim$ 17 km a.s.l., the view cone to 1.2° and the impact parameter up to 300 m. In total $\sim 308 \cdot 10^6$ Cherenkov photons survived the trigger conditions. The Cherenkov light from a muon is emitted parallel to particle direction, causing very narrow photon arrival time, as shown in figure 4.8. Since the arrival time is shorter than the time light needs to pass the distance between the mirror layers, two separated peaks show up for the chess board structured reflector. The time resolution of the current 300 MHz FADC system was determined to be 1.6 ns at the trigger threshold [129]. The additional split in the Cherenkov light arrival time of $\sim$ 0.5 ns will cause a worsening of the telescope time resolution by $\sim$ 0.08 ns, which has to be accepted.

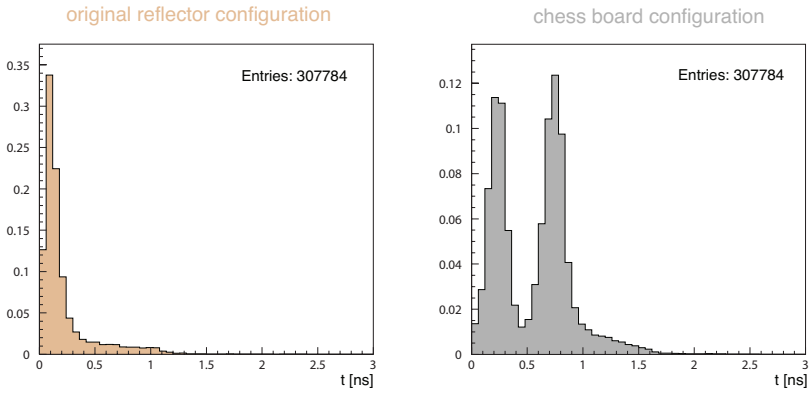

Figure 4.8: Arrival time distribution of muon introduced Cherenkov photons for the ideal parabolic (left) and chess board structured reflector (right).

The simulated impact of the chess board structured reflector showed that only for Cherenkov light emitted by muons is a detectable worsening of the time resolution of the order of 0.08 ns expected. There is no difference for γ and proton showers, which last longer than the muon Cherenkov light flash. A worsening of the PSF and aberration effects are thus not expected when moving to the chess board structure. These results lead to a major re-arrangement of all panels to the described chess board in mid 2005. The photograph on the right side shows a part of the MAGIC mirror area in the chess board arrangement.

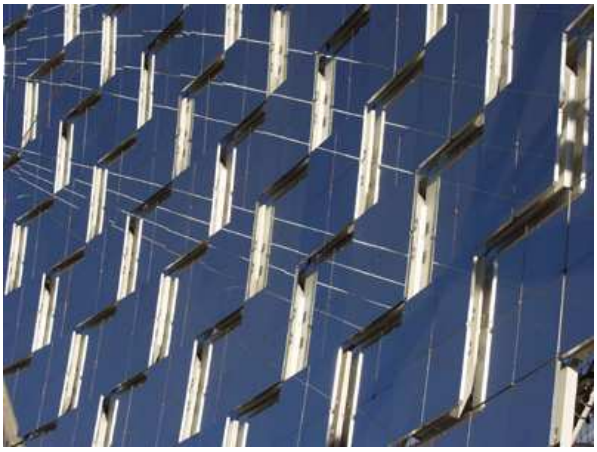

Figure 4.9: Photograph of the chess board assembling of the panels at MAGIC telescope dish.

4.2 High sensitive camera for optical measurements

In order to characterise the optical parameters of the MAGIC telescope, a new monitoring subsystem with a high performance CCD camera was built. The main purposes of this system are:

- Measurement of the overall PSF.
- Measurement of the mirror reflectivity.
- Study of long time degradation effects for individual mirror segments.
- Focussing of the mirror with a star as a light source.

The many different tasks required extensive tests of different cameras. Resolution, sensitivity and dynamic range of the CCD chip became the essential selection parameters for the cameras. I tested the following four cameras: *Sensicam QE* from the company PCO Imaging[1], $CoolSNAP_{ES}$ from the company Photometrics[2], *Alta U47+* from the company APOGEE Instruments[3] and the *STL-1001E* from the company Santa Barbara Instrument Group (SBIG)[4]. The latter, whose parameters are shown in table 4.3, turned out to be best suited for our purpose.

The astronomical camera was equipped with a Nikon MF 180/2.8 ED lens and

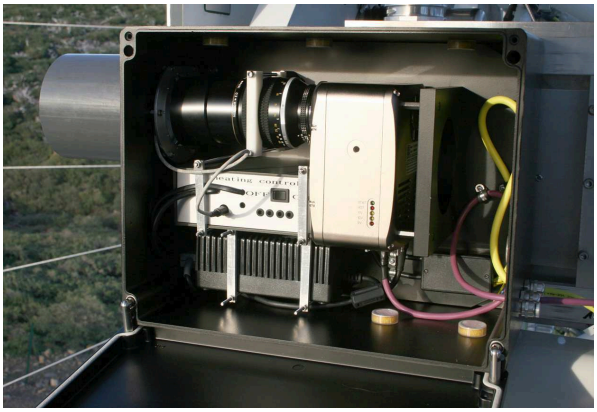

Figure 4.10: The custom-made housing of the SBIG camera mounted in the central part of the telescope dish structure.

[1] http://www.pco.de
[2] http://www.photomet.com
[3] http://www.ccd.com
[4] http://www.sbig.com

CCD SPECIFICATIONS	
imaging CCD	Kodak enhanced KAF-1001E
pixel array	1024×1024 pixels, 24.6×24.6 mm
total #pixels	1.0 million
pixel size	24×24 micron
full well capacity	$150.000\, e^-$
dark current	$34\, e^- \text{pixel}^{-1}\text{s}^{-1}$ at 0° C
READOUT SPECIFICATIONS	
shutter	electromechanical
exposure	0.11 to 3600 s, 10 ms resolution
A/D converter	16 bits
A/D gain	$2.2\, e^-$/ADU
read noise	$15\, e^-$ RMS
full frame download	2.5 s
SYSTEM SPECIFICATIONS	
cooling	two-stage thermoelectric
power	12 V max. 5 A
computer interface	USB 1.0
internal filter carousel	five filter positions (see figure 4.24)

Table 4.3: Specifications of the SBIG STL-1001E camera.

mounted inside a custom-made metal housing, shown in figure 4.10. I used a 10 W controlled heating system to prevent dew formation on the entrance window.

The data is transferred over USB to an optical fiber converter of the company S.I. Tech Inc.[5] to the 120 m distant computer in the counting house. The main power of the camera consists of the possibility to be completely remote controlled. I used an USB switch, connected with a semiconductor relay, able to handle the needed high currents. The camera features a filter reel inside the housing. I equipped the five filter positions with optical filters (shown in figure 4.24), which are now used for mirror reflectivity measurements. A new simple method to measure the reflectivity of the reflector was developed [130]. A description of the method and results are shown in § 4.5.

To allow measurements of the PSF and mirror reflectivity a high quality diffuse reflector was mounted on the lower MAGIC camera lid. The target is placed

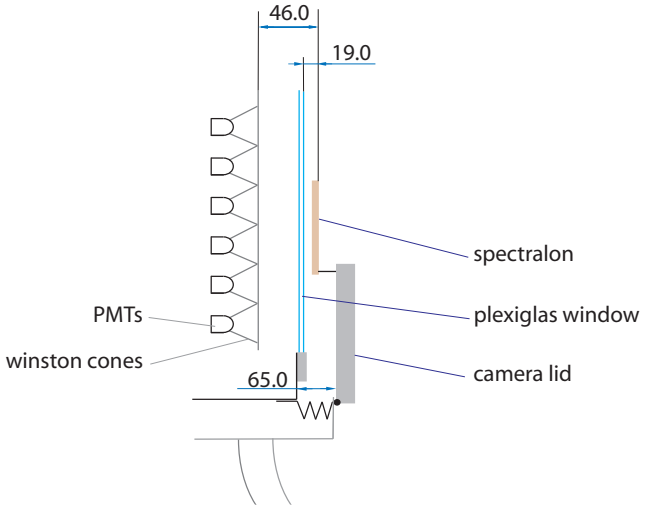

Figure 4.11: Schematic drawing of the Spectralon target mounted on the lower camera lid of the MAGIC telescope.

[5] http://www.sitech-bitdriver.com

near the focal plane for infinity focus[6], as shown in figure 4.11. The target is a 400 mm diameter, 6 mm thick disc made of Spectralon (see § 4.5.1). Figure 4.12 shows part of the MAGIC camera lid with the target and star field close to the optical axis, as seen with the the SBIG camera.

I wrote a C++ program interface to control all necessary functions of the camera: The exposure time, the CCD chip temperature and the filter reel position. The images are saved in *FITS* format [131] and later converted and processed with ROOT[7] macros.

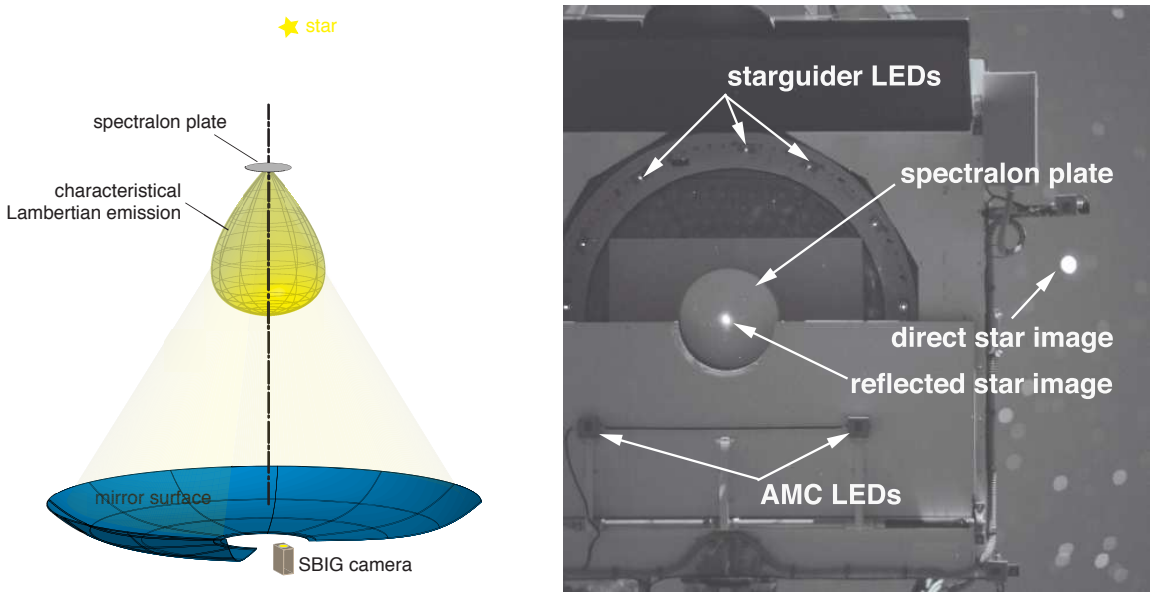

Figure 4.12: Field of view of the SBIG camera. *Left:* Schematic drawing of the SBIG camera installation. *Right:* Image taken with the SBIG camera. The field of view includes part of the MAGIC camera and stars close to the optical axis of the telescope.

4.3 Aberration errors of the MAGIC mirror

In an ideal optical system, all light rays from a point in the object plane would converge to the same point in the image plane, forming a clean image. The influences, which cause different rays to converge to different points and blur the image, are called **aberrations**. There are many types of aberrations categorised into 1st order, 3rd order, 5th order etc. The most common types of aberrations are the 3rd order aberrations, shown in figure 4.13.

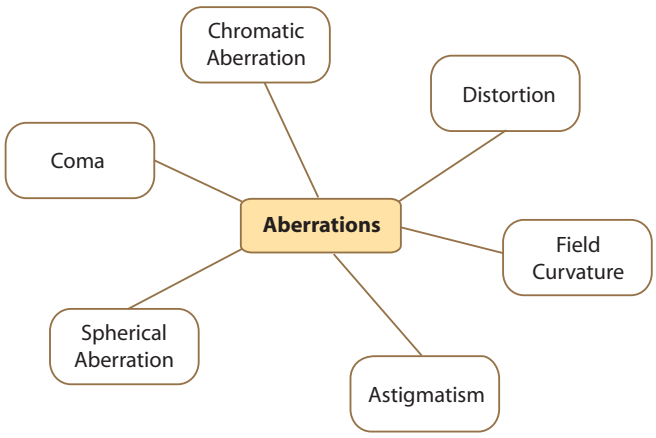

Figure 4.13: Different types of 3rd order aberrations.

[6]The telescope is focussed at 10 km distance so that the Cherenkov shower maximum is mapped with the best possible quality at the Winston cone plane. Objects at infinity (like stars) are focussed at $f_\infty = f_{10\,\mathrm{km}} - 30\,\mathrm{mm}$.

[7]`http://root.cern.ch`

The general equation for an aberration is [132]:

$$\Phi = W_{IJK} \cdot H^I \cdot r^J \cdot \cos^K \Theta \tag{4.2}$$

The coefficient W_{IJK} represents the magnitude of the aberration. The subscripts of W encode the exponents for the terms in the aberration. H is the height of the image, Θ is the off-axis angle and r the radial coordinate in the focal plane. In the following I will discuss briefly the different aberration forms. Further information can be found in [133, 134].

All aberrations, except the **chromatic aberration** affect both, refracting and reflecting telescopes; The chromatic aberration affects only refracting telescopes.

The **spherical aberration** plays a role for spherical mirrors and lenses. Rays parallel to the optical axis, striking the mirror surface at different distances from the center, are focussed at different focal lengths. The equation for spherical aberration is $\Phi = W_{040} \cdot r^4$.

The **curvature of field** occurs when the image is focussed on a curved plane. This is the case for typical IACTs, however the production of a curved camera plane is unrealistic and one needs therefore to accept this aberration form. The equation for the curvature of field is $\Phi = W_{220} \cdot H^2 \cdot r^2$.

The **distortion** shifts the image position. The images of lines that meet directly in the origin appear straight, but the images of any surrounding straight lines appear curved. There are two types of distortion: *pincushion* and *barrel*. The equation for distortion is $\Phi = W_{311} \cdot H^3 \cdot r \cdot \cos\Theta$. Optical systems without aperture, e.g. the MAGIC reflector, are free of distortion and are called *orthoscopic*.

The **astigmatic aberration** occurs when a mirror is not perfectly symmetric about the optical axis, e.g. if the focal length along one direction is slightly different to the focal length along the perpendicular direction. Instead of focussing rays to a point, they meet it two line segments perpendicular to each other. These are the sagittal and tangential focal lines. This aberration occurs in optical telescopes, as well as in human eyes. The equation describing the astigmatic aberration is $\Phi = W_{222} \cdot H^2 \cdot r^2 \cdot \cos^2\Theta$.

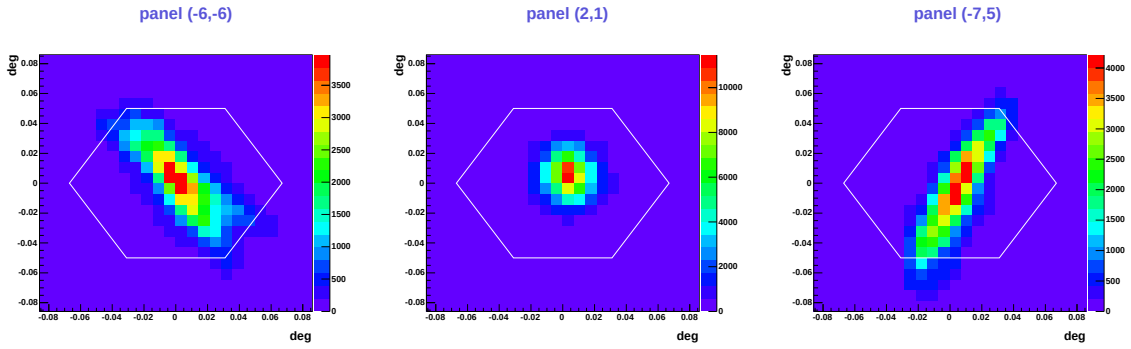

Figure 4.14: Examples of the impact of spherical and astigmatic aberrations of some MAGIC telescope mirrors. The central image is a panel mounted close to the dish center while the other images show panels mounted almost at the edges of the telescope dish, $\sim 8.5\,\mathrm{m}$ from the center. The size of the inner pixel light guide (Winston cone) is shown for comparison.

In the case of the MAGIC telescope the sum of the spherical and astigmatic aberration, as well as field curvature cause blurred and elongated spots by single mirrors, depending on their off-axis position from the center of the dish. Figure 4.14 shows the reflected spots in the camera plane for three random panels, affected by the aberrations. The impact for the

whole telescope is shown in figure 4.15. The optimal focussing is obtained with the existing spherical mirrors, which have nearly the same radius of curvature of the paraboloid. It is the case for the central reflector area. Far from the center of the dish, the difference between the shape of the paraboloid and the spherical mirrors increases and the dimensions of the spot too.

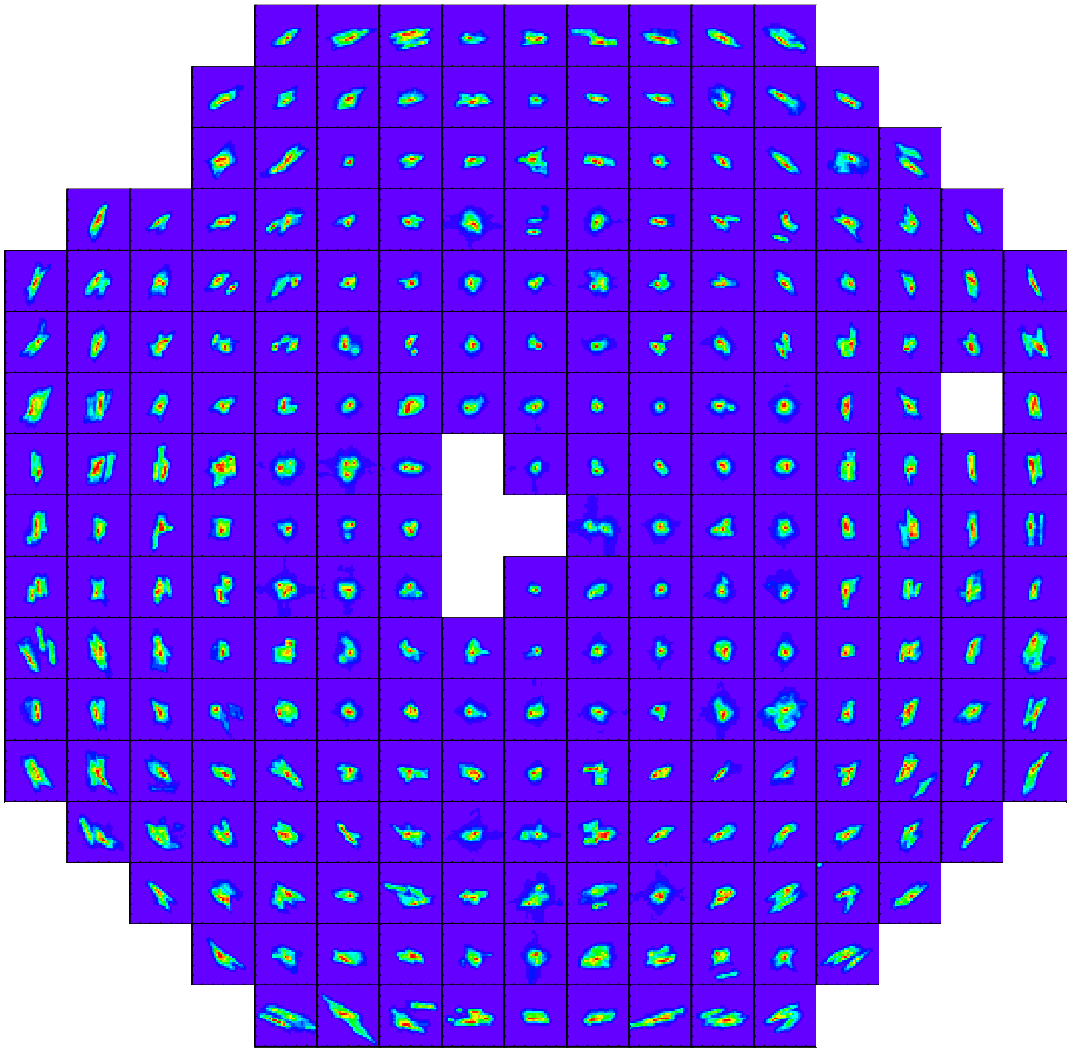

Figure 4.15: Reflected spot shapes of individual panels mounted at the telescope dish. The six white placeholders in the structure are either due to missing images or due to missing panels (two central panels). Each individual image has the size of $70 \times 70\,\mathrm{mm}^2$ at the camera focal plane. The elongated spots at the outer part of the telescope dish are caused due to aberration effects. There are few panels where the single mirror spots do not exactly overlap and show clearly separated spots. The figure shows that the outer most mirrors were not optimally chosen in the focal production. A focal setting resulting in a mean between the radial and tangential focus would be better.

Coma aberration is an inherent property of telescopes using parabolic mirrors. Light from a point source (such as a star) in the center of the field is perfectly focussed at the focal point of the mirror. However, when the light source is off-axis, the different parts of the mirror do not reflect the light to the same point. This results in a off-center mirror light spot looking wedge-shaped. The further the off-axis position, the worse this effect is. It causes stars to appear to have a cometary form, hence the name. The Cherenkov photons generated

in particle showers are emitted preferably in the direction of the primary particle, however, especially for hadron showers, deviations from the optical axis become significant and make the coma aberration an important obstacle for the analysis of the image parameters. The equation for coma is $\Phi = W_{131} \cdot H \cdot r^3 \cdot \cos\Theta$. The impact of the coma aberration is simulated in the MC data. It can also be shown directly by observing a star misplaced to the optical axis. This measurement was performed with the SBIG camera and the comparison between the measured and simulated PSF, at different optical axis distances to the star, are shown in the next chapter.

Formula 4.3 sums up all 3$^{\text{rd}}$ order aberration types, which have an impact on the optical performance of the MAGIC telescope. It is not easy to determine the individual aberration coefficients W_{IJK}. In practise they do not have big meaning and I have not studied them in more detail.

$$W(r,\Theta) = \underbrace{W_{040} \cdot r^4}_{\text{spherical}} + \underbrace{W_{220} \cdot H^2 \cdot r^2}_{\text{field curvature}} + \underbrace{W_{222} \cdot H^2 \cdot r^2 \cdot \cos^2\Theta}_{\text{astigmatism}} + \underbrace{W_{131} \cdot H \cdot r^3 \cdot \cos\Theta}_{\text{coma}} \quad (4.3)$$

4.3.1 Influence of coma and astigmatic aberration on the PSF

To understand the influence of coma and astigmatic aberrations, I have compared results of a self-written numerical ray-tracing simulation [128] with images taken from a bright star, when increasing the angular distance of the star w.r.t the optical axis of the telescope.

The simulation calculates the intersection point of the reflected light in the detector focal plane. In the ray-tracing procedure a parallel beam of light, inclined with an angle Θ to the optical axis of the telescope, was simulated. The reflector described the nominal shape of the MAGIC telescope: The overall reflector followed a paraboloid reproducing the MAGIC dimensions. It was composed of 964 spherical mirror segments with the size of $500 \times 500\,\text{mm}^2$. The radius of curvature for each individual mirror was set to its nominal value. The single mirror axis was perpendicular to the paraboloid surface on the central point of the mirror – it represented a perfect alignment of the system. One photon per $2 \times 2\,\text{cm}^2$ was incising the surface.

Formula 4.3 predicts a widening of the PSF with increased inclination angle Θ with respect to the optical axis. The effect is indeed observed and shown in figure 4.16: The aberrations cause an asymmetric tail away from the optical axis. A more quantitative description of the spot shape is provided by projections of the intensity distribution in the radial and tangential directions, shown in figure 4.18 for angles of 0°, 0.8° and 1.5° relative to the optical axis.

A quantitative comparison between the simulation and the measurement was done by comparing r_{80}: The radius, inside which 80% of the light content is found. The radius was determined from the radial and tangential projections of the PSF. The radial axis goes from the camera center to the spot and the tangential axis is the corresponding orthogonal direction. The measurements demonstrate that the spot width depends primarily on Θ. With increasing angle to the optical axis the spot width increases, following a second order polynomial function. The results are shown in figure 4.17. The simulated PSF is slightly better than the measured one. Taking into account that the ray-tracing simulation is based on ideal optical performance (parabolic shape of the reflector, spherical mirror segments with ideal radii of curvature and ideal alignment of the mirrors), this difference is not surprising. However, the fit to the measured and simulated data results in two parallel functions, indicating that the measurement is in good agreement with the numerical simulation.

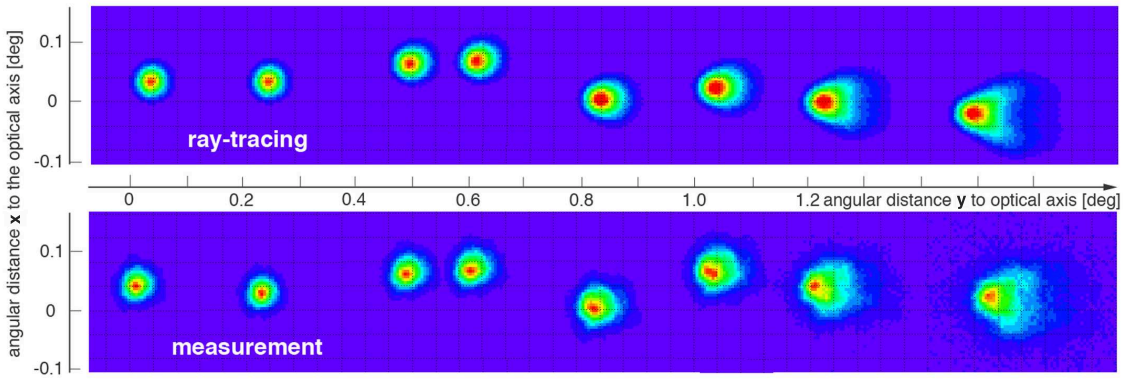

Figure 4.16: Comparison of the measured (bottom) and simulated (top) PSF with varying off-axis angle Θ. With increasing radial distance from the camera center the comet-like PSF becomes pronounced. The simulation was performed for the corresponding x and y distance to the camera center, determined with the starguider LEDs.

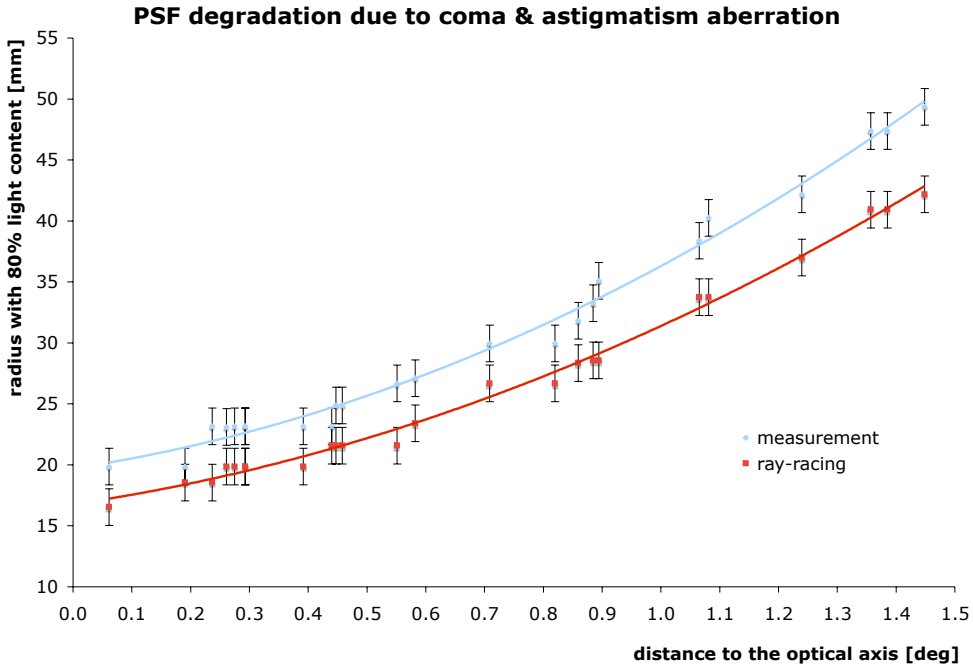

Figure 4.17: PSF degradation due to the influence of coma and astigmatic aberrations for off-axis pointing. Results from star measurements (blue) and numerical ray-tracing simulations (red) show acceptable agreement by considering slightly worse measurements than those obtained with the ideal PSF simulation.

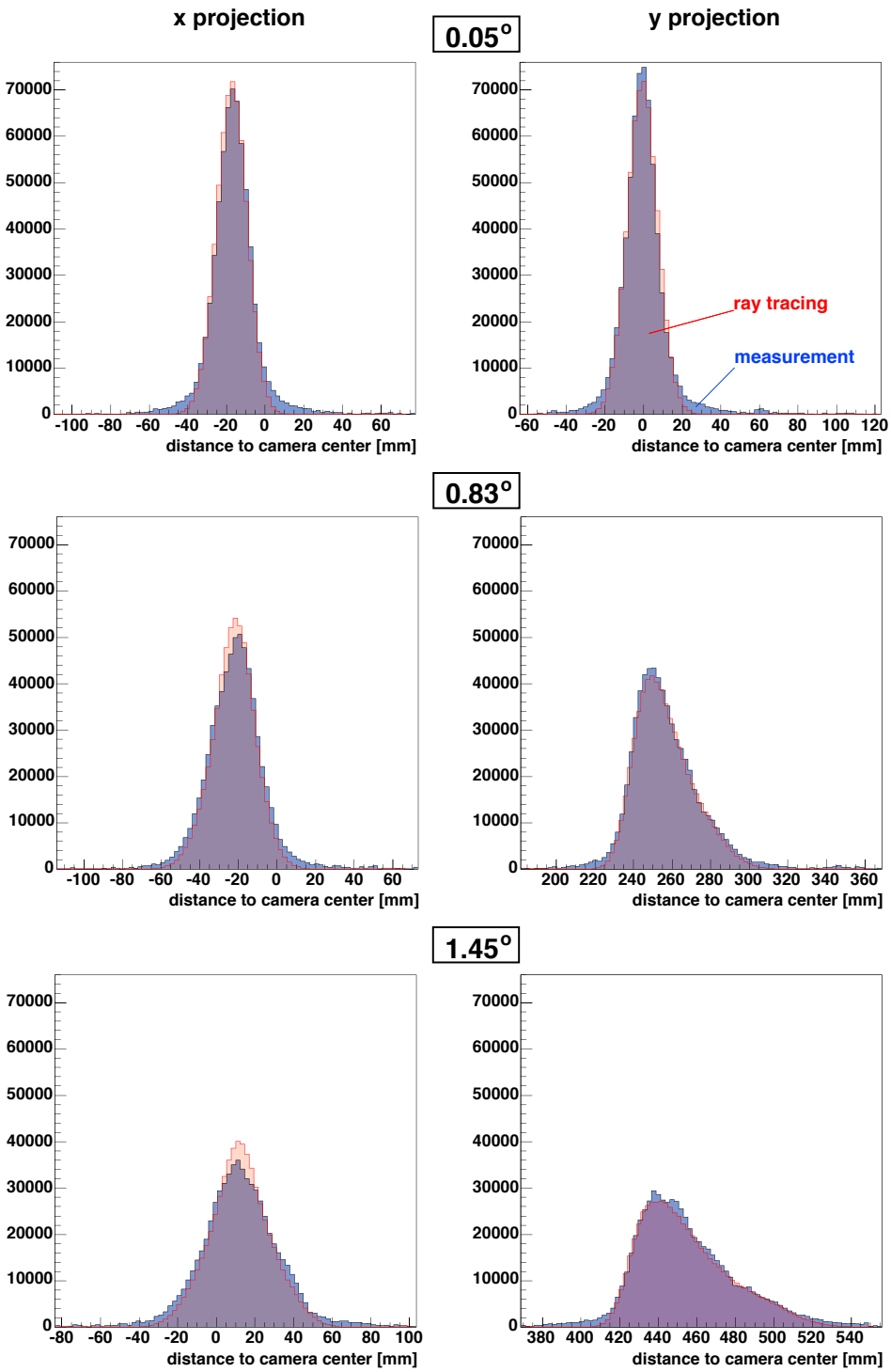

Figure 4.18: Radial and tangential projections of the PSF at different off-axis angles Θ. The blue area represents the measurement, the red overlaid area is the result of the ray-racing simulation. Comparing the on-axis view (upper plot at 0.05°), larger tails are visible for the measured PSF with respect to the simulated PSF. The simulation represents the ideal Gaussian distribution. The individual histograms are not normalised. The number of simulated photons is constant for the different off-axis angles. The simulation shows very good agreement with the real PSF. The displacement in the x projection is caused by the positioning accuracy during the measurement.

4.4 Point spread function of the telescope

The PSF is the distribution of photons from a point-like source at the focal plane of a telescope. It's FWHM defines the **angular resolution** of the telescope. In first approximation the PSF can be described by a bell-shaped distribution with $\rho(r)$ following a Gaussian distribution:

$$\rho(r) = K \cdot e^{-\frac{r^2}{2\sigma^2}} \quad \text{with} \quad r^2 = x^2 + y^2 \quad \text{and} \quad K = \left(\frac{1}{\sqrt{2\pi} \cdot \sigma}\right)^2 \tag{4.4}$$

where ρ is the event density and r the angular distance to the source position. A simple consequence of this definition is that the PSF falls with a factor $\sqrt{e} = 1.64$ at the angular distance σ from the source. Hence, the FWHM, which corresponds to a decrease of a factor 2 from the maximum, is slightly larger than σ.

Projection of the bell-shaped distribution

When projecting the bell-shaped distribution onto the x axis (equal for the y axis), one obtains again an Gaussian with σ equal to the bell-shaped distribution of equation 4.4:

$$V(x) = \int_{-\infty}^{\infty} K \cdot e^{-\frac{x^2}{2\sigma^2}} \cdot e^{-\frac{y^2}{2\sigma^2}}\, dy = K \cdot \frac{1}{2\sqrt{\pi}} \cdot e^{-\frac{x^2}{2\sigma^2}} \tag{4.5}$$

Determination of the PSF

In order to describe quantitatively the bell-shaped distribution, I derive the σ by integrating the distribution from its maximum in circles with increasing the radius r. Analytically, for a symmetric form ($\sigma_x = \sigma_y$), one transforms the equation 4.4 into polar coordinates and integrates over φ and r:

$$V(r) = \int_0^{2\pi} \int_0^{r_i} d\varphi \cdot r \cdot e^{-\frac{r^2}{2\sigma^2}}\, dr = 1 - e^{-\frac{r_i^2}{2\sigma^2}} \tag{4.6}$$

where r_i is the selected radius. It follows that 39% of the events lie below 1σ and $\sim 86\%$ of the events lie below 2σ. Note that these fractions are different than those for a one dimensional Gaussian distribution (68% and 95% respectively). The formula can now be rewritten into the form:

$$r_i = \sqrt{-2\sigma^2 \cdot \ln(1-p)} \tag{4.7}$$

where p is a quantity defining the percentage of the volume one integrates. In the following, when I talk about the PSF of the MAGIC telescope, the radius r_{80} is meant with 80% of the light content inside:

$$r_{80} = 1.794 \cdot \sigma = 1.524 \cdot \text{FWHM} \tag{4.8}$$

The PSF is one of the key parameters of a telescope, its monitoring is therefore very important. While optical telescopes have the advantage to determine the PSF from every exposure they make, the γ-ray sources observed by IACTs do not emit visible light, moreover star light is classified as disturbance for IACTs. Additionally, the telescope is not focussed to infinity during the normal data taking. Dedicated measurements need to be scheduled when the focussing of the telescope has to be measured. In case of the MAGIC telescope, these measurements are even more important since it is the first IACT equipped with an AMC system (see § 3). I will introduce in the following two methods used to determine the PSF of the telescope. The first method described in § 4.4.1 is rather direct and conventional: One analyses the distribution of the reflected light from bright stars in the camera focal plane. Since this method needs dedicated scheduling, with the consequence of reduced observation time, another method to extract the focus quality of an Cherenkov telescope was developed: One takes the advantage of the characteristic Cherenkov light images from muons triggering the telescope from time to time. I will show in § 4.4.2 that from the broadening of the muon rings the PSF of the reflector can be continuously determined from the data.

4.4.1 Measurement of the PSF with star images

The standard procedure to characterise mirrors is to quantify the reflected focal spot from a point like source. The light source needs to be placed either at twice the focus (for spherical mirrors only) or at infinity. Optical telescopes use bright stars for this purpose. This approach also became standard for IACTs, even if IACTs are usually not focussed at infinity (see § 2.1 and § 3.5). To perform a PSF measurement, a diffuse reflecting surface, e.g. white sheet of paper, is placed in the focal plane of the mirror. The optical axis of the telescope is then aligned towards the star and the reflected image on the white paper observed with a dedicated CCD camera. Such measurements need to be well prepared and scheduled. It is still common among the other IACT experiments to measure the PSF only a few times per year. However, in the case of MAGIC, the reflector is refocussed every time the observation zenith angle changed by more than $\Delta Zd \approx 10^\circ$ to compensate for the mirror dish deformations. Not only the prime focussing but also the functionality of the AMC therefore influence the optical performance.

The method to measure the PSF is standardised in MAGIC. The SBIG CCD camera and a fixed reflecting target on the camera lid allow to perform such measurements within a few minutes. The procedure is the following:

1. Choose a random star and align the telescope towards its direction.
2. Focus the mirrors accordingly to the standard procedure, either with lasers or LUTs (see § 3.5).
3. Open the upper MAGIC camera lid. The white spectralon plate mounted on the lower camera lid becomes visible (see figure 4.11). The Spectralon plate is mounted at the position where light from a point-like source at infinity is focussed best.
4. Record the reflected spot with the SBIG camera. The exposure time needs to be adjusted according to the star brightness.

The high sensitivity and large dynamic range of the SBIG camera provide a good signal/noise ratio for stars with magnitudes up to four. Stars with these brightness can be found at almost any sky position and the measurement is therefore possible at any time and

zenith angle range. The measurements are regularly scheduled during moon time, in parallel to the *TPoint* measurements, which are required to calibrate the telescope local coordinates, or on request. Figure 4.12 shows a typical image from the SBIG camera during the PSF measurement.

Images taken with the camera are processed off-line with ROOT routines following the steps outlined below:

1. Readout noise and hot pixels are removed by subtracting the so called *dark frame*: It is a dedicated exposure with closed CCD camera shutter.

2. Depending on the sky region and star brightness, usually no other bright stars are in the FOV of the camera. The main background contribution results then from the LONS. Since LONS is statistically distributed, it can be removed by analysing the analog digital converter (ADC) count levels close to the reflected spot. The background is removed by fitting a Gaussian to the height levels and subtracting the mean plus 3σ of the fit, as it is shown in the left bottom plot of figure 4.19.

3. In the final step, the spot maximum is calculated from the x and y projections. The ACD counts are integrated in circles around the spot maximum, by increasing the radius. The bottom right figure shows the result. The radius containing 80% of the total counts corresponds to r_{80}.

Attempts to fit a bell-shaped distribution from equation 4.4 to the reflected image were done. However, the method described here accounts better for the larger tail caused by aberrations or misaligned mirrors. The accuracy of this method is better than the fit.

Figure 4.19 shows the processed PSF image as described above. The corresponding PSF results are highlighted in the table 4.4. For conversion between the units[8] see equation 4.8.

	mm	**deg**	**mrad**
r_{80}	21.2 ± 1.5	0.070 ± 0.005	1.23 ± 0.09
σ	11.8 ± 0.8	0.039 ± 0.003	0.69 ± 0.05
FWHM	13.9 ± 1.0	0.046 ± 0.003	0.81 ± 0.06

Table 4.4: Results from the PSF measurement with the SBIG camera.

Figure 4.20 shows results from the PSF measurements performed over the last 1/2 year. The red points correspond to laser focussing and blue to LUT focussing. The period shown in the figure covers two new readjustments of the panels. The first Roque lamp re-focussing was done in September 2005, indicated by the significant improvement of the PSF between the first two data points. The second attempt to improve the PSF followed in April 2006, however, with only small improvement. This is mainly due to an interruption of the focussing procedure because of bad weather conditions. Results from the following star adjustment (which brought the spot quality again to its best performance of $\sigma = 0.025\,\mathrm{deg}$), are not included in the diagram.

The degradation of the PSF after laser adjustment (indicated with the red line) is the reason why in the past frequent refocussing of the whole telescope was necessary. The optical quality of the focussed spot degraded within $\sim 1/2$ year from 0.025° to 0.050°, by a factor of two. Extensive search for the reasons of the instability were traced back to the laser modules.

[8] $1\,\mathrm{mrad} = 0.0573^\circ = 17.19\,\mathrm{mm}$ in the camera plane.

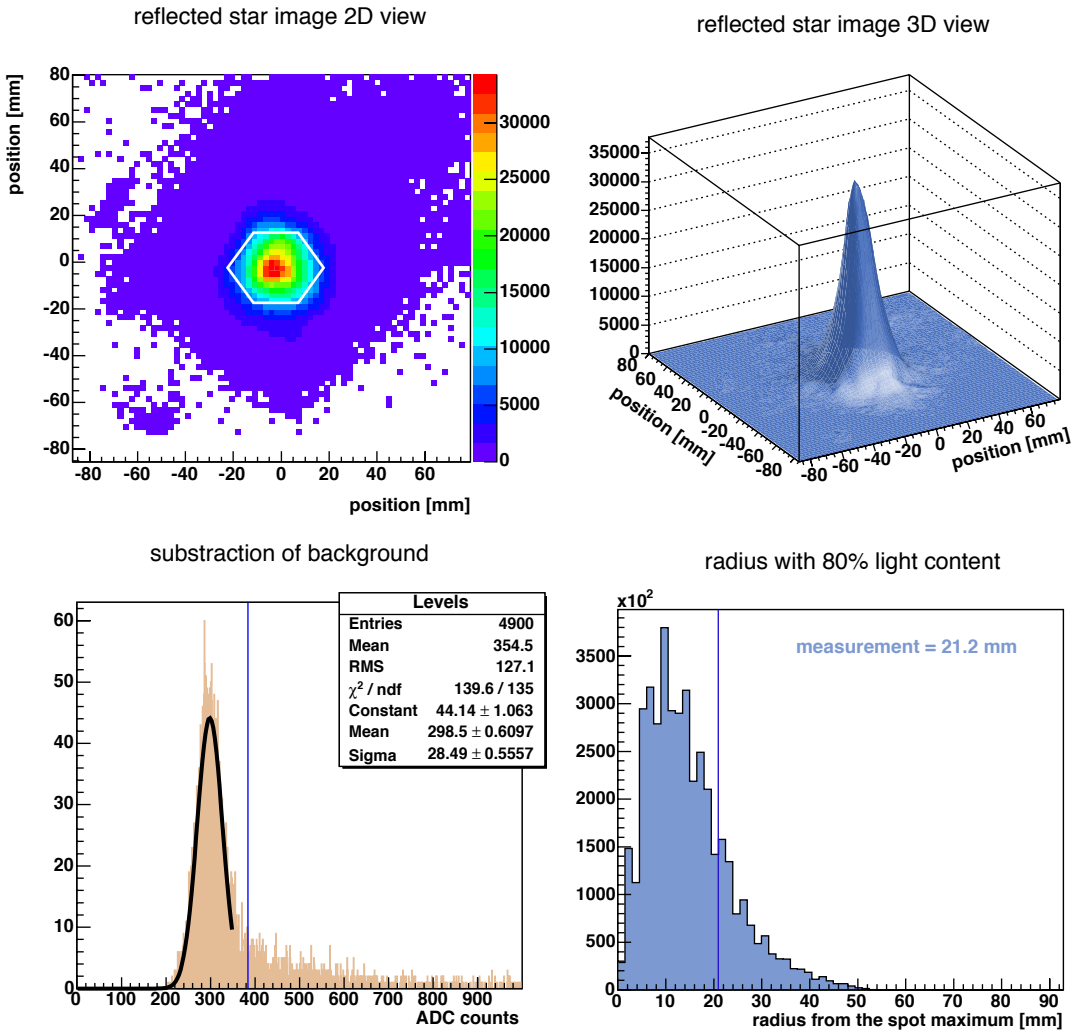

Figure 4.19: Analysis results of a reflected star image recorded with the SBIG camera. The upper two plots show the reflected star image at the spectralon plate. The size of the inner MAGIC camera pixel is shown for comparison. The LONS background was subtracted from the mean plus 3σ of the fitted Gaussian to the ADC count levels, as shown in the bottom left graph. The resulting radius with 80% of the light content is shown in the bottom right histogram.

Most probably local tensions and weather changes influence the fixation of the module together with the panel. Tests with a sample of laser modules are currently ongoing (see § 3.5.3). In the meanwhile the standard focussing procedure of the MAGIC telescope has changed. LUTs, which were implemented in the beginning only for the GRB manoeuvre, have also become standard during normal observations. The results from the LUT focussing are shown as blue points in the diagram on the next page. This method provides considerably better stability, even when telescope dish deformations, caused by temperature gradients, affect directly the quality of the focussing in this mode, as seen from the periodic evolution of the data points.

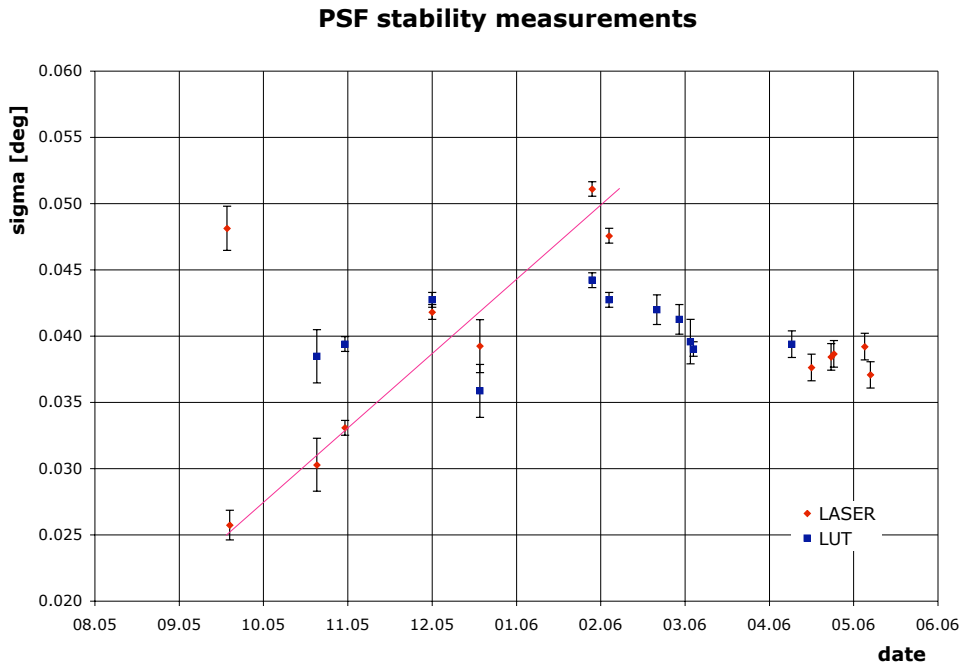

Figure 4.20: Long term behaviour of the PSF measured with the SBIG camera. The PSF obtained with laser focussing (red points) and LUT focussing (blue points) is shown. The red line indicates the degradation of the laser focussing with the time. The PSF achieved with LUT focussing is considerably more stable in this time period.

4.4.2 PSF measurements using muon shower images

Cherenkov light from muons generated in hadronic showers counts as background for IACTs. Their integral flux above 6 GeV is expected to $17.9\,\mathrm{m^{-2}s^{-1}sr^{-1}}$ [135], which corresponds to a rate of $\sim$ 4 Hz for muons hitting the reflector with an inclination angle $\leqslant 1°$. The actually measured rate of muon counts, without confusion of additional shower light, is lower by a factor three because of different selection criteria and the possibility of coincidence with electromagnetic showers. Two important telescope parameters can be derived with a dedicated analysis of the signal captured from muons: The total **photon detection efficiency** of the entire telescope and the **PSF**. Moreover, the muon rate as such reflects the atmospheric conditions.

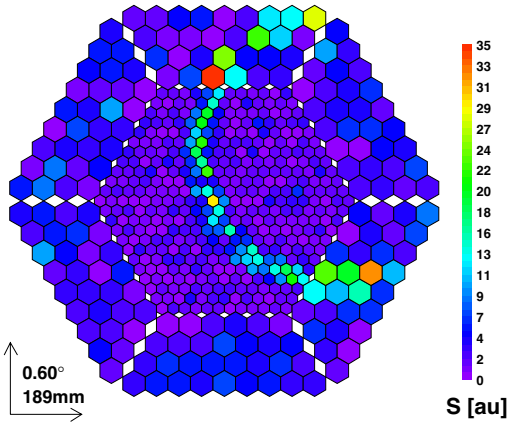

Figure 4.21: Example of a muon shower ring mapped in the MAGIC telescope camera.

Isolated muons passing close to the mirror give characteristics Cherenkov light ring section images in the camera and can be easily reconstructed, as shown in figure 4.21. The parametrisation of the images is based on the **RICH**-technique [136], commonly used in accelerator experiments. From the geometry of the image and the number of Cherenkov photons, emit-

ted per unit path length and unit wavelength interval, follows the number of photo-electrons $N_{\text{ph.e.}}$ collected per unit azimuth angle $d\phi$ in the focal plane [137]:

$$\frac{dN_{\text{ph.e.}}}{d\phi} = \frac{\alpha\, I}{2} \cdot \sin(2\,\theta_c) \cdot D(\phi) \tag{4.9}$$

with :

$$I = \int_{\lambda_1}^{\lambda^2} \frac{\epsilon(\lambda)}{\lambda^2}\, d\lambda$$

$$D(\phi) = R\left[\sqrt{1-(\rho/R^2)\sin^2\phi} + (\rho/R)\cos\phi\right] \qquad (\rho/R \leq 1)$$

where α is the fine structure constant, θ_c the Cherenkov angle, $\epsilon(\lambda)$ the photon detection efficiency, ρ the impact parameter of the muon and R the radius of the mirror.

From the muon ring radius, the impact parameter ρ can be reconstructed, while the integrated photon detection efficiency is estimated by comparison of the photo-electron intensity $dN_{\text{ph.e.}}/d\phi$ along the ring with MC simulated muons.

There are physical and technical reasons, which lead to the broadening of muon rings. Physical reasons are deviations of the ideal parallel Cherenkov radiation due to intrinsic broadening of the hadronic shower caused by:

- Changes in the refractive index with altitude and wavelength. The relative broadening decreases with higher muon energy E_μ and reaches $\sim 1\%$ at the minimum.
- Multiple scattering of the muons along their path and effects of the Earth magnetic field. The statistical broadening in the camera plane has an impact of $\sim 8\%$ for $E_\mu \sim 10\,\text{GeV}$ and decrease rapidly with increasing energy.
- Ionization losses along the muon path in the atmosphere. The decreasing Cherenkov angle due to the ionization causes a broadening of the muon ring by $\sim 1\%$.

The technical reasons are telescope-dependent and can be classified into four contributions:

- The camera pixel size and the ring dimensions. The smaller the pixel size in the central part of the MAGIC camera, the better the image parameters can be determined. The estimated contribution of a full ring is $\sim 0.5\%$.
- Aberration effects, especially the coma aberration for Cherenkov light from muons with large impact parameters.
- Focussing of the reflector to 10 km distance. The Cherenkov light from the short muon flashes is emitted along the path of the primary hadron. The focussing to 10 km blurs the image of the muon ring.
- The quality of the telescope focus. The PSF has a linear dependence on the broadening of muon rings.

Comparing the relative ring broadening of muons, extracted from observational data, with simulated Cherenkov light showers from muons, reflected at mirrors under different PSF, allows to trace back the actual PSF of the reflector. The precision of this method is in the range of ±10% [138]. Figure 4.22 shows the results from this analysis. In parallel to the measurement of the PSF with the SBIG camera, shown in the previous chapter, the muon analysis also shows an improvement of the PSF in October 2005. The advantage of this method is the continuous data set. The described analysis is implemented into the standard calibration process of the MAGIC telescope data. Quality checks of the telescope optics during data taking are therefore available to some extent.

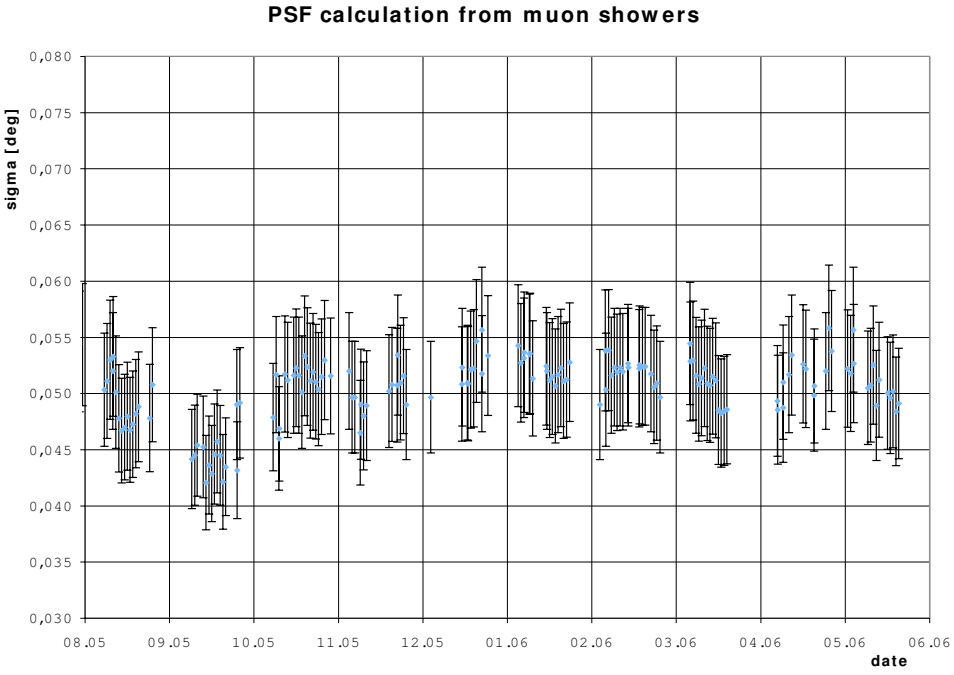

Figure 4.22: Long term behaviour of the PSF determined with the broadening of the muon ring images extracted from the data of the MAGIC telescope. Each point represents the averaged PSF from the complete data sample of one night. The error bars represent the ±10% systematical and statistical error of the measurement. Gaps in the data set represent the moon periods, as well as bad weather conditions.

4.5 Measurement of the mirror reflectivity

The mirror reflectivity is an another important parameter of the performance of an IACT. It has a direct impact on the absolute scale of the measured energy, as well as on the reconstructed flux of γ-rays from observed sources. In addition, the mirror reflectivity plays a key role in the determination of the energy threshold of an IACT. The latter is inversely proportional to the product of mirror reflectivity $\times$ mirror area [139].

4.5.1 Overall telescope mirror reflectivity

We have developed a simple method to measure the reflectivity of the telescope reflector [130]. While it is relatively easy to measure the reflectivity of the mirror material locally, it is not so straightforward to measure the amount of light focussed onto a given spot. The method is based on the use of the SBIG camera, able to see simultaneously part of the telescope's focal plane and the sky region along the optical axis. The reflectivity measurement can be done in parallel with the PSF measurement, by pointing the telescope to a star. The ratio of the integrated scattered starlight from the Spectralon plate $I_{\text{reflected}}$ to the integrated direct star spot I_{direct} provides a precise result of the product of mirror reflectivity $\times$ mirror area. It is given by the formula:

$$R_{\text{mirror}} \times A_{\text{mirror}} = \frac{I_{\text{reflected}}}{I_{\text{direct}}} \cdot \frac{\pi \cdot d^2}{\cos\alpha} \cdot \frac{1}{R_{\text{diffuser}}} \tag{4.10}$$

where $I_{\text{reflected/direct}}$ are the luminositys integrated in ADC counts from the CCD image, R_{diffuser} is the reflectivity of the plate placed in the focal plane, α is the angle between the normal of the plate and the line connecting the CCD lens and d the distance between the plate and the camera lens.

Formula 4.10 depends strongly on the diffuser reflectivity and reflection characteristics. In our case a self made plate composed of polytetrafluorethylene (PTFE) was used. The PTFE powder is pressed in a form with 525 kPa and sintered at 375° C [140]. The material has equal characteristics like Spectralon[9], with reflectivities higher then 99% for wavelengths from 400 nm to 1500 nm and an almost perfect Lambertian surface, scattering the light with a cosine intensity relationship $I(\alpha) = I(0) \cdot \cos\alpha$, where α is the incidence angle from the surface normal and $I(0)$ the incoming light intensity. Spectralon is used as a reference standard in many optical applications.

Before integrating the ADC counts from the reflected and direct spot, the pedestal has to be subtracted. This is done in analogy to the procedure described in § 4.4.1, by fitting a Gaussian to the statistically distributed background and subtracting the mean from all CCD pixels. The integral is then calculated by summing-up all pixels with charge $\geqslant$ mean $+ 3\sigma$. Figure 4.23 shows the direct star image (left) and the reflected spot at the Spectralon plate (right) of a second magnitude star with 10 s exposure time. The CCD camera lens is focussed at the 17 m distant Spectralon plate so that the star image at infinity is smeared out. This avoids saturation and in turn allows longer exposure times and therefore better signal/noise ratios. The quantities $\alpha = 4.69 \pm 0.03°$, $d = 17045 \pm 3$mm and $R_{\text{diffuser}} = 98 \pm 1\%$ were measured at the instrumental setup. The effective mirror area of $A_{\text{mirror}} = 230\,\text{m}^2$, accounted for 2.5% shadowed part due to the camera bowl, wires and the PMT camera can be assumed in the best case. One needs certain knowledge of the AMC performance to qualify the number

[9] `http://www.labsphere.com`

of panels whose spot is not contained in the overall focus (defocused or panels out of use). The preliminary effective reflectivity values R_{eff} were obtained from dedicated measurements, as shown in table 4.5. The optical filters[10] (see figure 4.24) mounted inside the camera filter reel, allow to quantify the differential reflectivities for the four optical bands.

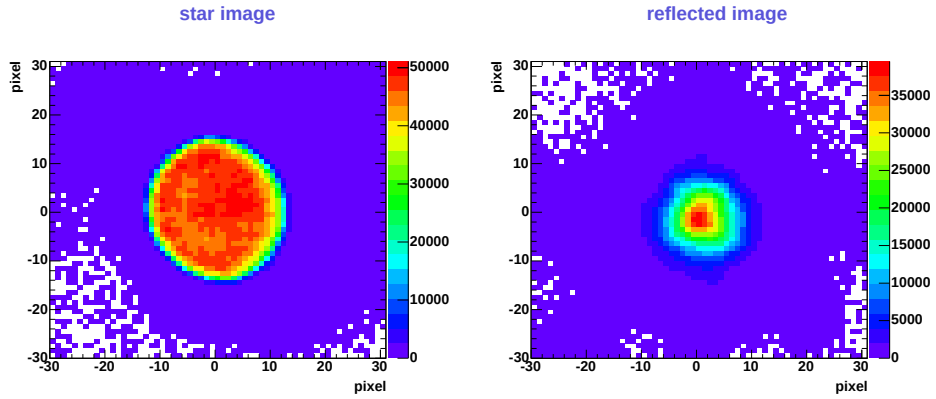

Figure 4.23: Examples of reflectivity measurements performed with the SBIG camera. *Left:* Direct star. *Right:* Reflected spot at the Spectralon plate. Due to the high dynamic range of the camera the star image is still not saturated (16 bits$\hat{=}$65536).

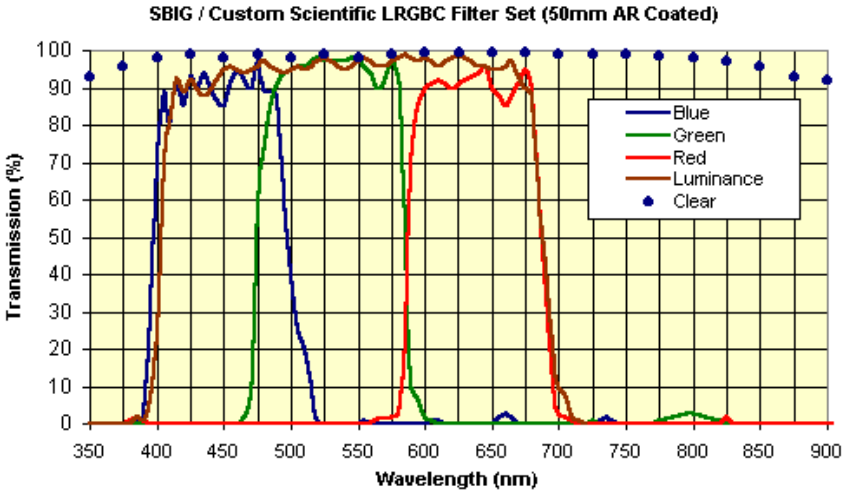

Figure 4.24: Transmission characteristics of the five optical filters mounted in the filter reel of the SBIG camera.

As mentioned before, the reflector reflectivity can be obtained from images taken during the PSF measurement, as long as the direct star image is not saturated. Figure 4.25 shows the reflectivity results for the last 1/2 year. Since the effective mirror area is required in formula 4.10, values of A_{mirror} are also shown in the plot. The number of focussed panels is extracted from the AMC system log files. The reflectivity does not show a significant degradation over the last 1/2 year. However, longer measurement periods are necessary to average variations due to dust deposits on the mirror surface.

[10] `http://www.sbig.com`

filter	wavelength λ [nm]	Reflectivity [%]	
		Alphecca	Dubhe
clear	–	80.4	80.5
luminance	380 – 700	82.5	85.2
blue	380 – 520	81.0	82.1
green	430 – 580	84.3	84.7
red	580 – 700	81.0	81.8

Table 4.5: Results for the effective reflectivity R_{eff} of the MAGIC reflector obtained from the SBIG image analysis from two stars Alphecca (2.23 mag) and Dubhe (1.79 mag). The error on the measurement is ±2%.

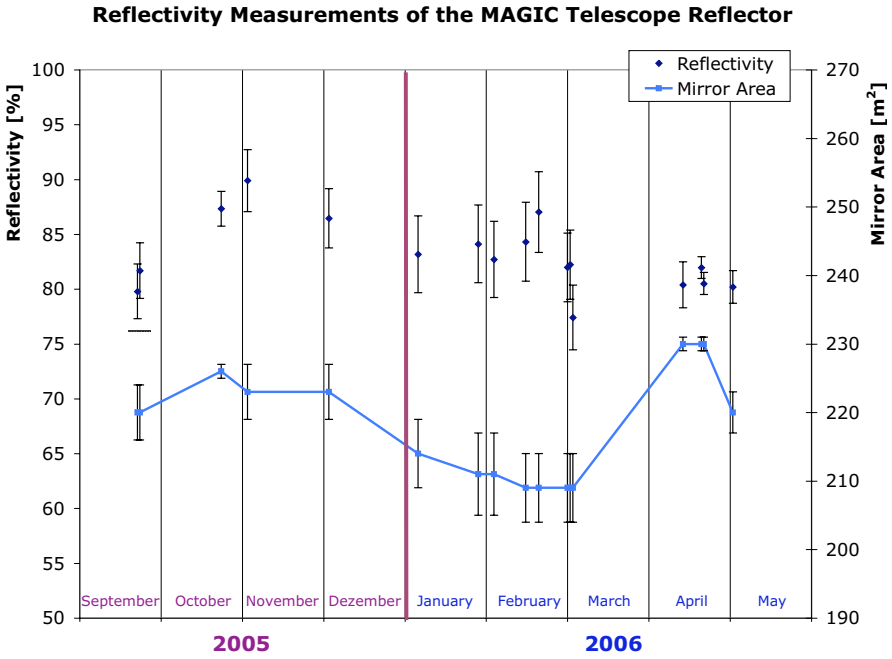

Figure 4.25: Reflectivity of the MAGIC telescope mirror during the last 1/2 year. The corresponding effective mirror area A_{mirror} required for the reflectivity calculation is shown in addition. The errors on A_{mirror} result from the performance of the AMC and represent the number of uncontrolled panels.

To crosscheck the method an independent measurement of R_{mirror} using a tungsten lamp located at ~ 1 km distance from the telescope was done. The uniform distributed light arriving to the telescope with the one being focused onto the Spectralon plate was compared. The former was measured by a large (9 cm^2) PIN diode, whereas the latter was measured by means of a matrix of 19 small (1 cm^2) PIN diodes located at the overall mirror focus. The value of R_{mirror} obtained with this method was in good agreement with the one determined from the SBIG image analyse.

4.6 Relative mirror reflectivity of individual panels

During the focussing with the Roque lamp, images of individual panels with the SBIG camera are stored. The individual spot images of each panel are shown in figure 4.15. In addition to the light distribution the relative mirror reflectivity of each panel can also be extracted from these images. Since the direct image of the lamp is saturated, only the relative mirror reflectivity – normalised to the panel with the highest integral – could be calculated. The histogram on the left hand side of figure 4.26 shows the integrated light content for the individual panels. The following corrections were applied:

- Panels assembled with three mirrors instead of four (panels at the four inclined edges of the telescope dish, as well as a few panels close to the elevation axis) are multiplied by the factor $b_{\text{mirror}} = 1.33$.
- Due to the parabolic shape of the reflector dish, panels distant from the center are inclined to the parallel beam of light. The reduced mirror area is dependent on the distance r to the dish center and the focal length $f = 17.0\,\text{m}$. This effect is corrected by multiplying with the following factor:

$$b_{\text{area}} = \frac{\sqrt{(\frac{r}{2})^2 + f^2}}{f}$$

It should be noted that the Munich design mirrors, allocated in the central part of the telescope dish, are made of AlMgSi 0.5 alloy. The outer region of the mirror area is assembled with the Padua design mirrors, made of AlMgSi 1.0 alloy. The different materials have different hardness and result due to the machining procedure in different reflectivities. This fact results in a higher overall reflectivity for the Munich design mirrors in the central part.

The histograms in the center and on the right show the profile along the telescope dish in horizontal and vertical directions. The shadowing from the camera bowl and the PMT camera itself is clearly visible in the horizontal projection and in the pattern on the left panel.

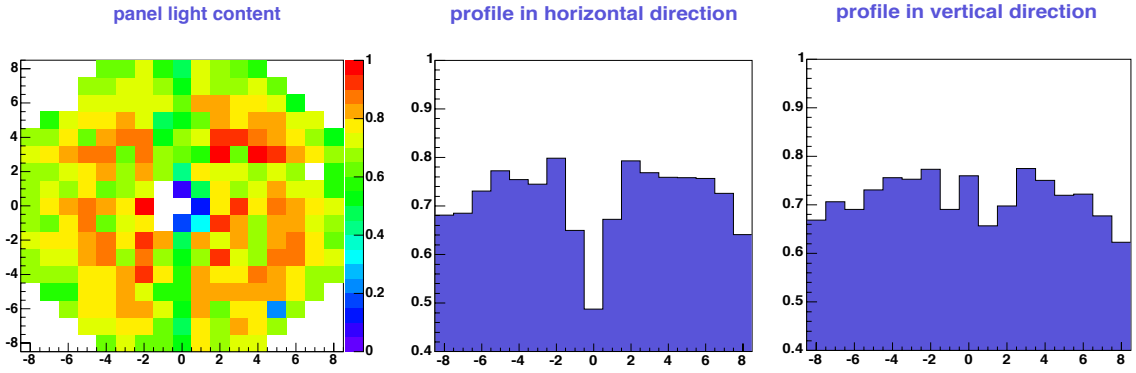

Figure 4.26: Relative mirror reflectivity of individual panels. The integrated light content of each individual panel (left) is normalised to the highest value. The central panels in the horizontal projection and the panels in the mirror dish center are partially shadowed by the camera bowl and the PMT camera itself. The central and right figures show the profile along the horizontal and vertical directions of the telescope dish.

Chapter 5

Analysis of the MAGIC telescope data

The following chapter gives an overview of the main analysis concepts developed to handle the data taken with the MAGIC telescope. There are three modes, in which IACTs are operating: The ON, the OFF and the WOBBLE data mode. **ON data** are collected when the telescope is pointing directly at the presumed source. **OFF data** are taken at a sky position of similar zenith angle, observational conditions and averaged star light intensity as the ON data. In case of **WOBBLE data** the telescope is pointing $\pm 0.4^{\circ}$ off the presumed source, alternating the offset at fixed time intervals. With steady, point-like sources and a assigned total amount of observation time, this mode yields higher sensitivities since no time is lost to take dedicated OFF data. Because of the dead time introduced when changing between the WOBBLE positions and the overall higher sensitivity when the telescope is pointing directly at the source, GRB observations are made normally in the ON mode. Given the lack of a strong γ-ray calibration source, ON and WOBBLE data analyses need dedicated MC simulated γ-ray showers; The analysis chains differ therefore dependent on the used mode. This chapter concentrates on the ON/OFF data analysis as it was applied to the GRB sample presented in this thesis.

5.1 Format and classification of the data

During telescope operation four types of raw data (so-called runs) are recorded:

Pedestal run: Contains 1000 randomly triggered events. The data are used to calculate the pedestal offsets and the LONS pedestal fluctuations for a given sky position and observational conditions during the calibration.

Calibration run: Contains usually 4000 events, taken with standard calibration light pulses from 10 UV LEDs, triggered by the calibration system. The data are used to calculate the conversion factors from extracted signals to photo-electrons, the arrival time offsets of the PMTs and for flatfielding of the camera.

Data run: Contains $\sim$ 50000 events taken from the sky direction of the source under study. The evens are triggered with the level-1 majority trigger, which requires four neighbouring channels to exceed a pre-set discriminator threshold (DT). The DT depends on the LONS and is adjusted accordingly. Galactic sources are typically observed with

25% higher DT than extragalactic sources (the sky is brighter in the galactic plane). Usually the data runs contain also *interlaced calibration events* taken at 50 Hz and used to update the slowly varying conversion factors due to the drift of the VCSELs.

Subsystem information: Essential information from the different subsystems of the telescope (central control, drive, camera, amc, starguider) are recorded every few seconds and are later added to the data stream.

When a trigger occurs, the amplified, transmitted and shaped signal of each PMT is stored in the raw data. The 300 MHz Flash Analog-Digital-Converter (FADC) system samples the signal into 30 slices, where the last 15 slices may be the same signal like as in the first 15 slices, although the amplitudes are divided by factor 10 and delayed by 55 s. This occurs only if the signal exceeds a preset threshold. Otherwise the large tail of FADC slices behind the triggered event contain only LONS noise and is used to update the pedestal parameters.

The **signal extractor** calculates the charges and arrival times from the slice contents. Different methods to extract the information from the FADC slices are used:

Fixed time window extractor: This extractor sums up the pedestal subtracted FADC slice contents for a fixed range of consecutive slices. The summation window has to be chosen to be wide enough to cover the complete pulse including some time jitter. The time jitter is caused by the trigger, more precisely by the discriminator-firing of the fourth pixel of the trigger criteria. This simple extractor is not able to retrieve the arrival time of the pulse.

Sliding window extractor: The extracted signal is the maximum one of possible contents of n consecutive FADC slices. The position of the signal is not fixed and can change from pixel to pixel and from event to event, depending on the arrival time of the Cherenkov light in different regions of the camera. The number of integrated slices can be chosen and represents the width of the time window, over which the signal is integrated. The sliding window does not include any assumptions of the expected pulse shape. The variance of its reconstructed signal is dominated by noise and the FADC digitisation jitter. Small signals are hardly distinguishable from background fluctuations.

Digital filter extractor: This extractor improves the previous one by fitting a standard pulse shape to the signal. The form can be determined from test signals obtained with pulse generator and fed through the same transmission and amplification chain. In this way, the effect of possible noise contamination on the extracted signal is strongly reduced.

The digital filter method is used as standard signal extraction algorithm in the MAGIC experiment [141].

The raw binary data from the data acquisition (DAQ) system is converted to the *MAGIC Analysis and Reconstruction Software* (MARS) format with the *MERging and PreProcessing* (merpp) tool. Additional information from subsystems like the telescope position from the drive system, the mispointing from the starguider, the FADC currents from the camera system, etc. are added to the data during this process.

The MARS [142] is a ROOT [143] based collection of C++ classes and macros. It is a combination of classes and executables, dedicated to the MAGIC telescope data analysis, developed by members of the collaboration.

Figure 5.1 shows the general flow chart of the standard analysis chain. The individual analysis steps will be described in the subsequent chapters.

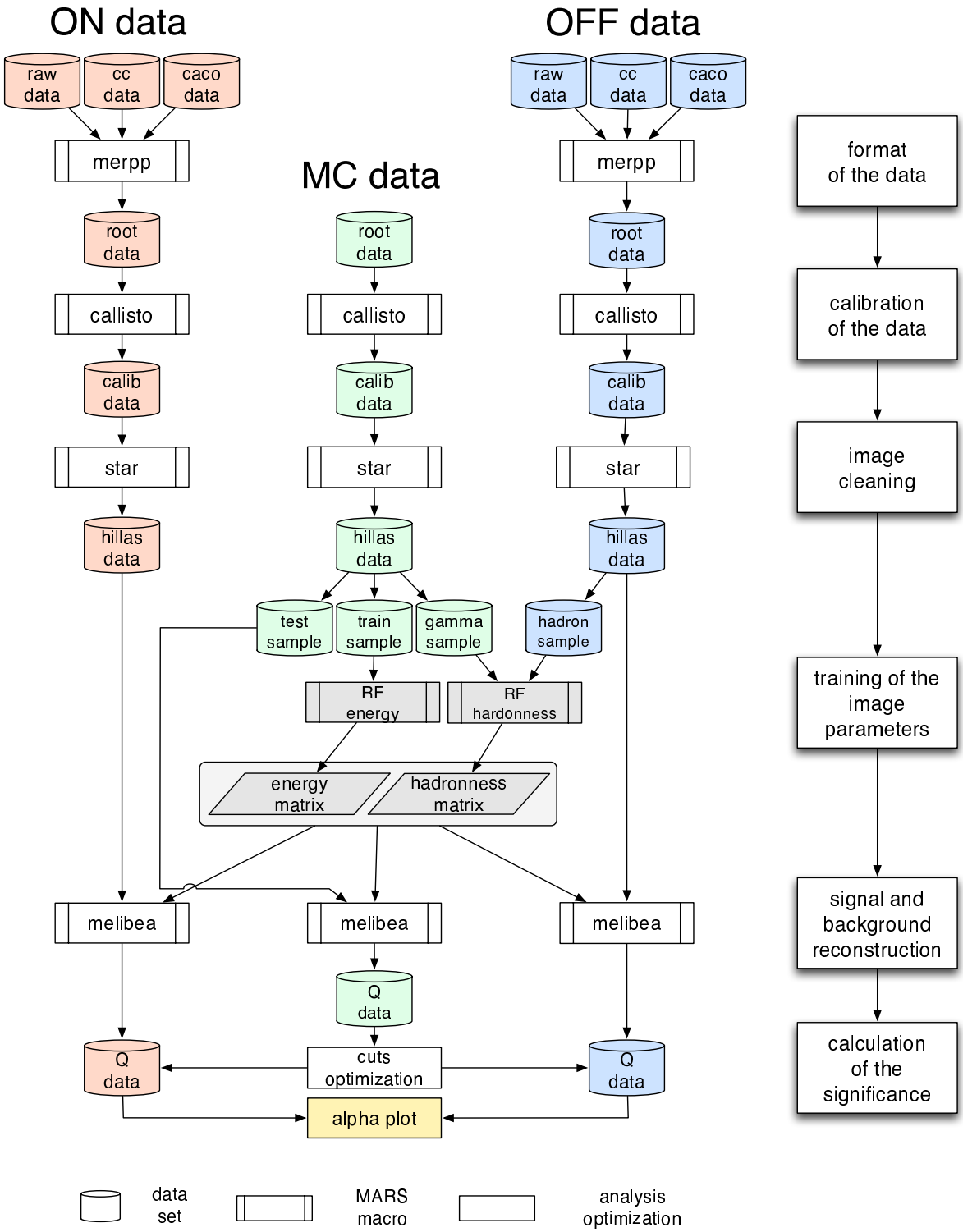

Figure 5.1: Data flow chart of the standard analysis chain of MARS.

5.2 Calibration of the PMT signal

The initial Cherenkov signal (number of photons) is eventually converted into a digital number of ADC counts per pixel. This conversion is a multistep process affected by a number of detector parameters (discriminator threshold, losses of jitter photons, the quantum efficiency, etc.). As not all of these parameters are well known one normally calibrates the telescope up to the digital output by signals of known quantity such as by light pulses of known number of emitted photons or electrical signals of known number of electrons. As the telescope detects optical light flashes, the standard calibration is a fast light-pulser of known spectra and intensity. In detail, the calibration system of the MAGIC telescope [129] is composed of the following components:

1. Pulser box with pulsed LEDs providing ultra fast light pulses in three different colours with externally controllable intensities, which can by varied by factor > 300. This allows to calibrate the whole dynamic range of the camera and the readout chain.

2. Continuous light sources in four different colours and adjustable intensities. In this mode star and moon light can be simulated.

3. Three blind pixels distributed along the circumference of the MAGIC camera. They are used to determine the absolute light flux by means of the single photo-electron counting method.

4. Calibrated PIN diode placed on one meter distance from the calibration box. This device helps to measure the absolute light flux by cross calibration of the optical signal against the signal of a low energy γ-line from a radioactive source.

Figure 5.2 shows a schematic view of the calibration system. The integrated signal, recorded in FADC counts, has to be converted to number of photons that hit the PMT. This is done in the calibration process. The *CALibrate LIght Signals and Time Offset* (callisto) program determines the conversion factors from the extracted signal to equivalent photo-electrons and the arrival time offsets. The program incorporates a series of checks to exclude malfunctioning PMTs (about $1-2\%$ under normal conditions). The signals of the excluded PMTs are later replaced by the mean signal of its direct neighbours. From a large sample of signals from the test pulses the number of photo-electrons $N_{\text{ph.e.}}$ is calculated using the excess-noise factor method, also called **F-factor method**[1] [144]:

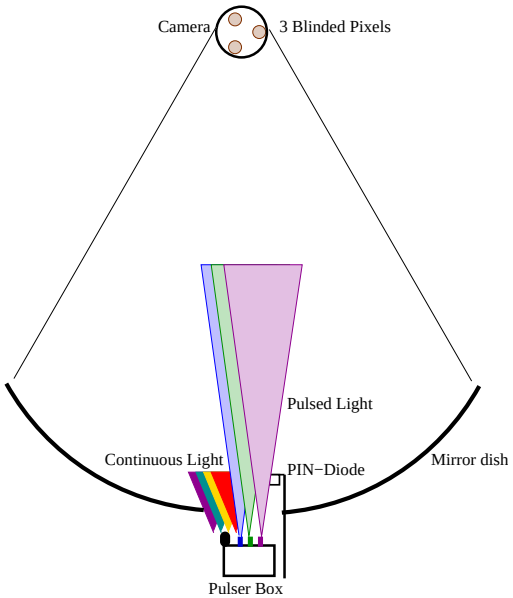

Figure 5.2: Schematic view of the calibration system of the MAGIC telescope. Figure from [129].

$$N_{\text{ph.e.}} = \frac{\langle Q \rangle^2}{\sigma^2} \cdot F^2 \tag{5.1}$$

[1] This method assumes that the dominant signal fluctuations are caused by the PMT photo-electron collection efficiency and gain fluctuations.

where F is a quantity representing the specific excess noise of the PMT, $\langle Q \rangle$ is the mean pedestal subtracted charge of the PMT (in FADC counts), and σ^2 is the reduced variance, calculated from the charge distribution and corrected for the contribution of the pedestal variance: $\sigma^2 = \sigma^2_{\langle Q \rangle} - \sigma^2_{\text{ped}}$. Finally the conversion factor $c.f.$ is obtained:

$$c.f. = \frac{\langle N_{\text{ph.e.}} \rangle}{\langle Q \rangle} = \frac{\langle Q \rangle}{\sigma^2} \cdot F^2 \tag{5.2}$$

where $\langle N_{\text{ph.e.}} \rangle$ is the average number of photo-electrons in the inner camera. For pixels of the outer camera $\langle N_{\text{ph.e.}} \rangle$ gets multiplied with the ratio of light sensitive areas, which is exactly four in our case (outer ring pixels have 0.2°Ø, while inner segment pixels have 0.1°Ø).

The conversion factor is composed of three values: The quantum efficiency (QE)[2] of each PMT, the photo-electron collection efficiency and the PMT gain. The gain of the PMT depends on the applied high voltage and varies with temperature and time. The QE estimates for MAGIC have shown that on average 18% of the initial Cherenkov photons (integrated between $300 - 650\,\text{nm}$) reaching the PMT cathodes of inner pixels are converted into photo-electrons.

The calibration of the GRB data is slightly different from the standard calibration. In order to reduce the time gap between the alert and data taking, no pedestal and calibration runs are taken at the beginning. Instead of extracting the parameters from the dedicated calibration runs, interlaced calibration events from the last data run of the previous source are used. The interlaced calibration light pulses can be extracted from the data files and allow to track possible gain drifts of PMTs and VCSELs. After every 10 s the conversion factors are updated, based on the results of 500 interlaced calibration pulses of the GRB data set.

5.3 Image cleaning

The next analysis step after calibration is the image cleaning, performed by the MARS executable `star`. The image cleaning removes pixels, which apparently do not form part of the shower image. Clever algorithms are needed to classify those pixels and ensure that the vast majority of the images are not affected by noise. Two algorithms have been used for the analysis of the GRB data. The **absolute cleaning** algorithm, which is used as standard method and the **time cleaning** algorithm, which uses in addition the time information. The later one promise improved reconstruction of shower images from low energy events.

Absolute image cleaning: The absolute image cleaning uses a fixed threshold on the number of reconstructed photo-electrons $N_{\text{ph.e.}}$ with reference values N_1 and N_2. Pixels, which exceeds the threshold N_1 are classified as *core* pixels and compose the main part of the shower. To pick up shower tails, neighbouring pixels with lower threshold N_2 are included in the second step. These pixels are called *boundary* pixels. This selection algorithm is simple and robust, if high enough threshold values are used. However, it significantly increases the analysis energy threshold. It is not strongly affected by different levels of LONS, whenever the levels N_1 and N_2 are higher than typical values of the pedestal RMS, e.g. $> 3 \cdot \text{RMS}$, respectively $> 1.5 \cdot \text{RMS}$. Reference values of $N_1 = 10$ and $N_2 = 5$ photo-electrons were chosen for the standard analysis. For the dedicated low energy analysis presented in § 6.1, reduced values of $N_1 = 7$ and $N_2 = 4$ were tested.

[2] The QE × collection efficiency is the ratio of photons converted to photo-electrons by the photo-cathode and focussed to the surface of the first dynode.

Time image cleaning: This algorithm is based on the available time information for each PMT channel. Shower images are reconstructed using the pulse peak arrival times δt, derived from neighbouring pixels compared to the mean shower arrival time T_{mean}. The maximally allowed time difference $\delta t^{\mathrm{max}} = T_{\mathrm{peak}} - T_{\mathrm{mean}}$ is fixed to 0.7 FADC slices (2.3 ns), which reflects the time resolution of the digital filter below five photo-electrons and additional spread of 500 ps due to the chess board structure of the mirror staggering (see § 4.1.4). The maximally allowed time offset δt_{max} of one channel to the mean shower time is fixed to 1.5 FADC slices (5.0 ns).

The comparison of both image cleanings is shown in § 6.1, by comparing the sensitivities of the analysis chain close to the threshold energy of the telescope.

5.4 Reconstruction of the image parameters

The parametrisation of the shower image composed of N pixels, which survived the image cleaning, is done in terms of the zeroth, the first, the second and the third moments of the image, called **Hillas parameters** [145].

In order to calculate these parameters, the weighted first and second moments are defined:

$$\langle x \rangle = \frac{\sum_{\mathrm{i}=0}^{N} x_{\mathrm{i}} w_{\mathrm{i}}}{\sum_{\mathrm{i}=0}^{N} w_{\mathrm{i}}} \qquad \langle y \rangle = \frac{\sum_{\mathrm{i}=0}^{N} y_{\mathrm{i}} w_{\mathrm{i}}}{\sum_{\mathrm{i}=0}^{N} w_{\mathrm{i}}}$$

$$\langle x^2 \rangle = \frac{\sum_{\mathrm{i}=0}^{N} x_{\mathrm{i}}^2 w_{\mathrm{i}}}{\sum_{\mathrm{i}=0}^{N} w_{\mathrm{i}}} \qquad \langle y^2 \rangle = \frac{\sum_{\mathrm{i}=0}^{N} y_{\mathrm{i}}^2 w_{\mathrm{i}}}{\sum_{\mathrm{i}=0}^{N} w_{\mathrm{i}}}$$

$$\langle xy \rangle = \frac{\sum_{\mathrm{i}=0}^{N} x_{\mathrm{i}} y_{\mathrm{i}} w_{\mathrm{i}}}{\sum_{\mathrm{i}=0}^{N} w_{\mathrm{i}}} \qquad w_{\mathrm{i}} = \frac{N_{\mathrm{i}}}{\sum_{\mathrm{k}} N_{\mathrm{k}}}$$

weighted with the measured charges w_{i} in different PMTs. The shower image is parameterised as an ellipse, displayed in the scheme in figure 5.3.

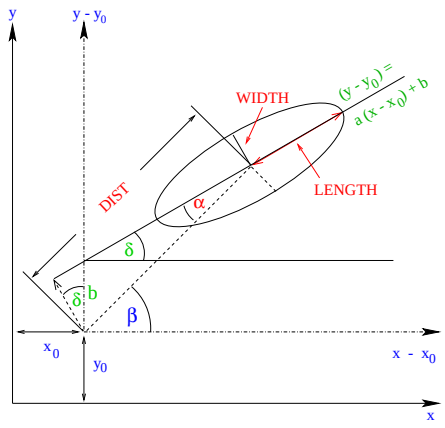

Figure 5.3: Scheme of the shower image parametrisation based on the Hillas method.

The Hillas parameters are:

SIZE represents the sum of the pixel charges of the image, expressed in photo-electrons. For not too high energies (< few TeV) and an impact parameter < 120 m, the number of electrons created in an electromagnetic shower is proportional to the energy of the shower. Furthermore, the number of emitted Cherenkov photons per unit path length of an electron is almost constant for ultra-relativistic particles. An electron emits ~ 4 photons/m at the height of ~ 20 km and ~ 40 photons/m at sea level. Therefore, the sampled part of the emitted shower light can in first approximation be used to estimate the shower energy.

The first moments can be combined into a parameter describing the distance of the center of gravity of the image ellipse from the tracked position in the camera:

$$DIST = \sqrt{\langle x \rangle^2 + \langle y \rangle^2} \tag{5.3}$$

DIST is the distance of the shower center of gravity with respect to the reference point. It is in first order the information of the distance between the shower maximum and the telescope axis correlated to the shower impact parameter. The parameter is included in the calculation of the primary particle energy.

In the following we set $\mathrm{var}(x) := \langle x^2 \rangle - \langle y \rangle^2$, $\mathrm{var}(y) := \langle y^2 \rangle - \langle y \rangle^2$ and $\mathrm{cov}(x,y) := \langle xy \rangle - \langle x \rangle \langle y \rangle$. The second moments get then combined in the covariance matrix M:

$$M = \begin{pmatrix} \mathrm{var}(x) & \mathrm{cov}(x,y) \\ \mathrm{cov}(x,y) & \mathrm{var}(y) \end{pmatrix} \tag{5.4}$$

which is then rotated by an angle δ, such that M^{rot} becomes diagonal in the new coordinate system:

$$M^{\mathrm{rot}} = \begin{pmatrix} \cos\delta & \sin\delta \\ -\sin\delta & \cos\delta \end{pmatrix} \cdot M \cdot \begin{pmatrix} \cos\delta & -\sin\delta \\ \sin\delta & \cos\delta \end{pmatrix} = \begin{pmatrix} \lambda_1 & 0 \\ 0 & \lambda_2 \end{pmatrix} \tag{5.5}$$

The solution of equation 5.5 and the requirement $\lambda_1 \geqslant \lambda_2$ yields the rotation angle and the diagonalised matrix:

$$\tan\delta = \frac{\mathrm{var}(y) - \mathrm{var}(x) + \sqrt{(\mathrm{var}(y) - \mathrm{var}(x))^2 + 4 \cdot \mathrm{cov}(x,y)^2}}{4 \cdot \mathrm{cov}(x,y)^2} \tag{5.6}$$

$$LENGTH^2 := \lambda_1 = \frac{\mathrm{var}(x) + 2 \cdot \tan\delta \cdot \mathrm{cov}(x,y) + \tan^2\delta \cdot \mathrm{var}(y)}{1 + \tan^2\delta} \tag{5.7}$$

$$WIDTH^2 := \lambda_2 = \frac{\mathrm{var}(x) - 2 \cdot \tan\delta \cdot \mathrm{cov}(x,y) + \tan^2\delta \cdot \mathrm{var}(y)}{1 + \tan^2\delta} \tag{5.8}$$

LENGTH is the half length of the major axis of the shower ellipse. The length of the image is correlated with the longitudinal development of the shower. Due to the lower hadronic absorption length compared to the radiation length of the atmosphere, the $LENGTH$ of hadronic showers is in general larger than that of electromagnetic showers. This difference can be used for gamma/hadron separation.

WIDTH is the half width of the minor axis of the shower ellipse. This parameter is correlated with the transversal development of the shower. Larger transverse momentum in hadronic interactions increases the width of the image and can therefore be used to separate γ from hadron showers.

Based on the definitions above, the unit vector $\vec{a}$ along the main axis of the ellipse is obtained:

$$\vec{a} = \frac{1}{1 + \tan^2\delta} \begin{pmatrix} 1 \\ \tan\delta \end{pmatrix} \tag{5.9}$$

and such the angle α can be calculated:

$$ALPHA := \alpha = \arccos\left(\frac{\langle x\rangle + \tan\delta \cdot \langle y\rangle}{DIST \cdot \sqrt{1+\tan^2\delta}}\right) \tag{5.10}$$

ALPHA is the angle between the shower axis and the direction determined by the image center of gravity and the reference point. $ALPHA$ ranges from $-90°$ to $+90°$, depending on whether the ellipse points towards right or left side of the line connecting the ellipse center with the source position. Electromagnetic showers parallel to the optical axis of the telescope yield $ALPHA$ values concentrated around zero. Hadronic showers on the other hand, do not show any preferred arrival direction. Often it is not possible to determine the ellipse orientation and $ALPHA$ is folded.

In case of HE showers the image is often larger than the camera radius. Thus, the recorded images are often truncated. One can (at least in part) correct for this loss by means of the so-called $LEAKAGE$ parameter [146]:

LEAKAGE is the fraction of signal distributed in the most external camera pixels ring with respect to $SIZE$. High values indicate a truncation of the shower image with losses of information. Showers with small impact parameter, reflected entirely in the camera, have $LEAKAGE$ values of zero.

Other commonly used Hillas parameters are:

CONCn (n = 1, ... 7) is the fraction of photons contained in the n brightest pixels per total image $SIZE$. It gives quantitative information about the shower core. Gamma showers have in general higher $CONC$ than hadronic showers.

ISLANDS is the number of separated areas with signal. This parameter may help to distinguish hadronic from electromagnetic showers, because hadronic showers have in general more $ISLANDS$.

M3LONG is the third moment of the image along the shower axis. It is positive when the head of the shower is closer to the source position than the tail. $M3LONG$ helps to solve the image orientation ambiguity for large $SIZE$ showers. For small $SIZE$ showers the correct assignment fails often due to the fluctuation of the PMT signal.

Figure 5.4 shows some of the Hillas parameter distributions for MC generated γ and proton showers.

5.5 Signal and background reconstruction

A physics experiment typically produces a large amount of data, which needs to be distilled down to something meaningful. The technique to distinguish images generated by γ's from the ones generated by hadrons is based on their different shower development, which lead to different image parameter distributions. Quality parameters based on the Hillas parameters are generated by training with MC simulated γ showers and a hadronic sample from the OFF data. The **Super Cut** [147], **Random Forest** [148] and the **Neural Network** [149] techniques are common. In this analysis only Random Forest (RF) was used to separate showers of a high probability to be initiated by primary γ-rays from the large hadronic background.

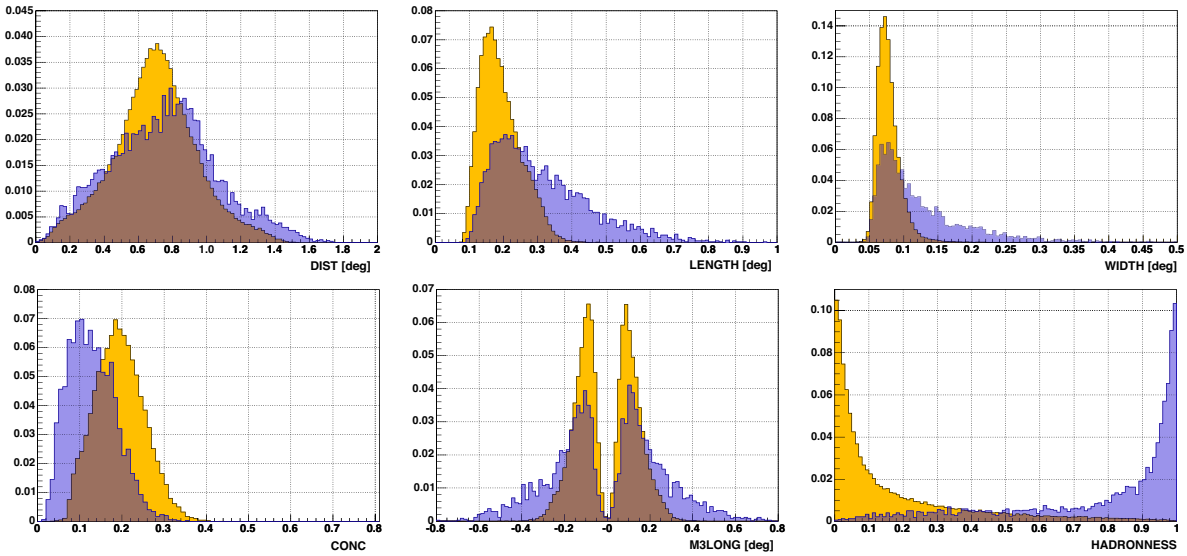

Figure 5.4: Distribution of the Hillas parameters for MC simulated γ showers (yellow shadowed area) and proton showers (blue shadowed area). In total $1.6 \cdot 10^5$ γ showers with the differential photon spectral index of -2.5 and $1.1 \cdot 10^4$ proton showers with the spectral index of -2.7 are included. As a filter cut only the $SIZE$ cut with > 200 ph.e. was applied. The proton shower distributions are normalised by the area to the larger fraction of γ showers.

The Random Forest method

The RF method is based on the construction of *decision trees*. Each of them uses three randomly chosen Hillas parameters out of the list, which were selected for the training[3]. The tree starts at the so called *root node*. The trees *grow* in the training such that at each step the *Gini index* of the two samples gets minimised. The **Gini index** can be expressed in terms of number of events N on the left or right side of the cut value:

$$Q_{Gini} = 2 \cdot \left(\frac{N^{\text{left}}_{\text{signal}} \cdot N^{\text{left}}_{\text{bg}}}{N^{\text{left}}_{\text{tot}}} + \frac{N^{\text{right}}_{\text{signal}} \cdot N^{\text{right}}_{\text{bg}}}{N^{\text{right}}_{\text{tot}}} \right) \tag{5.11}$$

In the next step another parameter is randomly chosen and the tree continues to grow from the obtained cut value of the *first node*. This procedure repeats until the node is *pure*, i.e. the Gini index is zero, or the number of remaining events is less than a certain threshold, e.g. < 10 events. The corresponding node is then called *terminal node*.

The RF is composed of many (in our case 100) decision trees, which classify an event independently with a number between 0 (for γ-like event) or 1 (for hadron-like event). The mean value of all classification trees is assigned as a new parameter to each event, called $HADRONNESS$.

HADRONNESS is a number between zero and one and associates to each shower image a probability to be a electromagnetic or hadronic shower. Electromagnetic showers have in general a $HADRONNESS$ of nearly zero. For large $SIZE$ events the separation is quite strong (see blue area in figure 5.5), while for small $SIZE$ the difference becomes washed out and the gamma/hadron separation often fails.

[3]It should be noted that the parameter $ALPHA$ is not included into the RF training.

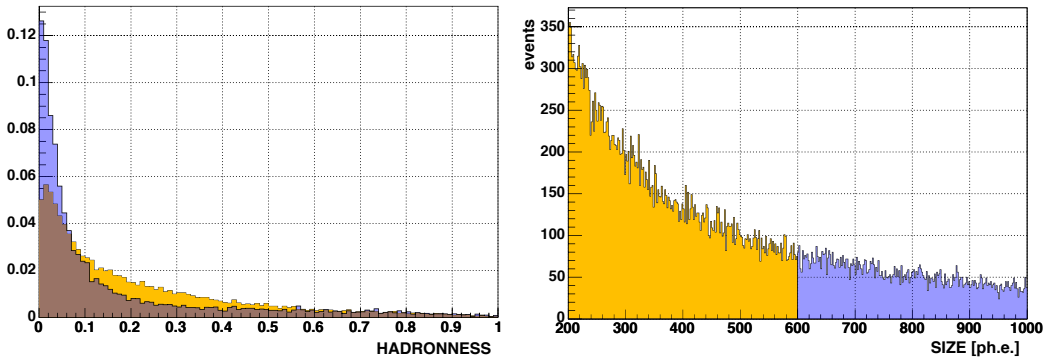

Figure 5.5: Distribution of the $HADRONNESS$ parameter from the MC simulated γ-ray showers (after the RF training). Normalised $HADRONNESS$ distributions (left) for two different $SIZE$ ranges (right). The smaller the $SIZE$, the less effective becomes the $HADRONNESS$ cut.

I used this new $HADRONNESS$ parameter and the $ALPHA$ parameter to separate signal from background events in the final step of my analysis.

Energy estimation

As mentioned in § 5.4 the $SIZE$ parameter is in first approximation a good estimate of the primary particle energy. Especially at higher energies ($< 5\,\mathrm{TeV}$) this approach works fine, although the conversion factor between $SIZE$ and energy has to be retrieved for each individual zenith angle. A more precise approach is to include also the image parameters, mainly $DIST$ and the combination of $WIDTH$ and $LENGTH$. Again, the RF method can be used here: Instead of separating signal from background distributions, MC generated shower events become classified according to their energy. The energy range can be divided into n bins and each MC γ-event gets a probability for every energy bin. This approach yields energy resolutions of the order of 25%, worsening towards the energy threshold. The distribution of the true γ-ray energy E_{true} from the MC data, versus the reconstructed energy E_{est} from the RF training, is shown in figure 6.9.

The outcome of the RF are two matrices, the $HADRONNESS$-matrix and the $ENERGY$-matrix (see figure 5.1). These matrices are applied to the ON and OFF data, as well as to the MC test sample using the melibea program.

5.6 Calculation of the significance of the signal

Finally, at the end of the analysis chain, one has MC, ON and OFF data sets, in which each event has been classified with the $HADRONNESS$ parameter and the angle $ALPHA$. At this stage, these two parameters are used to discriminate the γ from hadron showers.

The number of γ-events from the observed source N_{obs} can eventually be extracted from the $ALPHA$ plot: The distribution of angles of the shower axes towards the camera center. Figure 5.6 shows a typical $ALPHA$ distribution example from a strong γ-ray emitting object. Signal from a point-like source should pop up as an excess at small $ALPHA$ values. To retrieve N_{obs} one needs to subtract the background – determined from the OFF data – in the signal region. The availability of OFF data is often limited for the preferred ON source observations. Summing up different data sets, which match the same zenith angle range and observational conditions as the ON data, allows to increase the statistics. The ON and OFF data are normalised to each other by multiplying the OFF data with η, the ratio of the integral number of events in the background region between $30° \leqslant |ALPHA| \leqslant 80°$. This range is assumed to be free of signal [150].

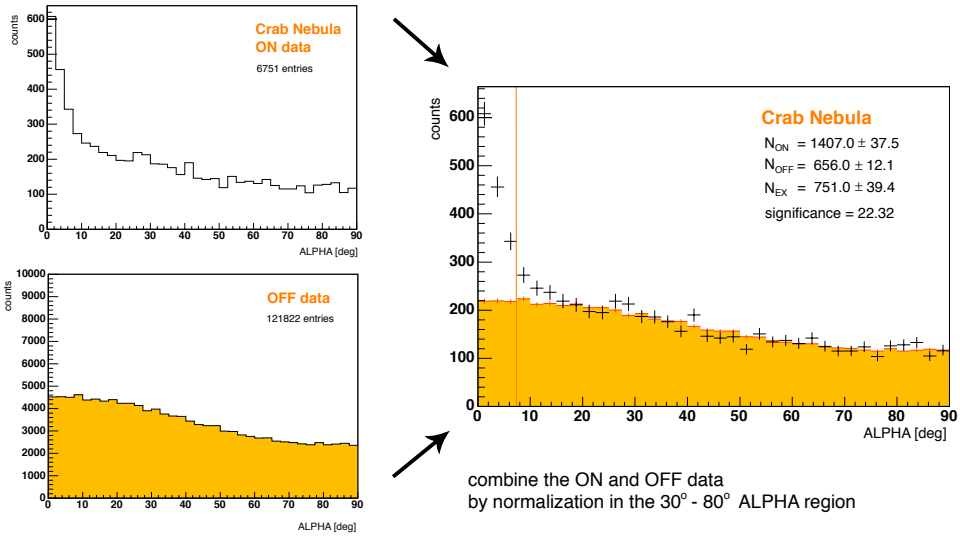

Figure 5.6: $ALPHA$ distribution example obtained from 95 min of Crab Nebula observation with the MAGIC telescope. The $ALPHA$ distribution of the ON and OFF data set is normalised to each other in the $30° \leqslant ALPHA \leqslant 80°$ region.

To extract the highest significance from the ON data, I have used the following methods to define cuts on $HADRONNESS$ and $ALPHA$:

1. I determined the cut on $ALPHA$ by fitting a Gaussian to the MC γ distribution in the corresponding energy bin. Because the shower axis can not more be extracted very precisely at small energies, the width of the $ALPHA$ distribution gets wider. I set the energy dependent upper cut on $ALPHA$ to $2.5\,\sigma$ of the Gaussian fit.

2. I determined the cut on the $HADRONNESS$ parameter by calculating test significances from the MC data, when scanning the parameter range from 0 to 1 in intervals of 0.05. The previously generated cut in $ALPHA$ was used to calculate the significance for the corresponding energy bin. I used the cut value, which yields the highest significance.

These cuts were applied to the test source (in my case Mkn 501) and finally to each GRB data sample. The significance S of the signal was calculated with the Ti-Pei Li and Yu-Qian Ma formula [151]:

$$S = \sqrt{2} \cdot \Bigg[\quad N_{\mathrm{ON}} \cdot \ln\left(\frac{1+\eta}{\eta} \cdot \frac{N_{\mathrm{ON}}}{N_{\mathrm{ON}} + N_{\mathrm{OFF}}}\right) + \quad N_{\mathrm{OFF}} \cdot \ln\left((1+\eta) \cdot \frac{N_{\mathrm{OFF}}}{N_{\mathrm{ON}} + N_{\mathrm{OFF}}}\right) \Bigg]^{1/2} \tag{5.12}$$

where N_{ON} and N_{OFF} are the number of events extracted from the $ALPHA$ distribution in the signal region for ON and OFF data, respectively and η is the normalisation factor.

5.6.1 Calculation of effective areas

To calculate the particle flux one also needs, in addition to the number of γ-events and the effective observation time, the effective area A_{eff} of the telescope. A_{eff} depends, besides all the applied cuts, on the γ-ray energy E and the zenith angle θ of the observation. The value can be extracted from the MC data, analysed by the same procedure (cuts) as the real data. At small energies the impact of the Earth magnetic field becomes relevant and azimuth angle dependence should be included. The effect is unaccounted in my analysis. I scaled the originally simulated area A_{MC} with the ratio of the number of events surviving the analysis steps $N_{\mathrm{analysis}}(E,\theta)$ and the originally simulated number of γ-rays $N_{\mathrm{MC}}(E,\theta)$ in the corresponding energy and zenith angle bin:

$$A_{\mathrm{eff}}(E,\theta) = A_{\mathrm{MC}} \cdot \frac{N_{\mathrm{analysis}}(E,\theta)}{N_{\mathrm{MC}}(E,\theta)} \tag{5.13}$$

Figure 5.7 shows the effective areas for a zenith angle observation at 40°. GRB observations by MAGIC are performed at a zenith angle range up to 60°. The figure at 40° is therefore a representative example.

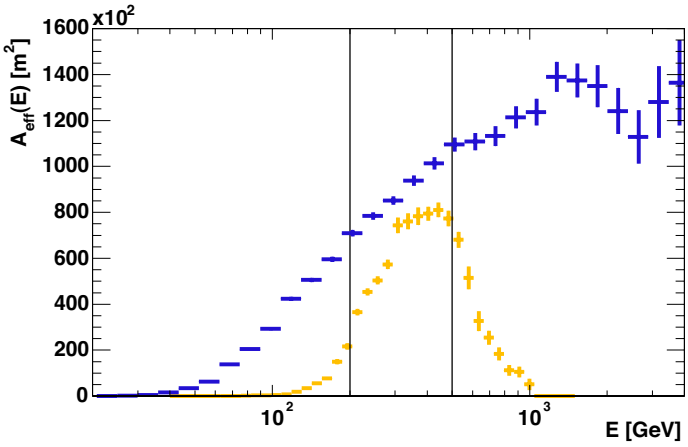

Figure 5.7: Distributions of effective areas from the MC data for the zenith angle of 40°. The blue crosses show the overall effective area while the orange crosses include only the energies 200 GeV $\leqslant E \leqslant$ 500 GeV. Shower fluctuations result in limited energy resolution. Therefore, the orange distribution does not have sharp cuts at the chosen energy limits.

5.6.2 Calculation of upper limits for number of observable events

In order to claim detection of a new source a high value of evidence is required. This can be expressed in units of standard deviations σ for a Gaussian random process. In this expression a 5σ excess is required for claiming a new detection. The absence of a significant excess means that the rate or magnitude of the physical effect is below the sensitivity of the instrument. The results can then be expressed quantitatively as an upper limit on the observable events.

In a counting experiment, the number of events, which satisfy a set of selection criteria, designed to keep most signal events (if any exists) and reject uninteresting events, is used to summarise the data. In my analysis, the following values can be extracted from the *ALPHA* distribution:

N_{ON}**:** Number of events in the signal region from ON data.

N_{OFF}**:** Number of events in the signal region from OFF data.

σ_{OFF}**:** Statistical error for the OFF data.

The upper limit value depends on the chosen confidence level (CL) α and is usually specified as a confidence interval. For the construction of confidence intervals the Feldman and Cousins [152] approach was used. It makes use of *Neyman's Construction* [153], which (for a single measurement parameter) is also called the method of confidence belts. This method adopts a certain probability density function for the obtained values of N_{ON}. Their distribution can follow, for example, a Poisson function of the form:

$$P\left(N_{\mathrm{ON}}|\mu_{\mathrm{ex}}\right) = \frac{\left(\mu_{\mathrm{ex}} + \mu_{\mathrm{OFF}}\right)^{N_{\mathrm{ON}}}}{N_{\mathrm{ON}}!} \cdot e^{-(\mu_{\mathrm{ex}}+\mu_{\mathrm{OFF}})} \tag{5.14}$$

where μ_{ex} and μ_{OFF} are the mean number of expected signal and background events, respectively. The model assumes a perfectly known background. Rolke et al. included additional probability model for the background [154] and later also the overall efficiency ϵ [155] in the construction of the confidence belts. I have used this method to determine the upper limits.

The actual value of μ_{ex} is unknown and the confidence belt provides a range of values for μ_{ex} at a desired CL. Figure 5.8 shows the confidence interval for the Poisson distribution, as presented in equation 5.14. Background of $\mu_{\mathrm{OFF}} = 3.0$ was adopted. For each μ_{ex}, the possible values for N_{ON} are contained in the corresponding confidence interval, assuming the probability of $\alpha = 0.1$. When the value N_{ON} is measured, one draws a vertical line, which intersects a range of confidence intervals. The confidence interval for the true value μ_{ex} is the range of all touched acceptance intervals between $\left[\mu_{\mathrm{ex}}^{low}, \mu_{\mathrm{ex}}^{up}\right]$. The result μ_{ex}^{up} is the value used as upper limit.

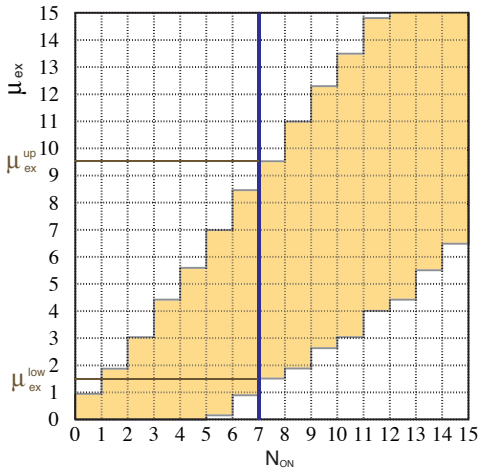

Figure 5.8: Example of confidence belt. Adapted from [152].

The construction of the confidence intervals for all possible $\mu_{\rm ex}$ values is done by defining L such that the following expression holds:

$$\int_{-\infty}^{L} P\left(N_{\rm ON}|\mu_{\rm ex}\right) dN_{\rm ON} = \alpha \tag{5.15}$$

The choice of α is free. The results shown in my thesis are determined with $\alpha = 0.05$ (corresponding to 95% CL). The rather complicated formulae used to calculate $N_{\rm ex}$ is fully described in [156]. It assumes a Poisson distributed $N_{\rm ON}$, down-scaled number of background events $\eta \cdot N_{\rm OFF}$, following a Gaussian with a width $\eta \cdot \sqrt{N_{\rm OFF}}$ and the mean efficiency of $\epsilon = 1$.

5.6.3 Calculation of particle flux and fluence upper limits

For unknown sources one has to make assumptions on the energy spectrum dN_γ/dE and the time evolution dN_γ/dt. One assumes for the VHE γ-rays typically power-law spectra with or without exponential cutoff:

$$\frac{dN_\gamma}{dE\,dA\,dt} = F_0 \cdot \left(\frac{E}{E_0}\right)^{-\alpha} \tag{5.16}$$

$$\frac{dN_\gamma}{dE\,dA\,dt} = F_0 \cdot \left(\frac{E}{E_0}\right)^{-\alpha} \cdot \exp\left(-\frac{E-E_0}{E_{\rm b}}\right) \tag{5.17}$$

with E_0 as the mean energy of the energy bin, $E_{\rm b}$ the break energy of the exponential cutoff, α the hypothetical spectral index and F_0 the particle flux of the source. To simplify the calculation a constant light curve during the observation period is assumed. Otherwise one would need to split the observation window into small time bins.

From the γ-ray flux $dN_\gamma/(dE\,dA\,dt)$ one can estimate the number of events $N_{\rm obs}$ observed by an experiment in the energy range $E_{\rm min} \leqslant E \leqslant E_{\rm max}$ using the following formula:

$$N_{\rm obs} = \int_0^\infty \int_{t_{\rm start}}^{t_{\rm end}} \frac{dN_\gamma}{dE\,dA\,dt} \cdot A\left(E|_{E_{\rm min}}^{E_{\rm max}}\right) \cdot \epsilon(t)\,dt\,dE \tag{5.18}$$

where $A(E)$ is the effective area in the corresponding energy range. To simplify the calculation, the effective on-time function $\epsilon(t)$ is set constant.

In case of no signal one obtains statistically distributed numbers with an average of zero events $\langle N_{\rm obs}\rangle = 0$. The result has to be converted then into an upper limit, following the description in § 5.6.2. Combining equation 5.16 with 5.18 one gets for the **flux upper limit** the following expression:

$$F_0 < \frac{N_{95\%}(E)}{\int_0^\infty \left(\frac{E}{E_0}\right)^{-\alpha} \cdot A(E)\,dE \cdot \int_{t_{\rm start}}^{t_{\rm end}} \frac{\epsilon(t)}{t} dt} \tag{5.19}$$

Equation 5.19 has been changed to un-equality in order to indicate that this is an upper limit. $N_{95\%}(E)$ is the corresponding upper limit with 95% CL. The unit of F_0 is conveniently $\mathrm{ph\,cm^{-2}\,s^{-1}\,TeV^{-1}}$.

For the **fluence upper limit**, the following expression holds:

$$\Phi_0 < \frac{N_{95\%}(E)}{\int_0^\infty \left(\frac{E}{E_0}\right)^{-\alpha} \cdot A(E)\, dE} \tag{5.20}$$

Φ_0 has conveniently the unit $\mathrm{ph\,cm^{-2}\,TeV^{-1}}$. To interpret the limit correctly the time interval, to which the limit applies, has to be given.

5.6.4 Calculation of spectral energy density upper limits

Spectral energy density (SED) plots are often used in the astronomy. In order to derive an upper limit in SED, the spectra shown in equation 5.16 and 5.17 have to be transformed by multiplying both sides with E^2:

$$E^2 \cdot \frac{dN_\gamma}{dE\, dA\, dt} = P_0 \cdot \left(\frac{E}{E_0}\right)^{-\alpha+2} \tag{5.21}$$

$$E^2 \cdot \frac{dN_\gamma}{dE\, dA\, dt} = P_0 \cdot \left(\frac{E}{E_0}\right)^{-\alpha+2} \cdot \exp\left(-\frac{E-E_0}{E_\mathrm{b}}\right) \tag{5.22}$$

The **SED upper limit** then has the form:

$$P_0 < \frac{N_{95\%}(E) \cdot \langle E(\alpha)^2 \rangle}{\int_0^\infty \left(\frac{E}{E_0}\right)^{-\alpha+2} \cdot A(E)\, dE \cdot \int_{t_\mathrm{start}}^{t_\mathrm{end}} \frac{\epsilon(t)}{t} dt} \tag{5.23}$$

where $\langle E(\alpha)^2 \rangle$ is the mean square energy extracted from the MC data simulated with the corresponding spectral index α. P_0 has the unit $\mathrm{erg\,cm^{-2}\,s^{-1}}$.

5.6.5 The Crab unit

In order to simplify the comparison of fluxes from different VHE sources the Crab Unit (CU) is often used. It represents the particle flux of the Crab Nebula, a steady SN remnant used for experiments in the northern hemisphere as a standard candle to calibrate their detectors. The conversion to CU is the following:

$$1\,\mathrm{CU} \equiv 1.5 \cdot 10^{-3} \left(\frac{E}{\mathrm{GeV}}\right)^{-2.58} \mathrm{ph\,cm^{-2}\,s^{-1}\,TeV^{-1}} \tag{5.24}$$

Chapter 6

VHE observations of GRBs

Follow-up observations of GRB alerts by the MAGIC telescope started with the begin of the first observation cycle in the year 2005 [157]. During this period alerts from HETE-2, INTEGRAL and SWIFT were accepted by gspot. In § 2.4.3 I summarise the GCN alert packages we have received. Out of the 23 MAGIC responses, 12 real GRB events were observed. In two cases: **GRB050713a** on July 13$^{\text{th}}$ and **GRB050904** on September 5$^{\text{th}}$, 2005, data taking started while the prompt emission phase was still ongoing. These data represent the **first GRB prompt emission phase measurements made with an IACT** and demonstrate the potential of the MAGIC telescope. I optimised and cross-validated the analysis chain for the GRB data set with data of the flare of the AGN Mkn 501, recorded on July 1$^{\text{st}}$, 2005. This flare yielded the highest γ-ray flux observed by MAGIC so far. It is therefore an optimal sample for training of the analysis at energies close to the threshold. The results obtained from Mkn 501 can be found in § 6.1. After validating the sensitivity of my analysis, I applied the same method to the GRB data set. The essential information and results for each GRB event are listed in § 6.2 and in chapters therein. I analysed the SWIFT satellite data by my own, extracting the BAT and XRT light curves, durations and spectra. Also these results are included in the forthcoming chapters. In order to keep the chapter compact, *ALPHA* figures from the MAGIC data analysis are shown in appendix A. To anticipate my final results: Three data sets had to be excluded from the analysis and for the remaining 9 GRBs no significant γ signal was found. However, for the first time strong upper limits on the VHE emission, during the prompt and early afterglow phase of the GRBs, could be set. Attempts to draw physics conclusions from the results obtained from MAGIC observations and an outlook to the near future are given in § 6.3.

6.1 Optimisation of the analysis chain with Mkn 501 flare data

Mkn 501 is a BL Lac object at the distance of $z = 0.034$ and therefore the second closest known VHE γ-ray emitting blazar after Mkn 421, which is located at $z = 0.031$. Since the discovery of TeV γ-ray radiation from Mkn 501 by the Whipple collaboration in 1995 [161], this object has been a subject of intensive studies at many different wavelengths. The source is highly variable with flaring activities rising to peak fluxes of up to 10 times the Crab Nebula flux. During the short lasting flares with time scales of days, Mkn 501 becomes the brightest TeV γ-ray source in the sky.

On July 1st, 2005, the MAGIC telescope was able to catch such a flaring activity. The light curve of Mkn 501 measured by MAGIC before, during and after the flare is shown in figure 6.2. The flux measured by MAGIC rose to up to $\sim$ 4$\times$ the Crab Nebula flux. The energy spectrum measured by MAGIC is shown in figure 6.1. This high flux is a record value for the telescope until now. The data set of the flare is highly enriched by γ showers and therefore the best sample for tests of new analysis methods.

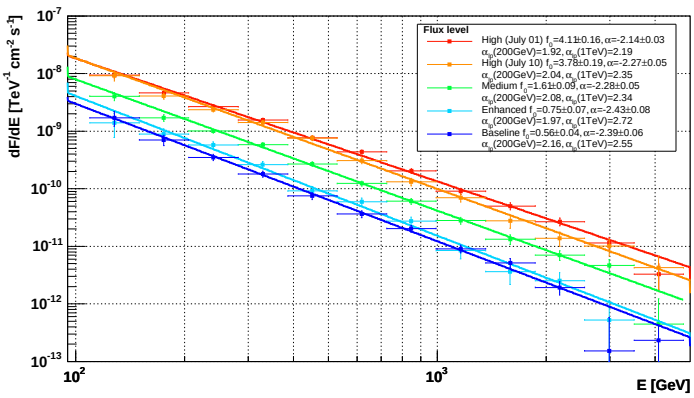

Figure 6.1: Energy spectra of Mkn 501 measured by the MAGIC telescope at different times. Figure from [104].

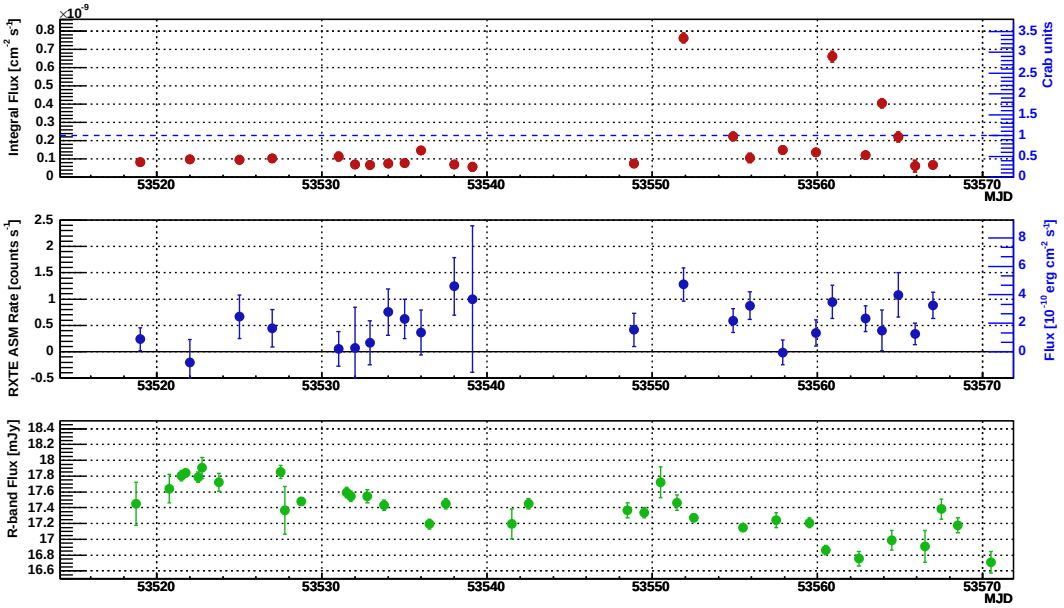

Figure 6.2: Light curve from MAGIC observations of Mkn 501 in the energy range 250 GeV $\leqslant E \leqslant$ 2 TeV. The period between June and July 2005 is shown. The flare on July 1st rises to fluxes of 4$\times$ Crab Nebula flux. The light curves in X-ray and optical wavelengths are also included. Figure from [104].

6.1.1 Filter and quality cuts for data reduction

Most of the raw triggered events are not γ-ray showers. They originate mainly from hadronic background showers or from fake events (accidental triggers). A large fraction of these events can be removed by applying *filter* and *quality cuts*. Figure 6.3 shows the cut efficiencies for the ON data set processed with the time image cleaning. The cuts, which I will introduce in the following, yield a reduction of the data by more than factor of two. The final $HADRONNESS$ and $ALPHA$ cuts will be discussed in § 6.1.4. To determine the cuts, one compares real data with MC simulated γ-ray showers. For the comparison the distributions of the Hillas parameters (see § 5.4) are used. Cuts on these parameters are defined, so that no MC events are lost, but a large fraction of the events in the ON and OFF data samples, which are obviously hadrons, are removed. Shower events, for which the Hillas parameters do not overlap with the MC simulated events, could result in wrong training of the RF.

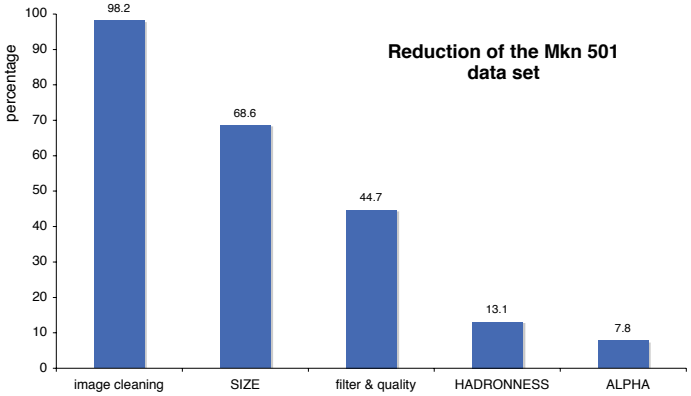

Figure 6.3: Cut efficiencies for the ON data set of Mkn 501.

The first cuts were set on the $LEAKAGE$ and $ISLANDS$ parameters. Concentrating on the lowest energies, a cut on small $LEAKAGE$ was used. Only showers with their center of gravity in the central part of the camera are kept. In addition a cut allowing up to one $ISLAND$ was set:

$$\begin{aligned} LEAKAGE &< 0.01 \\ ISLANDS &< 2 \end{aligned}$$

Furthermore, I used tight $SIZE$ limits. The lower $SIZE$ limit eliminates images, which can not be properly reconstructed. The upper $SIZE$ limit of 400 ph.e. is unusual in the standard analysis. It reflects the assumption that GRBs are expected not to have spectra extended to ultrahigh energies (which could not be accounted for by any acceleration process in the short time deviation of GRBs). It corresponds to an energy of ~ 300 GeV at low zenith angle and gives the priority to energies close to the threshold for the RF training:

$$60\,\text{ph.e.} < \quad SIZE \quad < 400\,\text{ph.e.}$$

Figure 6.4 shows the distributions of the $\log(SIZE)$ parameter for the Mkn 501 data samples. The distributions of the ON and OFF data are well in agreement with each other. I divided the ON data into two samples, according to the different DT, at which they were taken. The two samples show small, but still acceptable differences. The time image cleaning keeps more events with small $SIZE$ from the MC, compared with the absolute cleaning. The ON and OFF data sets contain mostly hadronic events, while the MC data is a pure sample of γ-ray showers. The γ showers have smaller $SIZE$ (at these low energies) than the hadronic showers, which explains the difference of the real data sample to the MC simulated sample. The cut in $SIZE$ is indicated with the vertical lines.

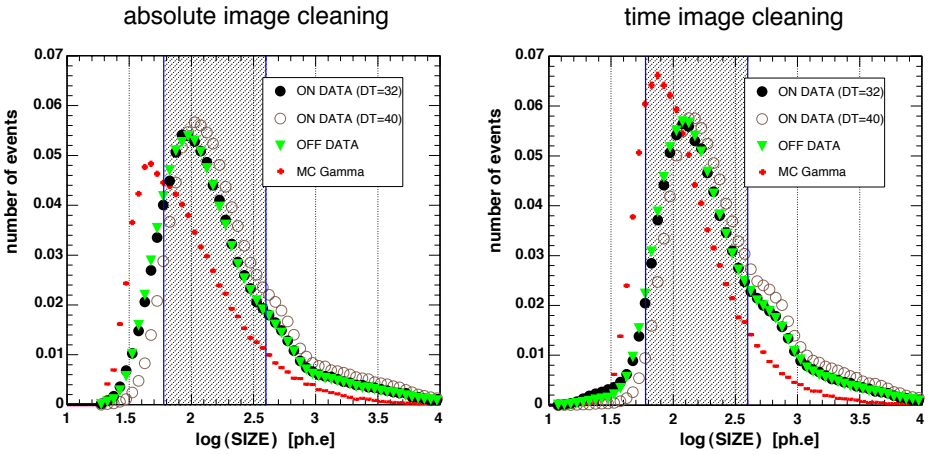

Figure 6.4: Normalised distributions of the log($SIZE$) parameter for the Mkn 501 data. The shadowed area shows the parameter space included in the analysis. Two different image cleaning algorithms are compared: *Left* the absolute and *right* the time image cleaning.

For ON data mode – telescope pointing directly towards the presumed source – low energy evens are expected to cluster in the central region of the camera, e.g. with an impact parameter up to $\sim 120\,\mathrm{m}$ (zenith angle dependent). The impact parameter is equivalent to the $DIST$ parameter. Events with an impact parameter $< 30 - 40\,\mathrm{m}$ ($DIST < 0.3 - 0.4°$) are not useful because a) the light stems from the shower tail and is therefore difficult to separate from hadronic showers and b) essential Hillas parameters ($ALPHA$, $WIDTH$, $LENGTH$, etc.) are badly defined. At large values of $DIST$ the number of low energy events decreases rapidly, because only a small fraction of the characteristic Cherenkov light it deposits is seen. Furthermore, trigger boundary effects at the edge of the trigger area affect the selection of events. I decided therefore to apply the following cuts on $DIST$:

$$0.33° < \quad DIST \quad < 0.86°$$

Figure 6.5 shows the distribution of the $DIST$ parameter vs. the logarithm of $SIZE$ and the applied cuts on both parameters as red lines. For the further analysis only events in the inner section were used.

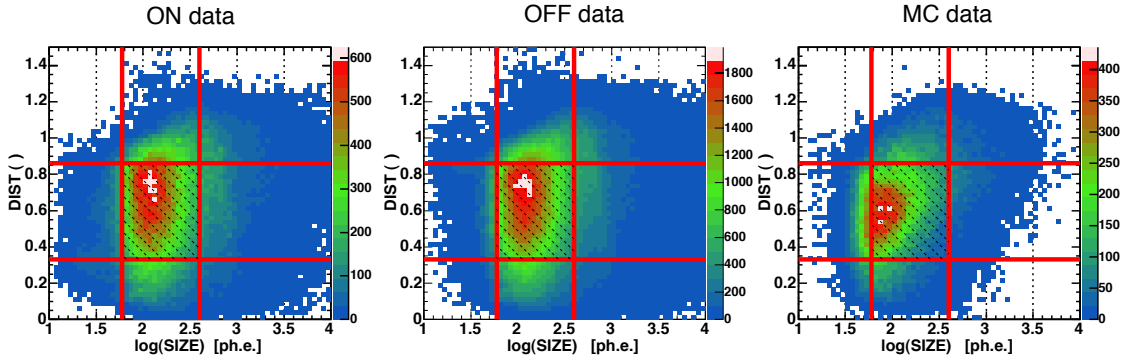

Figure 6.5: Distribution of the $DIST$ vs. log($SIZE$) parameters for the Mkn 501 data and the time image cleaning applied (similar results were obtained with the absolute image cleaning). The red lines show the cuts.

Spark events

The data taken from the GRBs are affected by false trigger events generated due to occasional discharges at some PMTs. The origin of these discharges is unknown. Presumably the so-called *spark events* were caused by discharges between the cathode of the PMT and the aluminised Mylar foil of the Winston cones. Light from the spark events is mainly concentrated in the triggering PMT and can therefore be removed efficiently with the help of the $CONC$ parameter. In order to study this effect, I analysed 30 min of dedicated data taken with closed camera lids. The 564 recorded spark events are shown as black points in the right hand side plot of figure 6.6. This figure shows the $\log(SIZE)$ vs. $\log(CONC)$ parameter distribution for the different data samples of the time image cleaning. The red lines show the cuts on $SIZE$, as well as the diagonal spark cut:

$$\log(CONC) \quad < \quad 0.65 - 0.45 \cdot \log(SIZE)$$

The spark events in the upper right corner are clearly seen in the ON and OFF data. They are absent in the MC data. With the chosen $CONC$ cut all spark events were rejected.

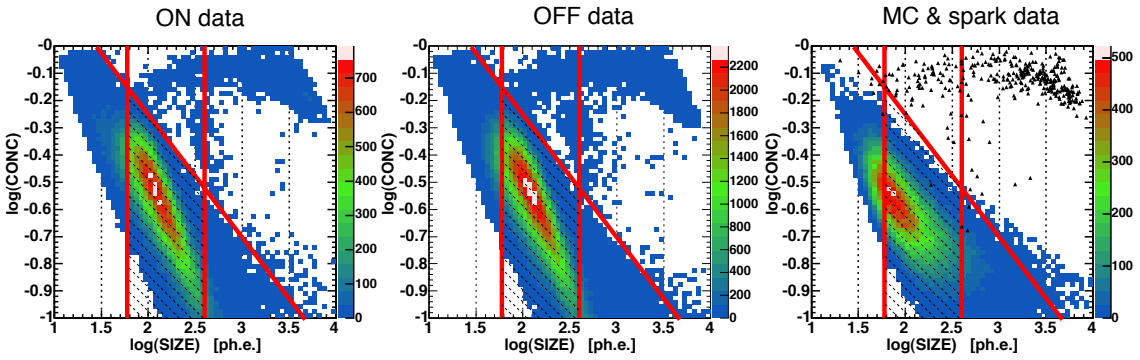

Figure 6.6: Distribution of the events in $\log(CONC)$ vs. $\log(SIZE)$ parameter space for the Mkn 501 data and the time image cleaning. The red lines indicate the cuts on both parameters. The black dots in the MC data illustrate the spark events triggered with closed camera lid. These events are extracted from the dedicated data sample. Results from the absolute image cleaning yield similar results.

Cut efficiencies

The figure 6.3 illustrates as an example the power of the data reduction after the image cleaning and chosen cuts. Table 6.1 lists the selection efficiencies for both image cleanings in detail. In general, the time image cleaning algorithm yields better efficiencies for all data sets. The bulk of events was rejected with the $SIZE$ cut. On average 44.8% of the events from the absolute and 46.0% events from the time image cleaning were kept after the filter and quality cuts.

image cleaning algorithm	MC γ's	OFF data samples (date)			ON data samples	
		29/06	02/07	08/07	DT = 32	DT = 40
total #events	122850	272040	344819	218245	263812	451979
	part of events surviving the image cleaning					
absolute	0.81	0.90	0.97	0.96	0.95	0.98
time	0.98	0.93	0.99	0.99	0.97	0.99
	part of events surviving the $SIZE$ cut					
absolute	0.44	0.61	0.67	0.65	0.65	0.70
time	0.48	0.66	0.71	0.71	0.69	0.68
	part of events surviving all filter and quality cuts					
absolute	0.34	0.42	0.45	0.44	0.44	0.49
time	0.37	0.44	0.47	0.47	0.46	0.46

Table 6.1: Selection efficiencies for the Mkn 501 data sets.

6.1.2 Training of cuts on the Hillas parameters using the RF method

I used the RF method to classify the events from the reduced data sample into γ-like and hadron-like (see § 5.5). In order to avoid biasing of the RF, I split the pool of MC data into three groups: *test*, *train* and *gamma* sample (see figure 5.1). The number of events from the gamma sample or hadron sample were reduced, until their amount in $SIZE$ bins became equal. The training of the RF was performed on these two resized samples. I used the following parameters for the RF training:

$$SIZE,\ DIST,\ WIDTH,\ LENGTH,\ CONC1,\ CONC4 \text{ and } M3LONG$$

Figure 6.7 shows the mean decrease of the *Gini index* for each parameter of the RF, after the training. The value represents the rejection efficiency of the background events of a given parameter, in the presence of the others. For the absolute image cleaning the $LENGTH$ parameter yields the strongest separation efficiency. In the case of time image cleaning the $CONC4$ parameter dominates. However, all parameters, which were chosen, have significant influence on the classification of the events and are therefore useful.

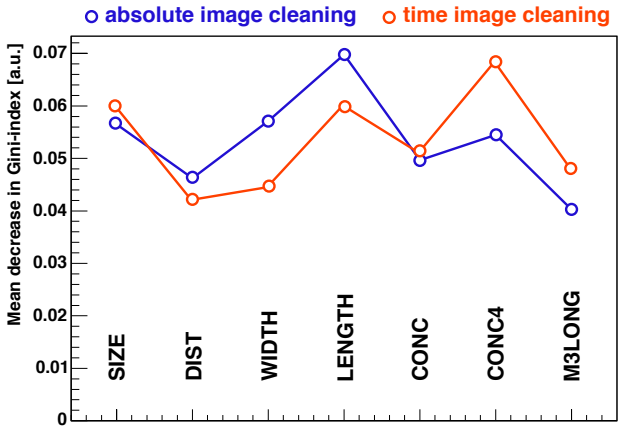

Figure 6.7: Mean decrease in Gini index for every parameter used in the RF training of the Mkn 501 data. Blue points represent absolute and red points the time image cleaning.

The outcome of the RF training is a matrix, which applied to a data set, classifies each event with a $HADRONNESS$ value. For a γ shower this number is more close to zero while for a hadron shower it is more close to one. Figure 6.8 shows the distribution of the $HADRONNESS$ parameters for the different data samples and image cleaning algorithms, after the RF training. The agreement between ON and OFF data is acceptable for both

cleanings. One has to mention, that these distributions represent the lowest energy bins. As a consequence of the fixed pixel size, γ showers at these energies tend to circular shapes, similar to the hadron showers. Their gamma/hadron separation becomes less effective at low energies and even the $HADRONNESS$ distribution of the pure MC γ sample smears out. The advantage of the time image cleaning over the absolute image cleaning i.e., where separation between the γ and hadron showers becomes better, is seen from this figures.

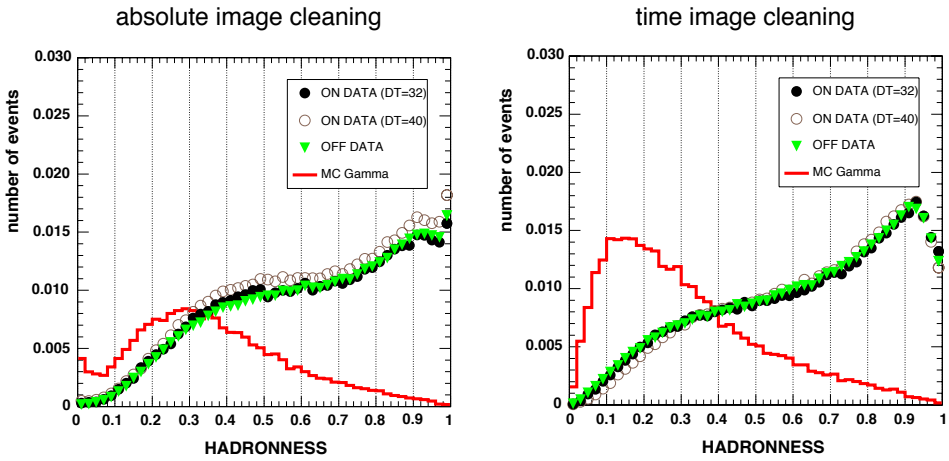

Figure 6.8: Distribution of the $HADRONNESS$ parameter for the Mkn 501 data and the two different image cleanings.

6.1.3 Energy reconstruction with the RF method

The RF method can also be used for the reconstruction of the particle energies. New decision trees, based on the previously defined Hillas parameters and in addition the zenith angle information, are generated to recognise the shower energies. MC simulated γ showers with known primary particle energies are used for the training. To avoid biasing, a separated *train* sample of the MC data was used. Figure 6.9 shows the outcome of the training: True simulated energy vs. the reconstructed energy from the MC *test* sample.

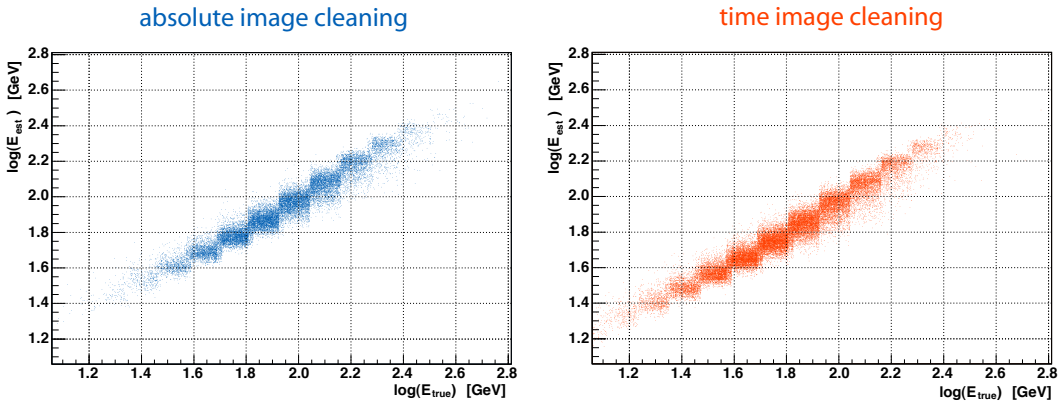

Figure 6.9: RF energy reconstruction quantity for Mkn 501 data sample. *Left:* The absolute and *right:* The time image cleaning are compared.

The energy reconstruction shows the expected linear dependence. The time image cleaning allows to reconstruct energies well below 30 GeV, at least for simulated MC γ showers. The absolute cleaning loses its power in this region. The energy resolution is $\sim 30\%$ at low energies, decreasing to $\sim 25\%$ above 200 GeV.

6.1.4 Final results after cut optimisation

Before generating the *ALPHA* figures, I decided to apply a stronger cut on the *DIST* parameter. Figure 6.10 shows the distribution of *DIST* vs. *ALPHA* for the various data sets. Especially in the case of the absolute image cleaning, one recognises structures at high *DIST* values. The increase at high *ALPHA* is caused due to the boundary effects in the transition region between the trigger area and the outer part of the camera. Events tangential to the camera center fulfil the trigger criteria more often than events in the perpendicular direction. In order to reduce this effect and flatten the *ALPHA* distribution, I narrowed the precut on *DIST*:

$$0.45^\circ < \quad DIST \quad < 0.78^\circ$$

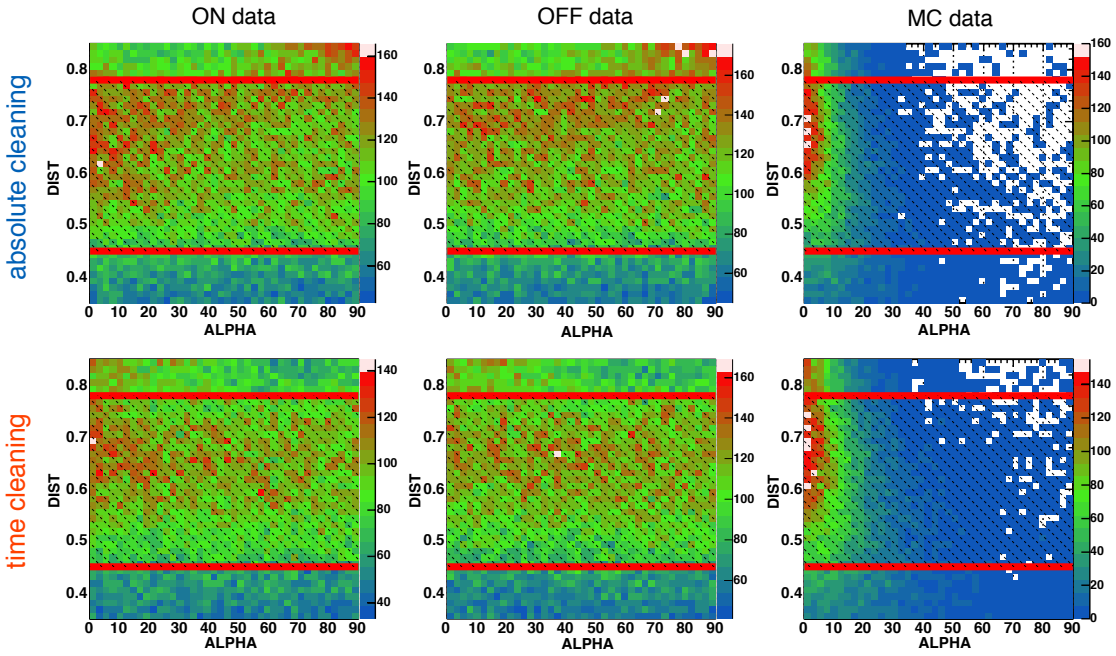

Figure 6.10: Distributions of the *DIST* vs. *ALPHA* parameter for the Mkn 501 data set. *Top:* Absolute image cleaning. *Bottom:* Time image cleaning. ON, OFF and MC data sets are compared and the final cuts shown as red lines.

ALPHA and *HADRONNESS* cuts were chosen according to the method outlined in § 5.6. Figure 6.12 shows an example of the test significances from the MC and OFF data, processed with the time image cleaning. I determined the cut values for each image cleaning and energy bin individually. The results are summarised in table 6.2 and the corresponding *ALPHA* distributions are shown in figure 6.11.

reconstr. energy range [GeV]	mean energy MC [GeV]	*HADRONNESS* cut	*ALPHA* cut [°]	number excess events	significance σ Li & Ma
absolute image cleaning					
$45-75$	70	0.69	26	375 ± 104	3.6
$60-100$	80	0.70	24	744 ± 170	4.4
$100-150$	120	0.61	20	603 ± 103	5.8
$150-300$	180	0.30	17	234 ± 24	9.4
time image cleaning					
$45-75$	60	0.53	31	424 ± 112	3.8
$60-100$	80	0.58	26	745 ± 134	5.5
$100-150$	125	0.54	22	280 ± 97	2.9
$150-300$	175	0.23	19	126 ± 18	7.1

Table 6.2: Results for the Mkn 501 data sets.

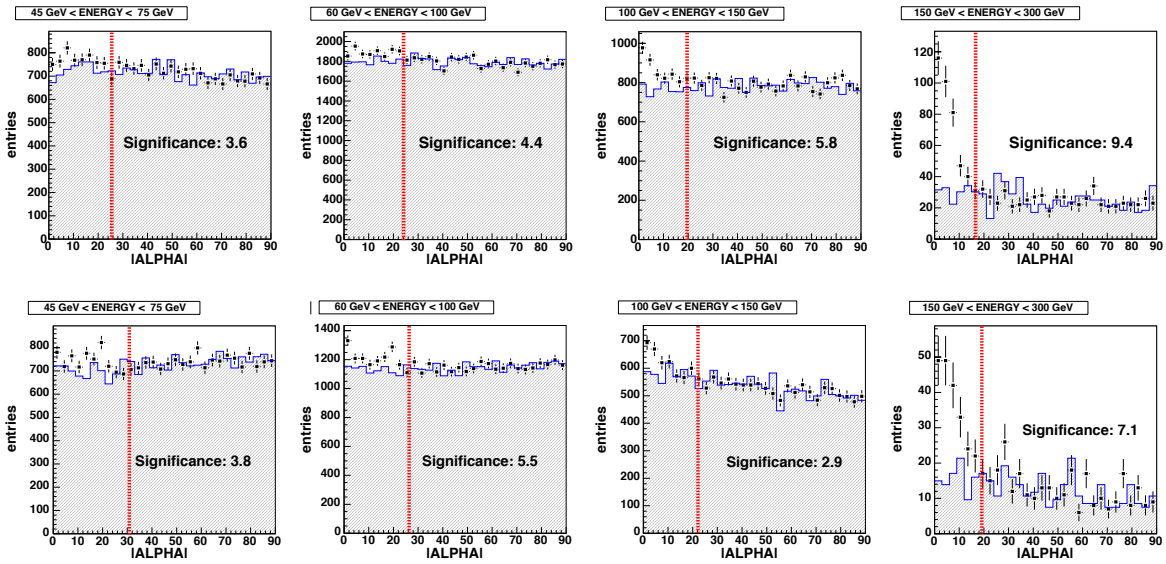

Figure 6.11: *ALPHA* figures for Mkn 501. *Top:* Absolute image cleaning. *Bottom:* Time image cleaning. The four figures show the different energy bins. The red lines indicate the cuts in *ALPHA*.

At energies below 100 GeV the time image cleaning yields slightly better significances. Fluctuations of the background in the third energy bin lead to reduced significances, however the gradient of the ON data indicates clearly signal at low *ALPHA* angles. Signals well above 5σ were extracted from the energy bin with $\langle E \rangle = 80$ GeV. The results can be improved easily with larger amounts of OFF data, by reducing the fluctuations in the signal region.

It was not my aim to draw physics conclusions from the test analysis presented here. The goal was to show, that with new methods, signals at energies close to the threshold energy of the MAGIC telescope can be extracted. The low energy range is the most promising band for the search of possible VHE γ-ray emission from GRBs.

I focussed therefore the analysis on the lowest energies and applied a tight $SIZE$ cut. Additional cuts were necessary to remove biasing of the low energy events at the trigger edge. Cuts on $HADRONNESS$ and $ALPHA$ were extracted from test significances obtained with MC data. The $ALPHA$ distribution smears out at low energies and cut values of up to 30° are necessary. The time information of the shower arrival time significantly improves the analysis at low energies.

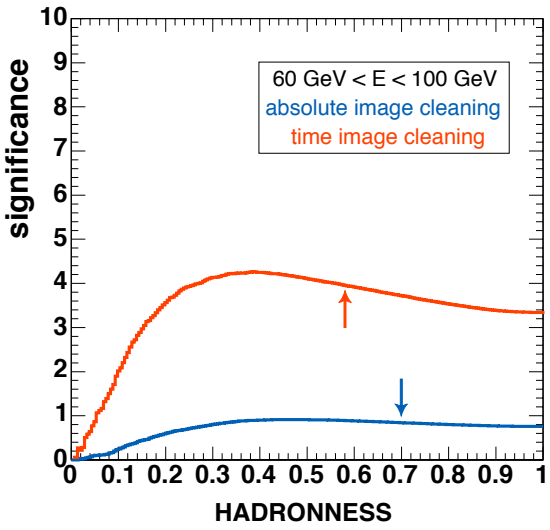

Figure 6.12: Test significances of the MC data for varying $HADRONNESS$ parameter and Mkn 501 OFF data set. The arrows indicate the cut values, which were used.

In the next chapter results from the nine GRBs observed by MAGIC are presented. The dedicated low energy analysis of Mkn 501 was initiated by the data set of GRB050713a (see § 6.2.5), the first GRB observed by an IACT in the prompt emission phase. Therefore, this data set was processed in the same way as tested on Mkn 501.

For the remaining bulk of data the absolute image cleaning algorithm was used. Some cuts needed also to be enlarged. The upper $SIZE$ cut from the low energy analysis was ignored and the $DIST$ cut adjusted accordingly to the $SIZE$ bin. Cuts on $HADRONNESS$ and $ALPHA$ were fixed to the corresponding $SIZE$ bin, without attempts to enhance the significance. The cuts used for the analysis are listed in the table below.

$SIZE$ ph.e.	$DIST$ [deg]	$HADRONNESS$	$ALPHA$ [deg]	$LEAKAGE$	$ISLAND$
$40 - 200$	0.2 ... 0.83	0.50	30		
$200 - 400$	0.2 ... 0.93	0.35	20	< 0.15	< 3
$400 - 30000$	0.2 ... 1.00	0.20	15		

Table 6.3: $SIZE$ dependent cuts on Hillas parameters used for the GRB data analysis (excepting GRB050713a).

6.2 GRB observations with the MAGIC telescope

Table 6.4 lists some key parameters of the 12 GRBs observed by MAGIC and summarises the instrument dependent observation time delays. Of special interest is the response time Δt_{accept} of the shift crew to accept the new target. This time is extracted from the end of the last data file, which is saved almost immediately after the confirmation by the telescope operator. For the presented bursts the average response time is $\langle \Delta t_{\text{accept}} \rangle = 17.8\,\text{s}$. Significant improvement of the response time by MAGIC can be achieved by eliminating this delay. It can be done by introducing a fully automatic, software controlled response to GRB alerts. Security regulations demand to ensure that no person is close to the telescope structure during the fast movement. This will be controlled in the near future by using safety measures on the entrance gates of the fence around the telescope area.

During the first nine GRB observations, the fast movement mode was still not implemented. Long slewing times were the consequence. Since December 2005 the repositioning speed was improved to the current values (see § 2.3.1). The shadowed column Δt_{obs} gives the time delay of the begin of the data taking from the GRB sky location to the burst onset T_0. It is a sum of the slewing time Δt_{slew}, the shifters response Δt_{accept} and the alert delay Δt_{alert} of the satellite and the GCN notice. The three last columns show the repositioning speed of the telescope. In some cases technical problems disturbed the movement and lead to longer delays. Figure 6.13 shows the distribution of the 12 GRBs, which have been observed by MAGIC, on the sky map in galactic coordinates.

GRB	satellite	Δt_{alert} [s]	Δt_{accept} [s]	Δt_{obs} [s]	Δt_{slew} [s]	ΔZd [deg]	ΔAz [deg]
GRB050408	HETE-2	6	-	16093	-	-	-
GRB050421	SWIFT	58	24	108	26	40	30
GRB050502a	INTEGRAL	39	15	689	223	25	254
GRB050505	SWIFT	540	87	717	90	30	114
GRB050509a	SWIFT	16	7	131	108	40	128
GRB050509b	SWIFT	15	10	108	83	28	86
GRB050528	SWIFT	43	22	77	12	2	7
GRB050713a	SWIFT	13	10	40	17	24	50
GRB050904	SWIFT	82	9	145	54	1	55
GRB060121	HETE-2	15	8	583	-	40	88
GRB060203	SWIFT	171	13	268	84	15	268
GRB060206	SWIFT	16	8	59	35	37	44

Table 6.4: Summary of GRB events observed by the MAGIC telescope in the first observation cycle. Δt_{alert} is the time from the burst onset T_0 until the receipt of the alert package by gspot. Δt_{accept} is the response time of the shift crew to approve the observation. Δt_{obs} is the begin of the observation in respect to T_0. Δt_{slew} is the telescope repositioning time from the previous source position with corresponding ΔZd and ΔAz slew in zenith and azimuth direction, respectively. The error on Δt_{slew} and hence also on Δt_{obs} is $\pm 5\,\text{s}$. The accuracy is based on the sequence the telescope position is saved in the data stream.

The following reasons lead to exclude some of the data sets presented in my thesis:

- **GRB050408:** The burst was triggered by the HETE-2 satellite at 16:22:51 UT. Due to daylight, data taking started about 4.5 h after the burst onset. This data sample was used as OFF data set for one other burst.

- **GRB050509b:** The burst was observed at a very high zenith angle of $\sim 70°$, giving a threshold energy of ~ 1 TeV. Because of the high zenith angle, the shift crew interrupted the observation after 11 min.

- **GRB050528:** Camera hardware problems during the observation resulted in bad data quality and lead to rejection of the data set.

Multiwavelength observations of GRBs do not always lead to significant detections at other wavelength bands. This can either originate from the nature of the burst, the duration of the emission, the time delay of the follow-up observation and also the accuracy of the determined position. Of course, observational conditions and sensitivity of the follow-up facilities play a very important role for the feasibility of the detection. Therefore some of the bursts observed by MAGIC have not been observed or detected by other observatories. Without sufficient observational information at other wavelengths, interpretation of MAGIC results are difficult. The next chapters summarise the knowledge of the selected GRB events. The information is mainly based on the observation reports distributed over GCN circulars or already published articles. My results, obtained from the analysis of the MAGIC data, are included in the second half of each chapter.

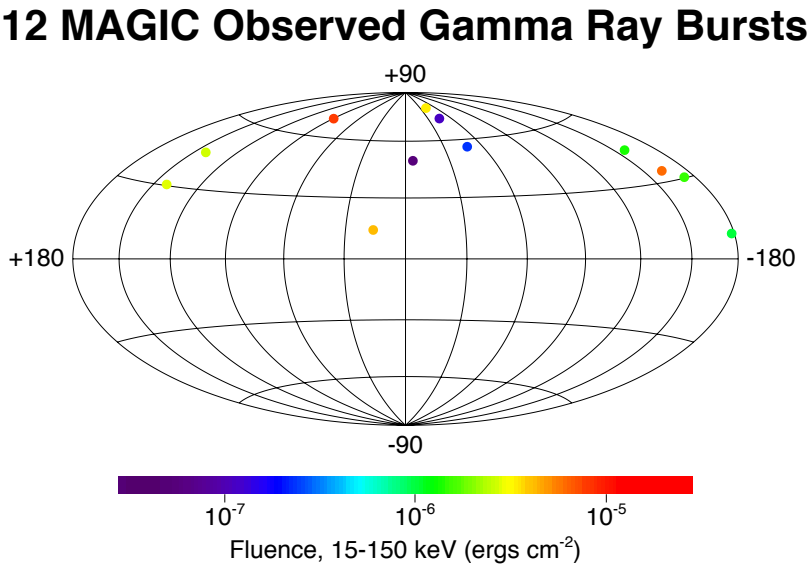

Figure 6.13: Distribution of the 12 GRBs with follow-up observations by the MAGIC telescope on the sky map in galactic coordinates. The colour code represents the fluence measured by BAT in the $15 - 150$ keV energy range.

Analysis of the SWIFT BAT and XRT data

The GRB satellite experiments – especially the SWIFT experiment – make their reprocessed data (level 2) available to the public[1]. I took therefore the opportunity to derive my own results from the SWIFT BAT and XRT data and included them in the following chapters. My results are compatible within errors with the published values in the GCN circulars and various publications.

- The level 2 BAT data for the GRB sample was processed using the standard BAT analysis software, following the description in [158]. The light curves were extracted in the energy range $15 - 150\,\mathrm{keV}$, correcting for the response matrix during slews[2]. For energies above 150 keV the BAT mask becomes transparent (see figure 6.20), reducing the max. energy of the detector to 150 keV. The obtained burst durations T_{90}, mean fluxes and spectral indices β_{BAT} are listed in the head of each individual GRB chapter. The spectral parameters for the BAT data were derived by fitting simple photon power-laws $A(E) = \kappa \cdot (E/1\,\mathrm{keV})^{-\beta_{\mathrm{BAT}}}$ over the period corresponding to T_{90} and the energy range between 15 keV and 150 keV. The normalisation factor κ has the unit photons $\mathrm{keV}^{-1}\,\mathrm{cm}^{-2}\,\mathrm{s}^{-1}$ at 1 keV and is also given with the resulting χ^2 of the fit. The single power-law provides statistically acceptable fits to the BAT data in all cases.
- The XRT data set was processed following the description in [159]. Data from the Windowed Timing (WT) and Photon Counting (PC) operating mode of the instrument were used. Processing of the data was done with the xrtpipeline script. I used the filtered event lists to generate the light curves and plot them together with the BAT data, when the observation window overlapped. The XRT count rates were converted to fluxes by fitting the spectra in the $0.3 - 10\,\mathrm{keV}$ energy range.

Fits and spectral analysis on both data sets were done using the X-ray spectral fitting package XSPEC [160]. Since both experiments cover different energy bands and seldom overlap in time, data from one experiment had to be converted into the bandpass of the other. I chose the $0.3 - 10\,\mathrm{keV}$ XRT bandpass to determine the fluxes. Errors on all values derived from this analysis include only statistical; No systematic values could be given.

Data from the two bursts observed by INTEGRAL (GRB050502a in § 6.2.2) and HETE-2 (GRB060121 in § 6.2.7) could not be analysed due to lack of time needed to understand the different analysis software of these satellites. In these cases figures were adopted from referenced publications.

[1] http://swift.gsfc.nasa.giv/docs/swift/archive/
[2] http://swift.gsfc.nasa.giv/docs/swift/analysis/

6.2.1 GRB050421: X-ray flares from an otherwise weak burst

Results from multiwavelength observations

Trigger:	
Satellite:	SWIFT / BAT
Time:	04:11:51 UT
Coordinates:	RA = 20h 29m 01s ; Dec = +73° 39' 17" (J2000)
Duration:	$T_{90} = 10.8 \pm 0.2\,\mathrm{s}$
Mean flux:	$15 - 150\,\mathrm{keV}$: $(1.01 \pm 0.27) \cdot 10^{-8}\,\mathrm{erg\,cm^{-2}\,s^{-1}}$
Spectral index:	$\beta_{\mathrm{BAT}} = 1.65 \pm 0.28$

GRB050421 was triggered by the BAT detector [162]. The BAT light curve and flux are shown in figure 6.14. It was a faint burst with total duration of 11.2 s in the BAT energy range ($15 - 150\,\mathrm{keV}$). The BAT spectrum could be fitted with a simple power-law model with $\beta_{\mathrm{BAT}} = 1.65 \pm 0.28$ and an normalisation factor $\kappa = 0.68 \pm 0.69$ ($\chi^2 = 31/58$). The fluence extracted for the T_{90} time window from the fit is $(1.1 \pm 0.3) \cdot 10^{-7}\,\mathrm{erg\,cm^{-2}}$.

The SWIFT spacecraft slewed to the BAT coordinates and began observations in X-rays, optical and UV wavelengths, 110 s after the burst onset T_0. While only upper limits in U, B and V wavelengths[3] were set ($< 17.5\,\mathrm{mag}$) [163], a fading X-ray counterpart by XRT was detected. The X-ray light curve shows at least two weak flares: The first flare peaking at $T_0 + 110\,\mathrm{s}$ and the second one peaking at $T_0 + 154\,\mathrm{s}$ [164]. Because of the large flux range shown in figure 6.14, the flares are hardly visible in this plot. The X-ray light curve is consistent with a rapid decline with a temporal index $\alpha_{\mathrm{XRT}} \sim 3.1$, which decays from $10^{-9}\,\mathrm{erg\,cm^{-2}\,s^{-1}}$ at $T_0 + 100\,\mathrm{s}$ to $< 7 \cdot 10^{-13}\,\mathrm{erg\,cm^{-2}\,s^{-1}}$ at $T_0 + 900\,\mathrm{s}$. A good joint fit to the BAT and XRT spectra before $T_0 + 171\,\mathrm{s}$ indicates that the early X-ray and γ-ray emissions are likely produced by the same mechanism.

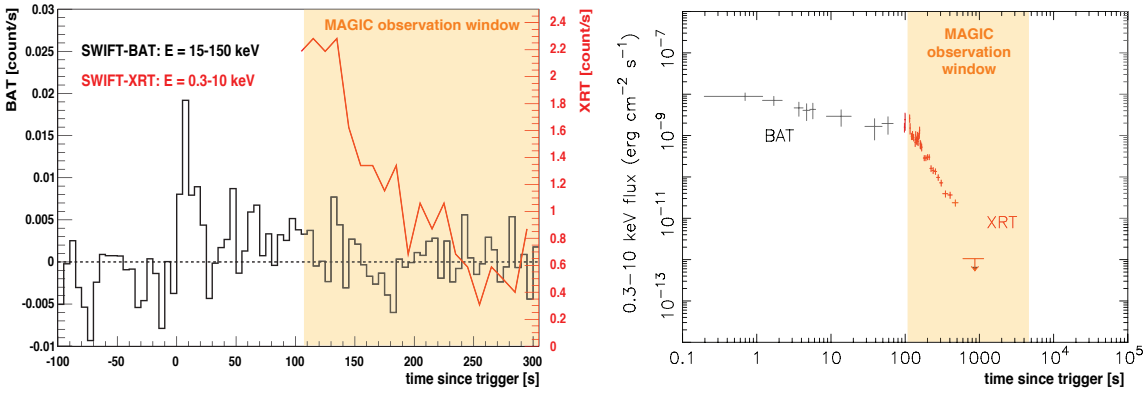

Figure 6.14: *Left:* Light curve of GRB050421 in two energy ranges measured by BAT and XRT. Because of low event rate, time bins of 5 s for the BAT and 10 s for XRT were selected. *Right:* Flux of GRB050421 measured by BAT and XRT. The orange shadowed area represents the start of MAGIC observation and the overlap with SWIFT data.

Various optical, IR and radio experiments performed follow-up observations of the burst afterglow, deriving only upper limits. No redshift was measured.

[3] The optical filter system of the three passbands U (ultraviolet), B (blue) and V (visible) is the standard among the astronomers.

Results from MAGIC observation

The alert was received by gspot at $T_0 + 58\,\mathrm{s}$. Because of moon time, hardware tests were ongoing and luckily the telescope was pointing towards the sky region close to the GRB. Accumulation of data started 50 s after receiving the alert, i.e. at $T_0 + 108\,\mathrm{s}$. The source was observed for 76 min until twilight. The zenith angle range of the observation was $54° \rightarrow 57°$.

No significant excess was detected by the MAGIC telescope. Due to the moon background light, high DT settings decreased significantly the sensitivity of the observation and resulted in very low trigger rates of $\sim 25\,\mathrm{Hz}$[4]. Table 6.5 summarises the results derived from my analysis. The upper limits are given in two energy bins, with the mean energy listed in the first column. The lowest energy range extracted in my analysis is $225 - 300\,\mathrm{GeV}$. It is slightly higher than the telescope threshold energy at this zenith angle range (from equation 1.6 follows: $E_{\mathrm{thr}}(50°) \approx 165\,\mathrm{GeV}$), caused by the high DT. The MAGIC observation overlapped with the X-ray flares detected by XRT. However, because of the extremely low trigger rate, no meaningful upper limits for the overlapping window could be extracted. Instead, I calculated the upper limits for the first 30 min of the MAGIC observation, covering the early afterglow period of the GRB.

$\langle E \rangle$ [GeV]	N_{ON}	N_{OFF}	σ_{OFF}	N_{ex} UL 95% CL	$\langle A_{\mathrm{eff}} \rangle$ $\times 10^8$ [cm^2]	Upper Limits		
						$\left[\frac{\mathrm{ph}}{\mathrm{cm^2\,keV\,s}}\right]$	$\left[\frac{\mathrm{erg}}{\mathrm{cm^2}}\right]$	C.U.
$T_0 + 108\,\mathrm{s} < t < T_0 + 1908\,\mathrm{s}$								
250	196	218	5.8	18.5	1.66	$1.16 \cdot 10^{-19}$	$0.38 \cdot 10^{-7}$	0.12
340	45	55.9	1.8	9.1	2.03	$0.33 \cdot 10^{-19}$	$0.21 \cdot 10^{-7}$	0.08

Table 6.5: Upper limits on VHE γ-ray emission from GRB050421. The upper limits correspond to the first 30 min of the MAGIC observation window and include a systematic uncertainty of 30%.

The two corresponding *ALPHA* distributions are shown in figure A.1, in the appendix.

I performed a search for short duration γ-ray emission above $E > 175\,\mathrm{GeV}$ in the MAGIC data set. The data was sampled in 20 s time bins, extracting the number of excess events from the *ALPHA* distributions in the signal region from the ON and OFF data. Figure 6.15 shows the results: A flat evolution centred around zero. No excess indicating delayed short emission period is visible. The slightly higher rate after $T_0 + 3500\,\mathrm{s}$ and the gap in the data is caused by manual change of the DT setting by the telescope operator.

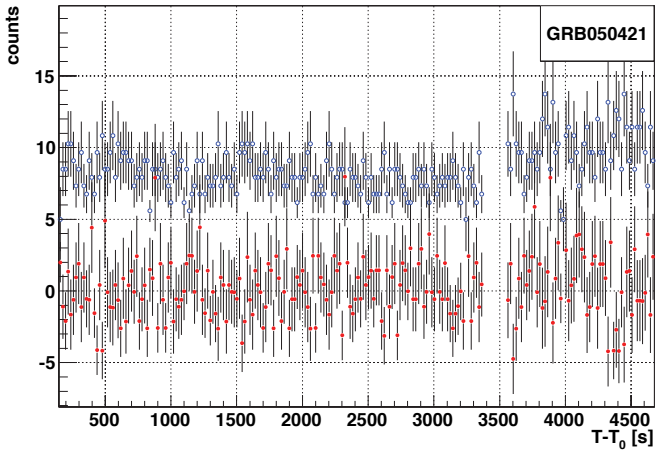

Figure 6.15: Light curve of GRB050421 for VHE γ-ray energies, as measured with the MAGIC telescope. Red filled circles denote the excess events while the blue open circles are the number of background events (the level is shifted by five counts per bin to separate the curves).

[4]The DT need to be adjusted according to the light of night sky, e.g. observation of a galactic or extragalactic sources, or moon light illumination. The event trigger rate should lie in the range between 100 Hz and 250 Hz.

6.2.2 GRB050502a: Early optical afterglow from a source at $z = 3.793$

Results from multiwavelength observations

Trigger:

Satellite:	INTEGRAL / IBIS
Time:	02:13:57 UT
Coordinates:	RA = 13h 29m 45s ; Dec = +42° 40' 26"
Duration:	$T_{90} = 20\,\mathrm{s}$
Fluence:	$20 - 200\,\mathrm{keV}$: $1.4 \cdot 10^{-6}\,\mathrm{erg\,cm^{-2}}$

GRB050502a was triggered by INTEGRAL IBIS [165], during the commissioning phase of the spacecraft. The light curve is shown on the left side of figure 6.16. Data gaps at $t < T_0 - 1\,\mathrm{s}$ and $T_0 + 14\,\mathrm{s}$ are associated with hardware response problems [166]. With a fluence of $1.4 \cdot 10^{-6}\,\mathrm{erg\,cm^{-2}}$ in the T_{90} integration window and a peak flux of $2 \cdot 10^{-7}\,\mathrm{erg\,cm^{-2}\,s^{-1}}$, this burst can be classified amongst the faint/intermediate fluence GRBs. The spectrum can be described by the Band function with $\alpha = 0.89 \pm 0.25$, $\beta = -3$ and a peak energy $E_{\mathrm{peak}} = 83 \pm 44\,\mathrm{keV}$ [166].

Many telescopes were able to detect the fading optical afterglow. The data spans nearly three decades in time and begin at $T_0 + 60\,\mathrm{s}$ (see diagram on the right side of figure 6.16) [167, 168]. A shallow break in the R light curve of the GRB afterglow at approximately 6000 s postburst is indicated with an arrow. It was interpreted as the passage of the synchrotron cooling frequency ν_c. Strong absorption features in the spectrum measured by Keck-I were interpreted as $\mathrm{Si_{II}}\,(1260)$[5], indicating a redshift of $z = 3.793$ [169].

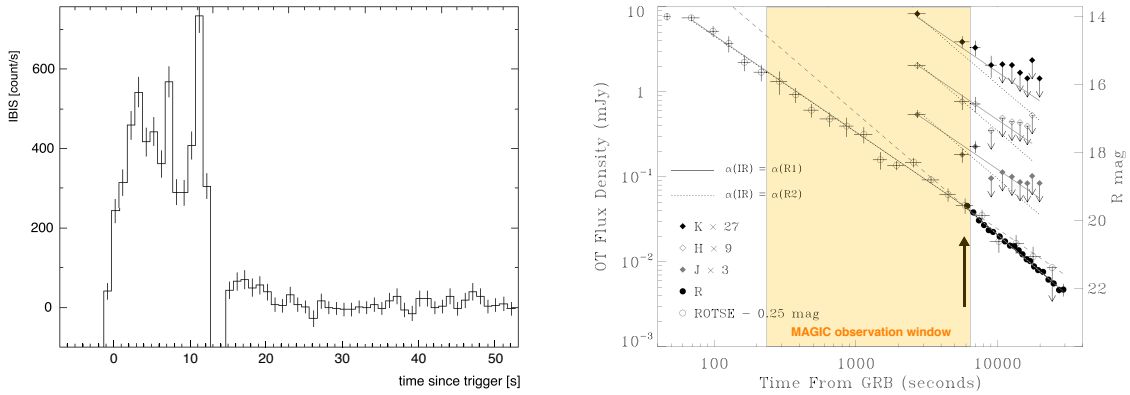

Figure 6.16: *Left:* Light curve of GRB050502a as measured by INTEGRAL IBIS. Data before $T_0 - 1\,\mathrm{s}$ is missing in the figure because the satellite was performing a slew and the gap at $T_0 + 14\,\mathrm{s}$ is due to satellite telemetry saturation. *Right:* Light curves of the optical-IR data of GRB050502a. The J, H and K bands are offset by factors of 3, 9 and 27, respectively, for clarity. The optical light curve is fit by a broken power-law, where t^{α} steepens from $\alpha = -1.13 \pm 0.02$ to -1.44 ± 0.02 at $\sim 5700\,\mathrm{s}$. The arrow denotes the jet break time. Figure from [167].

[5]The $\mathrm{Si_{II}}$ is produced by electron collision or photo-ionisation by the radiation of the central star or by increase of the trapped H Lyα radiation.

Results from MAGIC observation

The alert was received by gspot at $T_0 + 39\,\mathrm{s}$. The previously observed source was located at the opposite direction of the sky. It took 15 s to accept the new target by the shift crew and additional 223 s to reposition the telescope for $\Delta Az \approx 254°$. Furthermore, problems with the data acquisition in the first $\sim 11\,\mathrm{min}$ of data taking lead to reduction of the data set. Useful data from GRB050502a is available from $T_0 + 689\,\mathrm{s}$. The source was observed for 102 min, until the LONS due to moon shine became too bright. Changing moon light conditions are seen in the search for short lasting γ-ray emission shown in figure 6.17. The event trigger rate was at 240 Hz in the beginning of the observation, reducing to 160 Hz towards the end. The zenith angle of the observation span the range of $30° \rightarrow 50°$.

No significant excess was found in the MAGIC observation data. Also in this case, high DT settings during the moon time decreased the sensitivity of the observation. Table 6.6 lists the upper limits for the first 30 min of MAGIC observation. The corresponding $ALPHA$ Hillas distributions are shown in the figure A.2 in the appendix.

$\langle E \rangle$ [GeV]	N_{ON}	N_{OFF}	σ_{OFF}	N_{ex} UL 95% CL	$\langle A_{\mathrm{eff}} \rangle$ $\times 10^8$ [cm^2]	Upper Limits		
						$\left[\frac{\mathrm{ph}}{\mathrm{cm^2\,keV\,s}}\right]$	$\left[\frac{\mathrm{erg}}{\mathrm{cm^2}}\right]$	C.U.
$T_0 + 689\,\mathrm{s} < t < T_0 + 2489\,\mathrm{s}$								
190	2442	2423	27.0	166.3	1.23	$2.37 \cdot 10^{-18}$	$3.73 \cdot 10^{-7}$	1.20
250	530	462	11.5	191.7	1.89	$1.05 \cdot 10^{-18}$	$3.36 \cdot 10^{-7}$	1.07
340	177	146	8.0	94.3	2.35	$3.76 \cdot 10^{-19}$	$1.99 \cdot 10^{-7}$	0.85
560	158	116	7.1	116.7	4.45	$0.84 \cdot 10^{-19}$	$1.61 \cdot 10^{-7}$	0.69

Table 6.6: Upper limits on VHE γ-ray emission from GRB050502a. The results correspond for the first 30 min of the MAGIC observation window and include a systematic uncertainty of 30%.

The search for short lasting γ-ray emission period in the MAGIC data set did not arise any significant excess. Figure 6.17 shows the corresponding plot with the number of excess events in 20 s bins, extracted from the $ALPHA$ distributions for energies $E > 175\,\mathrm{GeV}$.

The non detection of VHE γ-rays by MAGIC is not in contradiction with any GRB model. Assuming that photons would be boosted to VHE by large Γ factors in the jet environment, the high redshift ($z = 3.793$) would lead to annihilation processes with the EBL. The resulting cut-off in the energy spectrum is expected to be far below the energy range accessible by MAGIC (see § 1.1.3).

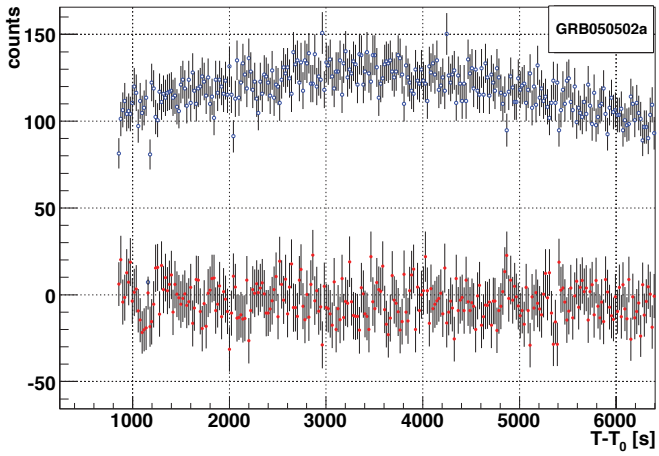

Figure 6.17: Light curve of GRB050502a for VHE γ-ray energies, as measured with the MAGIC telescope. Red filled circles denote the excess events while the blue open circles are the number of background events. Bins are integrated over 20 s.

6.2.3 GRB050505: Intrinsic burst parameters with $z = 4.27$

Results from multiwavelength observations

Trigger:	
Satellite:	SWIFT / BAT
Time:	23:22:21 UT
Coordinates:	RA = 9h 27m 03s ; Dec = +30° 16' 21"
Duration:	$T_{90} = 62.8 \pm 0.2\,\mathrm{s}$
Mean flux:	$15 - 150\,\mathrm{keV}$: $(3.75 \pm 0.43) \cdot 10^{-8}\,\mathrm{erg\,cm^{-2}\,s^{-1}}$
Spectral index:	$\beta_{\mathrm{BAT}} = 1.43 \pm 0.08$

GRB050505 was triggered by the BAT detector [170]. The BAT light curve shows a multi-peaked structure with a total duration of 69.2 s. The initial peak began at $\sim 15\,\mathrm{s}$ before the trigger and extended to 10 s after the trigger. There are three further short spikes at $T_0 + 23.3\,\mathrm{s}$, $T_0 + 30.4\,\mathrm{s}$ and $T_0 + 50.4\,\mathrm{s}$, as shown in figure 6.18. The $15 - 150\,\mathrm{keV}$ BAT spectrum during T_{90} can be approximated by a single power-law with a photon index of $\beta_{\mathrm{BAT}} = 1.43 \pm 0.08$ and a normalisation factor $\kappa = 1.05 \pm 0.31$ ($\chi^2 = 66/75$). The fluence in the $15 - 150\,\mathrm{keV}$ energy range, extracted from the fitted model, is $(2.4 \pm 0.3) \cdot 10^{-6}\,\mathrm{erg\,cm^{-2}}$ for the burst duration T_{90}. The burst fluence is slightly higher than the average one detected by SWIFT to date.

Due to earth limb observing constraint, SWIFT could slew to the BAT position only $\sim 47\,\mathrm{min}$ after the BAT trigger. No optical/UV transient was detected by the onboard narrow field instruments. Upper limits of $< 17.7\,\mathrm{mag}$ were set in both bands. XRT detected the fading X-ray afterglow during six days of follow-up observations. The combined BAT and XRT flux light curves are shown in figure 6.18.

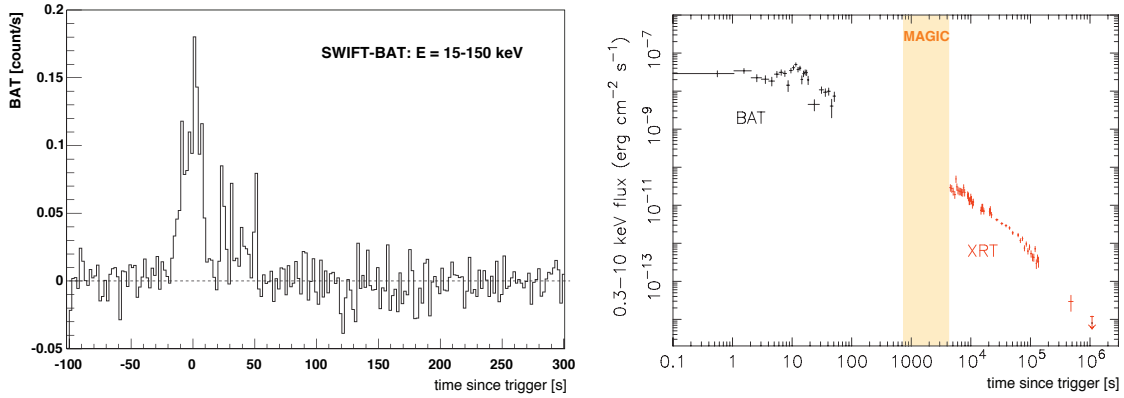

Figure 6.18: *Left:* Light curve of GRB050505 measured by BAT. There is no overlap between the BAT and the XRT observation. The time bins of the light curve are 2 s. *Right:* Flux of GRB050505 as measured by BAT and XRT. The shadowed area represents the MAGIC observation window, starting 717 s after the burst onset.

The X-ray data can be fit with a doubly broken power-law, where the first break at $T_0 + 7.4\,\mathrm{ks}$ can be explained by the end of energy injection into the forward shock. The second break at $T_0 + 58\,\mathrm{ks}$ is interpreted as the jet break [171].

Higher sensitivity of ground based telescopes made the discovery of the optical counterpart of this event possible. The first reported detection of the fading afterglow was from the Keck-I

telescope. The measured spectrum shows strong absorption lines, including Si_{IV} (1393, 1402) at a redshift of $z = 4.27$ [172].

Using the redshift and the measured jet break in the X-ray light curve, one can calculate the intrinsic parameters of the GRB. From the time of the jet break an opening angle of $2.2° \leqslant \Theta_j \leqslant 3.8°$ can be concluded. The energy released in γ-rays in this event is then in the range $3.17^{+0.86}_{-1.11} \cdot 10^{50} \leqslant E_\gamma \leqslant 9.99^{+3.00}_{-3.24} \cdot 10^{50}$ erg for a rest frame energy band of $1-10^4$ keV [171]. This burst agrees well with typical E_γ values determined from other bursts [173].

Results from MAGIC observation

The alert was received by gspot at $T_0 + 540\,\mathrm{s}$. Because of the long delay of the alert, and the observation gap from SWIFT, no overlap between satellite measurements and MAGIC observation took place. Data taking started 177 s after the alert, at $T_0 + 717\,\mathrm{s}$. The observation continued from a zenith angle of 50° and lasted for 105 min, until the maximum defined zenith angle of 70° was reached. The event trigger rate followed the large movement in zenith from 150 Hz in the beginning to 70 Hz at the end of the observation. No significant signal was detected by the MAGIC telescope.

$\langle E \rangle$ [GeV]	N_{ON}	N_{OFF}	σ_{OFF}	N_{ex} UL 95% CL	$\langle A_{eff} \rangle \times 10^8$ [cm^2]	Upper Limits $\left[\frac{ph}{cm^2\,keV\,s}\right]$	Upper Limits $\left[\frac{erg}{cm^2}\right]$	C.U.
$T_0 + 717\,\mathrm{s} < t < T_0 + 2517\,\mathrm{s}$								
180	428	370	7.3	163.6	0.89	$37.8 \cdot 10^{-19}$	$5.02 \cdot 10^{-7}$	1.66
240	1033	1013	19.9	123.7	1.73	$8.21 \cdot 10^{-19}$	$2.45 \cdot 10^{-7}$	0.76
320	940	968	8.4	48.1	2.20	$1.88 \cdot 10^{-19}$	$0.97 \cdot 10^{-7}$	0.36
530	428	404	2.5	91.1	4.92	$0.69 \cdot 10^{-19}$	$1.15 \cdot 10^{-7}$	0.49

Table 6.7: Upper limits on VHE γ-ray emission from GRB050505. The upper limits correspond to the first 30 min of the MAGIC observation and include a systematic uncertainty of 30%.

Table 6.7 summarises results derived from my analysis. Upper limits for the first 30 min of the early afterglow period are given. The *ALPHA* distributions are shown in figure A.3.

The non detection of VHE γ-rays from this object is a strict consequence of its redshift. As mentioned in the previous subparagraph, absorption of VHE photons by the EBL limit the observability of any hypothetical emission in the GeV energy range. The search for short lasting γ-ray emission period in the MAGIC data (as shown in figure 6.19) confirm the non detection.

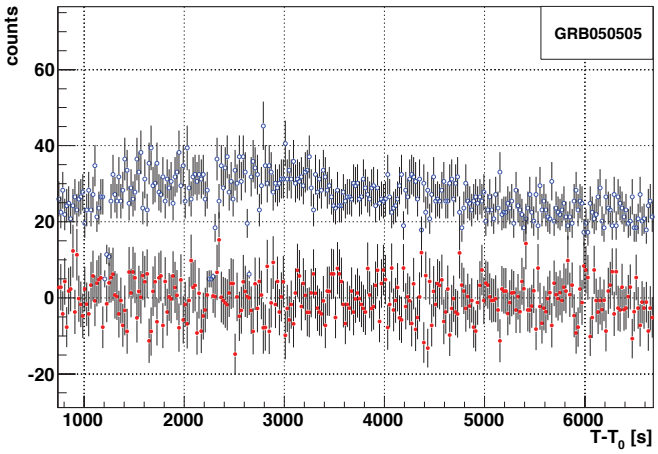

Figure 6.19: Light curve of GRB050505 for VHE γ-ray energies, as measured with the MAGIC telescope. Red filled circles denote the excess events while the blue open circles are the number of background events (shifted by five counts to separate the curves). Bins are integrated over 20 s.

6.2.4 GRB050509a: A faint burst without afterglow candidate

Results from multiwavelength observations

Trigger:

Satellite:	SWIFT / BAT
Time:	01:46:29 UT
Coordinates:	RA = 20h 42m 20s ; Dec = +54° 04' 16"
Duration:	$T_{90} = 10.6 \pm 0.2\,\mathrm{s}$
Mean flux:	$15 - 150\,\mathrm{keV}$: $(2.62 \pm 0.28) \cdot 10^{-8}\,\mathrm{erg\,cm^{-2}\,s^{-1}}$
Spectral index:	$\beta_{\mathrm{BAT}} = 2.07 \pm 0.11$

GRB050509a was triggered by the BAT detector [174]. The BAT light curve is shown in figure 6.20. It contains a single main emission part with a small peak on the rising edge at $T_0 - 6\,\mathrm{s}$. The total burst duration was 12.8 s. The BAT spectrum could be described with a single power-law with a photon index of $\beta_{\mathrm{BAT}} = 2.07 \pm 0.11$ and a normalisation factor $\kappa = 9.35 \pm 3.54$ ($\chi^2 = 61/58$). This power-law model predicts a fluence of $(2.8 \pm 0.4) \cdot 10^{-7}\,\mathrm{erg\,cm^{-2}}$ in the energy range $15 - 150\,\mathrm{keV}$ and burst duration T_{90}. This event can be classified as a weak GRB. Only very faint X-ray emission was detected from the afterglow [175]. The Nordic Optical Telescope (NOT) observed the sky location in the time between 20 min and 150 min after the burst onset. Non of these images showed a new source in the I band, resulting in an upper limit I < 22.5 mag. The redshift of this source was not measured.

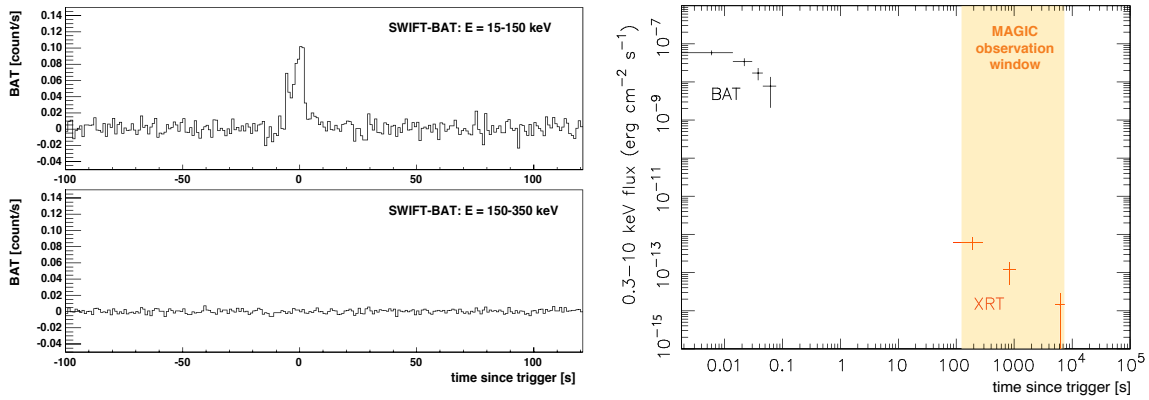

Figure 6.20: *Left:* Light curve of GRB050509a in two energy bins, as measured by BAT. The lower figure illustrates - representatively for all BAT data - that the BAT mask is transparent for energies above 150 keV. No signal can be measured by BAT above this energy. The time resolution is 1 s per bin. *Right:* Flux of GRB050509a, as measured by BAT and XRT.

Results from MAGIC observation

The alert was received by gspot at $T_0 + 16\,\mathrm{s}$. After affirmation by the shift crew the telescope needed to be repositioned in azimuth by almost 130°. The time required for the response until start of the data taking was 115 s. Starting at $T_0 + 131\,\mathrm{s}$, the sky location was observed for almost 120 min with decreasing zenith range 58° → 42°. The raw event trigger rate was in the beginning of the observation at 150 Hz, increasing linearly up to 180 Hz, by following the decreasing zenith angle of the observation.

No significant excess was detected by the MAGIC telescope. The upper limits for the first 30 min of the MAGIC observation from my analysis are shown in the table 6.8. Because of the relatively large zenith angle of the observation, the lowest energy bin, extracted from the absolute image cleaning, starts at 225 GeV. The corresponding $ALPHA$ distributions are shown in figure A.4. Results from the search for short VHE γ-ray emission in the whole MAGIC data set is shown in figure 6.21. Also this attempt yields no hint for significant excess during the first two hours of the GRB afterglow phase. Since the redshift of the source was not measured, conclusions on the existence of a VHE component in this event are not solid enough. Only if the source was located at $z < 1$, one could start to interpret the non detection by MAGIC. However, only a small fraction of the GRBs detected by SWIFT (30%) lie below this redshift.

$\langle E \rangle$ [GeV]	N_{ON}	N_{OFF}	σ_{OFF}	N_{ex} UL 95% CL	$\langle A_{\mathrm{eff}} \rangle$ $\times 10^8$ [cm^2]	Upper Limits		
						$\left[\frac{\mathrm{ph}}{\mathrm{cm^2\,keV\,s}}\right]$	$\left[\frac{\mathrm{erg}}{\mathrm{cm^2}}\right]$	C.U.
$T_0 + 131\,\mathrm{s} < t < T_0 + 1931\,\mathrm{s}$								
250	869	841	11.6	123.7	1.70	$7.54 \cdot 10^{-19}$	$3.87 \cdot 10^{-7}$	1.41
340	1651	1610	13.2	170.8	2.02	$6.25 \cdot 10^{-19}$	$3.87 \cdot 10^{-7}$	1.42
550	2355	2375	12.7	96.7	4.84	$6.74 \cdot 10^{-19}$	$1.25 \cdot 10^{-7}$	0.53

Table 6.8: Upper limits for the VHE γ-ray emission from GRB050509a. The upper limits correspond to the first 30 min of the MAGIC observation window and include a systematic uncertainty of 30%.

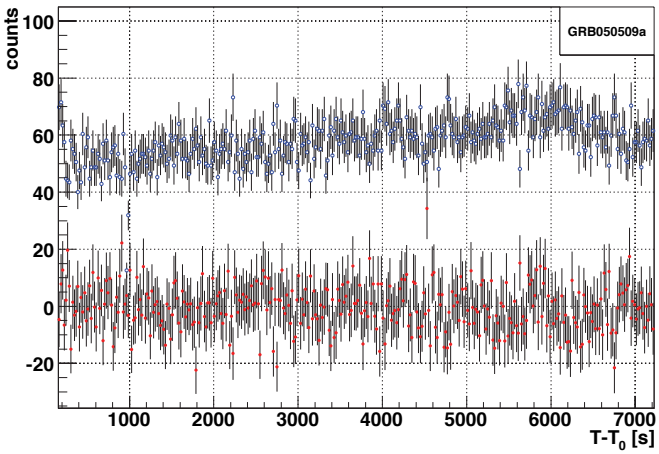

Figure 6.21: Light curve of GRB050509a for VHE γ-ray energies, as measured with the MAGIC telescope. Red filled circles denote the excess events while the blue open circles are the number of background events. Bins are integrated over 20 s.

6.2.5 GRB050713a: First GRB prompt emission phase observed by an IACT

Results from multiwavelength observations

Trigger:	
Satellite:	SWIFT / BAT
Time:	04:29:02 UT
Coordinates:	RA = 21h 22m 09s ; Dec = +77° 04' 24"
Duration:	$T_{90} = 129.2 \pm 0.2\,\mathrm{s}$
Mean flux:	$15 - 150\,\mathrm{keV}$: $(2.49 \pm 0.18) \cdot 10^{-8}\,\mathrm{erg\,cm^{-2}\,s^{-1}}$
Spectral index:	$\beta_{\mathrm{BAT}} = 1.45 \pm 0.05$

GRB050713a was triggered by the BAT detector [176]. The burst can be classified as a long, bright burst with a total duration of 186 s in the BAT energy range $15 - 150\,\mathrm{keV}$. The main peak, which lasted until $T_0 + 40\,\mathrm{s}$, had triggered the detector. A precursor at $T_0 - 60\,\mathrm{s}$ and three smaller flares at $T_0 + 50\,\mathrm{s}$, $T_0 + 65\,\mathrm{s}$, $T_0 + 105\,\mathrm{s}$ are present in the light curve, shown in figure 6.22. There is some hint of further emission at the onset of the flare seen in X-rays at $T_0 + 160\,\mathrm{s}$. The spectrum can be approximated by a power-law with a photon index $\beta_{\mathrm{BAT}} = 1.45 \pm 0.05$ and a normalisation factor $\kappa = 0.77 \pm 0.14$ ($\chi^2 = 66/58$). The fluence from the used model is obtained to be $(3.2 \pm 0.2) \cdot 10^{-6}\,\mathrm{erg\,cm^{-2}}$ in the $15 - 150\,\mathrm{keV}$ energy range and a burst duration T_{90}.

The main peak was also observed by the Konus-Wind satellite [177], which is less sensitive, but has a slightly wider energy range than the BAT detector. The joint data can be fit with a power-law photon spectrum with photon index of $\alpha = 1.29 \pm 0.07$ and $E_{\mathrm{peak}} = 443^{+134}_{-88}\,\mathrm{keV}$ [178].

The narrow field instruments of the SWIFT satellite started to observe the event at $T_0 + 72.6\,\mathrm{s}$. XRT began taking data during the latter portion of the flare detected in BAT at $T_0 + 65\,\mathrm{s}$. The subsequent flares were also seen by XRT.

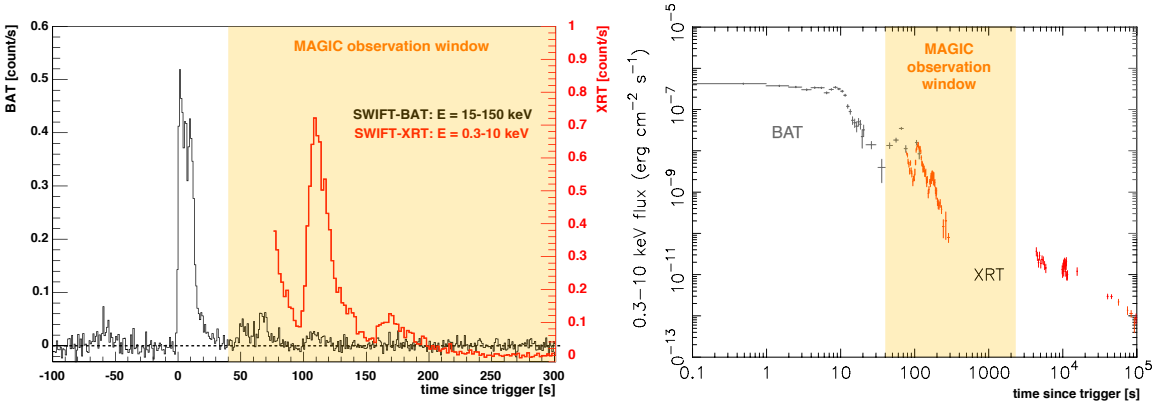

Figure 6.22: *Left:* Light curve of GRB050713a measured by BAT and XRT in two different energy bins. The time binning for BAT was chosen to 1 s and XRT to 2 s. *Right:* Flux of the prompt and afterglow emission measured by BAT and XRT. The orange shadowed areas illustrate the observation window of MAGIC.

It is the first time BAT and XRT produced a well sampled, simultaneous dataset covering multiple flares. Further simultaneous observation of the afterglow by XMM-Newton and XRT produced consistent results, showing a break in the light curve at $T_0 + 15\,\mathrm{ks}$. These measurements cover an unusually broad spectral range of the prompt emission and provide a detailed X-ray follow-up of the afterglow.

The decaying optical afterglow was detected by the RAPTOR-S robotic telescope at $R = 18.4 \pm 0.18$ and by the robotic Liverpool Telescope, located on La Palma close to MAGIC. Both observations started a few minutes after the burst onset. The X-ray, γ-ray and optical measurements are summarised in figure 6.23. No redshift could be determined.

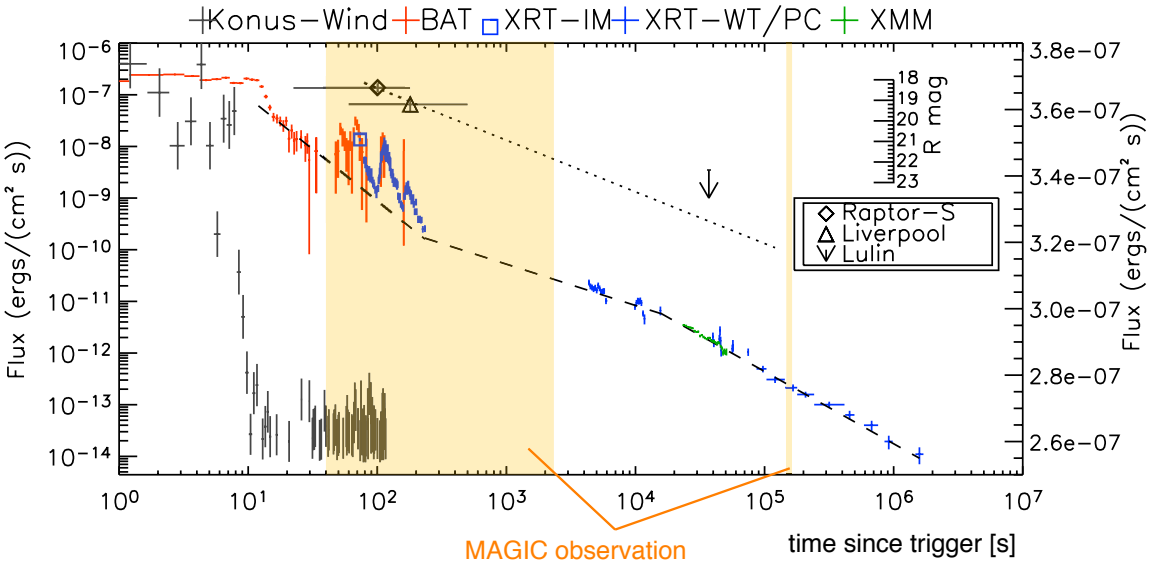

Figure 6.23: Broadband X-ray/γ-ray and optical light curve of GRB050713a. Results from SWIFT, Konus-Wind (axis on the right hand side), XMM-Newton and optical telescopes are shown. The time window of MAGIC observation is marked as a shadowed area. The dashed line is the supposed underlying power-law decay. Figure from [178].

Observation of the prompt and early afterglow phase by MAGIC

The MAGIC telescope was able to observe part of the prompt emission phase detected by BAT and Konus-Wind. The alert was obtained by gspot 13 s after the burst onset. Quick response of the shift crew and fast repositioning of the telescope allowed to start data taking at $T_0 + 40\,\mathrm{s}$, 27 s after the alert. In total 2200 s of data were collected until twilight. The observation window covered by MAGIC did not contain the main peak, detected in the keV − MeV energies, but overlapped with the strong X-ray flares measured by XRT. The same region of the sky was observed 48 h after the burst onset, collecting additional 49 min of data. This data was used to determine the background contamination (OFF data). The sky coordinates were observed at the zenith range of $47° \rightarrow 52°$.

Dedicated low energy analysis for GRB050713a

The data collected from GRB050713a by MAGIC represents the first successful GRB prompt emission observation by an IACT in the history. The rareness of such an observation provoked me and Markus Gaug [129] to develop a new analysis method for dedicated low energy signal extraction.

We cleaned the data using two different image cleaning algorithms. Beside the standard absolute image cleaning, a new algorithm using the time information, was used (see § 5.3). An upper $SIZE$ cut < 400 was applied. In this way we tried to keep only showers with energy $< 300\,\mathrm{GeV}$ and train the RF gamma/hadron separation in the low energy regime. We tested the complete analysis chain on the data taken from the flare of Mkn 501, yielding a 5σ detection in the energy range between 60 and 100 GeV (see § 6.1). When comparing with the standard analysis, we could extract at least three lower energy bins with our new analysis, thus significantly decreasing the analysis energy threshold. The data was divided into two energy bins: $100-200\,\mathrm{GeV}$ and $200-300\,\mathrm{GeV}$. The lower edge was limited by the observation zenith angle of $\sim 50°$, while the maximum energy was a consequence of the upper $SIZE$ cut.

We performed four different attempts to search for possible signals:

1. Search for a signal in the first 90 s of the observation. It represents the overlap with the BAT light curve until the end of T_{90}. The remaining data was used for OFF data.

2. Search for a signal within the first 1000 s of observation. Remaining data was used for OFF data.

3. Search for signal in the entire ON data sample. Data recorded during the dedicated observation two days after the GRB was used as OFF sample.

4. Search in the ON data set by means of a 100 s sliding interval for possible delayed short emission. The remaining ON data was used for background extraction.

None of these methods showed a significant excess over background. From the $ALPHA$ distributions, shown in the appendix A, upper limits on the number of excess events in the signal region for the three different time bins of 90 s, 1000 s and 2200 s were calculated. The search for possible 100 s short peak emission in the MAGIC observation time window was done for the entire data sample, which was divided into 22 equal time slices, sliding the window over the whole observation range. The remaining data was used for OFF data. A second search was performed, shifting the phase of the time slice by 50 s. Figure 6.24 shows the number of excess events in the corresponding time intervals and the significances. The distribution of the significances show the expected Gaussian distribution centred at zero with the width of 1σ, indicating the case of a non-detection. From the absence of a signal in the peak emission search, a global upper limit for any 100 s interval, based on the slice with the highest number of excess events, was derived (see figure A.8).

For the three fixed time intervals the limits on the number of excess events N_{ex} listed in table A.1, were converted to a flux and a fluence upper limits. The conversion was done assuming a power-law spectrum quoted in formula 5.16. Because of the not known spectral parameters, values for $\alpha = \{1.0, 2.0, 2.25, 2.5, 3.0\}$ were used. Finally we also calculated the upper limits assuming an exponential cutoff spectrum (formula 5.17) with a break energy of $E_{\mathrm{b}} = 200\,\mathrm{GeV}$ and HE spectral index $\alpha = 2.5$. The selection of the α-value was done by

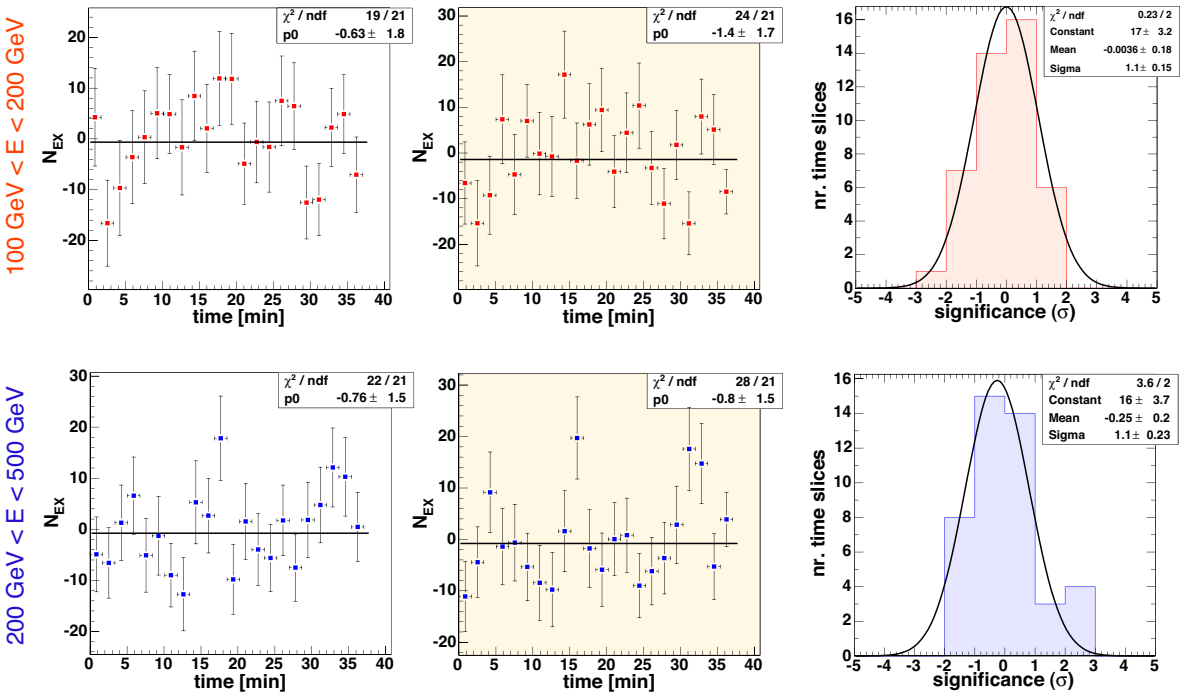

Figure 6.24: Excess events for the VHE γ-ray peak emission search in the GRB050713a data in bins of 100 s. The second column shows the results from the shifted phase by 50 s. The significances (right column) are centred around zero with a width of 1σ, making them compatible with pure fluctuations of the background in the energy range above 100 GeV.

using typical values determined from the BATSE bursts (see figure 1.10 and [20]). Table A.2 lists all upper limits for the different time bins and image cleaning algorithms. Whereas the spectral index α changes the limits only marginally, the time image cleaning gives on average 40% better results than the standard absolute cleaning. The final results obtained with the time image cleaning and the worst values of the corresponding sequence are summarised in table 6.9. Systematic uncertainties on the absolute energy calculation, trigger inefficiencies, as well as global MC agreement were summed up quadratically to about 30% and are also accounted for. The fixed time intervals used for the upper limit calculation scale in the ratio 1:10:25. The differential flux sensitivity should scale more or less with one over the square root of the measured time, which is the case.

For this data I also performed the search for short lasting VHE γ-ray emission in time bins of 20 s. Figure 6.25 shows the number of excess events in the signal region of the $ALPHA$ distribution for the ON and OFF data. No enhancement of the events measured by MAGIC, in correlation with the time of the X-ray flares, was seen. The scan over the whole data set did not retrieve any hint for delayed activity of the emission. Further physics discussion on this and the next event (GRB050904) is done in § 6.3.

$\langle E \rangle$ [GeV]	N_{ON}	N_{OFF}	σ_{OFF}	N_{ex} UL 95% CL	$\langle A_{\mathrm{eff}} \rangle$ $\times 10^8$ [cm^2]	Upper Limits		
						$\left[\frac{\mathrm{ph}}{\mathrm{cm^2\,keV\,s}}\right]$	$\left[\frac{\mathrm{erg}}{\mathrm{cm^2}}\right]$	C.U.
$T_0 + 40\,\mathrm{s} < t < T_0 + 130\,\mathrm{s}$								
160	74	74.8	1.2	17.5	3.1	$1.3 \cdot 10^{-17}$	$1.35 \cdot 10^{-7}$	4.2
280	46	49.0	0.8	12.1	5.3	$3.0 \cdot 10^{-18}$	$0.34 \cdot 10^{-7}$	4.1
$T_0 + 40\,\mathrm{s} < t < T_0 + 1040\,\mathrm{s}$								
160	474	465.9	9.3	60.4	2.5	$3.3 \cdot 10^{-18}$	$3.50 \cdot 10^{-7}$	1.1
290	167	167.8	7.3	31.1	3.4	$2.9 \cdot 10^{-19}$	$0.73 \cdot 10^{-7}$	0.4
$T_0 + 40\,\mathrm{s} < t < T_0 + 2240\,\mathrm{s}$								
160	1095	1101.4	13.6	74.1	2.8	$1.4 \cdot 10^{-18}$	$3.30 \cdot 10^{-7}$	0.4
290	99	82.7	1.0	37.6	3.7	$2.6 \cdot 10^{-19}$	$1.54 \cdot 10^{-7}$	0.4
peak emission search in any 100 s interval								
160	106	58.7	1.1	41.1	1.9	$1.6 \cdot 10^{-17}$	$1.40 \cdot 10^{-7}$	5.2
280	62	52.2	1.0	37.1	5.7	$2.8 \cdot 10^{-18}$	$0.52 \cdot 10^{-7}$	3.8

Table 6.9: Upper limits on VHE γ-ray emission from GRB050713a. The upper limits were obtained for the three fixed time bins of 90 s, 1000 s and 2200 s of the MAGIC observation. The last raw gives the upper limits for the peak emission search in 100 s bins. Results from the time image cleaning a systematic uncertainty of 30% are shown.

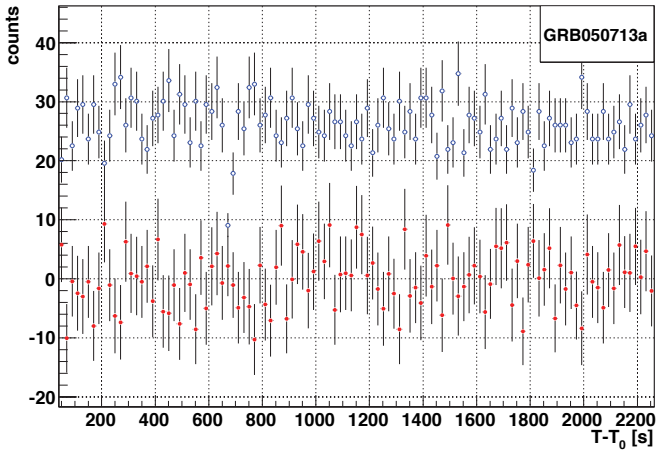

Figure 6.25: Light curve of GRB050713a for VHE γ-ray energies, as measured with the MAGIC telescope. Red filled circles denote the excess events while the blue open circles are the number of background events (the level is shifted by five counts to separate the curves). Bins are integrated over 20 s.

6.2.6 GRB050904: Second GRB observed by MAGIC during the prompt emission phase - most distant cosmic explosion ever observed

Results from multiwavelength observations

Trigger:

Satellite:	SWIFT / BAT
Time:	01:51:44 UT
Coordinates:	RA = 00h 54m 50s ; Dec = +14° 05' 04"
Duration:	$T_{90} = 228.2 \pm 0.2\,\mathrm{s}$
Mean flux:	$15 - 150\,\mathrm{keV}$: $(2.21 \pm 0.10) \cdot 10^{-8}\,\mathrm{erg\,cm^{-2}\,s^{-1}}$
Spectral index:	$\beta_{\mathrm{BAT}} = 1.24 \pm 0.04$

GRB050904 triggered the BAT detector [180]. The BAT spectrum can be approximated by a single power-law with a photon index $\beta_{\mathrm{BAT}} = 1.24 \pm 0.04$ and a normalisation factor $\kappa = 0.29 \pm 0.05$ ($\chi^2 = 50/58$). The fluence emitted within T_{90} in the BAT energy range was determined from the model to be: $(5.0 \pm 0.2) \cdot 10^{-6}\,\mathrm{erg\,cm^{-2}}$, consistent with the results quoted in [181].

Figure 6.26 shows the history of the burst. The BAT light curve shows two main peaks: The first one starting at $T_0 + 10\,\mathrm{s}$ and a long-lasting one starting at $T_0 + 80\,\mathrm{s}$. In addition two shorter emissions in between the peaks are present. The early XRT light curve (starting at $T_0 + 161\,\mathrm{s}$) fades with a steep power-law with an index $\beta_{\mathrm{XRT}} = 2.07 \pm 0.03$, overlapping with a re-brightening at $\sim 400\,\mathrm{s}$ after the burst onset. The X-ray emission was monitored by the XRT up to 10 days after the burst. The light curve reveals highly irregular intensity variations in the later period, interpreted as later internal shocks related to central engine activity. In this scenario, they would have the same origin as the first γ-ray emission, which would require the central engine to remain active for at least 5000 s.

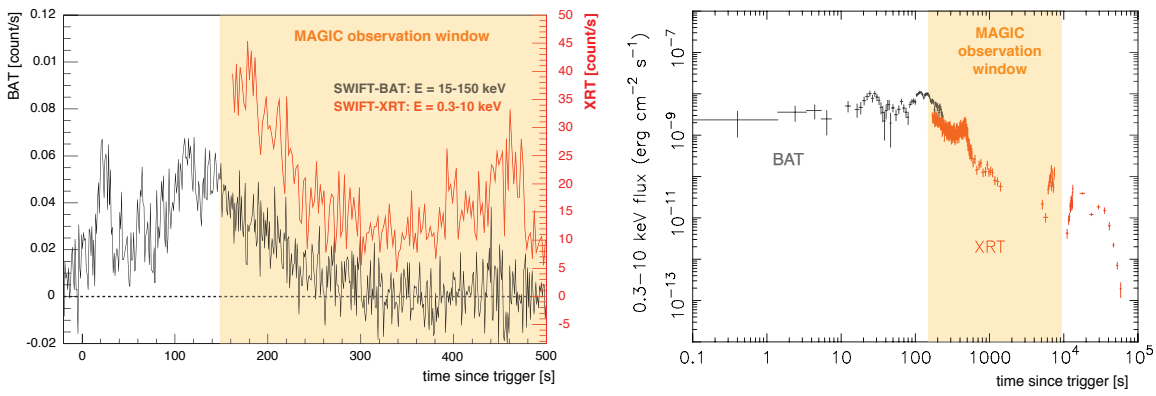

Figure 6.26: *Left:* Light curve of GRB050904 in two energy bins measured by BAT and XRT. The time binning was chosen to 1 s. *Right:* Flux measured by BAT and XRT in the prompt and afterglow emission. The MAGIC observation window is marked as shadowed area.

The optical spectrum measured with the Subaru telescope in Hawaii, revealed absorption lines of heavy elements as $\mathrm{S_{II}}$, $\mathrm{Si_{II}}$, $\mathrm{O_I}$ and $\mathrm{C_{II}}$ at a common redshift of $z = 6.295 \pm 0.002$ [182]. This makes the event by far the most distant GRB known to date, comparable to the farthest AGNs and galaxies.

Results from MAGIC observation

We received the alert 82 s after the burst onset. The fast reaction time of the shift crew and short repositioning range allowed to start data taking at $T_0 + 145$ s, before the end of T_{90}. This makes GRB050904 the **second candidate measured by MAGIC during the prompt emission phase**. The burst location was observed for ~ 153 min at a very low zenith range of $14° \rightarrow 23°$. The trigger rate stayed constant at 160 Hz during the observation. However, even when the observation was carried out close to the energy threshold of the MAGIC telescope, the extremely high redshift of this source rules out any chance of detection at energies above 10 GeV because of absorption of these photons by the EBL. Table 6.10 summarise the upper limits determined from my analysis.

$\langle E \rangle$ [GeV]	N_{ON}	N_{OFF}	σ_{OFF}	N_{ex} UL 95% CL	$\langle A_{\mathrm{eff}} \rangle \times 10^8$ [cm^2]	Upper Limits		
						$\left[\frac{\mathrm{ph}}{\mathrm{cm^2\,keV\,s}}\right]$	$\left[\frac{\mathrm{erg}}{\mathrm{cm^2}}\right]$	C.U.
$T_0 + 145\,\mathrm{s} < t < T_0 + 228\,\mathrm{s}$								
100	101	80.2	0.7	63.2	0.91	$4.45 \cdot 10^{-17}$	$9.98 \cdot 10^{-8}$	4.29
140	16	24	0.4	5.2	0.94	$0.29 \cdot 10^{-17}$	$1.11 \cdot 10^{-8}$	0.67
$T_0 + 145\,\mathrm{s} < t < T_0 + 1945\,\mathrm{s}$								
100	4024	3885	32.6	426.3	0.91	$1.38 \cdot 10^{-17}$	$6.73 \cdot 10^{-7}$	1.33
140	683	765	11.1	20.5	0.94	$5.25 \cdot 10^{-19}$	$4.38 \cdot 10^{-7}$	0.12
190	109	125	4.6	14.3	1.02	$3.24 \cdot 10^{-19}$	$0.42 \cdot 10^{-7}$	0.16
250	50	58	3.2	11.7	0.89	$1.80 \cdot 10^{-19}$	$0.46 \cdot 10^{-7}$	0.18
340	31	24	2.0	26.3	1.08	$3.20 \cdot 10^{-19}$	$1.22 \cdot 10^{-7}$	0.72
540	47	47	3.0	19.2	1.51	$0.61 \cdot 10^{-19}$	$0.85 \cdot 10^{-7}$	0.46

Table 6.10: Upper limits on VHE γ-ray emission from GRB050904. The upper limits are given in two time bins: The 83 s overlapping prompt emission phase starting at $T_0 + 145$ s and for the first 30 min of the MAGIC observation window. The upper limits include a systematic uncertainty of 30%.

The *ALPHA* distributions for the 30 min of MAGIC observation are shown in figure A.9. Figure A.10 shows the *ALPHA* distributions for the overlap with the prompt emission phase.

The light curve on number of excess events from the MAGIC data is shown on the right side. The values fluctuate around zero, with no hint for short lasting VHE γ-ray emission. Further conclusions from the observation and physics discussion are given in § 6.3.

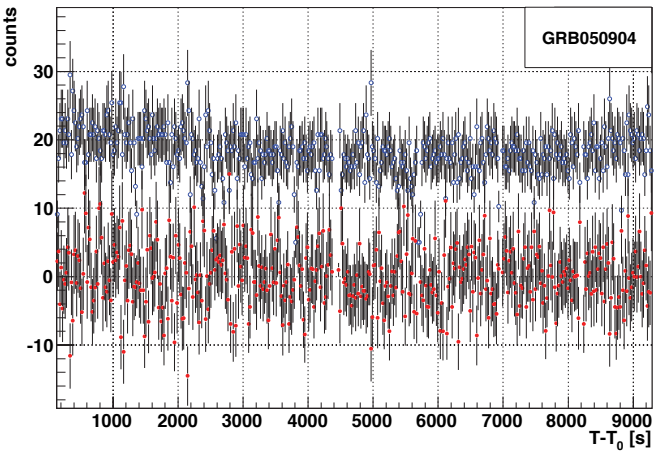

Figure 6.27: Light curve of GRB050904 for VHE γ-ray energies, as measured with the MAGIC telescope. Red filled circles denote the excess events while the blue open circles are the number of background events (shifted by five counts to separate the curves). Bins are integrated over 20 s.

6.2.7 GRB060121: Very distant ($z = 1.5$) short duration burst

Results from multiwavelength observations

Trigger:	
Satellite:	HETE-2 / Fregate
Time:	22:24:54 UT
Coordinates:	RA = 09h 09m 52s ; Dec = +45° 39' 44"
Duration:	$T_{90} = 1.97 \pm 0.06\,\mathrm{s}$
Peak flux:	$30 - 400\,\mathrm{keV}$: $(211 \pm 14) \cdot 10^{-8}\,\mathrm{erg\,cm^{-2}\,s^{-1}}$
Spectral parameter:	$\beta = 0.79 \pm 0.12$; $E_{\mathrm{peak}} = 114 \pm 11\,\mathrm{keV}$

GRB060121 was triggered by the HETE-2 satellite [183]. It was a bright, short-duration burst, for which both an X-ray and optical afterglow were detected, placing the burst on the short list of short GRBs with observed afterglows. The light curve, shown in figure 6.28, consists of a single spike. The burst had a T_{90} duration in the $30 - 300\,\mathrm{keV}$ energy band of $1.97 \pm 0.06\,\mathrm{s}$. The duration is longer at lower energies and reach $T_{90} \approx 10\,\mathrm{s}$ in the $2 - 10\,\mathrm{keV}$ energy band. The burst-average spectrum $[T_0, T_0 + 10\,\mathrm{s}]$ is adequately described by a cutoff power-law model ($\chi^2 = 111.8/134$), with the spectral index and the peak energy quoted in the head of this chapter [184]. The fluence of the event is calculated to be $(4.2 \pm 0.4) \cdot 10^{-6}\,\mathrm{erg\,cm^{-2}}$.

A fading X-ray afterglow was clearly detected in the three hours of delayed follow-up observation by XRT [185]. The accurate localisation provided by this measurement allowed to pinpoint the optical counterpart and to assign the host galaxy of the burst [186]. In fact, deep Hubble Space Telescope observations were necessary to locate the faint, red galaxy at the location of the afterglow. Observations in the I, R, and K bands and the upper limits derived for the U, B, and V bands indicate that the burst occurred at a redshift $z = 4.6 \pm 0.6$, or less probably, at a redshift $z = 1.5 \pm 0.2$ and with a large extinction [187].

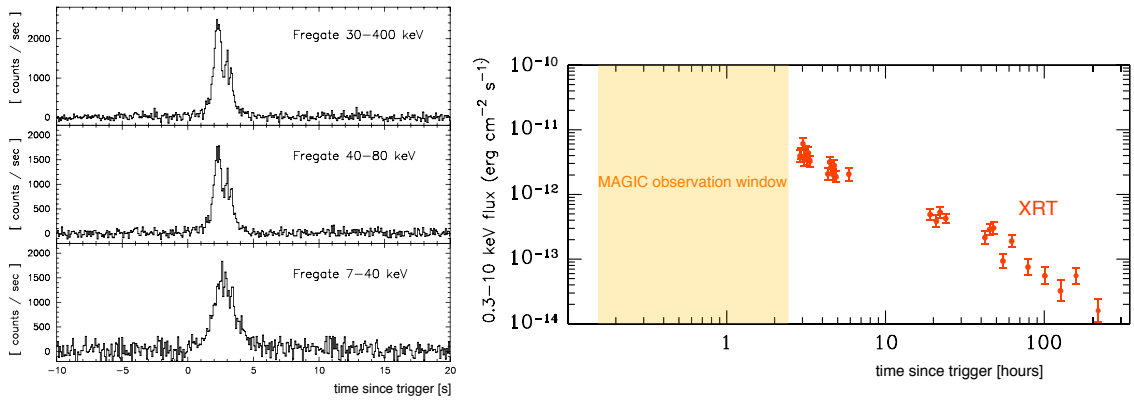

Figure 6.28: *Left:* Light curve of GRB060121 measured by HETE Fregate in three different energy bins. Figure from [184]. *Right:* Flux of the afterglow measured by the SWIFT XRT detector. The MAGIC observation window is shown as orange area.

Results from MAGIC observation

A failure during the repositioning to the GRB coordinates lead to a ~ 10 min delay for the start of the MAGIC observation. In total 79 min of data with the trigger rate of 170 Hz in the zenith range between $48° \rightarrow 38°$ were collected. The analysis of the data did not show a significant excess at energies above 175 GeV, as it is expected for a source at this redshift. The upper limits from my analysis for the four energy bins are shown in table 6.11. The corresponding *ALPHA* distributions are shown in figure A.11. The excess events light curve from the MAGIC observation is shown in figure 6.29, fluctuating around zero. My analysis did not show any hint for a VHE γ-ray component above 175 GeV from this event.

$\langle E \rangle$ [GeV]	N_{ON}	N_{OFF}	σ_{OFF}	N_{ex} UL 95% CL	$\langle A_{\mathrm{eff}} \rangle \times 10^8$ [cm^2]	Upper Limits		
						$\left[\frac{\mathrm{ph}}{\mathrm{cm^2\,keV\,s}}\right]$	$\left[\frac{\mathrm{erg}}{\mathrm{cm^2}}\right]$	C.U.
$T_0 + 583\,\mathrm{s} < t < T_0 + 2383\,\mathrm{s}$								
190	2704	2762	24.4	80.4	1.27	$11.2 \cdot 10^{-19}$	$1.77 \cdot 10^{-7}$	0.56
250	641	716	12.6	21.9	1.81	$1.25 \cdot 10^{-19}$	$0.40 \cdot 10^{-7}$	0.13
340	173	171	4.9	38.2	2.45	$1.46 \cdot 10^{-19}$	$0.78 \cdot 10^{-7}$	0.33
560	102	93	3.8	42.8	4.60	$0.30 \cdot 10^{-19}$	$0.56 \cdot 10^{-7}$	0.25

Table 6.11: Upper limits on VHE γ-ray emission from GRB060121. The upper limits correspond to the first 30 min of the MAGIC observation window and include a systematic uncertainty of 30%.

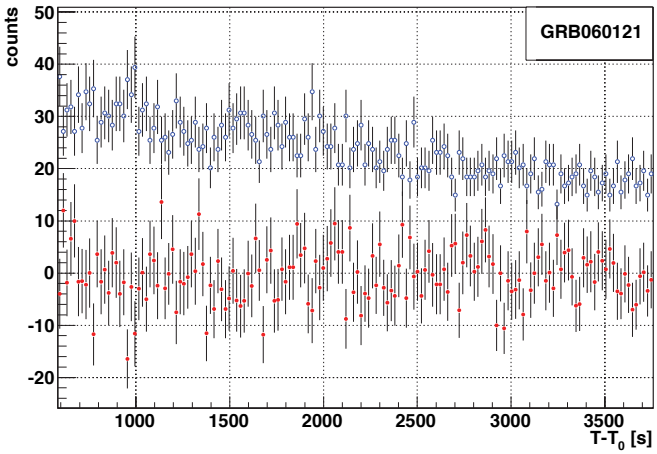

Figure 6.29: Light curve of GRB060121 for VHE γ-ray energies, as measured with the MAGIC telescope. Red filled circles denote the excess events while the blue open circles are the number of background events (shifted by five counts to separate the curves). Bins are integrated over 20 s.

6.2.8 GRB060203: A burst with a fast decaying optical afterglow

Results from multiwavelength observations

Trigger:	
Satellite:	SWIFT / BAT
Time:	23:55:35 UT
Coordinates:	RA = 6h 54m 04s ; Dec = +71° 48' 38"
Duration:	$T_{90} = 59.2 \pm 0.2\,\mathrm{s}$
Mean flux:	$15 - 150\,\mathrm{keV}$: $(1.28 \pm 0.16) \cdot 10^{-8}\,\mathrm{erg\,cm^{-2}\,s^{-1}}$
Spectral index:	$\beta_{\mathrm{BAT}} = 1.59 \pm 0.23$

GRB060203 was triggered by the BAT detector [188]. Initial doubts about the authenticity of the trigger vanished after the reanalysis of the complete data set. My analysis of the BAT data resulted in a total burst duration of 65 s. The BAT light curve is shown in figure 6.30. The time-averaged spectrum can be best described by a simple power-law model. The power-law index is $\beta_{\mathrm{BAT}} = 1.59 \pm 0.2$ and the normalisation factor $\kappa = 0.69 \pm 0.40$ ($\chi^2 = 63/58$). From the model a fluence of $(7.6 \pm 1.0) \cdot 10^{-7}\,\mathrm{erg\,cm^{-2}}$ in the $15 - 150\,\mathrm{keV}$ energy range for the burst duration T_{90} was extracted.

Because of observation constraints, follow-up observation with XRT could start only 3100 s after the burst trigger. A fading X-ray afterglow with a decay index of 0.6 was detected. The spectrum can be approximated with a power-law with a spectral index $\beta_{\mathrm{XRT}} = 2.24 \pm 0.3$. The flux in the $0.2 - 10\,\mathrm{keV}$ energy range, extracted from the model is about $10^{-11}\,\mathrm{erg\,cm^{-2}\,s^{-1}}$ [189].

Also in the case of GRB060203, the accurate position determined with XRT allowed to localise the optical afterglow counterpart. The fading afterglow was first detected at $T_0 + 54\,\mathrm{min}$ with $R \sim 19.9 \pm 0.1\,\mathrm{mag}$, decaying with a power-law decay slope of $\alpha = -0.90 \pm 0.04$ in the following four hours of observation [190], as shown in on the right side of figure 6.30. The redshift of GRB060203 could not be determined.

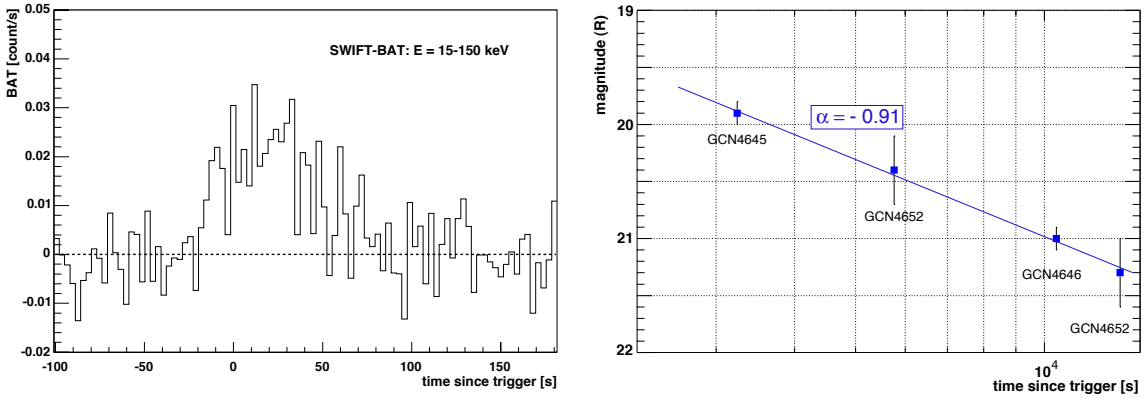

Figure 6.30: *Left:* Light curve of the GRB060203, as measured by BAT. The bin size in time is 3 s. *Right:* Fading optical transient in the R band.

Results from MAGIC observation

The GRB trigger was not generated onboard the satellite but during the ground analysis. Therefore the alert was sent almost three minutes after the burst onset. After acceptance by the shift crew and repositioning to the new target, which together took an additional 97 s, data taking started with the MAGIC telescope. It was one of the rare cases where repositioning over more than 270° in azimuth was necessary. At that time the fast movement mode of the telescope was implemented and the factor three higher maximum velocity reduced the delay significantly, e.g. when compared with GRB050502a (see § 6.2.2). The burst was observed for 43 min, starting at $T_0 + 268$ s. The observation was carried out at a zenith angle of $\sim 44°$ with a low trigger rate of 100 Hz. The bright Moon during the observation required increasing of the DT and lead to the low trigger rate. I did not find any significant VHE γ-ray signal in the MAGIC data and the upper limits are listed in the table 6.12. The corresponding $ALPHA$ distributions are shown in figure A.12.

$\langle E \rangle$ [GeV]	N_{ON}	N_{OFF}	σ_{OFF}	N_{ex} UL 95% CL	$\langle A_{\mathrm{eff}} \rangle$ $\times 10^8$ [cm^2]	Upper Limits		
						$\left[\frac{\mathrm{ph}}{\mathrm{cm^2\,keV\,s}}\right]$	$\left[\frac{\mathrm{erg}}{\mathrm{cm^2}}\right]$	C.U.
$T_0 + 268\,\mathrm{s} < t < T_0 + 2068\,\mathrm{s}$								
190	3512	3530	24.2	131.2	1.28	$18.1 \cdot 10^{-19}$	$2.89 \cdot 10^{-7}$	0.91
250	1148	1209	12.3	38.2	1.94	$2.04 \cdot 10^{-19}$	$0.65 \cdot 10^{-7}$	0.21
340	202	201	4.3	38.5	2.43	$1.48 \cdot 10^{-19}$	$0.75 \cdot 10^{-7}$	0.33
570	103	114	3.7	16.0	4.47	$6.90 \cdot 10^{-21}$	$0.14 \cdot 10^{-7}$	0.06

Table 6.12: Upper limits on VHE γ-ray emission from GRB060203. The upper limits correspond to the first 30 min of the MAGIC observation window and include a systematic uncertainty of 30%.

A search for an increase of excess events, caused by a possible short VHE emission activity, was performed and figure 6.31 shows the results. There is no hint for a short lasting VHE γ-ray emission in the first 43 min of the early afterglow phase. The lack of the distance measurement do not underline the non existence of a VHE counterpart, simply because of possible absorption by the EBL.

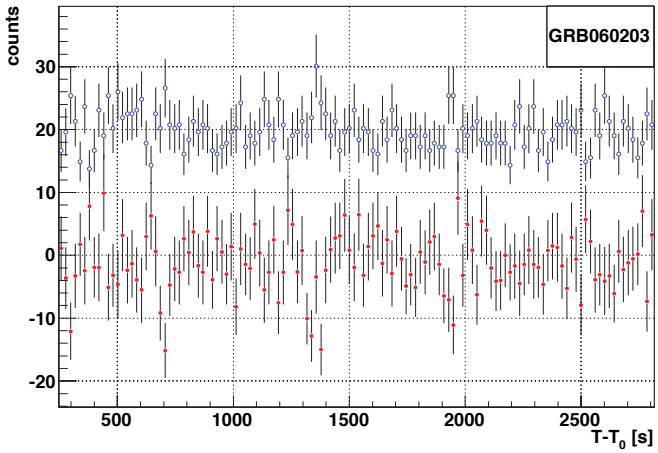

Figure 6.31: Light curve of GRB060203 for VHE γ-ray energies, as measured with the MAGIC telescope. Red filled circles denote the excess events while the blue open circles are the number of background events (shifted by five counts to separate the curves). Bins are integrated over 20 s.

6.2.9 GRB060206: Burst with long lasting central engine activity

Results from multiwavelength observations

Trigger:	
Satellite:	SWIFT / BAT
Time:	04:46:53 UT
Coordinates:	RA = 13h 31m 43s ; Dec = +35° 03' 02"
Duration:	$T_{90} = 6.2 \pm 0.2\,\mathrm{s}$
Mean flux:	$15 - 150\,\mathrm{keV}$: $(9.78 \pm 0.10) \cdot 10^{-8}\,\mathrm{erg\,cm^{-2}\,s^{-1}}$
Spectral index:	$\beta_{\mathrm{BAT}} = 1.73 \pm 0.05$

The burst triggered the BAT detector [191]. The BAT light curve shows one single, quasi Gaussian peak with total duration of 8.6 s. The spectrum can be approximated by a simple power-law with the index $\beta_{\mathrm{BAT}} = 1.73 \pm 0.05$ and a normalisation factor $\kappa = 9.22 \pm 1.63$ ($\chi^2 = 65/68$). Using this spectrum the burst fluence in the energy range between $15 - 150\,\mathrm{keV}$ was determined to be $(6.1 \pm 0.3) \cdot 10^{-7}\,\mathrm{erg\,cm^{-2}}$.

The XRT began observing 65 s after the BAT trigger, but the spacecraft entered soon afterwards the South Atlantic Anomaly, thus providing only a small amount of data during the first orbit [192]. Therefore no simultaneous BAT/XRT data can be plotted in the light curve shown in figure 6.32.

As usual, a number of ground-based facilities were activated for follow-up observations of the event. The redshift was spectroscopically measured to be $z = 4.048$ [193]. The 2 m robotic Liverpool Telescope, located at the Observatory del Roque de los Muchachos, started observing the optical afterglow at $T_0 + 309\,\mathrm{s}$. The optical light curve shows an early re-brightening, suggesting continued activity of the internal engine, extending well beyond the γ-ray prompt emission phase. An additional steep, double peak re-brightening occurred one hour after the burst onset. The increase in flux by a factor of four can be interpreted with late time energy injection [194].

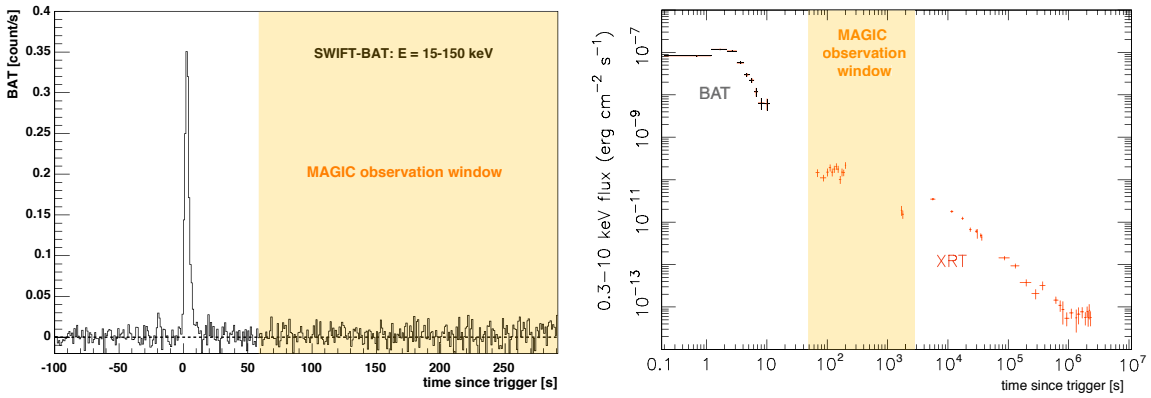

Figure 6.32: *Left:* Light curve of GRB060206, as measured by BAT, sampled in bins of 1 s. The MAGIC observation window is indicated by the shadowed region. *Right:* Flux measured by BAT and XRT.

Results from MAGIC observation

The alert, received by gspot 16 s after the burst onset, was accepted by the shift crew in less than 10 s. The telescope pointed automatically to the burst coordinates and started taking data 59 s after T_0. This is the second fastest reaction time after GRB050713a (see table 6.4). The burst was observed for 49 min at a very low zenith angle range, decreasing from $13° \rightarrow 6°$. The trigger rate of 240 Hz was constant during the whole observation. No significant signal was found after the analysis, which is obvious for a source at such high redshift. The upper limits are summarised in the table 6.13 and the *ALPHA* distributions shown in figure A.13.

$\langle E \rangle$ [GeV]	N_{ON}	N_{OFF}	σ_{OFF}	N_{ex} UL 95% CL	$\langle A_{\mathrm{eff}} \rangle$ $\times 10^8$ [cm^2]	Upper Limits		
						$\left[\frac{\mathrm{ph}}{\mathrm{cm^2\,keV\,s}}\right]$	$\left[\frac{\mathrm{erg}}{\mathrm{cm^2}}\right]$	C.U.
$T_0 + 59\,\mathrm{s} < t < T_0 + 1859\,\mathrm{s}$								
100	5387	5562	48.7	80.8	0.91	$26.3 \cdot 10^{-19}$	$1.28 \cdot 10^{-7}$	0.25
140	556	504	6.0	155.2	0.94	$39.9 \cdot 10^{-19}$	$3.33 \cdot 10^{-7}$	0.92
190	62	36	1.4	30.9	1.01	$7.03 \cdot 10^{-19}$	$0.92 \cdot 10^{-7}$	0.35
250	6	13	0.5	3.5	0.80	$0.54 \cdot 10^{-19}$	$0.14 \cdot 10^{-7}$	0.06

Table 6.13: Upper limits on VHE γ-ray emission from GRB060206. The upper limits correspond to the first 30 min of the MAGIC observation window and include a systematic uncertainty of 30%.

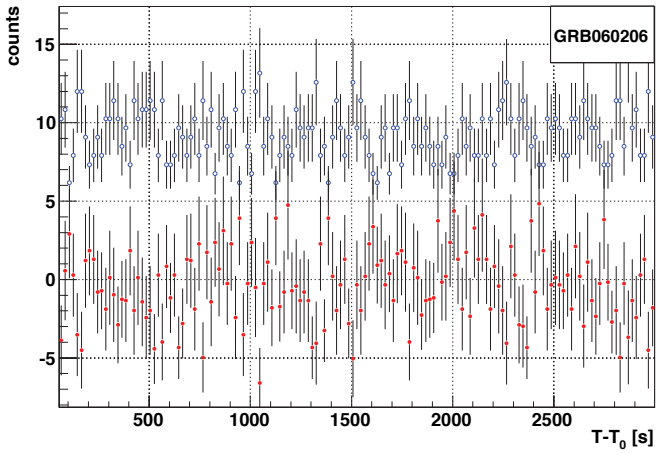

Figure 6.33: Light curve of GRB060206 for VHE γ-ray energies, as measured with the MAGIC telescope. Red filled circles denote the excess events while the blue open circles are the number of background events (shifted by five counts to separate the curves). Bins are integrated over 20 s.

6.3 Summary of one year of GRB observation with MAGIC

The search for VHE γ-ray components from GRBs has two obstacles. First, we have to assume that particles can be accelerated to such high energies and boosted with Γ factors of 1000 within the models describing the GRB explosions (see § 1.2.6). According to the fireball model, TeV photons can be produced in both internal and external shocks, either through electron inverse Compton or proton synchrotron emission. Without investigating the details of the way they are created, VHE photons are mostly absorbed through pair production with the EBL for distant sources (see § 1.1.3). The distance of the GRB is therefore the second constraint, which limits the detectability of VHE γ-rays.

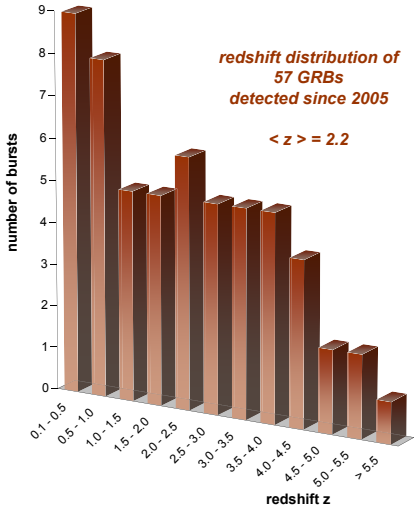

Figure 6.34: Redshift distribution of GRBs detected since 2005.

In the SWIFT era, 57 optical observations of GRB afterglows have led to successful determination of the redshifts up to now. The distribution, as shown in figure 6.34, has a median of $\langle z \rangle = 2.2$. Only 30% of the events lie below $z \approx 1$, which is theoretically the maximum distance VHE γ-rays at 100 GeV can propagate (see figure 1.2). This energy is close to the threshold energy of the MAGIC telescope, for a source observed at zenith. However, it has to be taken into account, that most of the GBRs are observed at higher zenith angles, where the threshold energy increases rapidly (see equation 1.6).

High redshift ($z \gg 3$) of five out of the nine GRBs observed by MAGIC, constrict interpretations on possible VHE γ-ray emission from the events: GRB050502a, GRB050505, GRB050904, GRB060121 and GRB060206, simply because any hypothetical particle with an energy in the lowest energy bin of my analysis, would interact with the EBL and never reach our detector.

For the remaining four events, the redshift was not measured and in the case of non detection, only weak statements on the existence of a possible VHE component can be made. GRB050421, GRB050509a and GRB060203 had fluences of $\sim 10^{-7}\,\mathrm{erg\,cm^{-2}}$ and can therefore be classified among the weak/intermediate GRBs. The observation with the MAGIC telescope started far beyond the prompt emission phase, in most cases in parallel with the observed decaying X-ray afterglow. However, upper limits for the early afterglow phase, with sensitivities in the lower energy range of $175 - 225$ GeV, where no competitor experiments to the MAGIC telescope exist, are placed.

GRB050713a

The GRB050713a became a very good example of the benefits from multiwavelength follow-up observations. The broad spectral coverage of simultaneous measurements allowed to test the early prompt emission, rapid decay and several flares in the early emission with different spectral shapes. The extended energy range between $15 - 1150$ keV from the BAT and Konus-Wind observations of the prompt emission phase, allowed to measure the spectrum up to the

break energy of the Band function. The HE spectral index could not be measured, however, it can be assumed to $\alpha = 2.5$, the mean value of the BATSE distribution at lower energies (see figure 1.10). The MAGIC telescope was able to catch 90 s of the prompt emission phase of the burst, the first time that observations ~ 100 GeV of the prompt emission phase were carried out.

Despite the optical and IR counterparts, the redshift of this burst could not be determined. This fact makes it difficult to draw conclusions whether any GRB model can be excluded by the limits obtained from the MAGIC observation. Only if $z < 0.5$ can one conclude that GRB050713a did not emit more than about 10% of its radiated energy in the hundreds of GeV energy band, during the time interval $[T_0 + 40\,\mathrm{s},\ T_0 + 130\,\mathrm{s}]$. This is in agreement with a pure synchrotron emission model with spectral index $\alpha > 2.05$. Only an unusually steep spectral index could be excluded by this scenario. Figure 6.35 combines the known spectra of the prompt emission phase and the upper limits derived from MAGIC observation. It is assumed that the spectrum extends to higher energies following the Band function. The red curve illustrates the T_{90} time window and the blue curve the spectrum during the overlap with the MAGIC observation. The spectral indices and fluxes for the corresponding time intervals were individually extracted from the BAT data. The upper green line shows the spectrum during the main emission peak, which has not been covered by MAGIC observation. It illustrates nevertheless the capabilities of the MAGIC telescope and the dedicated low energy analysis presented in § 6.2.5.

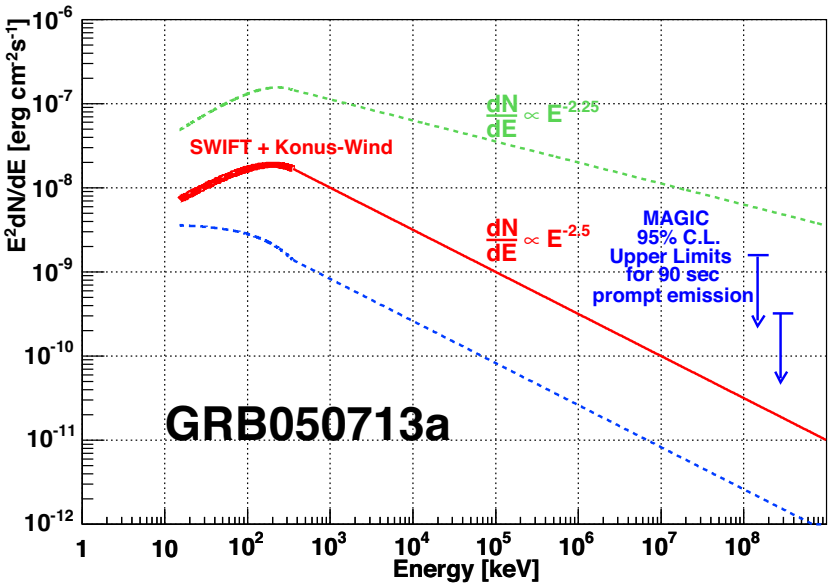

Figure 6.35: Spectrum of GRB050713a. The solid red line between $15 - 150$ keV is the flux extracted from the BAT data for the period of T_{90} extended to 355 keV and the break energy determined by Konus-Wind. Extrapolation to higher energies is done following the Band function with a simple power-law. The lower blue curve is the spectrum for the MAGIC observation window of 90 s. The upper green curve illustrates the spectrum during the main peak from $T_0 < t < T_0 + 20$ s.

The substantial improvement of the increased sensitivity and lower energy threshold from the dedicated analysis could not be done by other groups. Results from the standard analysis, based in large parts on my work, were published in [178, 179].

GRB050904

It was the second and the last GRB, which was observed in cycle-1 by MAGIC, while the prompt emission was still ongoing. GRB050904 is the most distant stellar explosion ever witnessed. It occurred when the Universe was about 7% of its current age, i.e. when it was only about 900 million years old (currently accepted age of the Universe is roughly 13.7 billion years). Broad band detection showed, that not only just galaxies can be spectroscopically identified at large distances, but also very bright individual star explosions.

It is unavoidable that VHE γ-rays from such distances are fully reprocessed by interactions with the EBL. The spectrum shown in figure 6.36 illustrates the measured BAT spectrum in the energy range $15 - 150\,\mathrm{keV}$ and the extrapolation to higher energies using the Band function. The exponential cutoff due to absorption of VHE γ-rays by the low energy photons of the evolving EBL for a source at $z = 6.3$ is implemented in the spectrum. I calculated the optical depth and the resulting attenuation using the number density of the evolving EBL, provided by the best fit model introduced in [6]. At this redshift the cutoff starts already at energies above 10 GeV. Upper limits derived for the overlap with the prompt emission phase $[T_0 + 145\,\mathrm{s}, T_0 + 228\,\mathrm{s}]$ are shown in the spectrum.

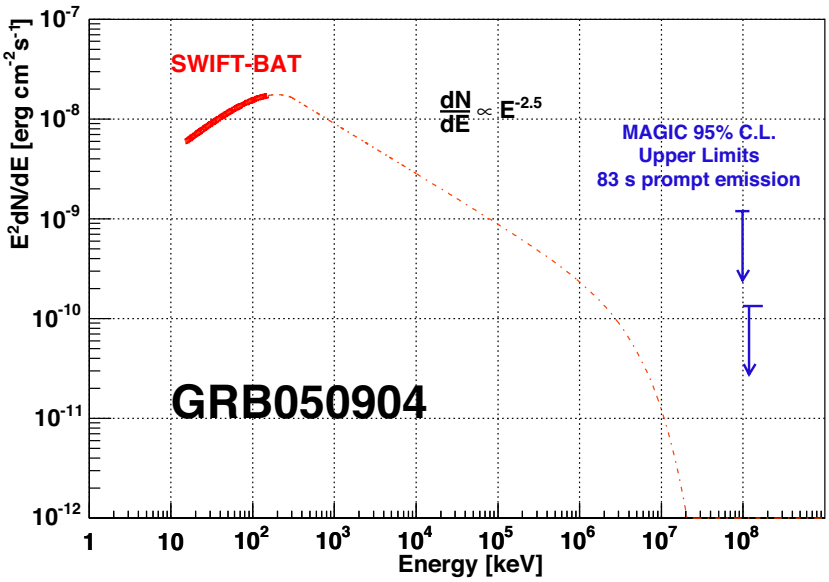

Figure 6.36: Spectrum of GRB050904. The thick line between $15-150\,\mathrm{keV}$ is the spectrum extracted from the BAT data for the period of T_{90} and extended to 355 keV, the assumed break energy. Towards higher energies, extrapolation following the Band function with a simple power-law is assumed. The exponential cutoff for a source at redshift $z = 6.3$ breaks the spectrum at energies close to 10 GeV. The upper limit derived from MAGIC observation for the 83 s overlap with the prompt emission phase T_{90} is shown.

Outlook

The sample of the nine GRBs presented in my thesis can be considered as the beginning of a new approach to search for VHE γ-ray emission from GRBs. The initial efforts of my thesis were focussed on preparing the instrument for the new observation method, e.g. on the implementation and improvement of the hardware components, which allow the fast follow-up response on GCN alerts. On the other hand, dedicated analysis methods and scripts were developed to allow the search for short duration signals in the MAGIC telescope data. These methods differ substantially from the standard analysis, where the significance can easily be increased by extending the observation time.

The success of observing during prompt emission from two GRBs in 2005 showed that the design goal of the MAGIC telescope have been mostly reached. There are still quite some possibilities to improve the response of the experiment to the GCN alerts:

- Implementation of the reverse mode in the elevation axis movements. The "turn over zenith" will in some cases significantly reduce the slewing time towards the GRB coordinates and enhance the possibility for further prompt emission observations.
- The use of the reverse mode will allow to change the mode of the fast slewing. It should be possible to increase the slewing velocity in azimuth direction by enlarging the path length between the slow-down switches and the hardware end-switches. Furthermore, additional capacitors in the motor drive electronics could be installed, which would provide short-term additional power during acceleration.
- Fully automatise the telescope response to the GRB alerts and eliminate the still required affirmation by the operator.

On the other hand, not only the hardware components are crucial for the observation of GRBs. Efforts must also be concentrated on lowering the analysis threshold of the MAGIC telescope data. The implementation of the time image cleaning was already an important step in the right direction. The future 2 GHz FADC system should also allow further improvements.

MAGIC is receiving GRB alerts regularly and follow-up observations are carried out at the rate of about one per two months. The rate of GCN alerts decreased in 2006 by factor two, when comparing with 2005. The reasons are associated with the functionality of satellite detectors. The shutdown of the HETE-2 satellite contributes partially to the lower follow-up observation rate. However, in 2007 the GLAST[6] satellite will be launched. The satellite will not only extend the energy range of space borne detectors up to 100 GeV, albeit with rather low statistics, but also provide additional GRB alerts to ground based telescopes.

Since March 2006, four more GRB observations by the MAGIC telescope have been carried out, however, still without significant detection of a VHE γ-ray emission component. In the

[6] `http://glast.gsfc.nasa.gov/`

case of GRB060825 [195] and GRB061028 [196] GCN circulars with upper limits from MAGIC observations were send within one week after the observation. The fast publication of our results is the consequence of our interests on these objects and the mature analysis of the MAGIC telescope data. It is only a question of time when the first close enough burst is observed by MAGIC and new chapters in the GRB physics might be opened.

By the end of 2007, the MAGIC-2 telescope will start its operation. New operation modes and improvements of some components were foreseen. The AMC will use IR laser modules, a wavelength band, at which the PMTs of the MAGIC camera are not sensitive. The IR lasers will allow the concurrent re-focussing of the mirror segments and correction of possible deformations caused by wind loads. The simultaneous observation with both telescopes will allow to further reduce the hadronic background, as well to lower the energy threshold. Both factors are very crucial for the observation of GRBs.

Appendix A

Figures and tables from the GRB data analysis

In the § 6.2 and chapters therein, I summarised the results of my analysis of the 9 GRBs observed by MAGIC during the first observation cycle. In order to keep the description compact and reduce the amount of figures, I sourced out the *ALPHA* figures from that chapter. The distribution of the *ALPHA* Hillas parameter is the final result of my data analysis. I extracted the number of excess and background events in the signal region (*ALPHA* value below the red line in the figures), as well as the error on the background from these figures and used them to calculate the upper limits. The *ALPHA* figures for all GRBs and some further tables from the analysis of the GRB050713a are included in this appendix.

ALPHA figures of GRB050421

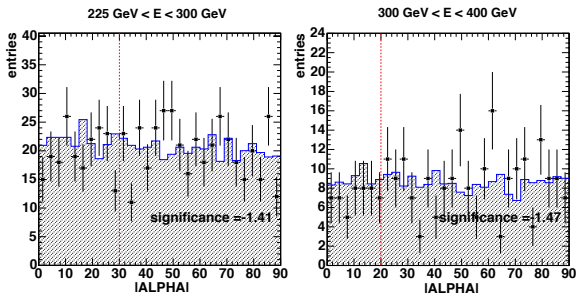

Figure A.1: *ALPHA* distributions of GRB050421 for the first 30 min of MAGIC telescope observation. Because of the moon background light high DT was set. The high DT setting resulted in a very low trigger rate of 25 Hz. Therefore solid upper limits could only be extracted in the energy bins between 225 GeV and 400 GeV. For further details on GRB050421 see § 6.2.1.

ALPHA figures of GRB050502a

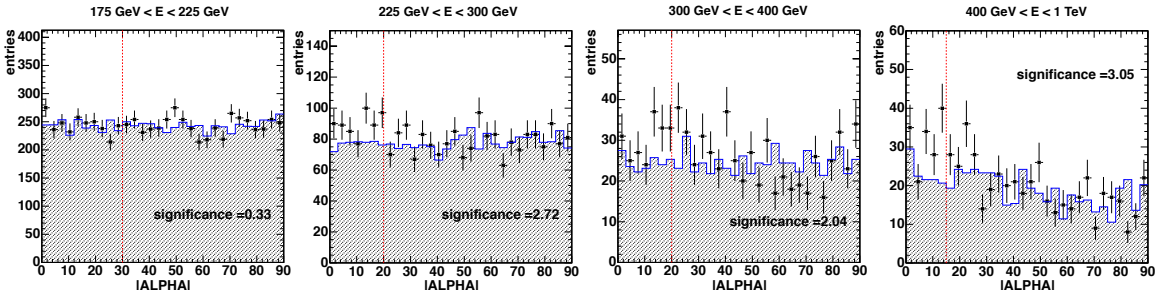

Figure A.2: *ALPHA* distributions of GRB050502a for the first 30 min of MAGIC telescope observation. For further details on GRB050502a see § 6.2.2.

ALPHA figures of GRB050505

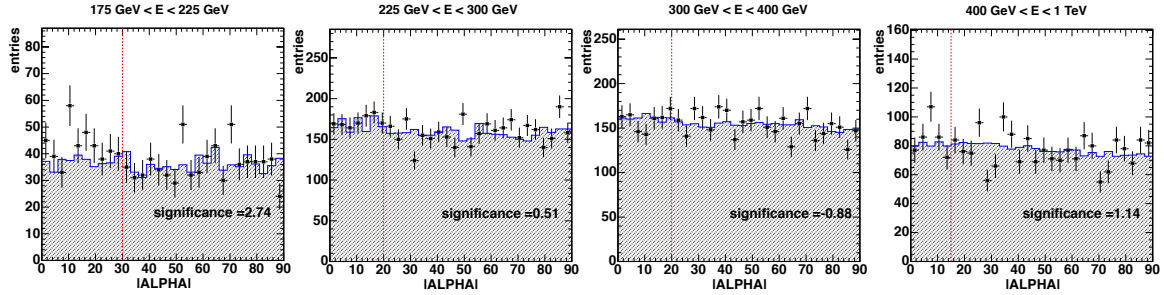

Figure A.3: *ALPHA* distributions of GRB050505 for the first 30 min of MAGIC telescope observation. For further details on GRB050505 see § 6.2.3.

ALPHA figures of GRB050509a

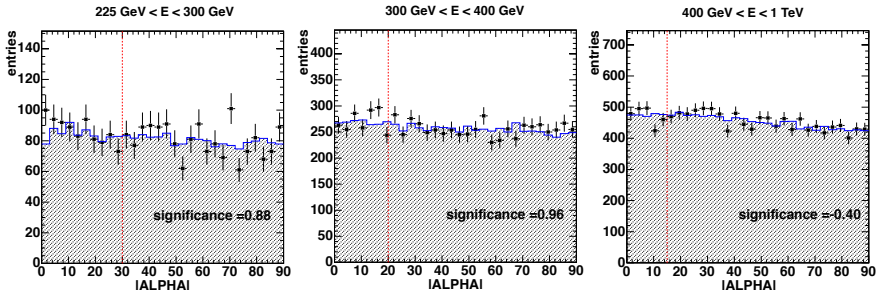

Figure A.4: *ALPHA* distributions of GRB050509a for the first 30 min of MAGIC telescope observation. Because of the high zenith angle of the observation (60°), I excluded the first energy bin from my analysis. For further details on GRB050509a see § 6.2.4.

Further information to the analysis of the GRB050713a

The results from the analysis of GRB050713a were shown in § 6.2.5. Since GRB050713a was the most important observation of a GRB event by the MAGIC telescope during the first observation cycle, I performed more extended attempts to extract low energy signal from this data set. The different searches were described at the pages 128 – 130. Tables with my results and figures are shown below.

image cleaning method	energy range [GeV]	$\langle E_\gamma \rangle$ [GeV]	*HADRON–NESS*	*ALPHA*	N_{ON}	N_{OFF}	N_{ex} UL 95% CL
Prompt emission phase: $T_0 + 40\,\mathrm{s} < t < T_0 + 130\,\mathrm{s}$							
absolute	100 – 200	175	0.59	23°	82	78.8	22.6
	200 – 500	290	0.47	16°	60	65.0	12.3
time	100 – 200	160	0.60	21°	74	74.8	17.5
	200 – 500	280	0.49	15°	46	49.0	12.1
First 1000 s of observation							
absolute	100 – 200	175	0.56	23°	854	836.3	84.7
	200 – 500	350	0.11	14°	37	34.3	16.1
time	100 – 200	160	0.46	20°	474	465.9	60.4
	200 – 500	290	0.29	15°	167	167.8	31.1
Entire ON data set (2200 s)							
absolute	100 – 200	175	0.58	23°	1902	1929.4	87.1
	200 – 500	350	0.11	15°	76	70.2	24.6
time	100 – 200	160	0.51	20°	1095	1101.4	74.1
	200 – 500	330	0.15	14°	99	82.7	37.6

Table A.1: Number of excess events extracted from the *ALPHA* figures from the GRB050713a. The first three different methods to search for the signal are included. The upper limits on the excess events N_{ex} are calculated following the method of Feldman and Cousins [152]. For further information on the methods see page 128.

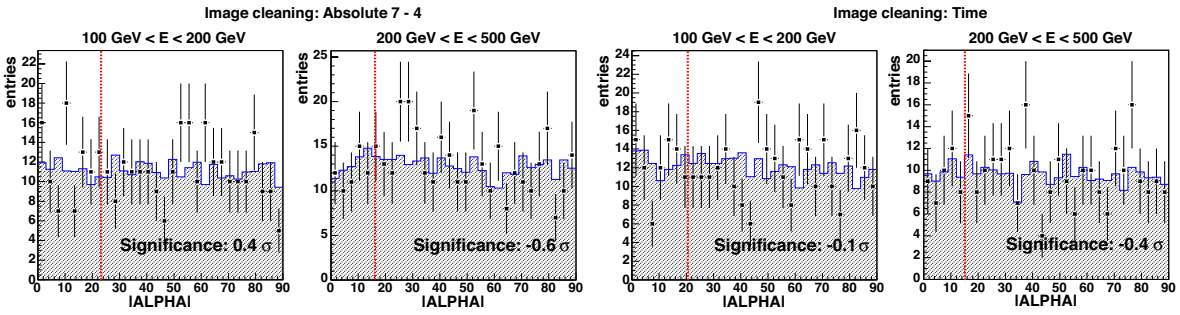

Figure A.5: *ALPHA* distributions of GRB050713a for 90 s prompt emission observation. The absolute image cleaning is shown on the left side and the time image cleaning on the right side.

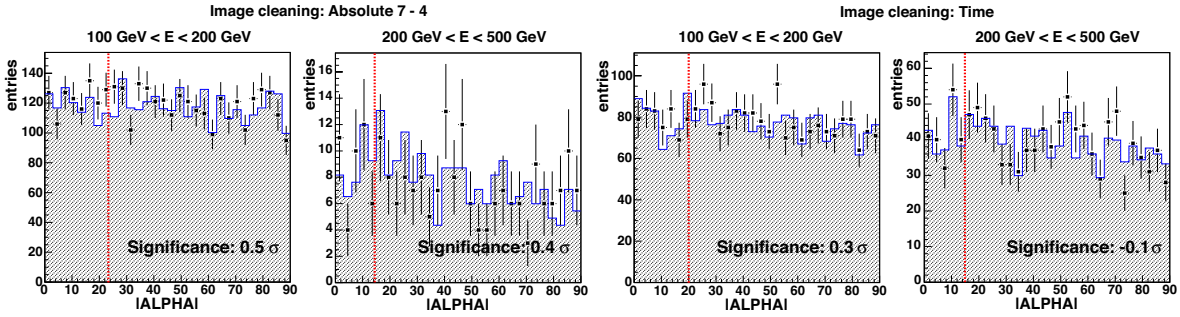

Figure A.6: *ALPHA* distributions of GRB050713a for the first 1000 s of the MAGIC telescope observation. The absolute image cleaning is shown on the left side and the time image cleaning on the right side.

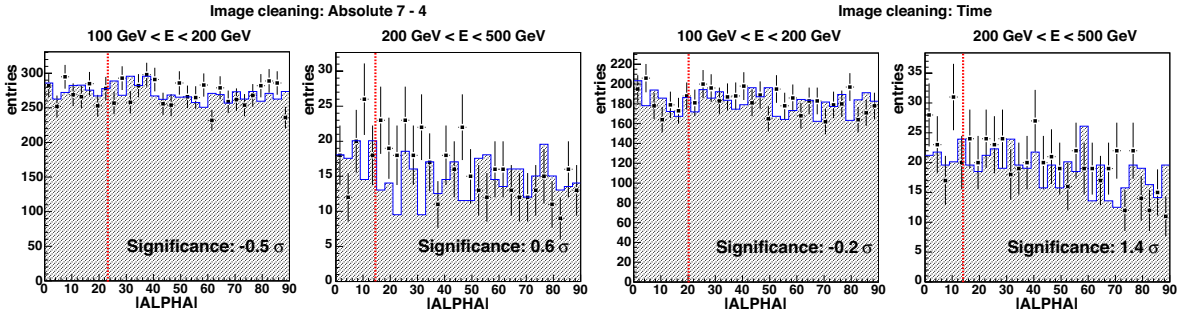

Figure A.7: *ALPHA* distributions of GRB050713a for the entire MAGIC data set of 2200 s. The absolute image cleaning is shown on the left side and the time image cleaning on the right side.

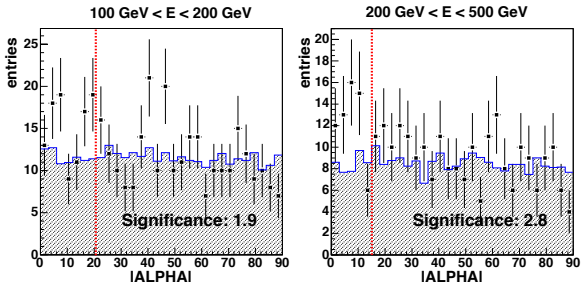

Figure A.8: *ALPHA* distributions for the bin with the highest significance of the sliding window test with the GRB050713a data set. *Left:* The ninth bin for the time window $T_0 + 890\,\mathrm{s} \leqslant t \leqslant T_0 + 990\,\mathrm{s}$ with the highest significance in the lower energy bin. *Right:* The eleventh bin for the time window $T_0 + 1090\,\mathrm{s} \leqslant t \leqslant T_0 + 1190\,\mathrm{s}$ with the highest significance in the higher energy bin.

image cleaning algorithm	$\langle E_0 \rangle$ [GeV]	$dN_{\mathrm{ex}}/dE \times 10^{-9}\,[\mathrm{cm}^{-2}\,\mathrm{s}^{-1}\,\mathrm{TeV}^{-1}]$					95% CL
		$\alpha = 1$	$\alpha = 2$	$\alpha = 2.25$	$\alpha = 2.5$	$\alpha = 3$	exp. cutoff
$T_0 + 40\,\mathrm{s} < t < T_0 + 130\,\mathrm{s}$							
absolute	175	6.3	7.4	7.5	7.6	7.6	7.8
	290	0.57	0.68	0.70	0.70	0.69	0.68
time	160	4.6	5.4	5.5	5.6	5.6	5.7
	280	0.70	0.84	0.85	0.85	0.84	0.82
$T_0 + 40\,\mathrm{s} < t < T_0 + 1040\,\mathrm{s}$							
absolute	175	2.9	3.4	3.4	3.5	3.5	3.6
	350	0.12	0.13	0.13	0.14	0.13	0.13
time	160	2.0	2.3	2.3	2.4	2.4	2.4
	290	0.19	0.22	0.23	0.23	0.23	0.22
$T_0 + 40\,\mathrm{s} < t < T_0 + 2240\,\mathrm{s}$							
absolute	175	1.4	1.4	1.4	1.5	1.5	1.5
	350	0.10	0.11	0.12	0.12	0.12	0.12
time	160	0.91	1.1	1.1	1.1	1.1	1.1
	290	0.14	0.16	0.16	0.16	0.17	0.17

Table A.2: Upper limits for the GRB050713a data analysis for the three time bins of 90 s, 1000 s and 2200 s. The limits are determined with different spectral power-law indices α. The last column takes an exponential cutoff with a break energy of $E_{\mathrm{b}} = 200\,\mathrm{GeV}$ and HE spectral index of $\alpha = 2.5$ into account.

ALPHA figures of GRB050904

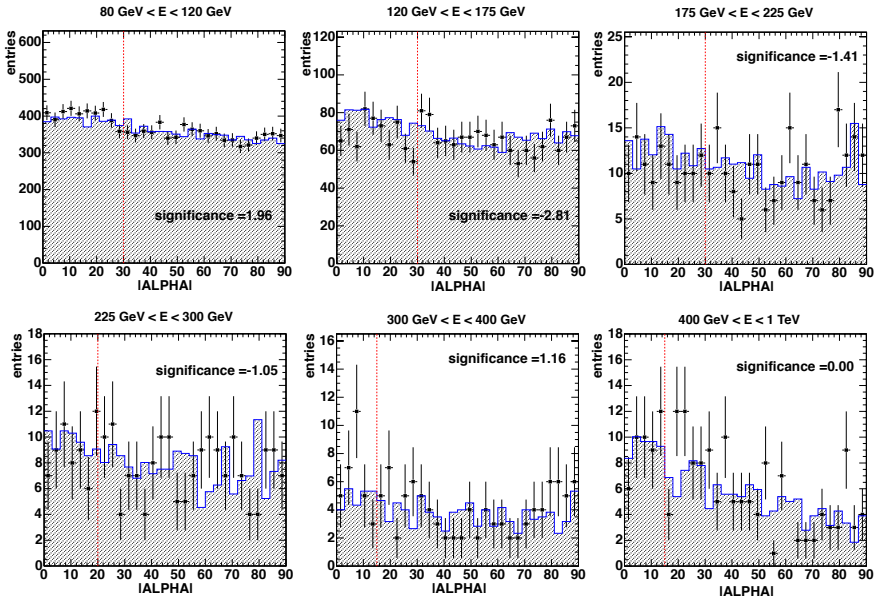

Figure A.9: *ALPHA* distributions of GRB050904 for the first 30 min of MAGIC telescope observation. Due to the low zenith range of the observation, upper limits for energies above 80 GeV could be determined. For further information on GRB050904 see § 6.2.6.

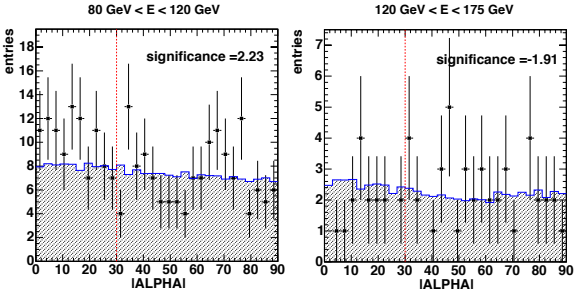

Figure A.10: *ALPHA* distributions for the prompt emission phase of GRB050904. The begin of the MAGIC telescope observation overlapped the prompt emission phase of the GRB. These figures are determined for the time starting at $T_0 + 145\,\mathrm{s}$ until $T_0 + 228\,\mathrm{s}$, the end of the prompt emission phase.

ALPHA figures of GRB060121

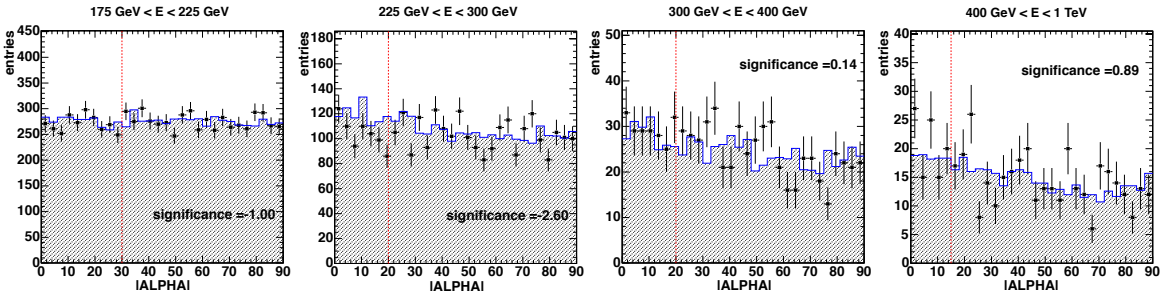

Figure A.11: *ALPHA* distributions of GRB060121 for the first 30 min of MAGIC telescope observation. For further details on GRB060121 see § 6.2.7.

ALPHA figures of GRB060203

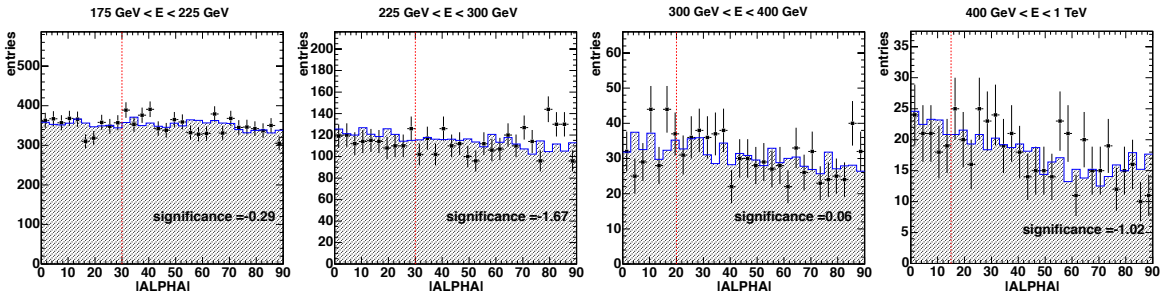

Figure A.12: *ALPHA* distributions of GRB060203 for the first 30 min of MAGIC telescope observation. For further details on GRB060203 see § 6.2.8.

ALPHA figures of GRB060206

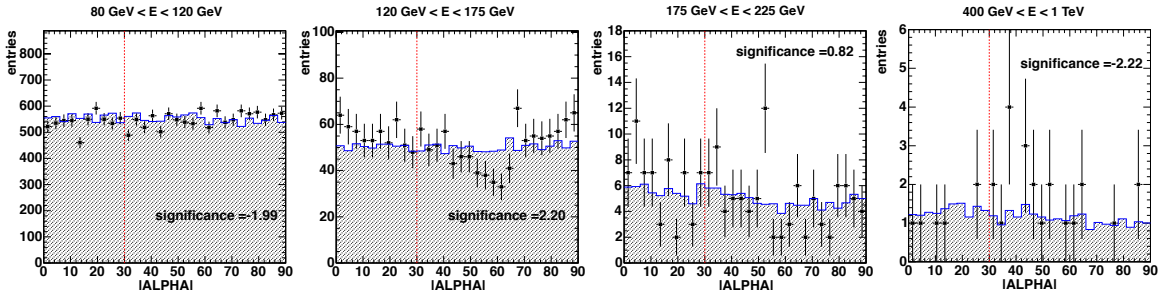

Figure A.13: *ALPHA* distributions of GRB060206 for the first 30 min of MAGIC telescope observation. For further details on GRB060206 see § 6.2.9.

Bibliography

[1] Bergström L. and Goobar A., *Cosmology and particle astrophysics*, Springer-Verlag (2004)

[2] Schönfelder V., *The Universe in Gamma Rays*, Springer-Verlag (2001)

[3] Aharonian F.A., *Very High Energy Cosmic Gamma Radiation. A Crucial Window on the Extreme Universe*, World Scientific (2004)

[4] Primack J. et al., *Probing Galaxy Formation with TeV Gamma Ray Absorption*, Astroparticle Physics, 11, 93-102 (1999)

[5] Vassiliev V.V., *Extragalactic background light absorption signal in the TeV gamma-ray spectra of blazars*, Astroparticle Physics, 12, 217-238 (2000)

[6] Kneiske T. et al., *Implications of cosmological gamma-ray absorption. II. Modification of gamma-ray spectra*, A&A, 413, 807-815 (2004)

[7] Kashlinsky A., *Cosmic infrared background and early galaxy evolution*, Physics Reports, 409, 361-438 (2005)

[8] Hauser M.G. and Dwek E., *The Cosmic Infrared Background: Measurements and Implications*, A&A Annual Review, 39, 249-307 (2001)

[9] Matsumoto T. et al., *Infrared Telescope in Space Observations of the Near-Infrared Extragalactic Background Light*, ApJ, 626, 31-43 (2005)

[10] Aharonian F. et al., *A low level of extragalactic background light as revealed by gamma-rays from blazars*, Nature, 440, 1018-1021 (2006)

[11] Sturrock P.A., *A Model of Pulsars*, ApJ, 164, 529-556 (1971)

[12] Ruderman M. and Sutherland P., *Theory of pulsars - Polar caps, sparks, and coherent microwave radiation*, ApJ, 196, 51-72 (1975)

[13] Cheng K., Ho C. and Ruderman M., *Energetic Radiation from Rapidly Spinning Pulsars. II. VELA and Crab*, ApJ, 300, 522-539 (1986)

[14] Chiang J. and Romani R.W., *Gamma radiation from pulsar magnetospheric gaps*, ApJ, 400, 629-637 (1992)

[15] Aharonian F. et al., *Discovery of Very High Energy Gamma Rays Associated with an X-ray Binary*, Science, 309, 746-749 (2005)

[16] Albert J. et al., *Variable Very High Energy Gamma-Ray Emission from the Microquasar LSI +61 303*, Science, 312, 1771-1773 (2006)

[17] Hartman R.C. et al., *The Third EGRET Catalog of High-Energy Gamma-Ray Sources*, ApJ Supplement Series, 123, 79-202 (1999)

[18] Klebesadel R. W., Strong I. B. and Olson R. A., *Observations of Gamma-Ray Bursts of Cosmic Origin*, ApJ, 182, L85-L88 (1973)

[19] Fishman G.J. and Meegan C.A., *Gamma-Ray Bursts*, A&A Annual Review, 33, 415-458 (1995)

[20] Preece R. and Band D., *The BATSE Gamma-Ray Burst spectral catalog. Hight time resolution spectroscopy of bright bursts using high energy resolution data*, ApJ Supplement Series, 126, 19-36 (2000)

[21] Kouveliotou C. et al., *Identification of two classes of gamma-ray bursts*, ApJ, 413, L101-L104 (1993)

[22] Band D. et al., *BATSE observations of gamma-ray burst spectra. I - Spectral diversity*, ApJ, 413, 281-292 (1993)

[23] Kaneko Y. et al., *The Complete Spectral Catalog of Bright BATSE Gamma-Ray Bursts*, `astro-ph/0605427` (2006)

[24] Boella G. et al., *BeppoSAX, the wide band mission for X-ray astronomy*, A&A Supplement Series, 122, 299-307 (1997)

[25] Gehrels N. et al., *The SWIFT Gamma-Ray Burst Mission*, ApJ, 611, 1005-1020 (2004)

[26] Barthelmy S.D. et al., *The Burst Alert Telescope (BAT) on the SWIFT Midex Mission*, Space Science Reviews, 120, 143-164 (2005)

[27] Burrows D.N. et al., *The SWIFT X-Ray Telescope*, Space Science Reviews, 120, 165-195 (2005)

[28] Roming P.W.A. et al., *The SWIFT Ultra-Violet/Optical Telescope*, Space Science Reviews, 120, 95-142 (2005)

[29] Zhang B. et al., *Physical Processes Shaping Gamma-Ray Burst X-Ray Afterglow Light Curves: Theoretical Implications from the Swift X-Ray Telescope Observations*, ApJ, 642, 354-370 (2006)

[30] Burrows D.N. et al., *Bright X-ray Flares in Gamma-Ray Burst Afterglows*, Science, 309, 1833-1835 (2005)

[31] Falcone A. et al., *The Giant X-Ray Flare of GRB 050502B: Evidence for Late-Time Internal Engine Activity*, ApJ, 641, 1010-1017 (2006)

[32] Pagani C. et al., *The Swift X-Ray Flaring Afterglow of GRB 050607*, ApJ, 645, 1315-1322 (2006)

[33] Paczynski B., *Gamma-ray bursters at cosmological distances*, ApJ, 308, L43-L46 (1986)

[34] Tang S.M. and Zhang S.N., *Time lag between prompt optical emission and γ-rays in GRBs*, A&A, 456, 141-143 (2006)

[35] Zheng Z., Lu Y. and Zhao Y.H., *A Comptonization Model for the Prompt Optical and Infrared Emission of GRB 041219A*, ApJ, 646, L25-L28 (2006)

[36] Rykoff E.S. et al., *Prompt Optical Detection of GRB 050401 with ROTSE-IIIa*, ApJ, 631, L121-L124 (2005)

[37] Campana S. et al., *The association of GRB 060218 with a supernova and the evolution of the shock wave*, Nature, 442, 1008-1010 (2006)

[38] Haislip J.B. et al., *A photometric redshift of $z = 6.39 \pm 0.12$ for GRB050904*, Nature, 440, 181-183 (2006)

[39] Paczyński B., *Are Gamma-Ray Bursts in Star-Forming Regions?*, ApJ, 494, L45-L48 (1998)

[40] MacFadyen A.L. and Woosley S.E., *Collapsars: Gamma-Ray Bursts and Explosions in "Failed Supernovae"*, ApJ, 524, 262-289 (1999)

[41] Gehrels N. et al., *A short γ-ray burst apparently associated with an elliptical galaxy at redshift $z = 0.225$*, Nature, 437, 851-854 (2005)

[42] Barthelmy S.D. et al., *An origin for short γ-ray bursts unassociated with current star formation*, Nature, 438, 994-996 (2005)

[43] Hjorth J. et al., *The optical afterglow of the short γ-ray burst GRB050709*, Nature, 437, 859-861 (2005)

[44] Rees M.J. and Mészáros P., *Unsteady Outflow Models for Cosmological Gamma-Ray Bursts*, ApJ, 430, L93-L96 (1994)

[45] Sari R. and Piran T., *Variability in Gamma-Ray Bursts: A Clue*, ApJ, 485, 270-273 (1997)

[46] Galama T. et al., *An unusual supernova in the error box of the gamma-ray burst of 25 April 1998*, Nature, 396, 670-672 (1998)

[47] Della Valle M. et al., *Evidence for supernova signatures in the spectrum of the late-time bump of the optical afterglow of GRB 021211*, A&A, 406, L33-L37 (2003)

[48] Stanek K.Z. et al., *Spectroscopic Discovery of the Supernova 2003dh Associated with GRB030329*, ApJ, 591, L17-L20 (2003)

[49] Hjorth T. et al., *A very energetic supernova associated with the γ-ray burst of 29. March 2003*, Nature, 423, 847-850 (2003)

[50] Malesani D. et al., *SN 2003lw and GRB031203: A Bright Supernova for a Faint Gamma-Ray Burst*, ApJ, 609, L5-L8 (2004)

[51] Della Valle M. et al., *Hypernova Signatures in the Late Rebrightening of GRB050525A*, ApJ, 642, L103-L106 (2006)

[52] Della Valle M., *Supernovae and GRB connection: Observations and Questions*, `astro-ph/0604110` (2006)

[53] Paczynski B., *Gamma-ray bursters at cosmological distances*, ApJ, 308, L43-L46 (1986)

[54] Goodman J., *Are gamma-ray bursts optically thick?*, ApJ, 308, L47-L50 (1986)

[55] Rees M. and Mészáros P., *Relativistic fireballs - Energy conversion and time-scales*, MNRAS, 258, 41P-43P (1992)

[56] Piran T., *The physics of gamma-ray bursts*, Reviews of Modern Physics, 76, 1143-1210 (2005)

[57] Dar A. and De Rujula A., *A cannonball model of gamma-ray bursts: superluminal signatures*, `astro-ph/0008474` (2000)

[58] Dar A. and De Rujula A., *Towards a complete theory of gamma-ray bursts*, Physics Reports, 405, 203-278 (2004)

[59] Dado S., Dar A. and De Rujula A., *On the optical and X-ray afterglows of gamma ray bursts*, A&A, 388, 1079-1105 (2002)

[60] Dado S., Dar A. and De Rujula A., *On the radio afterglow of gamma ray bursts*, A&A, 401, 243-263 (2003)

[61] Mirabel I.F. and Rodriguez L.F., *Sources of Relativistic Jets in the Galaxy*, A&A Annual Review, 37, 409-443 (1999)

[62] Frail D.A. et al., *Beaming in Gamma-Ray Bursts: Evidence for a Standard Energy Reservoir*, ApJ, 562, L55-L58 (2001)

[63] Ghirlanda G., Ghisellini G. and Lazzati D., *The Collimation-corrected Gamma-Ray Burst Energies Correlate with the Peak Energy of Their νF_ν Spectrum*, ApJ, 616, 331-338 (2004)

[64] Amati L. et al., *Intrinsic spectra and energetics of BeppoSAX Gamma-Ray Bursts with known redshifts*, A&A, 390, 81-89 (2002)

[65] Ghirlanda G. et al., *Cosmological constraints with GRBs: homogeneous medium vs. wind density profile*, A&A, 452, 839-844 (2006)

[66] Perlmutter S. and Schmidt B.P., *Measuring Cosmology with Supernovae*, Supernovae and Gamma-Ray Bursters, Lecture Notes in Physics, Springer-Verlag, 195-217 (2003)

[67] Hurley K. et al., *Detection of a γ-ray burst of very long duration and very high energy*, Nature, 372, 652-654 (1994)

[68] Dingus B.L., *EGRET Observations of $>$ 30 MeV Emission from the Brightest Bursts Detected by BATSE*, Astrophysics and Space Science, 231, 187-190 (1995)

[69] Dingus B.L., *Observations of the Highest Energy Gamma Rays from Gamma-Ray Bursts*, AIP Conference Proceedings, 662, 240-243 (2003)

[70] Gonzáles M.M. et al., *A γ-ray burst with a high-energy spectral component inconsistent with the synchrotron shock model*, Nature, 424, 749-751 (2003)

[71] Rees M. and Mészáros P., *Delayed GeV Emission from Cosmological Gamma-Ray Bursts - Impact of a Relativistic Wind on External Matter*, MNRAS, 269, L41 (1994)

[72] Zhang B. and Mészáros P., *High-Energy Spectral Components in Gamma-Ray Burst Afterglows*, ApJ, 559, 110-122 (2001)

[73] Katz J.I., *Delayed hard photons from gamma-ray bursts*, ApJ, 432, L27-L29 (1994)

[74] Totani T., *Very Strong TeV Emission as Gamma-Ray Burst Afterglows*, ApJ, 502, L13-L16 (1998)

[75] Cheng L.X. and Cheng K.S., *Delayed MeV-GeV Gamma-Ray Photons in Gamma-Ray Bursts: An Effect of Electromagnetic Cascades of Very High Energy Gamma-Rays in the Infrared/Microwave Background*, ApJ, 459, L79-L82 (1996)

[76] Dai Z.G. and Lu T., *Spectrum and Duration of Delayed MeV-GeV Emission of Gamma-Ray Bursts in Cosmic Background Radiation Fields*, ApJ, 580, 1013-1016 (2002)

[77] Wang X.Y. at al., *Constraining the Origin of TeV Photons from Gamma-Ray Bursts with Delayed MeV - GeV Emission Formed by Interaction with Cosmic Infrared/Microwave Background Photons*, ApJ, 604, 306-311 (2004)

[78] Razzaque S., Mészáros P. and Zhang B., *GeV and Higher Energy Photon Interactions in Gamma-Ray Burst Fireballs and Surroundings*, ApJ, 613, 1072-1078 (2004)

[79] Wang X.Y., Li Z. and Mészáros P., *GeV-TeV and X-Ray Flares from Gamma-Ray Bursts*, ApJ, 641, L89-L92 (2006)

[80] Amenomori M. et al., *Search for 10 TeV burst-like events coincident with the BATSE bursts using the Tibet air shower array*, A&A, 311, 919-926 (1996)

[81] Connaughton V. et al., *A Search for TeV Counterparts to BATSE Gamma-Ray Bursts*, ApJ, 479, 859-867 (1997)

[82] Connaughton V. et al., *A search for TeV gamma-ray bursts on a 1-second time-scale*, Astroparticle Physics, 8, 179-191 (1998)

[83] Padilla L. et al., *Search for gamma-ray bursts above 20 TeV with the HEGRA AIROBICC Cherenkov array*, A&A, 337, 43-50 (1998)

[84] Atkins R. et al., *The High-Energy Gamma-Ray Fluence and Energy Spectrum of GRB 970417a from Observations with Milagrito*, ApJ, 583, 824-832 (2003)

[85] Poirier J. et al., *Search for sub-TeV gamma rays in coincidence with gamma ray bursts*, Physical Review D, 67, 4, 042001-042006 (2003)

[86] Atkins R. et al., *Constraints on Very High Energy Gamma-Ray Emission from Gamma-Ray Bursts*, ApJ, 630, 996-1002 (2005)

[87] Parkinson S.P.M., *Milagro Search for VHE Emission from GRBs in the Swift Era*, `astro-ph/0611457` (2006)

[88] Jarvis A. et al., *GRB Observations around 100 GeV with STACEE*, Proc. 29$^{\text{th}}$ ICRC, Pune, India, 455-459 (2005)

[89] Baring M.G. and Harding A.K., *The Escape of High-Energy Photons from Gamma-Ray Bursts*, ApJ, 491, 663-686 (1997)

[90] Lithwick Y. and Sari R., *Lower Limits on Lorentz Factors in Gamma-Ray Bursts*, ApJ, 555, 540-545 (2001)

[91] Plaga R., *Detecting Intergalactic Magnetic Fields Using Time Delays in Pulses of Gamma-Rays*, Nature, 374, 430 (1995)

[92] Knapp J. and Heck D., *EAS Simulation with CORSIKA: A Users Manual* Forschungszentrum Karlsruhe (2004)

[93] Schmidt F., *Corsica shower images*, `http://www.ast.leeds.ac.uk/~fs/showerimages.html` (2006)

[94] Rossi B., *High-Energy Particles*, Prentice-Hall, New York (1952)

[95] Barrio J.A. et al., *MAGIC Design Report*, Max-Planck-Institut für Physik, Munich, Germany, MPI-PhE/98-5 (1998)

[96] Nishimura J. and Kamata K., *On the Theory of Cascade Showers, I*, Progress of Theoretical Physics, 7, 185-192 (1952)

[97] Greisen K., *Cosmic Ray Showers*, Annual Review of Nuclear and Particle Science, 10, 63-108 (1960)

[98] Gaisser T.K., *Cosmic Rays and Particle Physics*, Cambridge University Press (1990)

[99] Cawley M.F. and Weeks T.C., *Instrumentation for Very High Energy Gamma-Ray Astronomy*, Experimental Astronomy, 6, 7-42 (1995)

[100] Fuchs M., *Bestimmung der Transmission der Atmosphäre mittels Pyroskop und LIDAR für das MAGIC Teleskop in La Palma*, Diploma thesis, University of Applied Sciences, Munich, Germany (2006)

[101] Albert J. et al., *Physics and Astrophysics with a ground-based gamma-ray telescope of low energy threshold*, Astroparticle Physics, 23, 493-509 (2005)

[102] Ferenc D., *The MAGIC gamma-ray observatory*, NIM, Section A, 553, 274-281(2005)

[103] Bretz T., Dorner D. and Wagner R.M., *The tracking system of the MAGIC telescope*, Proc. 28$^{\text{th}}$ ICRC, Tsukuba, Japan, 2943-2946 (2003)

[104] Wagner R.M., *Measurement of VHE γ-ray emission from four blazars using the MAGIC telescope and a comparative blazar study*, PhD thesis, Technical University of Munich, Germany (2006)

[105] Barthelmy S.D. et al., *Progress with the Real-Time GRB Coordinates Distribution Network (BACODINE)*, Proc. 3$^{\text{rd}}$ Huntsville GRB Workshop, AIP (1996)

[106] Ricker G.R. et al., *The High Energy Transient Explorer (HETE): Mission and Science Overview*, Proc. Gamma-Ray Burst and Afterglow Astronomy, AIP, 662, 3-16 (2003)

[107] Schneider P., *Special Letters issue on: First science with INTEGRAL*, A&A, 411 (2003)

[108] Tamagawa T. et al., *Prompt Gamma-ray Burst Alert System of the HETE-2 Spacecraft*, Proc. 28$^{\text{th}}$ ICRC, Tsukuba, Japan, 2741-2744 (2003)

[109] Mereghetti S. et al., *The INTEGRAL Burst Alert System (IBAS)*, A&A, 411, L291 (2003)

[110] Galante N., *Very High Energy observation of GRBs with the MAGIC Telescope*, PhD thesis, Universitá degli studi di Siena, Italy (2006)

[111] Galante N., Bastieri D., Gaug M., Garczarczyk M. and Peruzzo L., *The MAGIC Telescope and the Observation of Gamma Ray Bursts*, Proc. 28$^{\text{th}}$ ICRC, Tsukuba, Japan, 2753-2756 (2003)

[112] Bradbury S.M. et al., *A Project for a* 17 m *Diameter Imaging Cherenkov Telescope*, Proc. 24$^{\text{th}}$ ICRC, Rome, Italy, Vol. 1, 1051-1054 (1995)

[113] Wacker A., *Entwicklung einer aktiven Spiegelsteuerung zur Korrektur der Verformung der Spiegeloberfläche des 17 m Luft-Cherenkov-Teleskops zur Hochenergie-Gamma-Astronomie*, Diploma thesis, University of Applied Sciences, Munich, Germany (1997)

[114] Garczarczyk M., *Konstruktion und Bau der aktiven Spiegelsteuerung für das 17 m Ø MAGIC Cherenkovteleskop zur Hochenergie-Gamma-Astronomie*, Diploma thesis, University of Applied Sciences, Munich, Germany (2001)

[115] Bretz T., *Observations of the Active Galactic Nucleus 1ES 1218 +304 with the MAGIC-telescope*, PhD thesis, University of Würzburg (2006)

[116] Bernlöhr K. et al., *The optical system of the H.E.S.S. imaging atmospheric Cherenkov telescopes. Part I: layout and components of the system*, Astroparticle Physics, 20, 111-128 (2003)

[117] Enomoto R. et al., *Design study of CANGAROO-III, stereoscopic imaging atmospheric Cherenkov telescopes for sub-TeV / γ-ray detection*, Astroparticle Physics, 16, 235-244 (2002)

[118] Holder J. et al., *The first VERITAS Telescope*, Astroparticle Physics, 25, 391-401 (2006)

[119] Ohishi M. et al., *Performance of the Reflector of the CANGAROO-III Imaging Atmospheric Cherenkov Telescope*, Proc. 28$^{\text{th}}$ ICRC, Tsukuba, Japan, 2855-2858 (2003)

[120] Cornils R. et al., *The optical system of the H.E.S.S. imaging atmospheric Cherenkov telescopes, Part II: mirror alignment and point spread function*, Astroparticle Physics, 20, 129-143 (2003)

[121] Cornils R. et al., *The optical system of the H.E.S.S. II telescope*, Proc. 29$^{\text{th}}$ ICRC, Pune, India, 101-106 (2005)

[122] Garczarczyk M., Merck M., Danielyan V., Lorenz E., Mirzoyan R. and Laille A., *The Active Mirror Control for the MAGIC Telescope*, Proc. 28$^{\text{th}}$ ICRC, Tsukuba, Japan, 2935-2938 (2003)

[123] Biland A., Garczarczyk M., Anderhub H., Danielyan V., Hakobian D., Lorenz E., Merck M. and Mirzoyan R., *The active mirror control for the MAGIC Telescope*, Towards a Network of Atmospheric Cherenkov Detektors, Palaiseau, France, 561-565 (2005)

[124] Mirzoyan R., Fonseca V., Garczarczyk M., Mariotti M., Martinez M., Lorenz E., Paoletti R., Peruzzo L., Teshima M., Turini N. and Ferenc D., *Technical Innovations for the MAGIC Project*, Proc. 28$^{\text{th}}$ ICRC, Tsukuba, Japan, 2963-2965 (2003)

[125] Beckers J.M., *Adaptive optics for astronomy - Principles, performance, and applications*, Annual review of astronomy and astrophysics, 31, 13-62 (1993)

[126] Mirzoyan R. et al., *The first telescope of the HEGRA air Cherenkov imaging telescope array*, NIM, Section A, 351, 513-526 (1994)

[127] Bastieri D., Garczarczyk M. et al., *The Mirrors of the MAGIC Telescope*, Proc. 29$^{\text{th}}$ ICRC, Pune, India, 5, 283-286 (2005)

[128] Tonello N., *Study of the VHE γ-ray emission from the Active Galactic Nucleus 1ES1959+650*, PhD thesis, Technical University of Munich, Germany (2006)

[129] Gaug M., *Calibration of the MAGIC Telescope and Observation of Gamma Ray Bursts*, PhD thesis, Universitat Autònoma de Barcelona, Spain (2006)

[130] Mirzoyan R., Paneque D., Garczarczyk M., Hose J., *A simple method to measure the reflectivity of the reflector of a prime focus telescope*, submitted to A&A (2006)

[131] Hanisch R.J. et al., *Definition of the Flexible Image Transport System (FITS)*, A&A, 376, 359-380 (2001)

[132] Longhurst R.S., *Geometrical and Physical Optics*, 3rd Edition, Continental Printing Co. Ltd. (1973)

[133] Schroeder D., *Astronomical Optics*, 2nd Edition, Academic Press (2000)

[134] Korsch D., *Reflective Optics*, Academic Press (1991)

[135] Motoki M. et al., *Precise measurements of atmospheric muon fluxes with BESS spectrometer*, Astroparticle Physics, 19, 113-126 (2003)

[136] Seguinot J. and Ypsilantis T., *A historical survey of ring imaging Cherenkov counters*, NIM, Section A, 343, 1-29 (1994)

[137] Vacanti G. et al., *Muon ring images with an atmospheric Cherenkov telescope*, Astroparticle Physics, 2, 1-11 (1994)

[138] Goebel F. et al., *Absolute energy scale calibration of the MAGIC telescope using muon images*, Proc. 29$^{\text{th}}$ ICRC, Pune, India, 179-183 (2005)

[139] Mirzoyan R. et al., *Contraints in Reducing the Threshold of Imaging Cherenkov Telescopes*, Proc. Towards a Major Atmospheric Cherenkov Detector, 298-315 (1997)

[140] Pichler B.J., Lorenz E., Mirzoyan R. et al., *Production of a diffuse very high reflectivity material for light collection in nuclear detectors*, NIM, Section A, 442, 333-336 (2000)

[141] Bartko H., Gaug M., Moralejo A. and Sidro N., *FADC pulse reconstruction using a digital filter for the MAGIC telescope*, astro-ph/0506459 (2005)

[142] Bretz T. and Wagner R., *The MAGIC analysis and reconstruction software*, Proc. 28$^{\text{th}}$ ICRC, Tsukuba, Japan, 2947-2951 (2003)

[143] Rademaker F. and Brun R., *ROOT: An Object-Oriented Data Analysis Framework*, Linux Journal, 51 (1998), `http://root.cern.ch`

[144] Mirzoyan R. and Lorenz E., *On the Calibration Accuracy of Light Sensors in Atmospheric Cherenkov, Fluorescence and Neutrino Experiments*, Proc. 25$^{\text{th}}$ ICRC, Durban, South Africa, 265-268 (1995)

[145] Hillas A., *Cherenkov light images of EAS produced by primary gamma showers*, Proc. 19$^{\text{th}}$ ICRC, La Jolla, USA, 445-448 (1985)

[146] Schweizer T., *Analysis of the Large Gamma Ray Flares of Mkn 421 as observed with HEGRA CT1 on the Island La Palma in 2001*, PhD thesis, Universitat Autònoma de Barcelona, Spain (2002)

[147] Reynolds P.T. et al., *Survey of candidate gamma-ray sources at TeV energies using a high-resolution Cerenkov imaging system - 1988-1991*, ApJ, 404, 206-218 (1993)

[148] Breiman L., *Random Forests*, Machine Learning, 45, 5-32 (2001)

[149] Chilingarian A. A., *Neural Net Classification of the gamma and proton images registered with Atmospheric Cherenkov Technique, Random Search Learning in Feed-Forward Networks*, Proc. 22$^{\text{nd}}$ ICRC, Dublin, Ireland, 540 (1991)

[150] Fegan D., *Topical Review: γ-hadron separation at TeV energies*, Journal of Physics G, Nuclear Physics, 23, 1013 (1997)

[151] Li T. and Ma Y., *Analysis methods for results in gamma-ray astronomy*, ApJ, 272, 314-324 (1983)

[152] Feldman G.J. and Cousins R.D., *Unified approach to the classical statistical analysis of small signals*, Physical Review D, 57, 3873 (1998)

[153] Neyman J., *Outline of a theory of statistical estimation based on the classical theory of probability*, Philos. Trans. R. Soc. London, A236, 333-380 (1937)

[154] Rolke W. and Lopez A., *Confidence intervals and upper bounds for small signals in the presence of background noise*, NIM, Section A, 458, 754-758 (2001)

[155] Rolke W., Lopez A. and Conrad J., *Limits and confidence intervals in the presence of nuisance parameters*, NIM, Section A, 551, 493-503 (2005)

[156] Conrad J., Trolke, ROOT class, `http://root.cern.ch/root/html1510/TRolke.html` (2005)

[157] Garczarczyk M., Bastieri D., Galante N., Gaug M. and Mizobuchi S., *Search for Gamma Ray Bursts with the MAGIC Telescope*, Proc. 29$^{\text{th}}$ ICRC, Pune, India, 4, 435-438 (2005)

[158] Krimm H., Parsons A. and Markwardt C., *BAT Ground Analysis Software Manual*, `http://heasarc.gsfc.nasa.gov/docs/swift/analysis/` (2004)

[159] Capalbi M., Perri M., Saija B. and Tamburelli F., *The SWIFT XRT Data Reduction Guide*, `http://heasarc.gsfc.nasa.gov/docs/swift/analysis/` (2005)

[160] Arnaud K. in Jacoby G., Barnes J. eds, *Astronomical Data Analysis Software and systems*, ASP Conference Series, 101, 17 (1996)

[161] Quinn J. et al., *Detection of gamma rays with $E > 300\,\mathrm{GeV}$ from Markarian 501*, ApJ, 465, L83-L86 (1996)

[162] Barbier L.M. et al., GCN circular 3296 (2005)

[163] Blustin A. et al., GCN circular 3307 (2005)

[164] Godet O. et al., *X-ray flares in the early Swift observations of the possible naked gamma-ray burst 050421*, A&A, 452, 819-825 (2006)

[165] Gotz D. et al, GCN circular 3323 (2005)

[166] Private communication with McBreen S., responsible person for INTEGRAL GRB data analysis

[167] Yost S.A. et al, *Optical light curve and cooling break of GRB050502a*, ApJ, 636, 959-966 (2006)

[168] Guidorzi C. et al., *The early (< 1 hr) multi-color afterglow of GRB050502a: Possible evidence for a uniform medium with density clumps*, astro-ph/0507639 (2005)

[169] Chen H.W. et al., GCN circular 3332 (2005)

[170] Barthelmy S. et al., GCN circular 3360 (2005)

[171] Hurkett C. et al., *GRB050505: A high redshift burst discovered by SWIFT*, MINRAS, 368, 1101, astro-ph/0602236 (2006)

[172] Cenko Bradley S. et al., GCN circular 3366 (2005)

[173] Bloom J.S., Frail D.A. and Kulkarni S.R., *Gamma-Ray Bursts Energetics and the Gamma-Ray Burst Hubble Diagram: Promises and Limitations*, ApJ, 594, 647-683 (2003)

[174] Hurkett C. et al., GCN circular 3379 (2005)

[175] Kennea J.A. et al., GCN circular 3380 (2005)

[176] Falcone A. et al., GCN circular 3581 (2005)

[177] Aptekar R.L. et al., *Konus-W Gamma-Ray Burst Experiment for the GGS Wind Spacecraft*, Space Science Reviews, 71, 265-272 (1995)

[178] Morris D.C., Reeves J., Pal'shin V., Garczarczyk M., Falcone A.D., Burrows D.N., Krimm H., Galante N., Gaug M., Golenetskii S., Mizobuchi S., Pagani C., Stamerra A., Teshima M., Beardmore A.P., Godet O. and Gehrels N., *GRB050713a: High energy observations of the GRB prompt and afterglow emission*, accepted by ApJ (2006), astro-ph/0602490 (2006)

[179] Albert J. et al., *Flux Upper Limit on Gamma-Ray Emission by GRB050713a from MAGIC Telescope Observations*, ApJ, 641, L9-L12 (2006)

[180] Barthelmy S. et al., GCN circular 3910 (2005)

[181] Watson D. et al., *Outshining the quasars at reionisation: The X-ray spectrum and lightcurve of the redshift 6.29 γ-ray burst GRB050904*, astro-ph/0509640 (2005)

[182] Kawai N. et al., *An optical spectrum of the afterglow of a γ-ray burst at a redshift of $z = 6.295$*, Nature, 440, 184-186 (2006)

[183] Lamb D. et al., GCN circular 4550 (2006)

[184] Donaghy T.Q. et al., *HETE-2 Localizations and Observations of Four Short Gamma-Ray Bursts: GRBs 010326B, 040802, 051211 and 060121*, astro-ph/0605570 (2006)

[185] Mangano V. et al., GCN circular 4560 (2006)

[186] Levan A.J. et al., *The faint afterglow and host galaxy of the short-hard GRB060121*, astro-ph/0603282 (2006)

[187] Postigo A. et al., Nature, submitted

[188] Barthelmy S. et al., GCN circular 4641 (2006)

[189] Morris D. et al., GCN circular 4651 (2006)

[190] Khamitov I. et al., GCN circular 4652 (2006)

[191] Palmer D. et al., GCN circular 4682 (2006)

[192] Morris D. et al., GCN circular 4694 (2006)

[193] Fynbo J.P.U. et al., *Probing Cosmic Chemical Evolution with Gamma-Ray Bursts: GRB060206 at $z = 4.048$*, astro-ph/0602444 (2006)

[194] Monfardini A. et al., *High quality early time light curves of GRB060206: Implications for gamma ray burst environments and energetics*, astro-ph/0603181 (2006)

[195] Garczarczyk M. et al., GCN circular 5571 (2006)

[196] Garczarczyk M. et al., GCN circular 5789 (2006)

Acknowledgments

I am extremely fortunate to have had the support from so many people during the course of my study, and to be a part of such a wonderful collaboration, the MAGIC project. First and foremost, I would like to thank my advisor Eckart Lorenz. He supported me from the beginning of my studies in the Max-Planck-Institute and encouraged me to continue my scientific career. I am also very grateful to Masahiro Teshima and Razmik Mirzoyan who guided me so patiently through the research projects and for providing me the opportunities to follow and extend my scientific interests, through visiting several conferences and schools.

I am also very grateful to Henning Schröder and to David Blaschke for advocating. Without their recommendation and assistance at the University of Rostock, my thesis would not have been possible. At the same time I am very thankful to Michael Bayer and Roland Waldi for the fruitful discussions during my visits at the University Rostock and the summer schools in Prerow.

Over the years, I had the privilege of working with many wonderful scientists. I especially thank Adrian Biland and Martin Merck for the fruitful team work on the improvements of the AMC system. Also, I thank Mosè Mariotti and Denis Bastieri for the support and help during the mirror installation.

Special thanks are directed to Markus Gaug for the wonderful cooperation and numerous useful discussions during the analysis of the GRB data. His assistance and advice in the analysis of the MAGIC telescope data helped me to understand many important details of the analysis chain. Thanks are addressed to him, to Patrick Phelan and Kenji Shinozaki for cross-reading of the thesis.

I would like to thank all the members of the MAGIC group in Munich. Many thanks to Nadia Tonello, Satoko Mizobuchi, Ching Cheng Hsu, Daniel Mazin, Florian Göbel, Hendrik Bartko, Jürgen Hose, Kenji Shinozaki, Masaaki Hayashida, Nepomuk Otte, Pratik Majumdar, Ralf Kosyra, Robert Wagner, Rudolf Bock and Wolfgang Wittek. Special thanks are addressed to the Spanish members Toni Coarasa, David Paneque and Emiliano Carmona for many enjoying and interesting discussions.

The drawing in the beginning of the thesis was made by Brigit Pflügler. It illustrates a small part of the sky in VHE, as seen by an artist (real drawing, shown only in the original version).

Finally, I wish to extend my most heartfelt thanks to my mother Helena, my father Franz Garczarczyk, my uncle Alois, as well as the entire family of my brother Adam. They have constantly encouraged and supported me during my thesis and suffer long years of my absence at home: Dziękuję moja kochana rodzinko.